POLITECNICO DI MILANO

DOCTORAL PROGRAM IN "ENERGY AND NUCLEAR SCIENCE AND TECHNOLOGY"

XXV CYCLE

Experimental Investigation and Numerical Simulation of the Two-Phase Flow in the Helical Coil Steam Generator

TUTOR: Prof. Marco Enrico Ricotti

SUPERVISOR: Dr. Antonio Cammi

Dr. Luigi Colombo

PhD CANDIDATE:
Marco Colombo
753261

FEBRUARY 2013

CONTENTS

ACRONYMS

AGR	Advanced Gas Reactor
ALMR	Advanced Liquid Metal Reactor
BWR	Boiling Water Reactor
CFD	Computational Fluid Dynamics
DWO	Density Wave Oscillation
EHRS	Emergency Heat Removal System
ELSY	European Lead-cooled System
EVET	Equal Velocity Equal Temperature
GCR	Gas Cooled Reactor
GIF	Generation IV International Forum
HTGR	High Temperature Gas Reactor
IAEA	International Atomic Energy Agency
IRIS	International Reactor Innovative and Secure
KAERI	Korean Atomic Energy Research Institute
LFR	Lead Fast Reactor
LMFR	Liquid Metal Fast Reactor
LMFBR	Liquid Metal Fast Breeder Reactor
LOCA	Loss Of Coolant Accident
LWR	Light Water Reactor
ODE	Ordinary Differential Equation
PWR	Pressurized Water Reactor
QUICK	Quadratic Upstream Interpolation for Convective Kinetics
RELAP	Reactor Excursion and Leak Analysis Program
RNG	ReNormalization Group
RSM	Reynolds Stress Model
RWST	Refueling Water Storage Tank
SBLOCA	Small Break LOCA
SFR	Sodium-cooled Fast Reactor
SG	Steam Generator
SIET	Società Informazioni Esperienze Termoidrauliche
SIMPLE	Semi-Implicit Method for Pressure-Linked Equations
SIMPLEC	SIMPLE-Consistent
SMART	System-integrated Modular Advanced Reactor
SMR	Small-medium Modular Reactor
SST	Shear Stress Transport
THTR	Thorium High Temperature Reactor
UVUT	Unequal Velocity Unequal Temperature

NOMENCLATURE

A	cross sectional area [m^2]
A_1, A_2, A_3	empirical constants [-]
a	empirical constant [-]
C	exchange coefficient in the Eulerian model [kg/m^3s]; constant in Eq.(5.10)
C_0	distribution parameter
C_w	thermal capacity of the wall [J/kg°C]
c	coefficient [-]
D	coil diameter [m]
d	pipe diameter [m]
d_p	diameter of the dispersed phase [m]
De	Dean number [-]
E	constant [-]
e	error [-]
F	force [N]
Fr	Froude number [-]
f	friction coefficient [-]; drag function [-] in Eq.(4.4) and Eq.(4.6)
G	mass flux [kg/m^2s]
g	gravitational acceleration [m/s^2]; general function in Eq.(7.57)
H	height [m]
h	enthalpy [J/kg]; heat transfer coefficient [W/m^2K] in Eq.(6.49) and Eq.(6.50)
h_s	coil pitch per revolution of the coil [m]
I	turbulence intensity [%]
j	superficial velocity [m/s]
K	valve loss coefficient [-]
K'	Karman constant [-]
K_B	Bankoff parameter [-]
k	turbulent kinetic energy [m^2/s^2]
L	length [m]
L'	turbulence characteristics length scale [m]
M	Interaction term between the phases in the Eulerian model [kg/ms^2]
M_w	mass of the tube wall [kg]
m	mass [kg]
N_{pch}	phase-change number [-]
N_{sub}	subcooling number [-]
P	perimeter [m]
p	pressure [Pa]
p_s	coil pitch per radiant [m/rad]
q	thermal power [W]

q''	thermal flux [W/m^2]
R	coil radius [m]
Re	Reynolds number [-]
r	pipe radius [m]
S	tube surface [m^2]
T	temperature [°C]; period of the oscillations [s] in sections 2.4.6 and 6.5.1.2
t	time [s]
V	volume [m^3]
V_{gj}	drift velocity weighted on the void fraction [m/s]
v	velocity [m/s]
v^*	dimensionless velocity [-]
v_{gj}	local drift velocity [m/s]
v	specific volume [m^3/kg]
x	quality [-]
x_v	volumetric flow quality [-]
Y	general function
y	general function
y^+	dimensionless distance from the wall [-]
We	Weber number [-]
z	axial coordinate [m]
z_b	boiling boundary [m]

Greek symbols

α	void fraction [-]
β	inclination angle of the helix [°]
β_0	torsion parameter [-]
γ	density ratio [-]
δ	dimensionless curvature [-]
Γ	mass flow rate [kg/s]
Γ_g	volumetric rate of vapor production [kg/m^{3}s]
ε	turbulent kinetic energy dissipation rate [m^2/s^3]
θ	angle [°]
λ	dimensionless curvature [-]
μ	viscosity [Pa·s]
ρ	density [kg/m^3]
σ	surface tension [N/m]
τ	wall shear stress [N/m^2], transit time in the heated channel [s] in Chapter 2
τ_{rt}	particle relaxation time [s]
Φ	two-phase friction multiplier [-]
χ	Martinelli parameter [-]
Ω	frequency of phase change [1/s]
ω	specific dissipation rate [1/s]

Subscripts

1θ	single-phase
2θ	two-phase
a	air
acc	accelerative
c	coil
cent	centrifugal
cr	critical
D	Darcy
e	effective
exp	experimental
FR	Friedel
f	fluid
fr	friction
g	gas-phase
grav	gravitational
in	inlet
LM	Lockhart-Martinelli
l	liquid
lo	liquid-only
m	mixture
out	outlet
R	riser
s	straight
sat	saturation
theo	theoretical
tp	two-phase
v	vapor
vo	vapor-only
w	water; wall in Eq.(6.49) and Eq.(6.50)
%	percentage

Superscripts

1θ	single-phase
2θ	two-phase
R	riser

INTRODUCTION

Numerous nuclear reactor projects of both Generation III+ and Generation IV presently under development are expected to use helically coiled pipes for the Steam Generator (SG). The improvement of such an important plant component is vital as much as the research for new technological solutions for future nuclear power plants. Indeed, they are designed to reach the goal of improved safety, performance and cost established by the world nuclear community. Numerous favorable characteristics justify the renewed interest for the helical tube SG developing in the nuclear field. In particular, helical tubes provide enhanced heat and mass transfer rates, a higher critical heat flux during boiling and evaporation and a better capability to accommodate the thermal expansion, in addition to allow a more compact design of the SG. Helical coils are particularly attractive for Small-medium Modular Reactors (SMRs) of Generation III+, since many of them adopt an integral layout. Compactness and efficiency improvement become particularly important for this type of reactors, as all the primary system components are located inside the reactor vessel.

Within these respects, the thesis work is the natural prosecution of the recent efforts made by the Nuclear Engineering Division of the Department of Energy at the Politecnico di Milano. The group has been involved since many years into the study of SMRs. In particular, as regards the thermal hydraulics, the research has been focused on the helically coiled SG and the passive safety systems. The Division has been a member of the IRIS project (International Reactor Innovative and Secure), an integral Pressurized Water Reactor (PWR) of 335 MWe of power, developed by an international consortium. In the frame of the IRIS project, an experimental facility was built at the SIET laboratories, in Piacenza, to simulate the SG and the Emergency Heat Removal System (EHRS) of the reactor. The availability of the facility allowed the execution of numerous experiments, presented in two past doctoral works (Santini, 2008; Papini, 2011).

In this doctoral thesis, to make a further step forward on the study of the thermal hydraulic of the helically coiled SG tube, different subjects are addressed. Since helically coiled pipes have been utilized in many industrial fields, numerous researches have been conducted in the past. Although, improvements are still necessary, for an improved efficiency through an optimized design and a better understanding of the component operation. The latter, in particular, is crucial for the application of a component in the nuclear field, which requires the assurance of a safe operation of the nuclear system. The thesis work discusses different subjects, dealing with the characterization of the system through the study of the frictional pressure drop, the two-phase flow structure and the void fraction. At the same time, also the dynamic behavior is addressed with the study of the two-phase flow instabilities in parallel channels. A careful characterization and a precise quantification of all of them are of fundamental importance, not only for the design of the SG but of the whole secondary system. To the aim, simple but precise simulation tools are required, together with modeling instruments able to describe in detail the phenomena of interest and the interrelation between

the physical quantities involved. Analytical and empirical models are developed for a reliable estimation of the physical quantities under study, which become particularly important for the engineers involved in the design process. Furthermore, also the additional level of complexity introduced by the helical geometry is addressed, especially for the two-phase flow. As a consequence, the work is also focused on the improvement of the understanding of some basic physical phenomena, as for example the influence of the centrifugal force on the phase distribution and the interaction between the phases. For this second main objective, the Computational Fluid Dynamics (CFD) is selected as the main research tool, since it can provide the required level of detail. In particular, the ANSYS FLUENT code is applied. In view of the pointed out diversified necessities, an overall analysis method is employed throughout the whole thesis work, based on the application and strict and continuous interrelation between experimental data, numerical simulations and development of analytical and empirical models.

Starting point of the research activity is the availability of a large number of experimental data, which are necessary for model development and validation of numerical results. The data were measured in the mentioned SIET experimental facility. In particular, the database built during the three year doctoral program includes measurements of frictional pressure drop and instability of the two-phase flow. In particular, the frictional pressure drops were measured for a single-phase liquid flow and an adiabatic two-phase flow. The instability database includes instead the Density Wave Oscillations (DWOs) and some experiments on the Ledinegg instability.

The first section of the work analyzes the single-phase flow. The experimental data are compared with some empirical correlations for the friction factor and the laminar to turbulent flow transition. However, correlations are not sufficient when a more detailed description of the system is desirable, requiring the support of more complex but powerful tools. Therefore, the single-phase flow is characterized in detail with CFD numerical simulations. In the laminar region, the effect of the centrifugal force field on the flow is studied in particular, whereas a comparison of numerous turbulence models is proposed for the turbulent region. In the whole chapter, a particular attention is always reserved to the frictional pressure drop, with numerical predictions validated through comparison with the experimental data.

The larger part of the thesis is dedicated to the two-phase flow. The CFD analysis is applied also to the two-phase flow, together with the development of new empirical correlations, following the structure of the work established at the beginning. Therefore, a more detailed numerical study, necessary to understand the effect of the centrifugal force on the phase distribution, is coupled with the development of more simple tools useful for a quantification of the physical quantities of interest. The two-phase flow is modeled through the Eulerian – Eulerian multiphase model. An adiabatic flow is simulated, that is phase change and energy exchanges between the phases are neglected. In addition, only the drag force is considered as a term of momentum exchange between the phases. Initially, an air-water flow at atmospheric pressure is considered, as a larger quantity of available experimental data allows a more comprehensive validation of the numerical results. After the validation of the air-water results, also the SIET steam-water case is simulated, comparing the results with the experimental data of adiabatic frictional pressure drops. In addition, starting from the CFD simulations, an explanation is proposed for the pronounced peak of the frictional pressure drop profile observed during the experiments. Finally, numerical results are

used to overcome the shortage of available experimental data on the void fraction, not measurable in the SIET facility. A new empirical correlation is proposed for the void fraction, starting from the drift-flux formulation. A further validation of the CFD local velocity fields and void fraction distributions is also proposed, based on the parameters of the drift-flux model.

A new empirical correlation is also developed for the two-phase frictional pressure drop. The new correlation is developed with the aim to obtain a formula accurate in a large range of geometries and operating conditions. Actually, numerous correlations are available in literature, but none of them is reliable in a wide range of parameters.

The global approach adopted in the whole thesis is even reinforced for the last subject, that is the study of the DWOs in parallel channels. An existing non linear analytical dynamic model, based on the homogeneous flow theory, is upgraded to a drift-flux formulation. The empirical correlations developed for the frictional pressure drop and the void fraction are included into the model. The improved predictions of the stability boundary are validated with comparison against the experimental stability maps. At the same time, also an assessment of the results of the RELAP5 numerical code is carried out, as it is largely adopted for transient simulation and safety analysis of nuclear plants.

CHAPTER 1

THE HELICAL TUBE

This first brief chapter aims to be a quick introduction to the subject of the whole thesis work. Initially, the most important parameters introduced with the helical geometry are identified, together with some related dimensionless quantities, as coil curvature and torsion. Dimensionless quantities will become important in the following to characterize the effect induced by the centrifugal force field on the fluid flow.

The second part of the chapter discusses the numerous applications of the helical pipe in different industrial fields. Past and future applications in the nuclear industry are presented in details, with particular attention to the Small-medium Modular Reactor (SMR) concept, which will be frequently addressed during the thesis work.

1.1 The helical geometry

All the thermal hydraulic studies presented in the thesis work are focused on the helically coiled tube, due to the increasing appeal it is experiencing in the nuclear field, being of interest for a growing number of reactor projects. The change in the geometry with respect to a straight vertical, inclined or horizontal tube introduces new geometrical quantities. A schematic representation of an helical coil with its main geometrical parameters is shown in Figure 1.1. In addition to the pipe diameter *d*, the helically coiled pipe is characterized also by the diameter of the coil *D* and the angle of inclination β, which represents the inclination of the pipe with respect to the horizontal direction. The other fundamental parameter is the coil pitch p_s, which is the change in elevation per radiant, which leads also to the increase in elevation per revolution of the coil, $h_s = 2\pi p_s$.

The new geometrical quantities require the definition of new parameters, necessary to quantify the influence of the geometry on the fluid flow. In particular, the helical geometry introduces a centrifugal force field which acts on the fluid flow modifying the parabolic shape of the flow field, typical of a straight duct. The centrifugal force is function of mass, velocity and curvature radius, that in this case is exactly the radius of the coil:

$$F_{cent} = \frac{m\mathrm{v}^2}{R} \tag{1.1}$$

To characterize the geometry, new important dimensionless parameters were introduced, the dimensionless curvature λ and the dimensionless torsion δ. The introduction of an helical

orthogonal coordinate system leads some authors to the following definitions (Germano, 1982; Huttl and Friedrich, 2000):

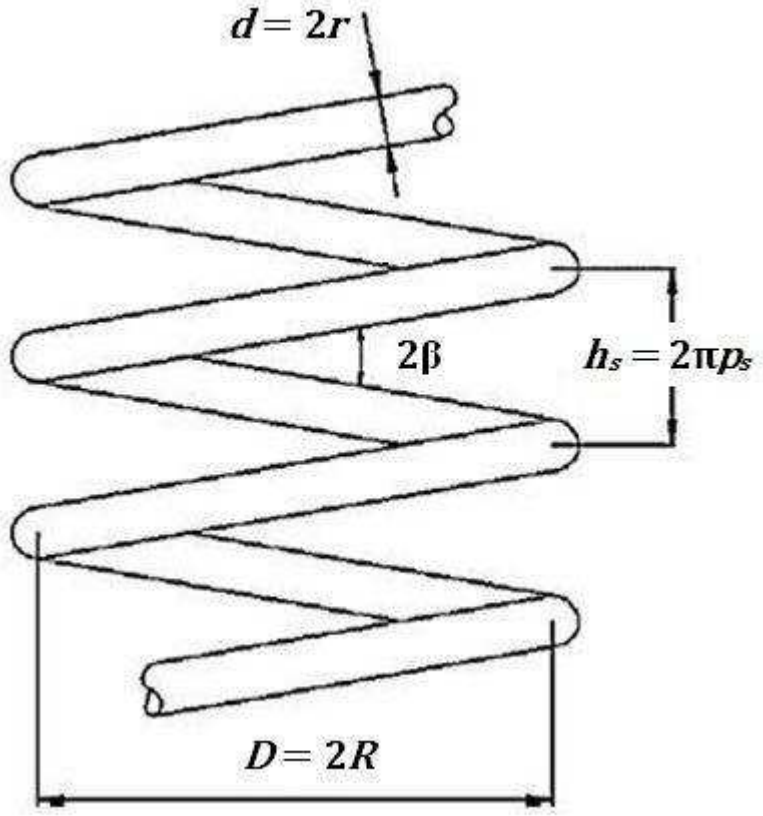

Figure 1.1 Sketch of an helical pipe.

$$\lambda = \frac{R^2}{\sqrt{R^2 + p_s^2}} \tag{1.2}$$

$$\delta = \frac{p_s}{\sqrt{R^2 + p_s^2}} \tag{1.3}$$

Also the torsion parameter β_0 is often used, defined as:

$$\beta_0 = \frac{\lambda}{\sqrt{2\delta}} \tag{1.4}$$

Eq.(1.2) and Eq.(1.3) were not universally adopted by all the authors, as other definition of dimensionless curvature and torsion have been defined during the years. Here, two other definitions are proposed, one from the work of Yamamoto et al.(1995):

$$\lambda = \frac{rR}{R^2 + p_s^2} \tag{1.5}$$

$$\delta = \frac{r p_s}{R^2 + p_s^2} \tag{1.6}$$

and a different one from the work of Di Piazza and Ciofalo (2010):

$$\lambda = \frac{r}{R} \tag{1.7}$$

$$\delta = \frac{p_s}{R} \tag{1.8}$$

The identification of the better expression for both curvature and torsion is out of the scope of this section. The different formula have been reported for major information, as the aim is to underline their meaning, which is the same independently from their numerical value. The dimensionless curvature takes into account the effect of the coil diameter, that is of the centrifugal force. An higher value of the curvature means a more tight coil, so an higher centrifugal force. The dimensionless torsion, instead, takes into account the effect of the coil pitch. An higher dimensionless torsion means an higher inclination of the coil with the same coil diameter or a more twisted pipe with the same total tube length. While the curvature has a first order effect on the flow, the torsion is known to have a second order effect (Germano, 1982; Yamamoto et al., 1995; Huttl and Friedrich, 2000). The effect on the fluid flow of the curvature in particular, but in more general of the helical geometry will be discussed in details in Chapter 3.

1.2 Industrial application of the helical pipe

Helical pipes provide a substantial improvement in heat and mass transfer rates and, most important for boiling and evaporation, a significant enhancement of the critical heat flux. Contributes also to a higher heat transfer the combination of the positive features of a local cross-flow distribution with the global counter-flow along the exchanger tube (Bejan and Kraus, 2003). Helical geometry permits handling of high temperatures and extreme temperature differentials without high induced stresses (Cinotti et al., 2002). In addition, helical coil SGs and heat exchangers can assure compactness of the design with reduction of the required floor space. As a consequence, helical pipes and helically coiled tube heat exchangers are extensively used in different industrial fields and applications, including hot water heaters, chemical process reactors, industrial and marine boilers, cooling systems and blood oxygenators, among many others. In the numerous industrial fields, helically coiled heat exchangers accomplish many purposes, including liquid heating or cooling, steam heating, fluid boiling, cryogenic cooling, vent condensing and separation of liquid and/or solid particles from gas streams (Lines).

For their favorable properties, helical coiled pipes have been used in the past for the SGs of more than one nuclear reactors, although they have been applied mainly in prototypes or for some special applications. Nowadays, they are object of a renewed interest in the frame of the reactor projects of Generation III+ and Generation IV.

1.2.1 The helical pipe in the nuclear industry

Helically coiled pipes found some applications mainly in a couple of reactor technologies, the Gas Cooled Reactor (GCR) and the Liquid Metal Fast Reactor (LMFR).

Among the nuclear reactors cooled by gas, the Advanced Gas Reactor (AGR), cooled by carbon dioxide and moderated by graphite, has been equipped with 12 once-through, helically coiled pipe SGs, placed in the annulus between the reactor core and the pressure vessel. The AGR was developed and built in the Great Britain for a total of 8 units, with 7 of them still in operation (Lombardi, 2009). The helical coil SG was also used in the two main prototype of High Temperature Gas Reactor (HTGR), studied in the past as an evolution of the AGR, then abandoned from the 90's and recently object of new research programs. Both the Fort St. Vrain 330 MWe HTGR, built in the United States, and the Thorium High Temperature Reactor (THTR-300) of 300 MWe, built in Germany, were equipped with once-through, vertically oriented helical coil SGs (Lombardi, 2009).

Even more examples regarding the use of helical pipes in the SG of nuclear reactors can be found in the field of LMFR (IAEA, 1996; 2006). The most significant case is the Super-Phénix reactor, the worldwide first large LMFR, built in France and connected to the grid on January 14, 1986. Super-Phénix was a 1200 MWe, sodium cooled fast reactor. Helical SG units with a power of 750 MWt were installed and very successfully operated until the definitive closure of the reactor in 1997. Also the Japanese prototype of Sodium-cooled Fast Reactor (SFR) Monju (280 MWe) is provided with three SGs equipped with helical pipes. Other SFRs include the experimental Enrico Fermi Fast Breeder Reactor in the United States, the SNR-300 in Germany and the Advanced Liquid Metal Reactor (ALMR) also in the United States.

Following the mentioned past projects, helical tubes are again proposed for the present Generation IV reactors considering gas and liquid metal as the coolant (GIF, 2011). In particular, some studies are made in the United States for a helical tubes SG and its application in an HTGR (Hoffer et al., 2011; Sabharwall et al., 2012). In the framework of LMFR, coiled pipes are involved in the new projects of Lead Fast Reactors (LFRs), cooled by molten lead. In more details, spiral tube SGs were considered in the European project ELSY (European Lead-cooled System; Alemberti et al., 2011), whereas helical coils are the selection for the Russian project of LFR, the BREAST reactor.

1.2.2 Application in Small-medium Modular Reactors

In addition to Generation IV projects, helically coiled pipes are taken into consideration especially for Small-medium Modular Reactors (SMR) of Generation III+ (IAEA, 2005). Among others, the focus is on Pressurized Water Reactors (PWRs) which adopt an integral layout, with all the primary system located inside the reactor vessel. For an integral layout, the compactness of the SG guaranteed by the helical pipe layout is really attractive.

SMR concept aims to provide a more safe and sustainable energy, looking at the same time to a near-medium term deployment. The design rely on a "safety by design" approach, that is the elimination of the possibility of accidents from occurring rather than deal with their consequences, thus significantly improving the defence-in-depth and safety charactheristics.

In this perspective, the integral layout permits to reduce by design risks and effects of different postulated accidents, such as large releases of primary coolant (Large Break LOCA accidents). In addition, SMR projects foresee the incorporation of many inherent safety features and a large utilization of the natural circulation, for passive safety systems at least, or in some cases even for core cooling during normal operations. Benefits come also form a general simplified design or a reduced number of required safety systems, which enhance the safety of the reactor (IAEA, 2005).

The Nuclear Engineering Division has been involved since many years in the IRIS (International Reactor Innovative and Secure) project. IRIS is a pressurized water SMR concept of small-medium power (335 MWe), developed until 2011 by an international consortium lead by Westinghouse (Carelli et al., 2004). IRIS reactor adopts an integral layout and relies on the mentioned "safety by design" approach (Figure 1.2). The EHRS (Emergency Heat Removal System), which is the reactor main safety system for the core cooling, is a passive safety system and relies entirely on natural circulation to accomplish its designated safety functions (Cammi and Cioncolini, 2003). The reactor response shows special features also in case of a Small Break LOCA (LBLOCA are eliminated by design). IRIS response is based on a coupled dynamic behavior between the pressure vessel and the containment. During the first part of the transient, the pressure vessel depressurizes as water inventory is loosed to the containment. At the same time, the pressure in the containment increases until it reaches the value of the pressure inside the vessel and the loss of mass from the vessel to the containment is stopped. After the pressure equalization, further depressurization of the coupled system and long term core cooling is guaranteed by the EHRS operating in natural circulation (Papini et al., 2010).

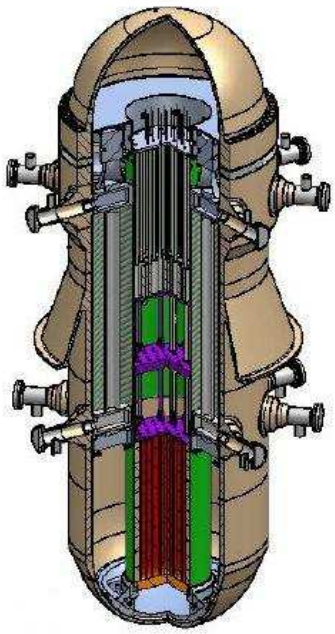

Figure 1.2 Scheme of the IRIS pressure vessel.

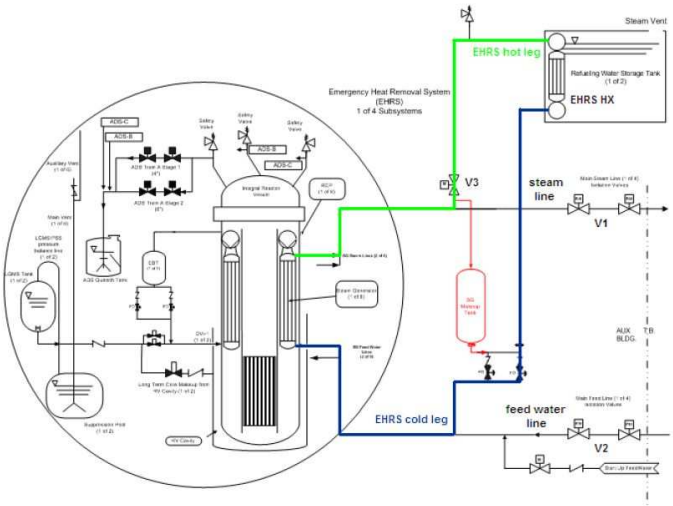

Figure 1.3 Sketch of the IRIS Emergency Heat Removal System (1 of 4), and of its connections with steam and feed water lines.

The four EHRS trains are placed outside the reactor vessel and each one is provided with an heat exchanger submerged in the Refuelling Water Storage Tanks (RWST), which acts as the heat sink. Each loop is connected to one of the helically coiled SGs, located inside the reactor vessel and used for exchange heat with the primary side also during accidents (Figure 1.3). As a consequence, the helically coiled SG plays a very important role not only during normal operations but also for accident mitigation. The IRIS reactor is provided with 8 once-through SG modules that are located in the annular region between the core barrel and the reactor pressure vessel (Figure 1.4). Each module consists of 656 tubes, with an inner tube diameter of 1.32 cm, an average length of 32 m and a total height of about 8 m (Cinotti et al., 2002).

SMART reactor is a an integral type PWR of 330 MW_{th} developed by the Korean Atomic Energy Research Institute (KAERI). The reactor adopts simplified passive safety systems and a simplified modular design of all the primary system components, located inside the reactor vessel (Kim et al., 2003). The rector is provided with 8, once-through helically coiled pipe SGs, located in the annulus between the reactor core and the pressure vessel.

NuScale Power is developing in the United States a modular, scalable, 45 MWe LWR nuclear power plant. Each NuScale module has its own combined containment vessel an reactor system, and its own turbine generator. The NuScale power plants are scalable, with the capability to have up to 12 units in a single facility. In addition, each unit can be put out of service without affecting the operation of the other units. The NuScale reactor relies on the natural circulation of water also during normal operation, that is no pump are required to circulate the coolant through the primary system. The reactor is equipped with an helical coil SG, located around the riser placed above the reactor core.

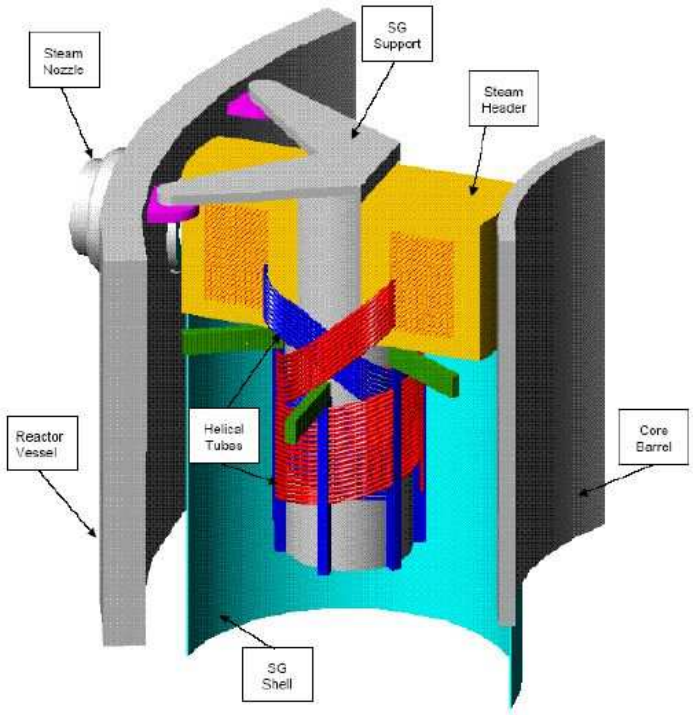

Figure 1.4 IRIS SG module and bundle configuration.

References

A. Alemberti, J. Carlsson, E. Malambu, A. Orden, D. Struwe, P.Agostini, S. Monti, 2011. European lead fast reactor – ELSY. Nuclear Engineering and Design 241, 3470-3480.

A. Bejan, A.D. Kraus, 2003. Heat Transfer Handbook. Wiley.

A. Cammi, A. Cioncolini, 2003. IRIS passive Emergency Heat Removal System – PEHRS: state of the art design and RELAP model. IRIS internal report, Westinghouse Proprietary Class 2.

M.D. Carelli, L.E. Conway, L. Oriani, B. Petrovic, C.V. Lombardi, M.E. Ricotti, A.C.O. Barroso, J.M. Collado, L. Cinotti, N.E. Todreas, D. Grgic, M.M. Moraes, R.D. Boroughs, H. Ninokata, D.T. Ingersoll, F. Oriolo, 2004. The design and safety features of the IRIS reactor, Nuclear Engineering and Design 230(1), 151-167.

L. Cinotti, M. Bruzzone, N. Meda, G. Corsini, C. Lombardi, M. Ricotti, L. Conway, 2002. Steam Generator of the International Reactor Innovative and Secure. Proceedings of the 10th Conference on Nuclear Engineering (ICONE 10), Arlington, VA, USA, 14-18 April.

I. Di Piazza, M. Ciofalo, 2010. Numerical prediction of turbulent flow and heat transfer in helically coiled pipes. International Journal of Thermal Sciences 49, 653-663.

M. Germano, 1982. On the effect of torsion on a helical pipe flow. Journal of Fluid Mechanics 125, 1-8.

GIF, 2011. Generatiov IV 2011 Annual Report.

N.V. Hoffer, P. Sabharwall, N.A. Anderson, 2011. Modeling a helical-coil steam generator in RELAP5-3D for the next generation nuclear plant. INL/EXT-10-19621.

T.J. Hüttl, R. Friedrich, 2000. Influence of curvature and torsion on turbulent flow in helically coiled pipes. International Journal of Heat and Fluid Flow 21, 345-353.

IAEA, 1995. Innovative small and medium sized reactors: design features, safety approaches and R&D trends. IAEA-TECDOC-1451, Final report of a technical meeting held in Vienna, 7-11 June 2004.

IAEA, 1996. Fast reactor database. IAEA TECDOC-866, IAEA, Vienna.

IAEA, 2006. Fast reactor database 2006 update. IAEA TECDOC-1531, IAEA, Vienna.

S.H. Kim, K.K. Kim, J.W. Yeo, M.H. Chang, S.Q. Zee, 2003. Design verification program of SMART. International Conference on Global Environment and Advanced Nuclear Power Plants, Kyoto, Japan, 15-19 September.

J.R. Lines. Helical coil heat exchangers offer advantages. Graham Manufacturing Co. Inc.

C. Lombardi, 2009. Impianti nuclear. Polipress.

D. Papini, D. Grgic, A. Cammi, M.E. Ricotti, 2010. Analysis of different containment models for IRIS small break LOCA, using GOTHIC and RELAP5 codes. Nuclear Engineering and Design 241, 1152-1164.

P. Sabharwall, J. Collins, D. Clark, A. Siahpush, W. Phoenix, M. McKellar, M. Patterson, 2012. Technology development roadmap for the advanced high temperature reactor secondary heat exchanger. INL/EXT-12-26219.

K. Yamamoto, T. Akita, H. Ikeuchi, Y. Kita, 1995. Experimental study of the flow in a helical circular tube. Fluid Dynamics Research 16, 237-249.

CHAPTER 2

THE EXPERIMENTAL ACTIVITY

When approaching the study of every thermal hydraulic subject, the availability of a large number of experimental data becomes of fundamental importance for the understanding of the physical phenomenon and the verification of any developed model. Keeping that in mind, it appeared straightforward to start the doctoral thesis with the description of the experimental databases built during the three doctoral years. The experimental measures constitute the core of the whole activity and the starting point for the study of the two-phase thermal hydraulics of the helical coil, presented in the following chapters. The experimental data, in addition to give information on the phenomena under study, will allow the assessment of the numerical results and the validation of the developed empirical and analytical models.

The first section of the chapter describes the experimental facility used for the experiments. Installed at the SIET laboratories, it served since some years for the experimental researches of the Nuclear Reactor Group of the Politecnico di Milano, focused on the helically coiled SG for application in the SMR technology.

After the presentation of the facility, the different experimental studies are presented. They are divided in two main subjects: the frictional pressure drop and the instability of the two-phase flow. Section 2.2 is dedicated to the frictional pressure drop in single-phase flow and the laminar to turbulent flow transition. After Section 2.2, the attention is rapidly focused on the two-phase flow, with the experiments on the frictional pressure drops presented in Section 2.3. The frictional pressure drop was measured in adiabatic conditions, that is at an almost constant flow quality along the test section.

Section 2.4 and Section 2.5 are dedicated to the two-phase flow instability in helical parallel channels. In particular, two different type of instability have been studied, the Density Wave Oscillations (DWOs) and the Ledinegg instability. In Section 2.4 the data on the DWO are presented, while the Ledinegg instability is the subject of Section 2.5. The DWO is probably the most common type of instability encountered in boiling channels. It is characterized by oscillations of the flow rate between the different parallel channels (as the tubes of a SG), with consequent oscillations of all the other system thermal hydraulic parameters. As the total system mass flow rate remains constant, DWOs are particularly difficult to detect and can cause significant problems to the operation of the system, up to the burn out of the heat transfer surface in extreme circumstances.

The Ledinegg is instead a static type of instability, characterized by wide flow excursions between the channels when the system operates in the negative slope region of the pressure drop versus flow rate curve (channel characteristics). The channel characteristics has been also determined through experiments, to find the regions potentially affected by the Ledinegg instability. The availability of data on both types of instability allowed to draw stability maps

with complete stable and unstable system operating regions. The two-phase flow instabilities, the DWO in particular, are presented in great details, being of particular complexity. Other than its peculiar characteristics, the phenomena at the origin of the instability mechanism are explained. Influence of system parameters as mass flow rate, pressure and inlet temperature are underlined through dedicated parametric studies.

2.1 The experimental facility

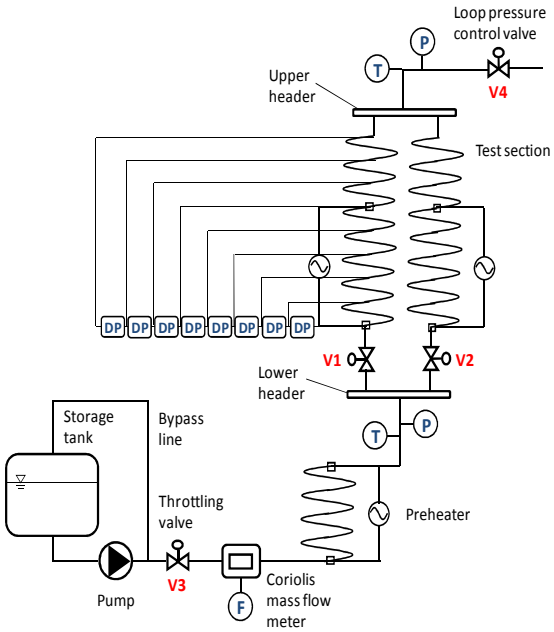

Figure 2.1 Sketch of the experimental facility installed at SIET laboratories.

The whole experimental activity was made in an experimental facility built and operated at SIET laboratories. Its present configuration is the extension of an electrically heated test section used for the study of the IRIS reactor secondary system (Santini, 2008). Initially designed as a single helically coiled SG tube facility, it was used for the study of the two-phase pressure drop and the thermal crisis (Santini et al., 2008). Original design included also a closed loop circuit, to simulate the reactor passive heat removal system operating in natural circulation (Santini et al., 2010). Recently, a second helical tube identical to the first one was added, for the study of the DWO in parallel channels.

The facility is provided with the full scale dimensions of the IRIS SG. Coil diameter (1 m) is a representative mean value between the SG different helices, while tube inner diameter (12.53 mm) is the commercially scheduled value nearer to the IRIS real value (13.24 mm). Full scale tube length (32 m) and SG height (8 m) are also reproduced. In addition, the facility is designed for the operating thermal hydraulic conditions of the IRIS SG. The conceptual sketch of the new facility is depicted in Figure 2.1, the flow diagram in Figure 2.2 and global views are provided in Figure 2.3 and Figure 2.4. Geometrical data of the two helical tubes are listed in Table 2.1.

Table 2.1 Test section geometrical data.

Tube material	SS AISI 316L
Tube inner diameter [mm]	12.53
Tube outer diameter [mm]	17.24
Coil diameter [mm]	1000
Coil pitch [mm]	800
Tube length [m]	32
Heated section length [m]	24
Riser length [m]	8
Steam generator height [m]	8

The whole facility is made by a supply section and a test section. The supply section feeds demineralized water from a tank to the test section, by means of a centrifugal booster pump and a volumetric three cylindrical pump with a maximum head of about 200 bar. The flow rate is controlled by a throttling valve (V3) positioned downwards the feed water pump and after a bypass line. System pressure control is accomplished by acting on a throttling valve (V4) placed at the end of the SG (Figure 2.5). An electrically heated preheater is located before the test section, to establish the desired inlet temperature.

The test section is electrically heated via Joule effect by DC current. It is divided into two independently controlled sections (a first 24 m section and a last 8 m section), to simulate different power distributions and consider the presence of an unheated riser. The two pipes, connected in parallel with common lower and upper headers, are thermally insulated by means of rock wool. Thermal losses were evaluated in the work of Santini (2008). They were measured via runs with single-phase hot pressurized water and estimated as a function of the temperature difference between the external tube wall and the environment. Each tube is provided at the inlet with a calibrated orifice (with a differential pressure transmitter), used to measure the flow rate in each channel. Two inlet valves are also installed, to impose a concentrated pressure drop (Figure 2.6). V1 and V2 represent the total pressure drop (instrumented orifice + valve) introduced at the inlet of the two helical tubes, respectively.

Numerous instruments are installed on the facility, to allow the measurement of all the thermal hydraulic parameters of interest. The water pressures at inlet and outlet headers are measured by absolute pressure transducers; nine pressure taps are disposed nearly every 4 m along one tube (Table 2.2) and eight differential pressure transducers connect the pressure taps (Figure 2.7). An accurate measurement of the total flow rate is obtained by a Coriolis flow meter (Figure 2.8), placed between the pump and the preheater. Bulk temperatures are measured with K-class thermocouples at SG inlet and outlet headers. Wall thermocouples (K-class) are mounted throughout the two coils, with fining near the ends to identify the risk of dryout occurrence.

Table 2.2 Pressure tap distribution along the test section (Channel A).

	Tap 1	Tap 2	Tap 3	Tap 4	Tap 5	Tap 6	Tap 7	Tap 8	Tap 9
Distance from tube inlet [m]	0.20	5.17	9.19	13.15	17.14	21.64	25.59	29.09	32.06

Table 2.3 List of the uncertainties of the measured physical quantities.

Water flow rate	± 1%
Fluid bulk and wall temperature	± 0.7 °C
Absolute pressure	± 0.1%
Differential pressure	± 0.4%
Supplied electrical power	± 2.5%
Evaluated thermal losses	± 15%

Electrical power is obtained via separate measurements of current (by a shunt) and voltage drop along the test section by a voltmeter. All the measurement devices have been tested and calibrated at the certified SIET labs. A summary of the uncertainties is reported in Table 2.3.

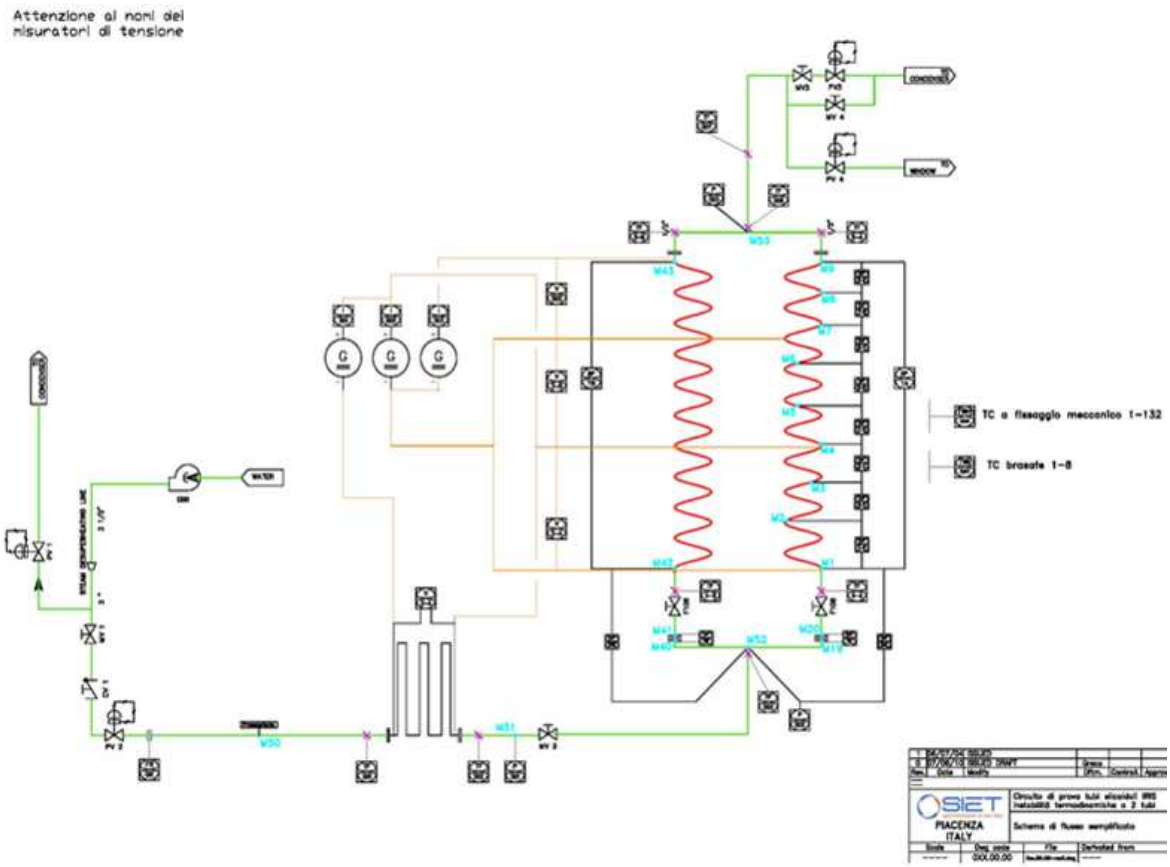

Figure 2.2 Flow diagram of the experimental facility.

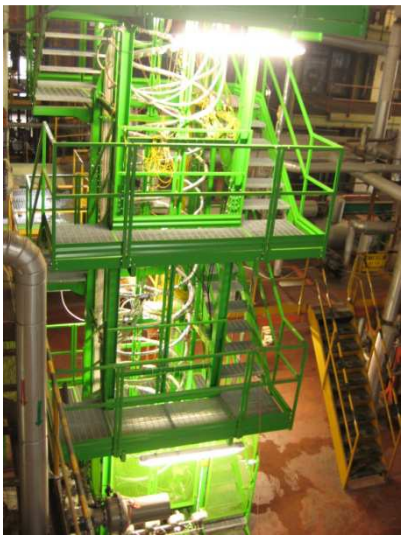

Figure 2.3 Global view of the facility test section.

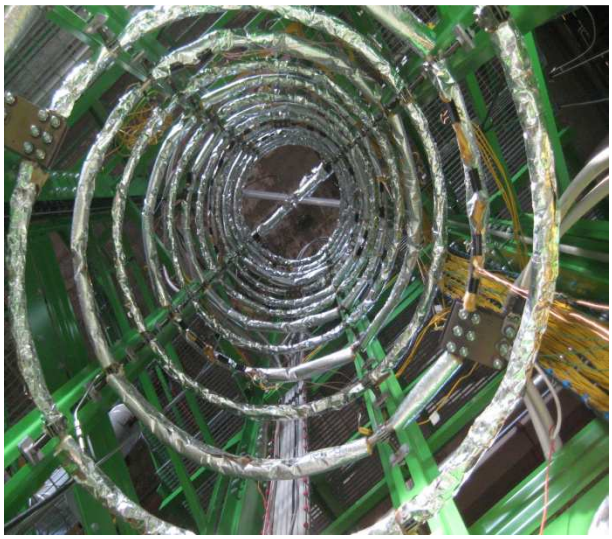

Figure 2.4 Inner view of the test section.

Figure 2.5 Pneumatic actuator of loop pressure control valve (V4).

Figure 2.6 Calibrated orifice and channel inlet valve.

Figure 2.7 Differential pressure transducers installed along channel A.

Figure 2.8 Coriolis flow meter.

2.2 Single-phase frictional pressure drop

The first series of experimental measurements regarded the single-phase flow. The single-phase pressure drop has been measured in a wide range of Reynolds numbers, starting from the condition of laminar flow. Various measurements were taken increasing gradually the mass flow rate up to a Reynolds of about 3000, where a first discontinuity is encountered, that attests the beginning of the transition region. Numerous experimental data have been recorded also in the transition and in the turbulent regions, up to a Reynolds number of about 35000. The database contains almost 80 experimental values of the friction factor. Experiments were made with water at nearly atmospheric temperature and pressure, and Reynolds numbers in the range 1500 – 35000, which corresponds to a velocity in the range between 0.1 m/s and 2.25 m/s. The experimental conditions are summarized in Table 2.4. Together with the friction factor, the range of the experiments allows to characterize also the laminar to turbulent flow transition. The single-phase pressure drop can be expressed as the sum of three different terms, respectively due to friction, gravitation and acceleration of the flow:

$$p_{in} - p_{out} = \Delta p_{fr} + \Delta p_{grav} + \Delta p_{acc} \tag{2.1}$$

Since the accelerative pressure drop can be considered negligible, the value of the frictional pressure drop is calculated subtracting the gravitational pressure drop from the experimental value:

$$\Delta p_{fr} = \Delta p_{exp} - g\rho_l H \tag{2.2}$$

The Darcy friction coefficient is then calculated as:

$$f_D = 2\frac{\Delta p_{exp} d}{\rho_l v_{in}} \tag{2.3}$$

Experimental friction factors are shown in Figure 2.9 as a function of the Reynolds number. In general, in the single-phase flow the frictional pressure drop represents a small amount of the total pressure drop, that is composed mainly by the gravitational term, making critical the error analysis. However, numerous experimental acquisitions were available for every experimental condition, each one including the data from the different pressure transducers. As a consequence, each experimental point is a mean between numerous equivalent measurements, with an error bar calculated as the standard deviation.

Table 2.4 Range of parameters for the single-phase flow measurements.

p [bar]	almost atmospheric
T [°C]	20-25
Γ [kg/h]	23.8 – 1000.7
v [m/s]	0.1 – 2.25
Re [-]	1500 - 35000

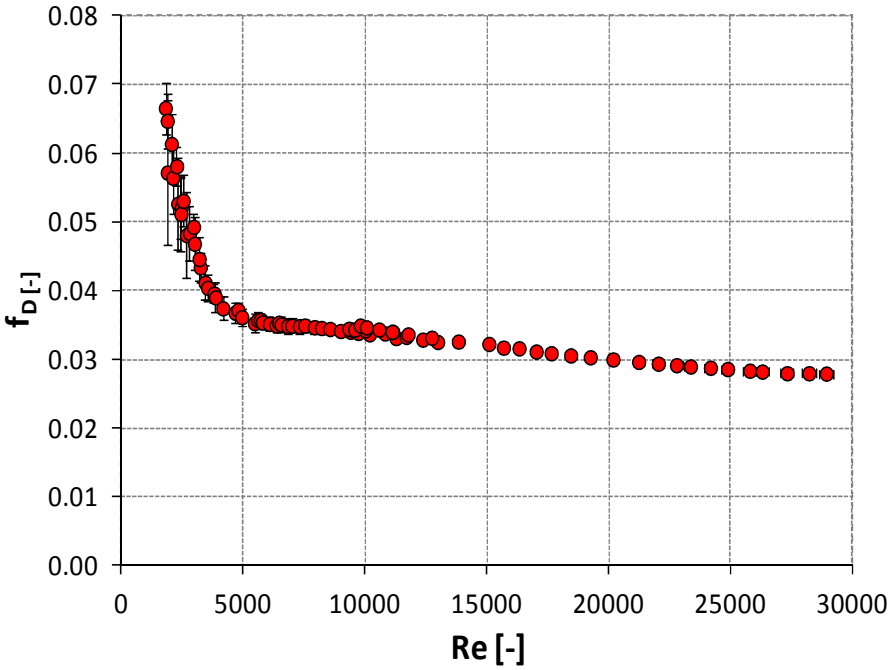

Figure 2.9 Single-phase friction factor as a function of the *Re* number.

2.3 Two-phase frictional pressure drop

A large database of two-phase frictional pressure drops has been built, including 130 experimental measures made in adiabatic conditions. During the experiments, all the thermal power was supplied to the fluid in the preheater, to reach the desired flow quality of the mixture at the test section inlet. Only a very small fraction of the thermal power was supplied to the test section, to balance the thermal losses and maintain as much as possible a constant flow quality along the pipe. The measures cover the following operating conditions:

- pressure: 30, 40 and 60 bar;
- mass flux: 200, 400 and 600 kg/m^{2}s;
- flow quality: from 0.1 to 1.0.

The two-phase pressure drop can be expressed with a steady-state momentum balance:

$$p_{in} - p_{out} = \Delta p_{fr} + \Delta p_{acc} + \Delta p_{grav} \tag{2.4}$$

Since the two-phase mixture flows at an almost constant flow quality along the test section, the accelerative pressure term can be neglected and the balance equation reduces to frictional and gravitational pressure terms:

$$p_{in} - p_{out} = \frac{f_D}{2}\frac{G^2 L}{\rho_m d} + g\rho_m H \tag{2.5}$$

To evaluate the pressure drop due to friction is then necessary to define the mixture density. Since the homogeneous equilibrium model has been applied for the analysis, no slip between the phases is assumed and the mixture density reads:

$$\rho_m = \left(\frac{1-x}{\rho_l} + \frac{x}{\rho_v}\right)^{-1} \tag{2.6}$$

where x is equal to the thermodynamic quality:

$$x = \frac{h - h_l}{h_v - h_l} \tag{2.7}$$

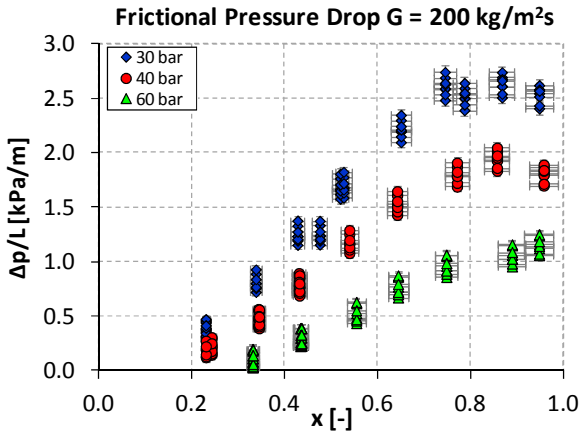

Figure 2.10 Adiabatic frictional pressure drop as a function of the mixture quality at G = 200 kg/m^{2}s and p = 30, 40, 60 bar.

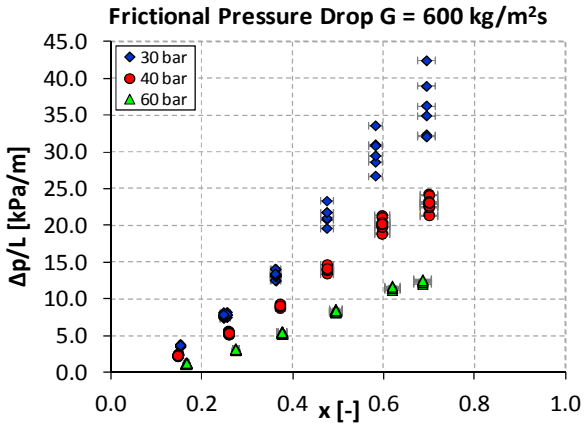

Figure 2.11 Adiabatic frictional pressure drop as a function of the mixture quality at G = 600 kg/m^{2}s and p = 30, 40, 60 bar.

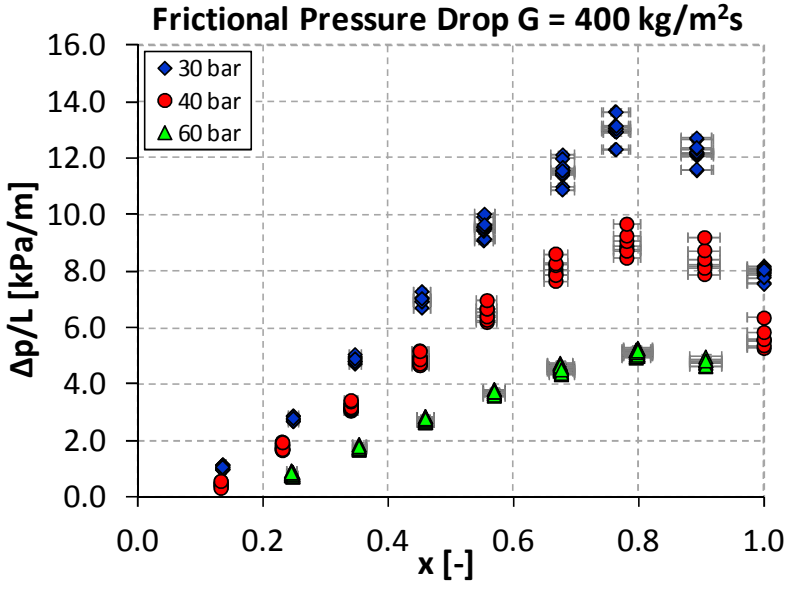

Figure 2.12 Adiabatic frictional pressure drop as a function of the mixture quality at G = 400 kg/m^{2}s and p = 30, 40, 60 bar.

The mixture enthalpy can be calculated from an energy balance over the system preheater, to finally obtain the frictional pressure drop. As for the single-phase flow, an equivalent Darcy friction coefficient can be evaluated rearranging Eq.(2.3):

$$f_D = \frac{2\rho_m d}{G^2 L} + [(p_{in} - p_{out}) - g\rho_m H] \tag{2.8}$$

The frictional pressure drop per unit length, shown in Figure 2.10, Figure 2.11 and Figure 2.12, exhibit a parabolic shape as a function of the mixture quality, as it increases up to an *x* value of about 0.7, to subsequently decrease toward the vapor single-phase value. Although this behavior has been observed also in experimental studies realized in straight ducts (Brega et al.; Muller-Steinhagen and Heck, 1986), the peak seems to be more marked in helical pipes, in addition to be shifted in a lower quality value. The parabolic shape, which will be discussed in more details in Chapter 5, could be explained with a change in the flow regime, from an annular flow to the rupture of the thin liquid film and the establishment of a dispersed liquid flow. As expected, the frictional pressure drop decreases with pressure, keeping fixed system mass flow rate and flow quality. Error bars have been introduced in the figures following an analysis based on the error linear propagation technique (Moffatt, 1988) and more details can be found in Appendix A.

2.4 Density Wave Oscillations

Density Wave Oscillations (DWOs) were investigated as the main "dynamic type" instability mode occurring in parallel boiling channels. The classical interpretation ascribes the origin of the instability to waves of "heavier" and "lighter" fluids, and respective delays through the channel. The difference in density between the fluid entering the heated channel (subcooled liquid) and the fluid exiting (low density two-phase mixture) triggers delays in the transient distribution of pressure drops along the tube, which may lead to self sustained out of phase oscillations of the flow rate in the parallel channels (Yadigaroglu, 1981). The constant pressure drop boundary, required to excite the flow rate perturbations, is provided in both the real SG and the SIET experimental facility by the lower and upper headers, common to all the channels.

2.4.1 Ranges of explored variables

Due to the complex nature of DWOs, to fully characterize the system stability and the instability phenomena, it is necessary to determine instability thresholds in a wide range of system operating parameters. To study the effects of the system pressure, the mass flow rate and the inlet subcooling on the system stability, the test matrix includes more than 150 unstable conditions:

- 4 levels of pressure: 80 bar, 40 bar, 20 bar and 10 bar;
- 4 levels of mass flux: 600 kg/m^{2}s, 400 kg/m^{2}s, 200 kg/m^{2}s and 100 kg/m^{2}s;
- several values of the inlet subcooling between x_{in} = -30% and x_{in} = 0%.

The entire test matrix refers to an inlet valve configuration corresponding to a valve loss coefficient K_{in} = 45 (a detailed description of the valve calibration procedure is provided by Papini (2011)). The effect of the inlet throttling was also studied by progressively closing the valves and repeating the stability map at p = 40 bar and G = 400 kg/m^{2}s.

2.4.2 Experimental procedure

Unstable conditions were reached increasing gradually the supplied electrical power starting from a stable operating system, up to the appearance of the flow instability. The experimental procedure can be summarized in the following steps:

(1) Registration of the gravitational head of the different instruments.
(2) Characterization of the normal behavior of the system (for instance, check that, at open V1 and V2 valves, the flow rate is reasonably balanced between the two coils).
(3) Impose the defined position of V1 and V2 valves.
(4) Define the pressure level.
(5) Impose a value of flow rate.
(6) Impose a value of the inlet subcooling by means of the preheater.
(7) Reach the desired pressure level by generating vapor with power increase. When the desired pressure is obtained, keep the system in a steady-state condition (measurements of temperature, pressure, flow rate and heat input).
(8) The electrical power is progressively increased by small amounts (small steps of 2-5 kW per tube), until sustained oscillations are observed (check that the system pressure remains more or less constant).
(9) Once the instability is recorded, take the system back to step 6, and change the subcooling. Repeat steps 7 and 8 up to the instability (same operating pressure).
(10) Once all the subcooling values are tested for a flow rate level, change the flow rate and repeat steps 6-9.
(11) Once all the flow rate values defined in step 5 are completely explored (every subcooling value), change the desired pressure level and repeat steps 5-10.

2.4.3 *DWO characterization*

An unstable system can be identified by monitoring the oscillation of the flow rate, which starts when the threshold power is reached. The quantification of the flow rate in each tube is made possible from the measure of the pressure drop across the calibrated orifices. Thus, the experimental power threshold is defined as the power corresponding to permanent and regular flow oscillations, detected by visual observation of the pressure drop recording of the calibrated orifices (within V1 and V2 of Figure 2.1). The system is considered completely unstable when the flow rate oscillation amplitude reaches the 100% of its steady-state value.

In an unstable system, flow rate in the two channels oscillates in counter phase, being the total system mass flow rate imposed as in Figure 2.13, that shows a fully developed DWO. The “square wave” shape of the curves is due to the reaching of instrument full scale.

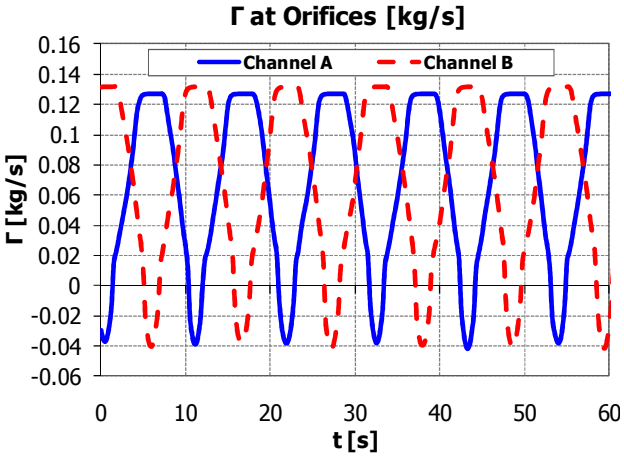

Figure 2.13 Flow rate oscillations during fully developed instability. Data collected with: p = 83 bar; T_{in} = 199 °C; G = 597 kg/m^{2}s; q = 99.3 kW.

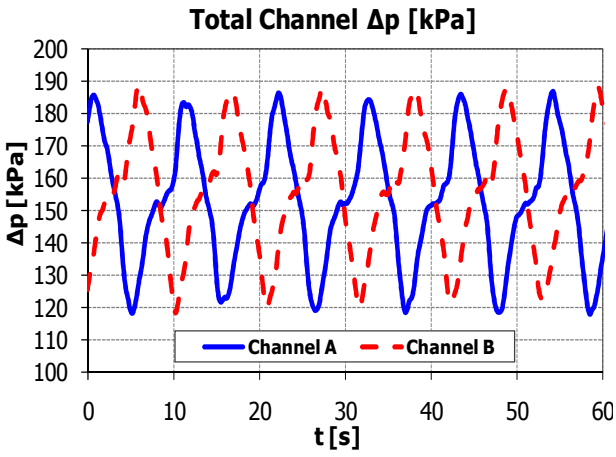

Figure 2.14 Counter-phase pressure drop oscillations in the two parallel tubes. Data collected with: p = 83 bar; T_{in} = 199 °C; G = 597 kg/m^{2}s; q = 99.3 kW.

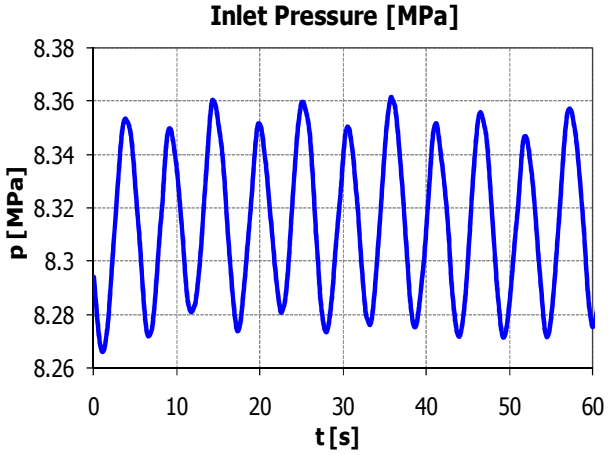

Figure 2.15 System pressure oscillations in the inlet header. Data collected with: p = 83 bar; T_{in} = 199 °C; G = 597 kg/m^{2}s; q = 99.3 kW.

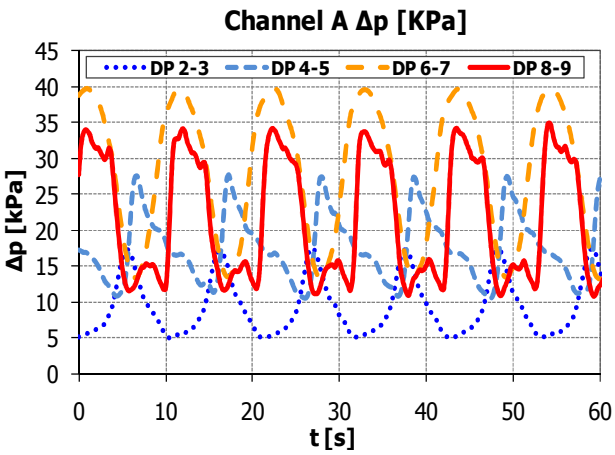

Figure 2.16 Pressure drop oscillations in different regions of channel A: single phase (DP 2-3), low quality two-phase (DP 4-5), two-phase (DP 6-7 and DP 8-9).Data collected with: p = 83 bar; T_{in} = 199 °C; G = 597 kg/m^{2}s; q = 99.3 kW.

The large amount of data collected during the experiments allowed the characterization and the understanding of the distinctive features of DWOs. Total pressure drops across the tubes oscillate in counter phase too (Figure 2.14). Instead, the system pressure oscillates with a frequency that is double if compared with the frequency of the pressure drop oscillation (Figure 2.15). Counter phase oscillation of the single-phase and the two-phase pressure drop within each channel is known to be one of the events triggering the appearance of DWOs. Figure 2.16 compares the pressure drop between the pressure taps placed on different regions of Channel A (according to the distribution depicted in Table 2.2). Pressure drop in the single-phase region (DP 2-3) oscillates in counter phase with respect to the two-phase pressure drop (DP 6-7 and DP 8-9). However, the phase shift is not abrupt, but it appears gradually along the channel. In fact, the pressure term DP 4-5 (low quality two-phase region) shows only a

limited phase shift with respect to the single-phase zone (DP 2-3). Furthermore, large amplitude fluctuations in the channel wall temperatures, so named “thermal oscillations” (Kakac and Bon, 2008), always occur (Figure 2.17), produced by intermittent film boiling conditions triggered by the instability.

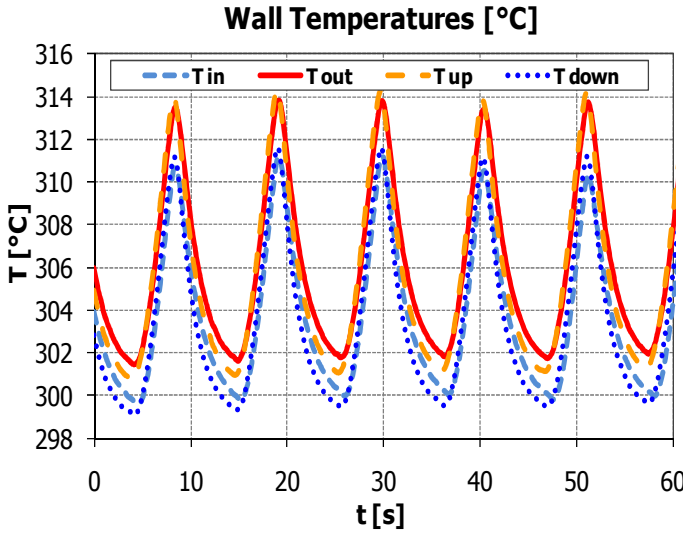

Figure 2.17 Fluctuations of tube wall temperatures during DWOs. Data collected with: p = 83 bar; T_{in} = 199 °C; G = 597 kg/m^{2}s; q = 99.3 kW.

2.4.4 *Experimental results*

To study the stability of the system, the regions of stable and unstable operation must be identified in the three-dimensional space given by channel flow rate Γ, thermal power q and inlet subcooling Δh_{in} (at a given pressure level). In this respect, dimensionless stability maps provide a powerful but easy tool to cluster the information on the stability of the system. The most popular dimensionless stability map was introduced by Ishii and Zuber (1970), based on a subcooling number N_{sub} and a phase change number N_{pch}. The phase change number is the ratio of the characteristic frequency of phase change Ω to the inverse of a single-phase transit time in the system:

$$N_{pch} = \frac{\Omega}{\frac{v_{in}}{L}} = \frac{\frac{q}{AL}\frac{v_{lv}}{h_{lv}}}{\frac{v_{in}}{L}} = \frac{q}{\Gamma h_{lv}}\frac{v_{lv}}{v_l} \tag{2.9}$$

The subcooling number scales the inlet subcooling:

$$N_{sub} = \frac{\Delta h_{in}}{h_{lv}}\frac{v_{lv}}{v_l} \tag{2.10}$$

The effect of the pressure is taken into account in Eq.(2.9) and Eq.(2.10) by the specific volume ratio, on the limit of a small pressure variation.

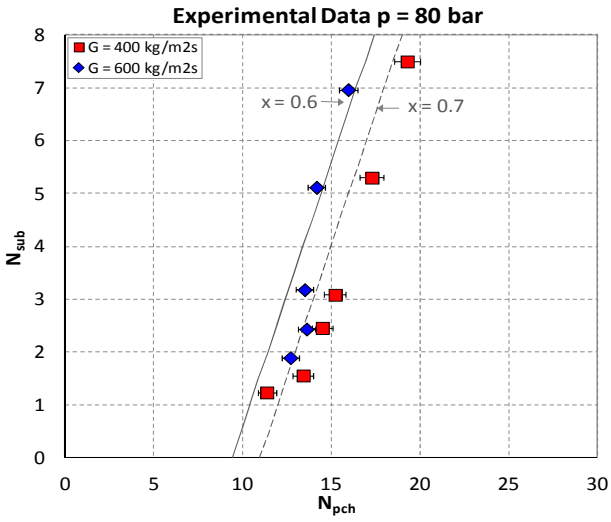

Figure 2.18 Stability map recorded at system pressure p = 80 bar and G = 400, 600 kg/m^{2}s.

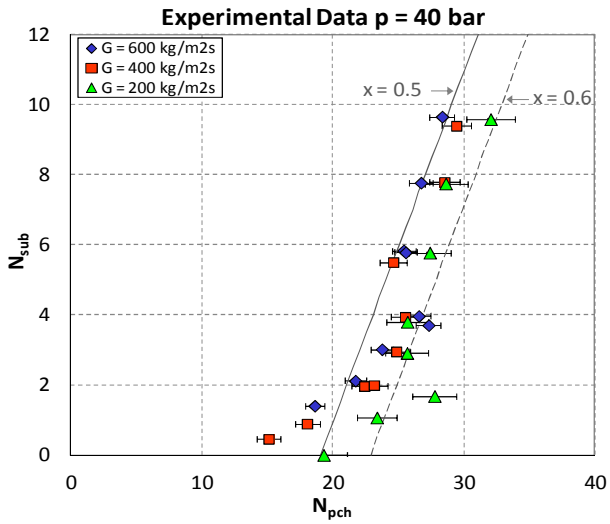

Figure 2.19 Stability map recorded at system pressure p = 40 bar and G = 200, 400, 600 kg/m^{2}s.

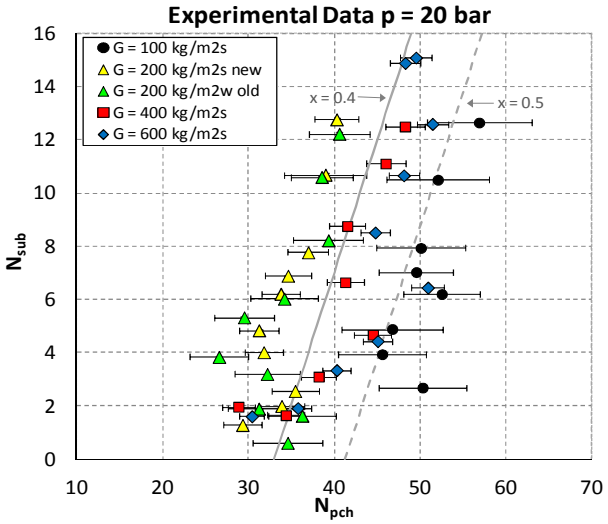

Figure 2.20 Stability map recorded at system pressure p = 20 bar and G = 100, 200, 400, 600 kg/m^{2}s.

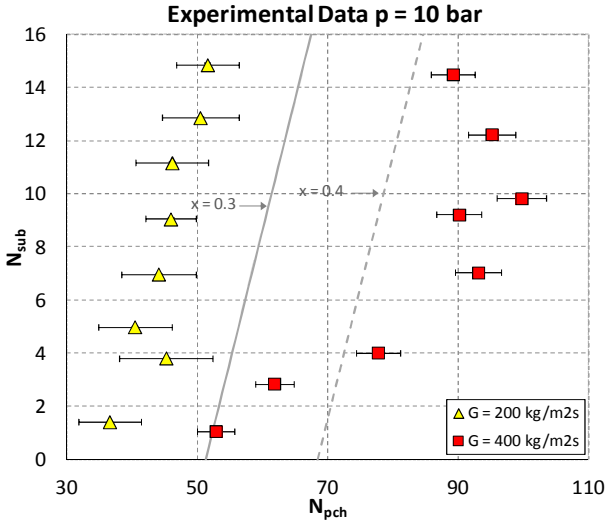

Figure 2.21 Stability map recorded at system pressure p = 10 bar and G = 200, 400 kg/m^{2}s.

Figures from Figure 2.18 to Figure 2.21 show the experimental stability maps obtained at the four pressure levels. Error bars are introduced following an uncertainty analysis based on the error linear propagation technique (Moffatt, 1988). More details can be found in Appendix A. In each graph, the instability threshold at a given pressure level is represented for all the mass fluxes tested and the different values of the inlet subcooling. At 80 bar only two mass fluxes have been considered, because plant operations resulted difficult at low flow rates. As expected, the stability boundaries at different mass fluxes are almost overlapped. Thus, it is the ratio q/Γ that determines the onset of instability, once the characteristics of the channel and the inlet conditions are set. Figures from Figure 2.22 to Figure 2.25 confirm that a mass flow rate variation induces a proportional variation of the thermal power needed to trigger the instability. Therefore, an increase of the thermal power or a decrease of the mass flow rate can

cause the onset of a DWO. Indeed, both of them increase the exit quality, which turns out to be a key parameter for the stability of a boiling channel. To sum up, the effects of the thermal power and the mass flow rate do not show differences in the helical geometry when compared to a straight tube. For comparison, some examples of a typical stability map obtained in two straight vertical parallel pipes are depicted in Figure 2.26. Experimental data are taken from the noteworthy work of Masini et al. (1968). The different stability boundaries displayed in Figure 2.26 correspond to different configurations of the valves installed on the test section.

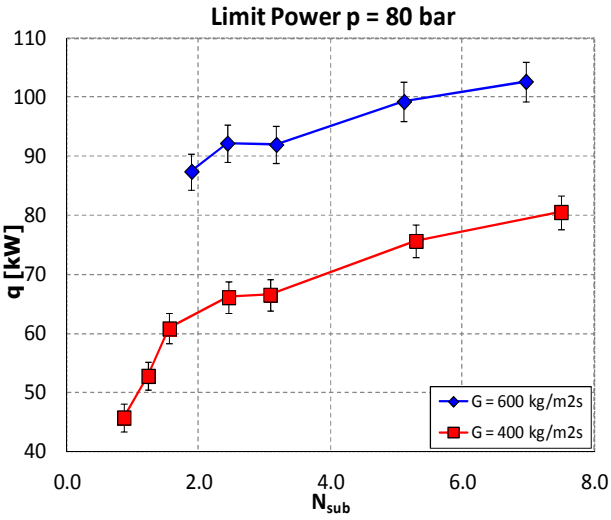

Figure 2.22 Limit power for instability inception at p = 80 bar as a function of the inlet subcooling.

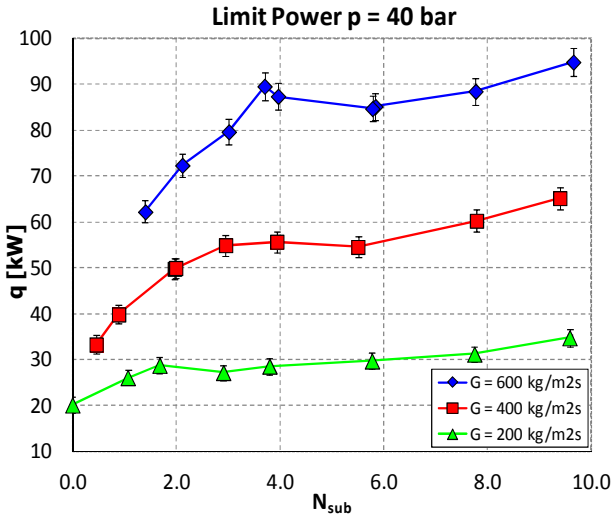

Figure 2.23 Limit power for instability inception at p = 40 bar as a function of the inlet subcooling.

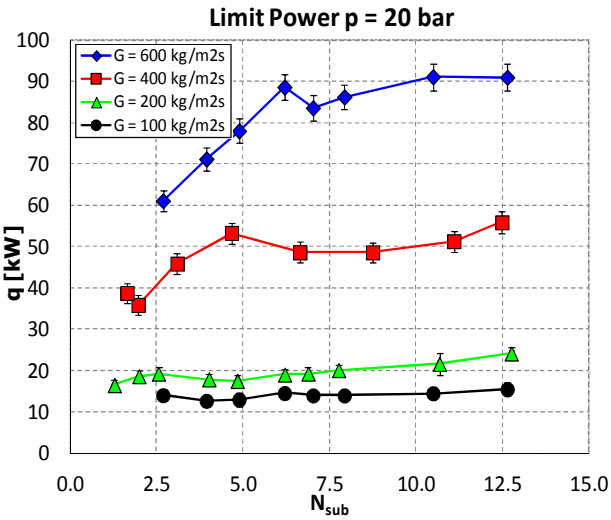

Figure 2.24 Limit power for instability inception at p = 20 bar as a function of the inlet subcooling.

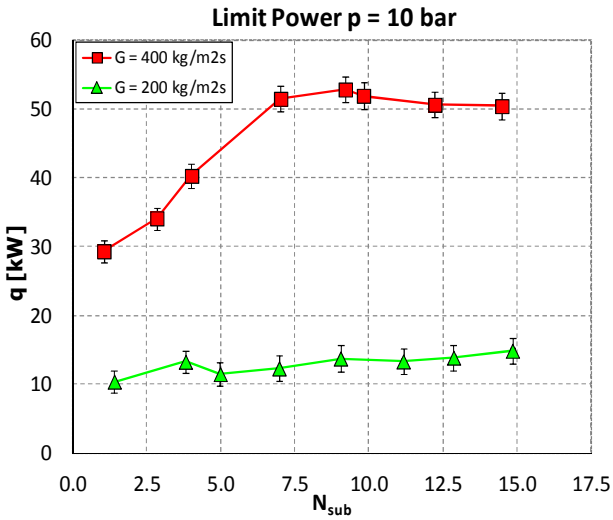

Figure 2.25 Limit power for instability inception at p = 10 bar as a function of the inlet subcooling.

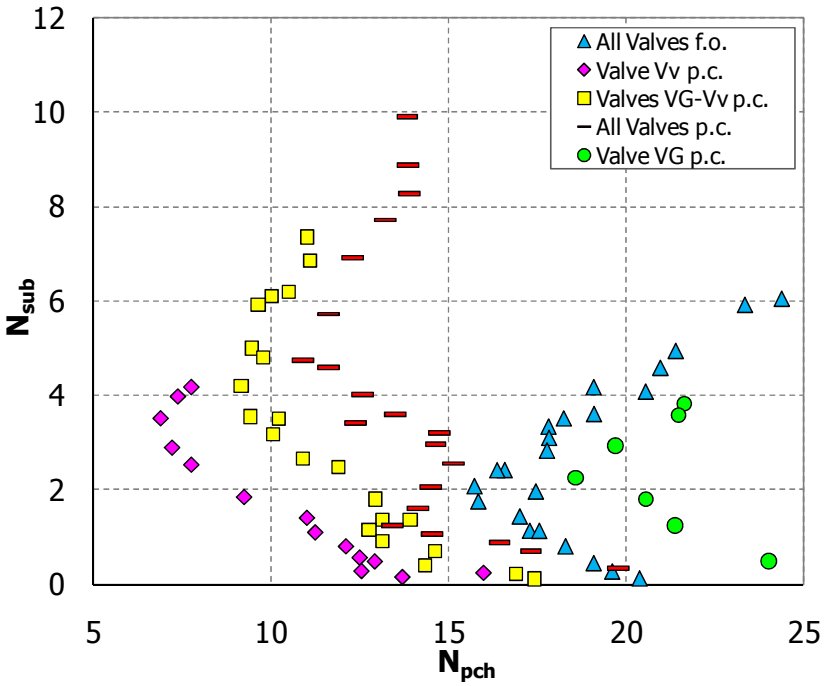

Figure 2.26 Stability maps from the experimental work of Masini et al. (1968), made in straight vertical parallel tubes. p = 50 bar; G = 364 kg/m^{2}s; Valves: VG inlet; Vv outlet. Valve positions: f.o. fully open; p.c. partially closed.

Instead, it is interesting to focus the attention on the inlet subcooling. It is known from literature that an increase in the inlet subcooling is stabilizing at high subcoolings and destabilizing at low subcoolings (Yadigaroglu, 1981). This behavior results in the classical "L shape" of the stability boundary, exhibited by the dimensionless maps obtained in straight pipes (Ishii and Zuber, 1970; Masini et al., 1968; Ambrosini et al., 2000). The present study on the helical geometry confirm the stabilizing effect at high subcoolings. The experiments show indeed two different behaviors:

- "conventional" at medium-high subcoolings, with the iso-quality stability boundary and a slight stabilization in the range N_{sub} = 3 ÷ 6 (close to the "L shape");
- "non-conventional" at low subcoolings, with a marked destabilizing effect as the inlet temperature increases and approaches the saturation value.

Such different behavior exhibited by the stability boundary at low subcoolings can be ascribed to the helical shape of the parallel channels and to the related centrifugal force field effect on the thermal hydraulics of the two-phase flow. Also the full scale length of the test section and the small inclination angle of the helix, which affects the two-phase flow pattern, may explain the experimental findings. It is finally noticed that a first set of data obtained at low system pressure and low mass flux (p = 20 bar and G = 200 kg/m^{2}s, see Figure 2.20) showed a different stability boundary shape, more similar to the classical behavior. In particular, the effect of an inlet subcooling increase resulted stabilizing at high subcoolings, and destabilizing at low subcoolings.

Consequently, additional measures at 10 bar and 100 kg/m^{2}s were added to the initially planned database, to study in more detail the low pressure and low mass flow rate region.

After the additional experiments, the distinct subcooling stabilizing effect is confirmed also at low pressure and low mass flow rate. Even a repetition of the stability map at 20 bar and 200 kg/m^{2}s, in contrast with the first map recorded on the same conditions, confirms the differences with the classical "L shape". However, it is also evident how results at low pressure and low mass flow rate are characterized by an higher uncertainty.

As a final remark, the map at 10 bar (Figure 2.21) shows discrepancies between the stability boundaries at different mass flow rates, in contrast with what stated before on the effect of the mass flow rate. However, at 400 kg/m^{2}s and a value so low of the system pressure, the pressure drop is considerably high. Therefore, outlet pressure was close to the atmospheric value and a chocked flow condition was frequently obtained, questioning the reliability of that particular stability boundary.

2.4.5 *Effect of the system pressure*

The system pressure was always found to be stabilizing, although the effect of the system pressure is less important if compared with other system parameters (Yadigaroglu, 1981). Figure 2.27 and Figure 2.28 show the limit power for the various pressure levels at a fixed value of the mass flow rate (G = 400 kg/m^{2}s and 600 kg/m^{2}s). The higher is the pressure, the higher is the exit quality required for the instability inception, so more stable is the system. This concern is evident by considering the iso-quality lines reported in the stability maps (Figure 2.18 – Figure 2.21). The behavior of the thermal power in Figure 2.27 and Figure 2.28 also confirms the subcooling stabilizing effect for small values of N_{sub}.

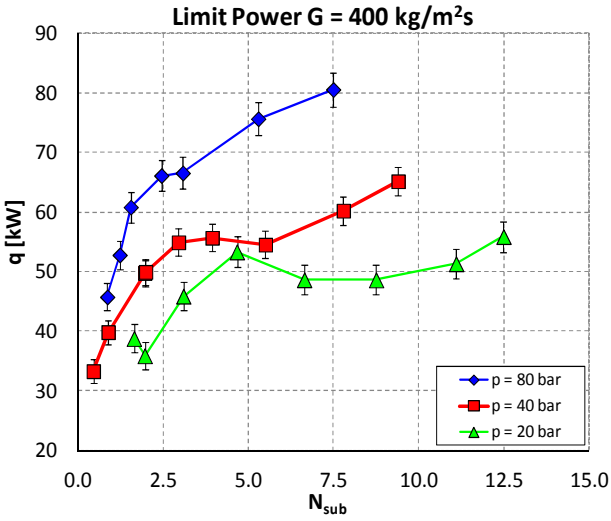

Figure 2.27 Limit power for instability inception at G = 400 kg/m^{2}s as a function of the inlet subcooling.

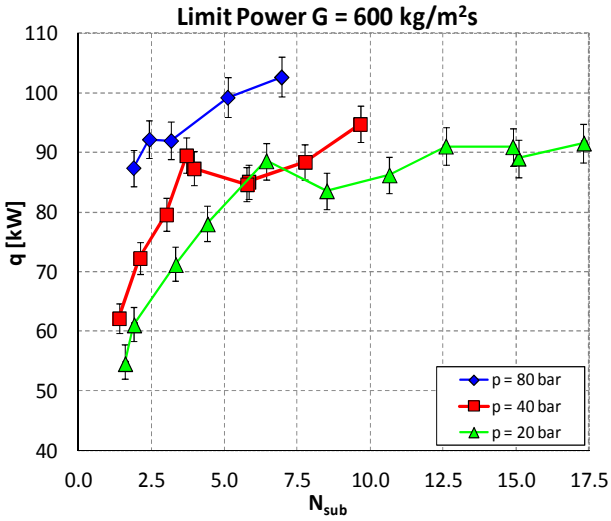

Figure 2.28 Limit power for instability inception at G = 600 kg/m^{2}s as a function of the inlet subcooling.

2.4.6 Period of oscillations and transit time

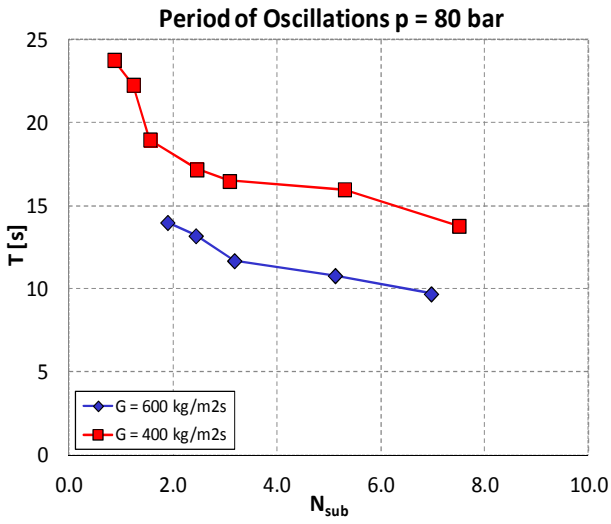

Figure 2.29 Period of oscillations at 80 bar as a function of the inlet subcooling.

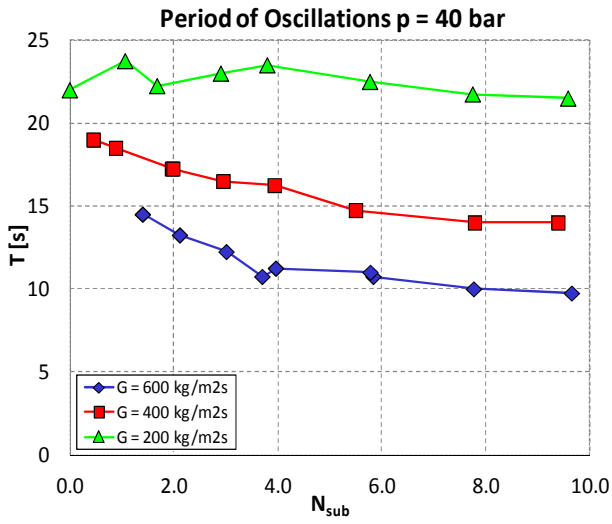

Figure 2.30 Period of oscillations at 40 bar as a function of the inlet subcooling.

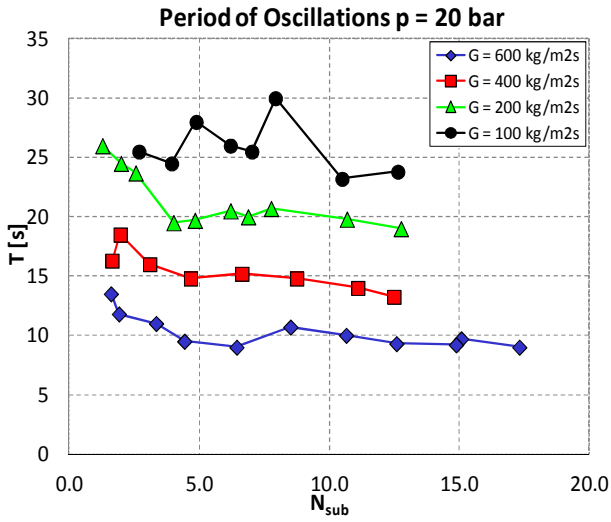

Figure 2.31 Period of oscillations at 20 bar as a function of the inlet subcooling.

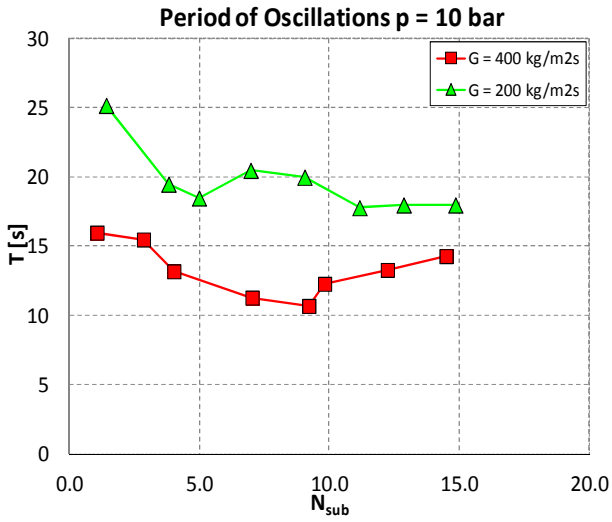

Figure 2.32 Period of oscillations at 10 bar as a function of the inlet subcooling.

Since DWOs are characterized by waves of heavier and lighter fluid which travel alternatively along the boiling channel, two perturbations are required to complete each cycle. Accordingly, the period of oscillations should be of the order of twice the mixture transit time. As a matter of fact, literature results report a period of oscillation T almost equal to twice the mixture transit time τ at high inlet subcoolings, and a reduction of the T/τ ratio with a reduction of the subcooling number (Yadigaroglu, 1981).

The experimental results show a completely different trend. The period of oscillations to transit time ratio is found to be very low at high inlet subcoolings, whereas it grows reducing the subcooling number N_{sub}. Actually, the period of oscillations (Figure 2.29 - Figure 2.32) results rather independent on the inlet subcooling, while it increases lowering the mass flow

rate. Accordingly, the T/τ ratio (Figure 2.33 - Figure 2.36), that is quite constant following a mass flux variation, results considerably lower than one (~0.5) at high inlet subcoolings (where the fluid transit time in the heated channel is higher due to the long single-phase region), whereas it increases up to a value of nearly two as the inlet temperature approaches the saturation.

For the analysis, the mixture transit time was calculated with the classical homogeneous flow theory, by adding the single-phase region transit time $\tau_{1\phi}$ and the two-phase region transit time $\tau_{2\phi}$ (Masini et al., 1968):

$$\tau = \tau_{1\theta} + \tau_{2\theta} = \frac{\rho_{in}\Delta h_{in}}{\frac{q}{AL}} + \frac{h_{lg}}{\frac{q}{AL}v_{lg}} \ln\left(1 + \frac{v_{lg}}{v_l}x_{out}\right) \tag{2.11}$$

With some algebra, Eq.(2.9) can be rearranged as:

$$\tau = \frac{ALh_{lg}}{q}\left[-\rho_{in}x_{in} + \frac{1}{v_{lg}} ln\left(1 + \frac{v_{lg}}{v_l}x_{out}\right)\right] \tag{2.12}$$

As well as from the helical geometry, the discussed behavior seems to be induced also by the peculiar length of the test section and by the presence of an unheated riser above. These conclusions are somehow confirmed by Masini et al. (1968), who found out a more complicated correlation between period of oscillations and transit time in certain conditions. Actually, the presence of a long riser downstream the heated test section may influence the oscillation frequency.

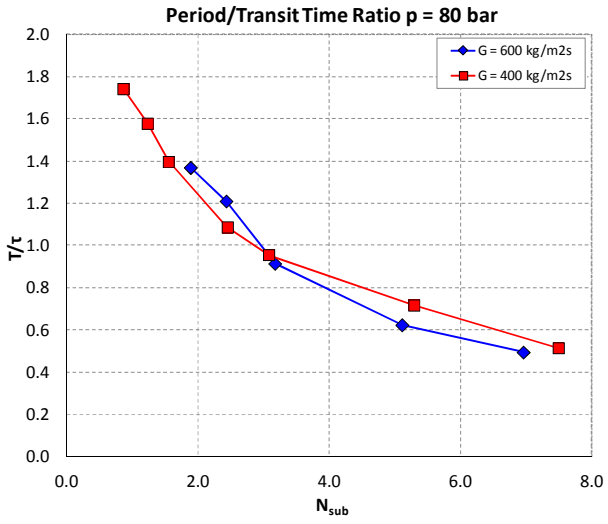

Figure 2.33 Period of oscillations to transit time ratio at 80 bar as a function of the inlet subcooling.

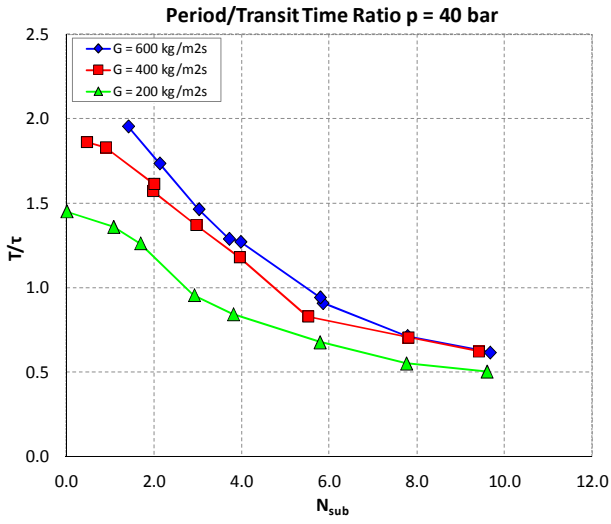

Figure 2.34 Period of oscillations to transit time ratio at 40 bar as a function of the inlet subcooling.

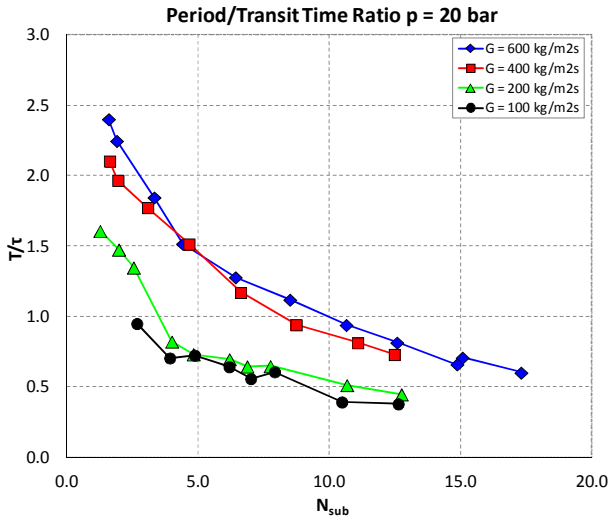

Figure 2.35 Period of oscillations to transit time ratio at 20 bar as a function of the inlet subcooling.

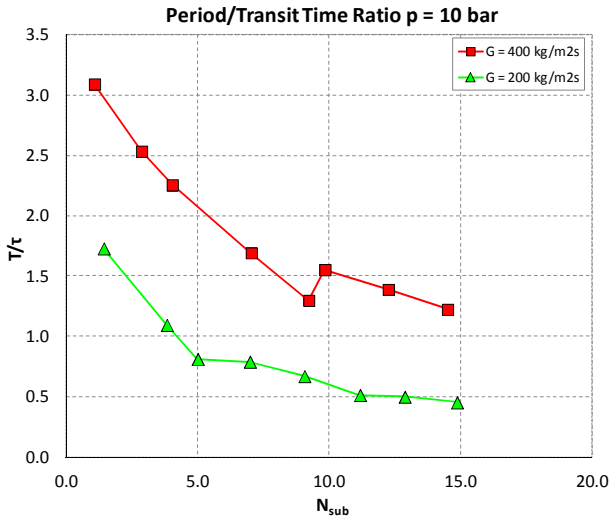

Figure 2.36 Period of oscillations to transit time ratio at 10 bar as a function of the inlet subcooling.

2.4.7 *Effect of the inlet throttling*

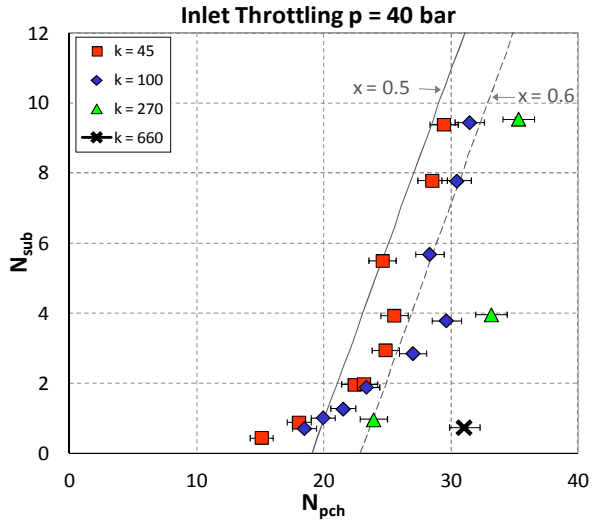

Figure 2.37 Stability map obtained with different values of the inlet throttling

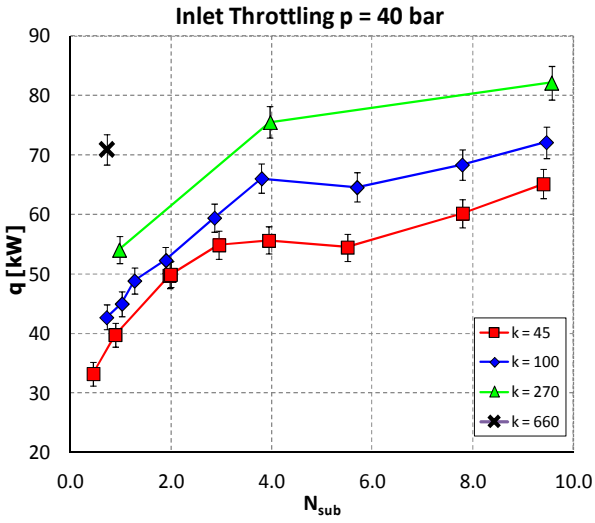

Figure 2.38 Limit power for instability inception at different values of the inlet throttling.

It is well known that a concentrated pressure drop located at channel inlet is stabilizing. The effect of the inlet throttling was studied in the SIET facility repeating the stability map at p = 40 bar and G = 400 kg/m^{2}s , following progressive closures of V1 and V2 valves. Four valve positions were tested, up to a valve coefficient K = 660. It is just recalled that all the other experiments were made with the valve coefficient K = 45.

The stability maps are shown in Figure 2.37, whereas the limit power in Figure 2.38. The results confirm the stabilizing effect of a concentrated pressure drop located at the inlet of the boiling channel. Nevertheless, the effect of the inlet throttling turns out to be rather weak.

Actually, the system remains prone to instability even after a remarkable closure of the inlet valves. Only a strong increase of the inlet throttling, so of the corresponding concentrated pressure drop, allows to avoid the instability occurrence. In particular, for the last valve position tested, the dryout is observed before any flow oscillations, except for a low subcooling condition, as indicated in Figure 2.37.

2.5 Ledinegg instability

Ledinegg type instabilities occur when a heated channel operates in the negative slope region of the pressure drop versus flow rate curve (channel characteristics). In this respect, the boundary condition of constant pressure drop given by the parallel channels acts as a flat pump external characteristics. Each channel is forced into a wide flow excursion to reach a new operating point on the internal characteristics (Figure 2.39). A flow excursion observed during an experiment on the Ledinegg instability is shown in Figure 2.40. While flow rate increases in Channel A, it reduces proportionally in Channel B, to preserve the imposed total mass flow rate. The constant total pressure drop condition is respected across the two tubes.

The Ledinegg instability characterizes the region of low thermal power and high inlet subcooling and it vanishes increasing the thermal power before the reaching the DWO stability boundary. Before starting the experiments on the Ledinegg instability, the channel characteristics was determined in different system conditions, to identify the negative slope regions necessary to trigger the flow excursion.

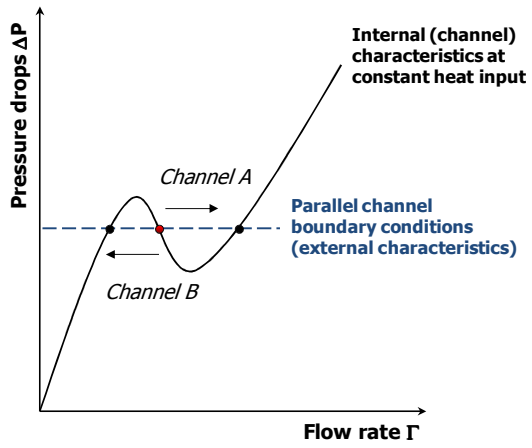

Figure 2.39 Ledinegg instability mechanism under the parallel channel boundary condition.

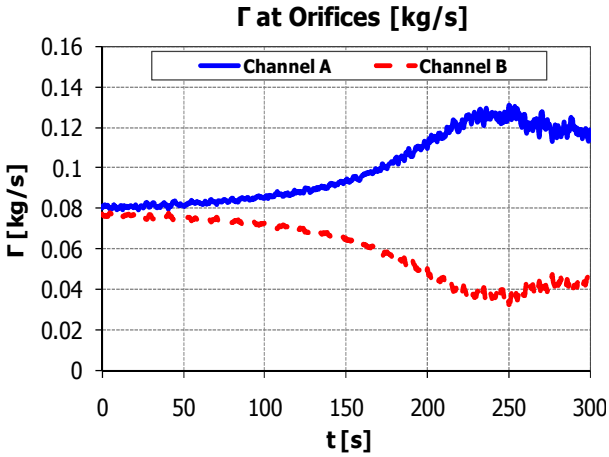

Figure 2.40 Flow rate in the two channels during a Ledinegg transient. System conditions: p = 24 bar; T_{in} = 134°C; G = 600 kg/m^{2}s; q = 50 kW.

In particular, the pressure drop was measured at 10, 20 and 40 bar, at inlet subcoolings $0.350 < x < -0.125$ and for a thermal power between 20 kW and 60 kW. Starting from a mass flow rate value high enough to have a single-phase liquid flow in the entire tube, the mass flow rate was gradually reduced to finally obtain an high quality two-phase flow at the outlet of the channels. Figure 2.41 shows different channel characteristics, in which negative slope

regions can be distinctly identified. Their amplitude is increased reducing the inlet temperature or increasing the thermal power, but the most important effect is due to the system pressure, which reduces the amplitude of the negative slope region.

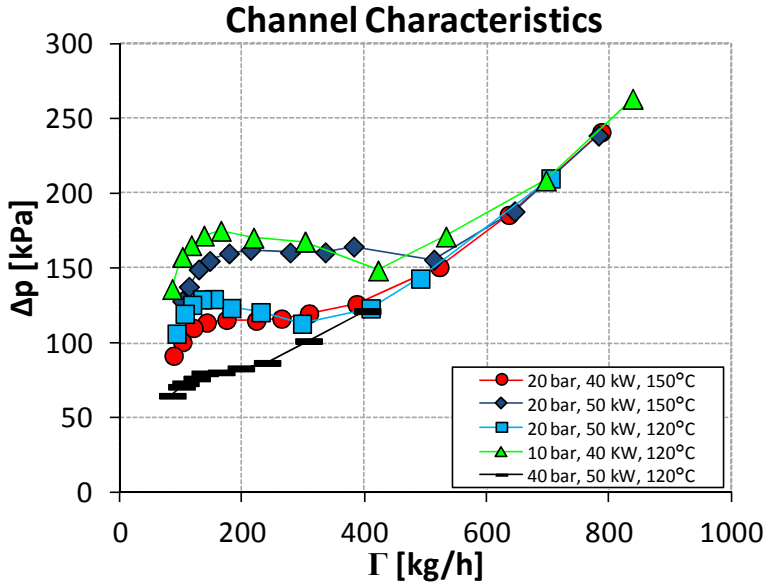

Figure 2.41 Channel characteristics depicted in different system operating conditions.

From Figure 2.41, the Ledinegg instability characterizes the low pressure region, whereas a small unstable region can be expected for a system pressure equal to or greater than 40 bar.

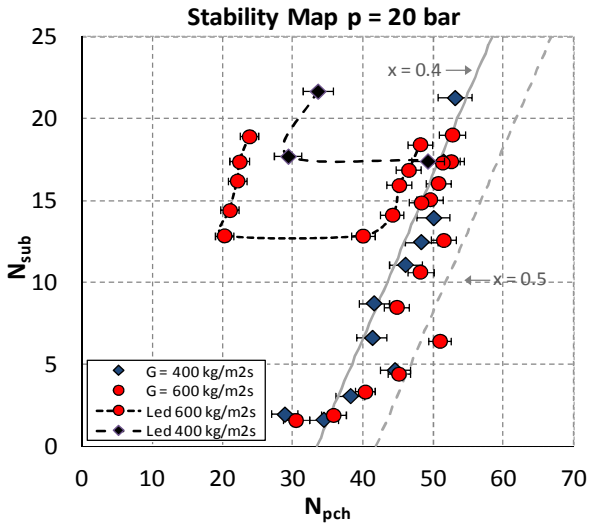

Figure 2.42 Stability maps at 20 bar and 400 and 600 kg/m^{2}s with both the DWO stability boundary and the Ledinegg unstable region.

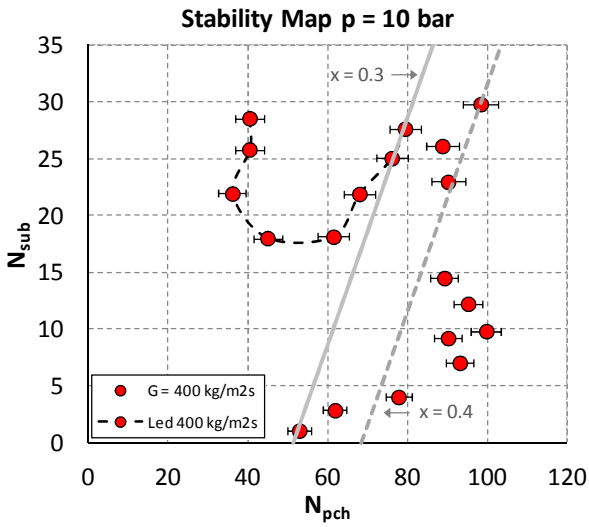

Figure 2.43 Stability map at 10 bar and 400 kg/m^{2}s with both the DWO stability boundary and the Ledinegg unstable region.

Figure 2.42 reports a complete stability map in the $N_{sub} - N_{pch}$ plane, including the DWO stability boundary and also the Ledinegg unstable region. For each inlet temperature, starting from a low value, the thermal power was gradually increased until the flow excursion. The power was then further increased to leave the Ledinegg region and reach the DWO stability

boundary. For the same value of the system pressure and the mass flow rate, the procedure was repeated changing the inlet temperature, to explore a wide range of inlet conditions. Data were collected at 20 bar and 400 and 600 kg/m^{2}s, 10 bar and 400 kg/m^{2}s (Figure 2.43) and also some experiments were made at 40 bar and 400 and 600 kg/m^{2}s.

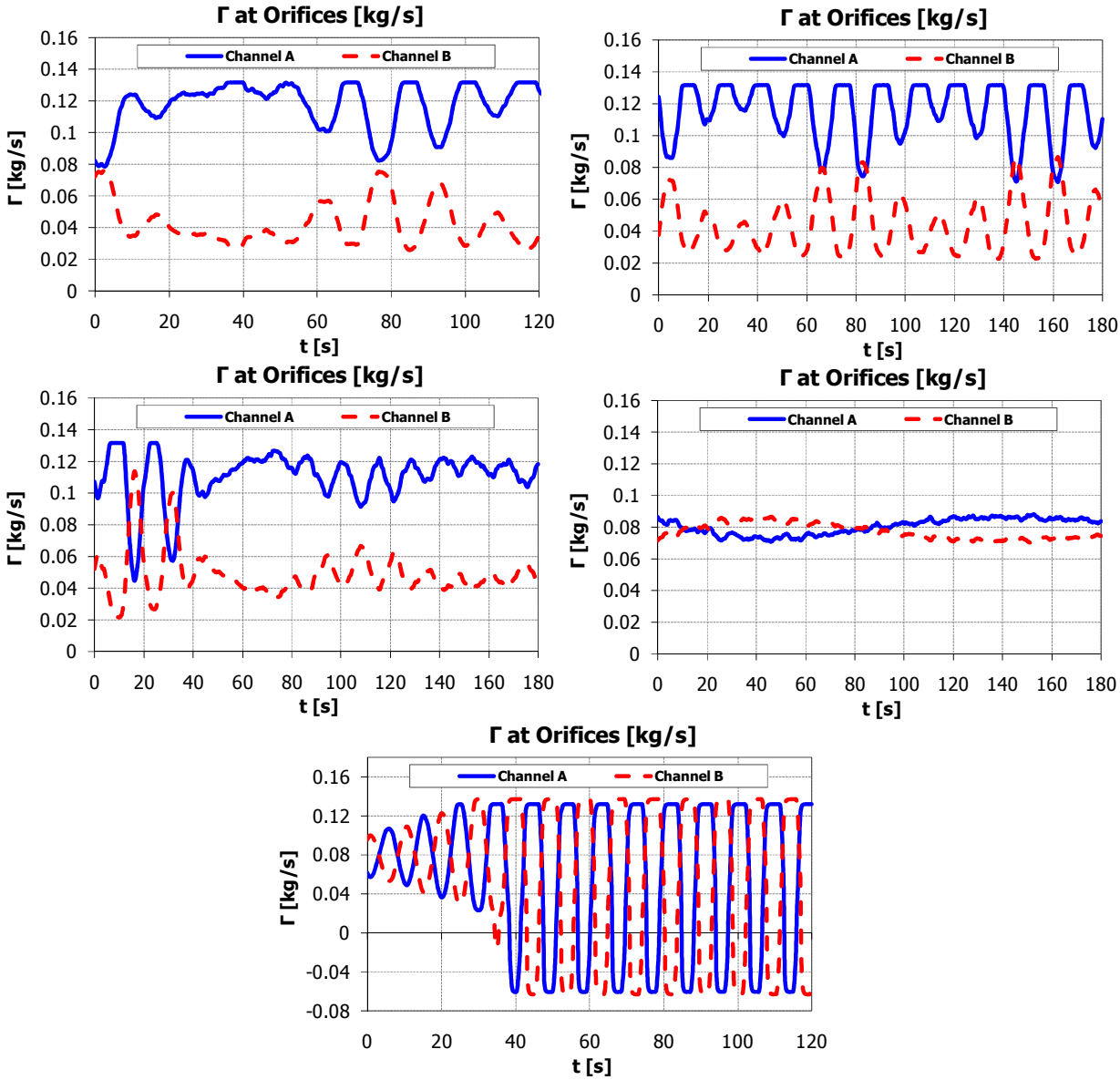

Figure 2.44 Flow rate transients during superimposition of Ledinegg type instabilities with DWOs. Data collected with: p = 21 bar; T_{in} = 122 °C; G = 603 kg/m^{2}s.

The Ledinegg region grows with the inlet subcooling and also with the mass flow rate, as it means a higher thermal power to obtain the same flow quality. Also a decrease in the system pressure promotes the instability, as it is possible to observe comparing the unstable regions at 10 and 20 bar and 400 kg/m^{2}s. In agreement with the previous analysis, Ledinegg instability was recorded only in a narrow range of system conditions at 40 bar. The power difference between Ledinegg and DWO stability boundary is reduced increasing the inlet subcooling and the two tend to superimpose at very high inlet subcoolings. As a consequence, the complete stability boundary shows the typical “noose” shape reported in literature (Ishii

and Zuber, 1970; Yadigaroglu, 1981). In addition to the superimposition of the two instability modes in some particular regions of the map, an anticipated DWO onset was sometimes recorded in the channel with the lower flow rate during the flow excursion. The latter phenomenon is evident in the Ledinegg transient reported in Figure 2.44. The initial flow excursion leads to an increase of the channel A flow rate and decrease of the channel B flow rate. The drop in the channel B flow rate is indeed enough to yield an anticipated inception of the DWO, which causes the channel A to oscillate too. An increase of the thermal power is then sufficient to switch off the flow excursion and to damp out the DWO. Finally, a further increase of the thermal power causes a fully developed DWO to occur.

2.6 Conclusions

In this chapter all the experimental work made during the three doctoral years has been presented. It constitutes the basis of all the thesis work and the starting point for the study of the thermal hydraulic of the helically coiled tube presented in the next chapters. Experimental data will be used to achieve a major understanding of the physical phenomena under study and for the validation of the numerical simulations and the empirical and the analytical models that will be developed.

All the experimental activity was made in a facility installed at the SIET laboratories, including two helically coiled tubes connected in parallel. The facility reproduces in full scale a SG for the SMR technology (it was originally built for the study of the IRIS reactor) and is designed for the simulation of the real reactor operating conditions.

Experiments were focused on two main subjects, the frictional pressure drop and the instability of the two-phase flow in a parallel channel system. For the former, two databases where built, respectively of single-phase frictional pressure drop and two-phase adiabatic frictional pressure drop. Among other findings, the latter confirmed a more distinct peak in the frictional pressure drop profile as a function of the flow quality with respect to straight tubes.

In the field of the two-phase flow instability, the attention was mainly focused on the DWOs. Furthermore, some data were collected also on the Ledinegg instability. Being a very complex phenomenon, the DWO in parallel channel has been extensively characterized along the chapter. The parametric effects of thermal power, flow rate, inlet subcooling and inlet throttling have been studied and the results were clustered in dimensionless stability maps, that exhibits the stable and unstable operating regions of the system. Discrepancies with the DWO classical theory were observed in the effect of the inlet subcooling and in the period of the oscillations to transit time ratio. For the inlet subcooling in particular, an increase maintains its stabilizing effect also at low subcoolings, in contrast with what happens in straight parallel vertical tubes. The period of oscillations to transit time ratio, lower than one at high inlet subcoolings, increases up to a value of nearly two as the inlet temperature approaches the saturation. The differences with respect to classical instability results were ascribed to the geometry of the helical channel and the particular characteristics of the facility, that is its length and almost horizontal orientation. Actually it must be noticed that the helical

geometry and the characteristics of the test section make the experimental database a unique test case in the field of DWO studies.

References

W. Ambrosini, P. Di Marco, J.C. Ferreri, 2000. Linear and nonlinear analysis of density wave instability phenomena. International Journal of Heat and Technology 18(1), 27-36.

E. Brega, B. Brigioli, C.G. Carsana, C. Lombardi, L. Maran. MIDA: data bank of pressure drops and densities of two-phase mixtures flowing in rectilinear ducts. CeSNEF, Politecnico di Milano, ENEL/CRNT, Milano, Italy.

M. Ishii, N. Zuber, 1970. Thermally induced flow instabilities in two-phase mixtures. Proceedings of the 4th International Heat Transfer Conference, vol. 5, paper B5.11, Paris, France.

S. Kakac, B. Bon, 2008. A review of two-phase flow dynamic instabilities in tube boiling systems. International Journal of Heat and Mass Transfer 51, 393-433.

G. Masini, G. Possa, F.A. Tacconi, 1968. Flow instability thresholds in parallel heated channels. Energia Nucleare 15(12), 777-786.

R.J. Moffat, 1988. Describing the uncertainties in experimental results. Experimental Thermal and Fluid Science 1, 3-17.

H. Muller-Steinhagen, K. Heck, 1986. A simple friction pressure drop correlation for two-phase flow in pipes, Chemical Engineering and Processing 20, 297-308.

D. Papini, 2011. Modelling and experimental investigation of helical coil steam generator for IRIS Small-medium Modular Reactor. Ph.D. Thesis, XXIII Cycle, Politecnico di Milano, Milano, Italy.

L. Santini, 2008. Thermalhydraulic issues of IRIS nuclear reactor helically coiled steam generator and emergency heat removal system. Ph.D. Thesis, XX Cycle, Politecnico di Milano, Milano, Italy.

L. Santini, A. Cioncolini, C. Lombardi, M.E. Ricotti, 2008. Two-phase pressure drops in a helically coiled steam generator. International Journal of Heat and Mass Transfer 51, 4926-4939.

L. Santini, D. Papini, M.E. Ricotti, 2010. Experimental characterization of a passive emergency heat removal system for a Gen III+ reactor. Science and Technology of Nuclear Installation, Volume 2010, Article ID 864709, 12 pages.

G. Yadigaroglu, 1981. Two-phase flow instabilities and propagation phenomena. In: J.M. Delhaye, M. Giot, M.L. Riethmuller, Thermohydraulics of two-phase systems for industrial design and nuclear engineering, 353-396, Hemisphere Publishing Corporation, Washington.

CHAPTER 3

THE SINGLE-PHASE FLOW

The study of the flow inside the helically coiled tube is started in this chapter with a detailed analysis of the single-phase flow. Even if the single-phase flow has been studied by many researchers in the past, it represents the most appropriate starting point approaching the study of the helically coiled pipe, before addressing the more complex field of the two-phase flow thermal hydraulics.

Starting from the analysis of the frictional pressure drop experimental data, a comparison is made with some of the most famous correlations available from literature, to further verify their accuracy with the new dataset. In addition to the friction factor in the laminar and turbulent regions, also the laminar to turbulent flow transition and its peculiar characteristics are studied.

Most of the chapter is dedicated to the numerical study of the flow. Since the CFD has been selected as the principal tool for the numerical studies, it is at first applied to the single-phase flow. In the laminar regime, a complete characterization of the single-phase flow is proposed, with a particular attention to the effect on the velocity and the pressure fields of the centrifugal force, introduced by the geometry. The unique features of the flow inside an helical tube are emphasized and the numerical results are validated with a comparison against the friction factor experimental data and some literature correlations.

In the turbulent region, different turbulence models are compared with the experimental data to assess their estimation of the frictional pressure drop. The treatment of the near-wall region is identified as the most critical subject for the presence of the secondary motion that characterizes the flow.

3.1 Literature review

The problem of the flow in curved pipes, and in helical pipes in particular, has been addressed by many researchers and the large amount of works available on the subject can be found in different literature reviews (Berger et al., 1983; Shah and Joshi, 1987; Naphon and Wongwises, 2006).

The first experiments were conducted by Eustice (1910), who firstly noticed a certain decrease in the mass flow rate (at constant Δp) in curved pipes with respect to straight pipes having the same diameter. He also noticed a difference in the transition between laminar and turbulent regimes characterized by a smoother behavior of the friction factor across the critical value of the Reynolds number Re_{cr}. Dean (1927; 1928) first derived a solution for the laminar flow in a toroidal pipe of small curvature with the Navier-Stokes equations written in

a cylindrical reference frame. He obtained a set of equations describing the velocity field within the tube cross section as that of a straight duct with a centrifugal force. Dean derived also a correlation for the friction factor along the tube, introducing a non-dimensional quantity defined as:

$$De = Re\sqrt{\frac{d}{D}} \tag{3.1}$$

The above parameter, function of the tube to coil diameter ratio, was later renamed the Dean number and used in several correlations concerning the curved pipes. White (1929) conducted several tests on helically coiled tubes with different values of *d/D*, in order to verify the validity of the Dean model. He also confirmed the effect of the curvature on the transition to the turbulent regime. The same author developed later a correlation for the frictional pressure drop (White, 1932). Ito (1959; 1969), following experimental and analytical studies, proposed correlations for the friction factor in both laminar and turbulent conditions. Yamamoto and co-authors (1995) investigated in detail the effect of the pipe torsion on the flow. The authors found that for increasing values of the torsion at fixed curvature the friction factor tends to become similar to those of a straight tube. That is, the torsion acts to break and reduce the effect of the coil curvature on the flow field.

Cioncolini and Santini (2005) analyzed in detail the effect of curvature and torsion on the onset of turbulence. In particular, they tested twelve different pipes, characterized by different curvature and torsion. They found quite a complex tendency of the critical Reynolds number Re_{cr}, completing the description introduced by White (1929): for mild curvatures, the behavior of f_D is similar to straight pipes, with a sudden increase around the critical Reynolds number. Instead, for very high curvatures, a single discontinuity marks the transition between laminar and turbulent flow. Finally, for medium curvatures, a mild depression characterize the intermediate zone between the fully developed laminar and turbulent regions.

As concerns theoretical analysis, Wang (1981) expanded the work of Dean (1927) to curved pipes with a non-zero torsion, in order to understand its effect on the flow. He developed a non-orthogonal coordinate system, which required a tensorial analysis to derive the desired conservation equations. According to the author, the effect of the torsion on the velocity is of the first order, thus comparable to that of the curvature. Germano (1982; 1989) introduced proper modifications in order to obtain an orthogonal coordinate system, that allowed to write directly the differential operators necessary to the definition of the conservation equations. In contrast with the results of Wang, he concluded that the effect of the torsion is of second order, therefore negligible with respect to the curvature in the majority of the engineering applications. Based on the analysis of Germano, a number of authors completed some asymptotic analyses of the laminar flow to study the effect of the torsion on the flow (Kao, 1987; Xie, 1990; Chen and Jan, 1992).

In the latest decades, thanks to the diffusion of more and more powerful computers, several authors have faced the problem also with numerical methods. McConalogue and Srivastava (1968) treated Dean equations through an expansion in Fourier series and calculated the relative coefficients with an iterative scheme. They showed the shift of the axial velocity maximum towards the outer wall of the tube and the corresponding increase in the

shear stress at the wall. Greenspan (1973) analyzed the problem of a toroidal pipe. He underlined in particular the distortion of the streamlines of the secondary flow with increasing *De*, together with the displacement of the maximum of axial velocity from the center of the tube. Murata et al. (1981) studied the helical coil both from an analytical and a numerical point of view. They described the influence of the helix inclination angle on the symmetry of the secondary flow and the displacement of the maximum of the axial velocity. Hüttl and Friedrich (2000; 2001), starting from the system of equations introduced by Germano (1982), studied the effect of curvature and torsion on the flow through direct numerical simulation in both the laminar and the turbulent regions.

As concern the numerical study of the turbulent flow, the standard k-ε turbulence model was firstly applied by Yang and Ebadian (1996), to study the fully developed turbulent flow and the convective heat transfer in an helically coiled pipe of finite pitch. The same turbulence model was used by Lin and Ebadian (1997) to study the turbulent developing heat transfer. Same authors (Lin and Ebadian, 1999) addressed the effect of the inlet turbulence on the development of the flow and the heat transfer. Li et al. (1998) simulated the mixed convective heat transfer in the entrance region of the helical pipe with the renormalization group (RNG) k-ε model. Kumar et al. (2006) addressed the pressure drops and the heat transfer in a tube-in-tube helical coil heat exchanger with the standard k-ε turbulence model. Jayakumar et al. (2008) evaluated the performance of an helically coiled heat exchanger with the realizable k-ε model. More recently, the same turbulence model was used to study pressure drops and heat transfer in an helical pipe and the effect of different geometrical parameters on the results (Jayakumar et al., 2010). A first attempt to assess the applicability of different turbulence models to the prediction of the pressure drop and the heat transfer in coiled pipes was made by Di Piazza and Ciofalo (2010). The authors compared results from the k-ε model, the Shear Stress Transport (SST) k-ω model and the Reynolds Stress-ω Model (RSM-ω).

3.2 The experimental analysis

The single-phase frictional pressure drop experimental data measured in the SIET facility were presented in Section 2.2. Figure 3.1 shows the experimental friction factor in both the laminar and the turbulent regions. The data are compared with other data from one coil of the work of Cioncolini and Santini (2006), named Coil6 in Figure 3.1. Coil6 has lower pipe and coil diameters and a slightly higher dimensionless coil curvature with respect to the SIET pipe. On the contrary, the SIET pipe presents an higher dimensionless torsion δ. Geometrical data of the two pipes are compared in Table 3.1.

Coil6 friction factor is slightly higher in the laminar region, in virtue of the higher coil curvature, which is confirmed to play the major role with respect to the torsion of the pipe. The curvature effect is then less important in the turbulent region, where the two profiles are almost overlapped. As observed by Cioncolini and Santini (2006), the emergence of turbulence is a very smooth process in the helically coiled pipe and the Reynolds number necessary to achieve the fully turbulent flow condition is higher with respect to straight pipes.

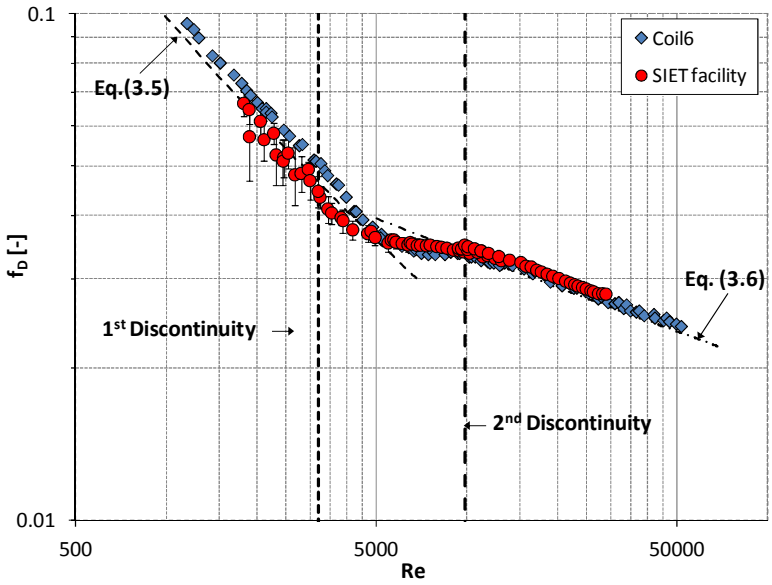

Figure 3.1 Single-phase Darcy friction factors from the SIET facility and Coil 6 of the work by Santini and Cioncolini (2006).

Two different discontinuities are observable in the friction factor profile. A first discontinuity attests the emergence of turbulence, while a second discontinuity marks the end of the turbulence emergence process and the reaching of fully turbulent flow conditions. Between the two discontinuities, a slight depression in the friction factor profile is clearly observable. In the SIET pipe, the two discontinuities are well predicted by the two following formulas (Cioncolini and Santini, 2006):

$$Re = 12500\left(\frac{D}{d}\right)^{-0.31} = 3216 \tag{3.2}$$

$$Re = 120000\left(\frac{D}{d}\right)^{-0.57} = 9886 \tag{3.3}$$

Numerous correlations are available for the prediction of the friction factor in both the laminar and the turbulent regions. Some of them, used for the comparison with the experimental data, are presented in Table 3.2. In Figure 3.2, the experimental data in the laminar regime are compared with different correlations presented in literature: as it is shown in the figure, all the tested correlations are in good agreement with the experimental results.

Table 3.1 Geometrical parameters of the two pipes.

	SIET	**Coil6**
D [m]	1	0.3629
d [m]	0.01253	0.00681
λ	0.0116	0.0188
δ	0.002906	0.000329
β_0	0.0191	0.0017

Table 3.2 List of the correlations compared to the SIET experimental data.

Laminar regime		
Correlation	**Validity range**	**Reference**
$f_s/f_c = 1 - [1 - (11.6/De)^{0.45}]^{1/0.45}$	11.6 < De < 2000	White (1929)
$f_c/f_s = 0.37(0.5De)^{0.36}$	40 < De < 2000	Prandtl (1949)
$f_c/f_s = 0.556 + 0.0969\sqrt{De}$	Laminar flow	Hasson (1955)
$f_c/f_s = 21.5De /(1.56 + \log_{10} De)^{5.73}$	13.5 < De < 2000	Ito (1959)
$f_c/f_s = 0.509 + 0.0918\sqrt{De}$	Laminar flow	Barua (1963)
$f_c/f_s = 1080\sqrt{De}/(1 - 3.253\sqrt{De})$	13.5 < De < 2000	Mori and Nakayama (1967)
$f_c = 32/Re$	11.6 < De <30	
$f_c = 5.22(Re\sqrt{r/R})^{-0.6}$	30 < De < 300	Srinivasan et al. (1968)
$f_c = 1.8(Re\sqrt{r/R})^{-0.5}$	300 < De < De_{cr}	
Turbulent regime		
Correlation	**Validity range**	**Reference**
$f_D = 0.32Re^{-0.25} + 0.048(d/D)^{0.5}$	15000 < Re < 100000	White (1932)
$f_D = 0.304Re^{-0.25} + 0.029(d/D)^{0.5}$	0.034 < Re(d/D)^2 < 300	Ito (1959)
$f_D = 0.3164Re^{-0.25} + 0.03(d/D)^{0.5}$	4500 < Re < 100000	Mishra e Gupta (1979)

For the SIET data, the accuracy of the correlations is also tested in a section of the transition region, enlarging the comparison up to a Reynolds number of 5000. After a *Re* equal to about 3200, almost all the correlations start to lose accuracy in predicting the real value of the friction factor, because of the onset of turbulence. In particular, the correlations that underestimate the friction factor in the laminar region agree better with the experimental data for the particular trend of the friction coefficient.

Table 3.3 Average errors between the correlations and the experimental data in the laminar region.

	SIET pipe		**Coil6**
Correlation	**Error** $_{(Re \le 3200)}$	**Error** $_{(Re \le 5000)}$	**Error**
Ito	4.14%	4.03%	1.59%
White	3.70%	4.92%	4.16%
Prandtl	3.57%	4.40%	3.34%
Mori and Nakayama	4.88%	6.55%	6.74%
Hasson	3.40%	4.33%	3.25%
Barua	6.56%	5.77%	3.43%
Srinivasan	9.53%	8.37%	3.98%

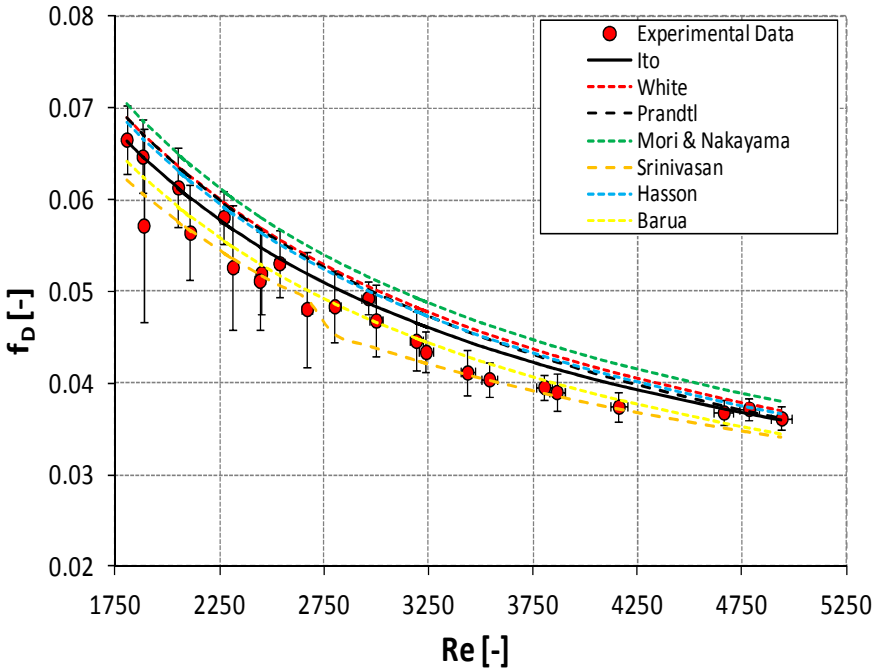

Figure 3.2 Comparison between the experimental friction factors from the SIET facility and some literature correlations valid in the laminar regime.

Results for the various correlations are reported in Table 3.3 for both the laminar and the transition regions. The mean relative error is adopted for the comparison:

$$e_{\%} = \frac{1}{n}\sum_{i=1}^{n}\frac{\left|f_{exp,i} - f_{theo,i}\right|}{f_{exp,i}} \tag{3.4}$$

To sum up, the selected correlations show a quite good agreement also in the transition region, at least for the geometry adopted in the experiments. Moreover, the Ito correlation returns the best results among all the correlations considered for both the laminar and the transition regimes. For the turbulent region, the comparison between correlations and experimental data is resumed in Table 3.4. Ito and Mishra and Gupta correlations agree very well with the experimental data, with average errors always lower than 5% and maximum errors that do not exceed the 7%.

Table 3.4 Average errors between the experimental data and the correlations in the turbulent region.

	Siet [%]			**Coil6 [%]**		
	Ito	White	M.&G.	Ito	White	M.&G.
Avg. Turbulent Region	3.75	7.50	1.12	0.69	14.05	4.14
Max. Turbulent Region	5.15	9.91	3.01	2.18	15.94	6.27
Avg. Transition Region	3.77	13.45	7.13	6.09	17.28	9.60
Max. Transition Region	8.99	17.85	11.12	10.75	23.62	15.19

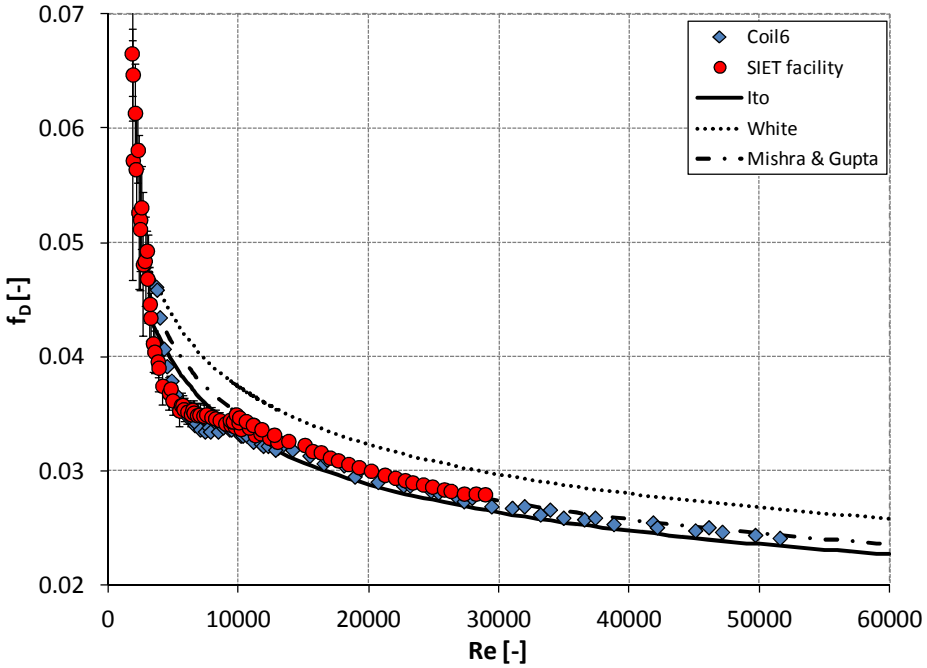

Figure 3.3 Comparison between the experimental friction factors from the SIET facility and some literature correlations with particular attention to the turbulent regime.

Even for the turbulent correlations, the results are satisfactory also in the transition region, where the average relative error is always lower than 10%. On the other hand, the White correlation overestimates the friction factor (Figure 3.3). Therefore, the correlations proposed by Ito provide globally the best results in both the laminar and the turbulent regimes. In addition, both can be used with a satisfactory accuracy in the transition region:

$$\frac{f_c}{f_s} = 21.5De/\left(1.56 + \log_{10} De\right)^{5.73} \tag{3.5}$$

$$f_D = 0.304Re^{-0.25} + 0.029(d/D)^{0.5} \tag{3.6}$$

3.3 Numerical analysis of the laminar flow

The laminar flow inside the helically coiled pipe has been addressed also numerically with a Computational Fluid Dynamic (CFD) study, made through the commercial code ANSYS FLUENT 14.0 (2011). As CFD numerical simulations will be used extensively over all the thesis work to characterize the thermal hydraulic of the helical pipe, it seemed straightforward to start the analysis from the most simple possible case. Even if there are a lot of work available in literature on the laminar flow, the availability of CFD results allows an additional and direct physical understanding of the basic features of the fluid flow in helical geometry. In addition, the availability of the experimental data make possible a validation of the numerical results, even though limited to the prediction of the frictional pressure drop.

3.3.1 *Numerical settings*

Incompressible, laminar, steady Navier-Stokes equations are solved. Second order upwind scheme is used for discretization. The coupling between velocity and pressure is solved through the SIMPLEC algorithm with a convergence criterion of 10^{-5}. The non-slip condition at the pipe wall and constant outlet pressure and inlet velocity are imposed as boundary conditions.

An helical pipe section geometrically identical to the one installed at SIET labs is simulated. The length of the pipe guarantees the reaching of fully developed turbulent conditions, together with the correct evaluation of the frictional pressure drop in the fully developed region. It must be noticed that fully developed conditions are reached within a shorter tube length with respect to straight pipes and the flow could be considered fully developed in about a quarter of a turn.

3.3.2 The mesh

A structured mesh is used for the simulations, implemented by sweeping a planar grid along the axial direction of the pipe. The grid is composed by five sections: the central area of the tube, meshed with a square grid, and the four sides, constructed in a polar form. The mesh is finer near the wall, while it maintains a proper spacing in the other regions, where such refinement is not necessary. The grid is presented in Figure 3.4. The optimal number of mesh elements follows from a grid sensitivity study. A general converging trend of the pressure gradient in the longitudinal direction is found to define the correct number of mesh elements. A total number of cells on the tube cross section equal to 1125 for the SIET pipe and 605 for the Coil6 is found as optimum for a correct simulation of the flow.

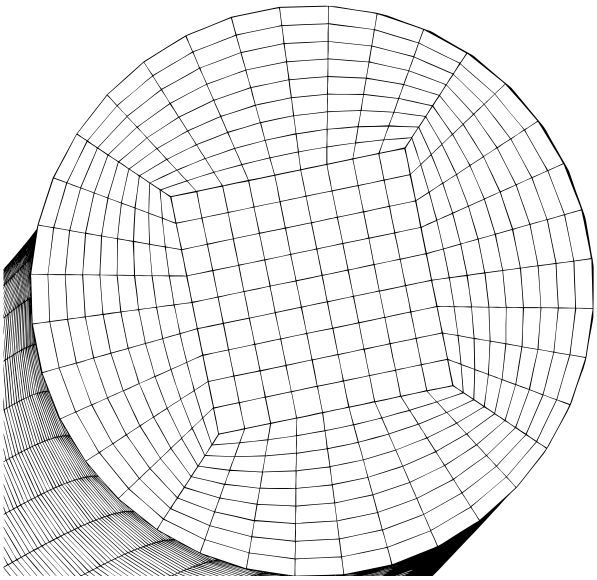

Figure 3.4 Mesh adopted for the CFD simulation of the laminar flow in the SIET pipe.

3.3.3 Numerical results

The CFD numerical results reveal the most important physical features of the fluid flow in the helical coil, in particular the influence of the centrifugal force on the velocity field. Actually, as the fluid flows along the pipe, its motion is influenced by the centrifugal force field introduced by the geometry. In particular, being the centrifugal force field proportional to the square value of the velocity, the faster fluid flowing in the channel core experiences an higher force and it is pushed toward the outer pipe wall. As a consequence, the velocity maximum is shifted toward the external region of the pipe, as it is visible in Figure 3.5 to Figure 3.8 (in these figures as in all the following ones, the left side always represents the external wall section).

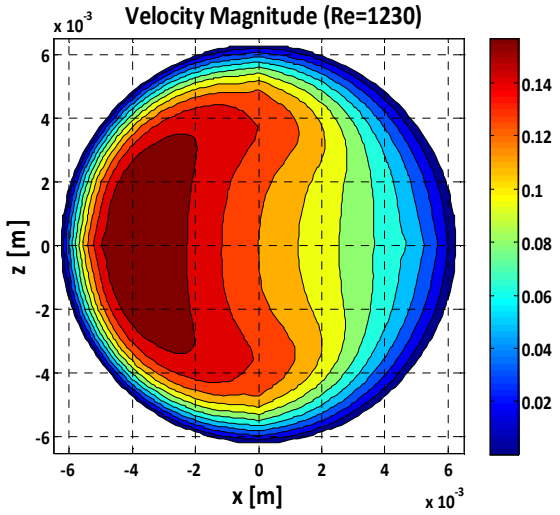

Figure 3.5 Profile of the velocity magnitude on the channel cross section of the SIET pipe (v_{in} = 0.1 m/s, *Re* = 1230).

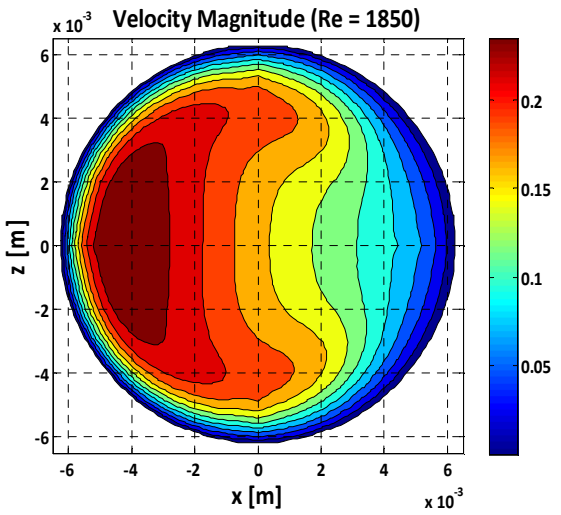

Figure 3.6 Profile of the velocity magnitude on the channel cross section of the SIET pipe (v_{in} = 0.15 m/s, *Re* = 1850).

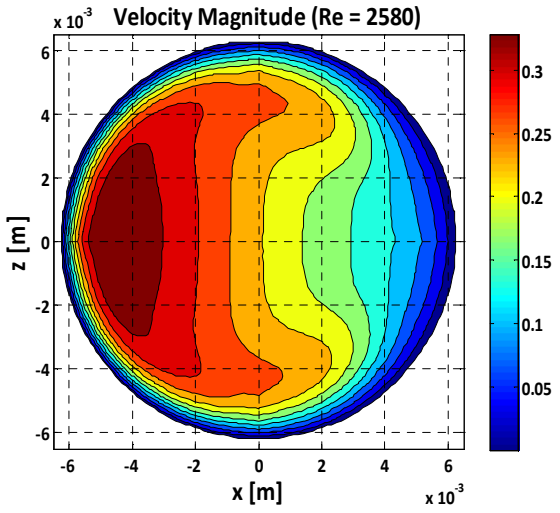

Figure 3.7 Profile of the velocity magnitude on the channel cross section of the SIET pipe (v_{in} = 0.21 m/s, *Re* = 2580).

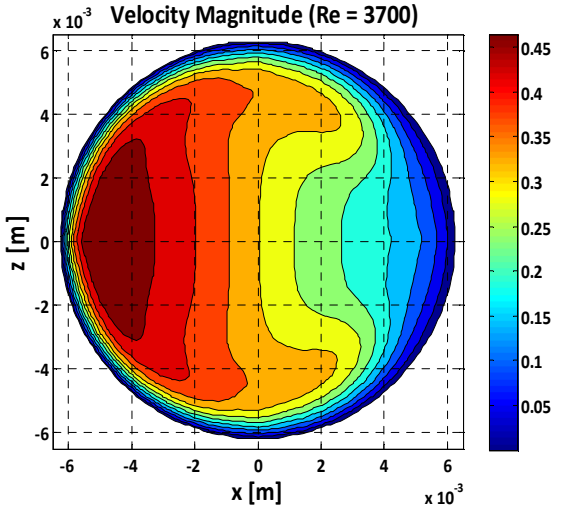

Figure 3.8 Profile of the velocity magnitude on the channel cross section of the SIET pipe (v_{in} = 0.3 m/s, *Re* = 3700).

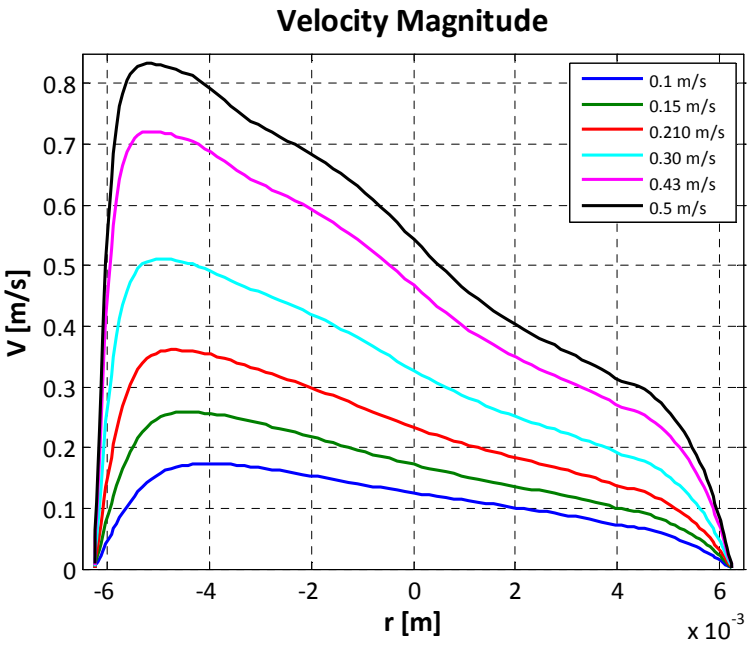

Figure 3.9 Velocity profile on the horizontal axis of the channel cross section for different values of the inlet velocity.

The shift of the maximum determines the increase of the frictional pressure drop, being higher the velocity gradient at the wall, proportional to the wall shear stress. As the Reynolds number increases, the maximum of the velocity is shifted more towards the external wall, as it shown in Figure 3.9. The profile of the velocity is depicted on the horizontal axis of the channel cross section for different values of the inlet velocity. The maximum of the velocity on the external side of the pipe and the minimum on the internal side are clearly visible, together with the slightly higher shifting of the maximum increasing the Reynolds number.

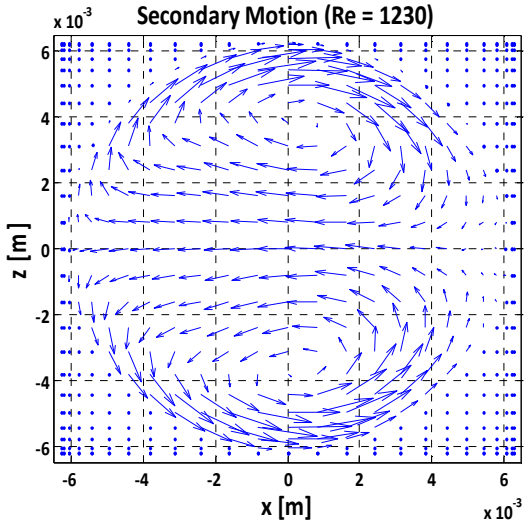

Figure 3.10 Secondary motion on the channel cross section of the SIET pipe (v_{in} = 0.1 m/s, *Re* = 1230).

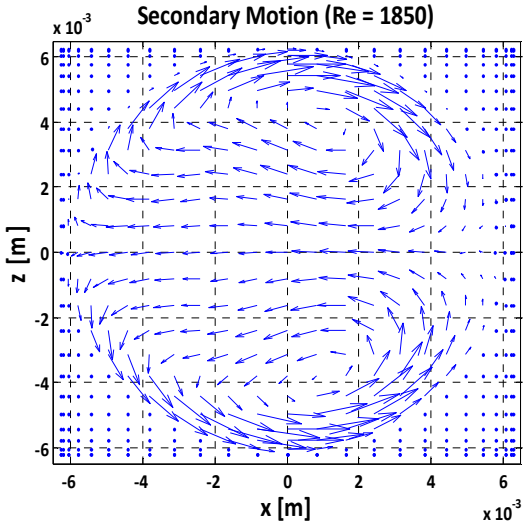

Figure 3.11 Secondary motion on the channel cross section of the SIET pipe (v_{in} = 0.15 m/s, *Re* = 1850).

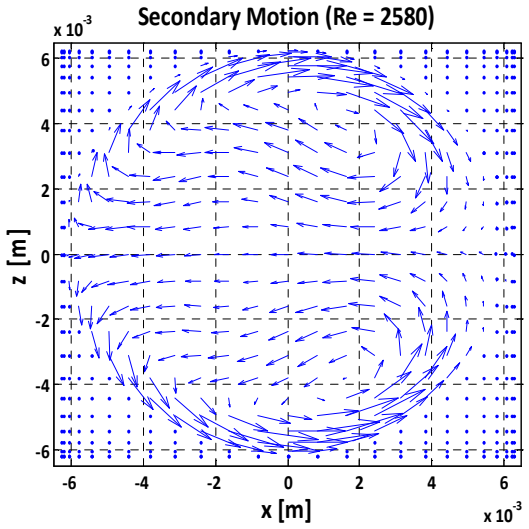

Figure 3.12 Secondary motion on the channel cross section of the SIET pipe (v_{in} = 0.21 m/s, *Re* = 2580).

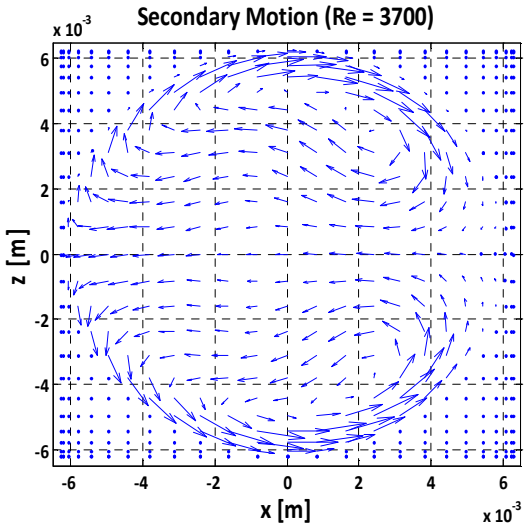

Figure 3.13 Secondary motion on the channel cross section of the SIET pipe (v_{in} = 0.3 m/s, *Re* = 3700).

Since the velocity is shifted, a secondary motion is established on the cross section, with recirculation of the fluid along the pipe wall toward the inner region. The secondary motion is characterized by two counter rotating vortices that are also responsible for the higher heat transfer rate and pressure drop, through the enhancement of the fluid mixing. The two vortices are clearly shown from Figure 3.10 to Figure 3.13 for an increasing value of the Reynolds number. With an increase of the Reynolds, the two vortices are somewhat distorted, their size becomes smaller and they are more closer to the tube wall. In addition, the center of each vortex is slightly shifted toward the inner wall.

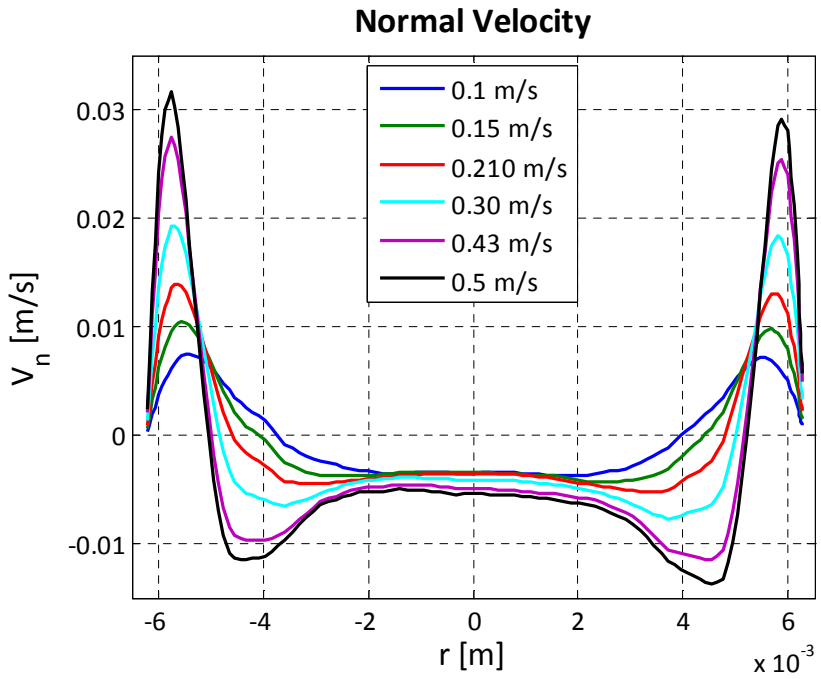

Figure 3.14 Component of the velocity in the normal direction along the vertical axis of the channel cross section for different values of the inlet velocity.

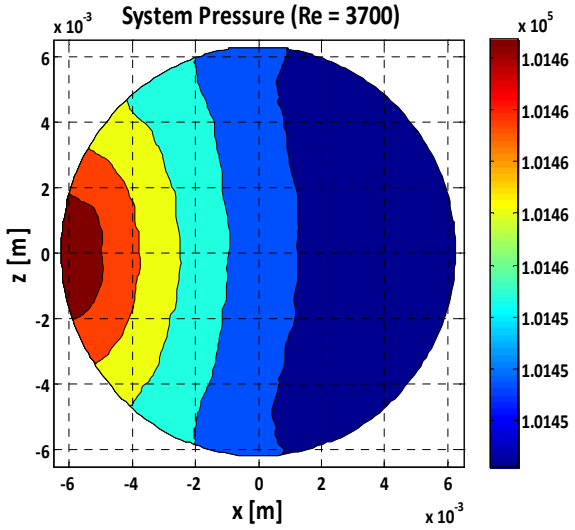

Figure 3.15 System pressure behavior on the channel cross section (v_{in} = 0.3 m/s, *Re* = 3700).

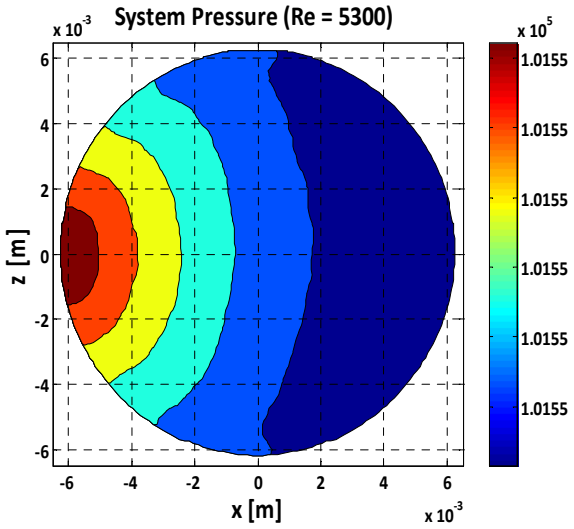

Figure 3.16 System pressure behavior on the channel cross section (v_{in} = 0.43 m/s, *Re* = 5300).

The value of the velocity in the normal direction, that is the direction perpendicular to the pipe axis, is shown in Figure 3.14 along the vertical axis of the channel cross section (the velocity is considered positive if oriented to the outside direction). Higher the Reynolds number, higher is the intensity of the secondary motion. Moreover, Figure 3.14 shows also how the two vortices are closer to the tube walls, with higher recirculation velocities in the external regions of the pipe. Instead, the normal velocity remains almost constant in the center of the pipe.

To maintain the velocity field, also the pressure field is distorted by the centrifugal field (Figure 3.15 and Figure 3.16). In particular, the pressure is higher in the external region of the pipe, whereas it results lower in the internal region. As for the velocity, the higher pressure zone is more shifted towards the outer wall increasing the Reynolds number.

To study the effect of the geometrical parameters on the laminar flow, an additional set of five helices is simulated. The pitch per radiant varies at a fixed value of the coil radius, to analyze the effect of the torsion parameter, defined in Chapter 1 with Eq.(1.3). Geometrical parameters of the simulated coils are reported in Table 3.5.

Table 3.5 Geometrical parameters of the helices used for the numerical study of the effect of the pipe torsion on the velocity field.

Helix	**r**	**p_s**	**λ**	**δ**	**β_0**
H_1	0.1 m	0.02 m	0.09615	0.01923	0.49
H_2	0.1 m	0.05 m	0.08	0.04	0.283
H_3	0.1 m	0.1 m	0.05	0.05	0.158
H_4	0.1 m	0.2 m	0.02	0.04	0.071
H_5	0.1 m	0.5 m	0.00385	0.01923	0.020

Results show an increasing deformation of the structure of the vortices with increasing torsion, which breaks the symmetry of the solution predicted by Dean (1927; 1928). The two

vortices, starting from an almost symmetrical configuration for β_0 = 0.2, change in dimensions, with the lower one enlarging while the upper one is pushed towards the upper wall, as shown in Figure 3.17 (for this case only, the right region corresponds to the outer region of the pipe). The increase in torsion also produces a progressive deformation of the axial velocity field. The maximum value is displaced from the radial direction of the helix of an angle that is dependent on the value of the torsion parameter, as evident from Figure 3.18.

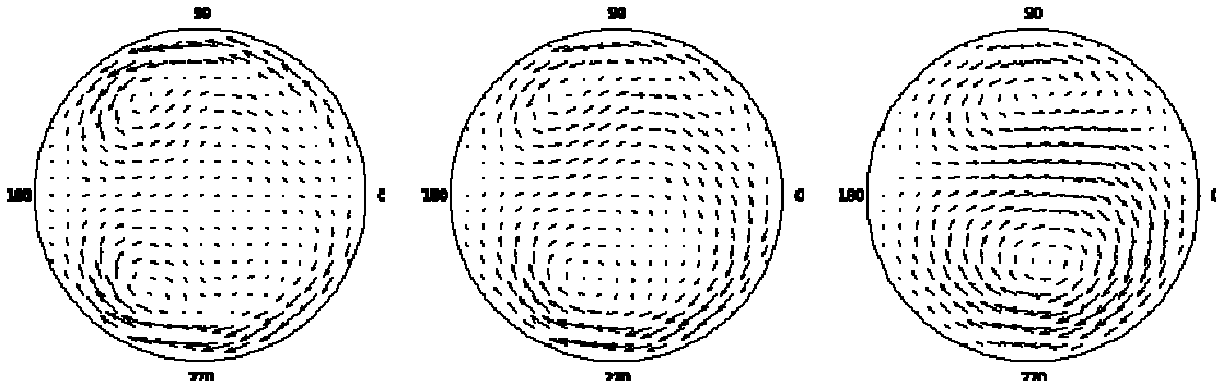

Figure 3.17 Structure of the secondary velocity field on the tube cross section as a function of the torsion of the helical pipe.

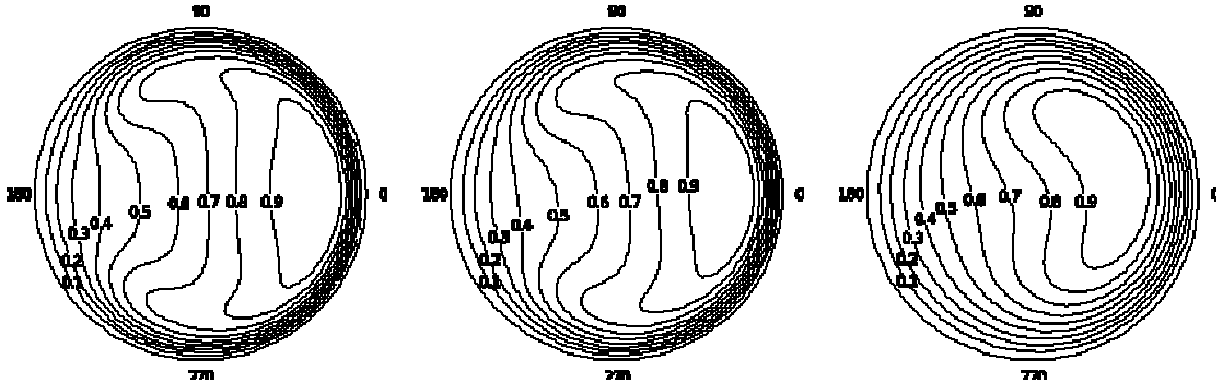

Figure 3.18 Velocity profile on the tube cross section as a function of the torsion of the helical pipe.

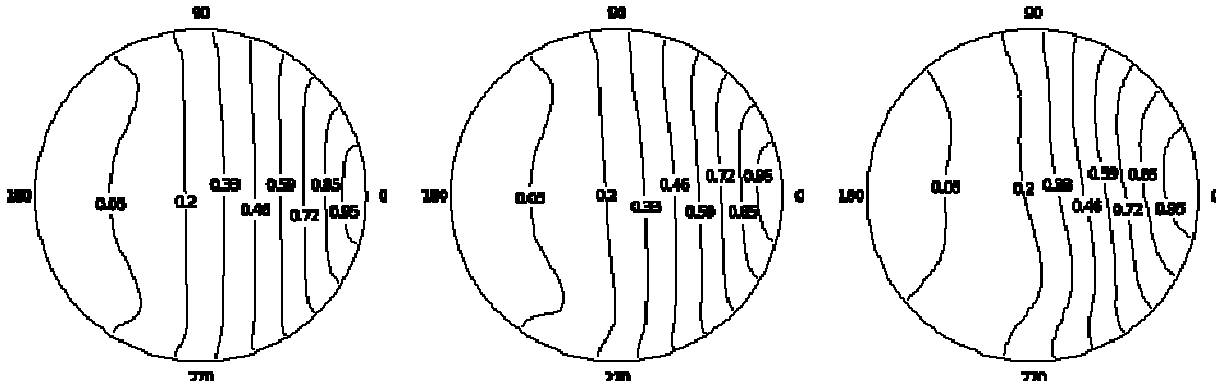

Figure 3.19 System pressure behavior on the tube cross section as a function of the torsion of the helical pipe.

In addition, a distortion of the pressure field, that actually drives and sustains the secondary flow inside the section, is evident from the computations, in agreement with the results of other authors (Murata et al., 1981; Yamamoto et al., 1995; Hüttl et al., 1999). As shown in Figure 3.19, a lower pressure region is created in the area near the center of the lower vortex, as the higher pressure region is shifted to the higher region of the pipe similarly to the maximum of the velocity.

3.3.4 *Comparison with experiments*

In order to validate the numerical results, they are compared to the experimental data of frictional pressure drop presented in Section 2.2. As in the comparison with literature correlations, also some more data obtained from the work of Cioncolini and Santini (2006) were considered, in particular the ones related to Coil6. In order to obtain the friction factor, the difference between the average pressure at two sections of the pipe far from outlet and inlet boundaries is calculated and substituted in Eq.(2.1). Numerical results for Coil6 show a fair agreement with the empirical correlations (average error is about 1.5 %) and the experimental friction factors, as it is shown in Figure 3.20. As concerns the SIET duct, results of the computations are compared with the experimental data in Figure 3.21: numerical results are in good agreement with the experimental data and show deviations comparable to the best literate correlations. Being the numerical model based on the laminar flow, a certain divergence between the numerical results and the experimental values of the friction factor is detectable starting from *Re* of about 3200, where the turbulence is expecting to appear.

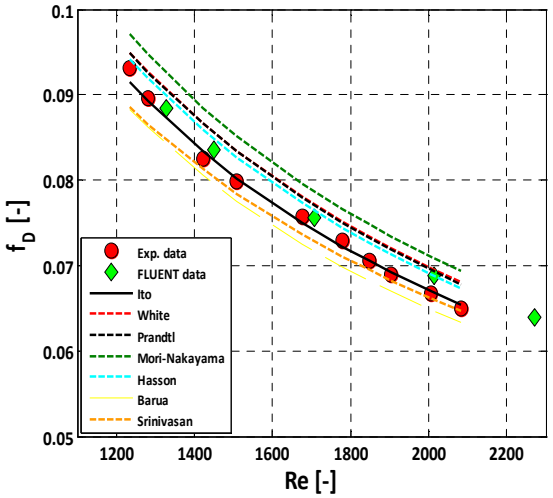

Figure 3.20 Comparison between experimental data, literature correlations and CFD simulations for Coil6 of the work of Cioncolini and Santini (2006).

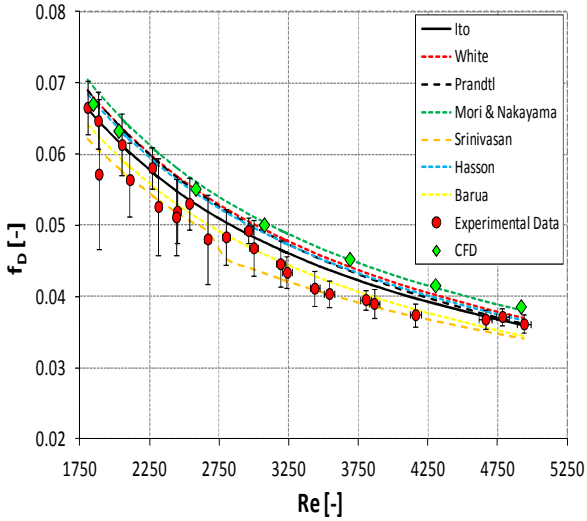

Figure 3.21 Comparison between experimental data, literature correlations and CFD simulations for the SIET facility.

3.4 Numerical analysis of the turbulent flow

After characterizing the single-phase flow in the laminar region, the numerical study of the turbulent regime has been focused on the applicability of different turbulence models to the helical pipe case. As pointed out in Section 3.1, numerous literature works handle the CFD simulation of the turbulent flow in the helical geometry, many of which individually assessed with experimental data or previous results. However, except for the work of Di Piazza and Ciofalo (2010), a comprehensive comparison between turbulence model results is lacking. Therefore, different turbulence models have been compared in relation to their capability to predict the frictional pressure drop. The validation was made through comparison with the experimental data and some of the most common correlations available in literature. As for the laminar regime, in addition to the experimental data collected at SIET labs, also some data obtained from the work of Cioncolini and Santini (2006) were used.

3.4.1 CFD modeling

Five different turbulence models were tested. The standard k-ε model proposed by Launder and Spalding (1972), with the same constant values recommended by the authors. The RNG k-ε model proposed by Yakhot and Orszag (1986), derived using the mathematical technique called Renormalization Group method (Choudhury, 1993). The model provides an analytical formula for the turbulent Prandtl number, includes the effect of swirl on turbulence and an analytically derived differential formula for the effective viscosity. The model resulted more accurate and reliable for rapidly strained flows, swirling flows and low Reynolds number flows. The realizable k-ε model (Shih et al., 1995) includes a new formulation for the turbulent viscosity and a new transport equation for the dissipation rate ε, derived from an exact equation for the transport of the mean-square vorticity fluctuations. The model is known to provide better performances for flows involving rotation, boundary layer under strong adverse pressure gradients, separation, recirculation and complex secondary flow features.

The SST k-ω model, proposed by Menter (1994), applies the k-ω formulation in the inner part of the boundary layer, to make the model directly usable all the way down to the wall through the viscous sub-layer. In addition the SST formulation switches to a k-ε behavior in the free stream.

The second order RSM involves calculation of the individual Reynolds stresses, using differential transport equations. The individual Reynolds stresses are then used to obtain closure of the Reynolds averaged momentum equations (Launder et al., 1975; Launder, 1989).

Besides the availability of numerous turbulence models, the FLUENT code allow to choose between two modeling approaches to solve the near wall region of a turbulent flow. In addition to the wall function, also a near wall model in which the near wall region is completely resolved all the way to the viscous sub layer is available. With the wall function, the viscosity affected region and the fully turbulent region are bridged with semi empirical formulas and the viscosity affected inner region is not resolved. Two types of wall function were tested, the standard two-layer based wall function (Launder and Spalding, 1972) and the

non equilibrium wall function (Kim and Choudhury, 1995). In both cases, the expression for the velocity in the region between the wall and the first mesh node reads:

$$\frac{\mathrm{v}}{\mathrm{v}^*} = y^+ \qquad y^+ < 11.225. \tag{3.7}$$

$$\frac{\mathrm{v}}{\mathrm{v}^*} = \frac{1}{K'}\ln(Ey^+) \qquad y^+ \geq 11.225 \tag{3.8}$$

The non equilibrium wall function adds to the standard treatment a sensitivity of the mean velocity log-law to pressure gradient effects. On the other hand, the FLUENT enhanced wall treatment considers a two layer model in which the viscosity affected near wall region is resolved all the way to the viscous sub-layer, provided that the mesh is sufficiently fine.

3.4.2 Grid and numerical settings

Momentum and turbulence model equations are discretized using the second order upwind scheme and the SIMPLEC algorithm is used to resolve the coupling between velocity and pressure. Convergence criterion used is 10^{-5} for velocities and 10^{-4} for *k*, *ε*, *ω* and Reynolds stresses. The same helical pipe section developed for the laminar study (Section 3.3.1) is used. At the inlet, uniform profiles for all the dependent variables are imposed:

$$\mathrm{v} = \mathrm{v}_0 \quad k = k_0 \quad \varepsilon = \varepsilon_0 \tag{3.9}$$

Pressure is fixed in the outlet section and the no-slip boundary conditions is imposed at the wall. Turbulence intensity *I* and the turbulence characteristic length scale *L* are imposed in the inlet section:

$$I = \frac{\mathrm{v}'}{\mathrm{v}}100\% \tag{3.10}$$

$$L' = 0.07\left(\frac{d}{2}\right) \tag{3.11}$$

Table 3.6 Grid independence study for the wall function grid (Mesh A) and both the SIET pipe and Coil6.

SIET pipe		**Coil6**	
Grid	f_D	Grid	f_D
405 x 240	0.0266	245 x 224	0.0268
720 x 240	0.0270	405 x 224	0.0265
1125 x 240	0.0275	605 x 280	0.0265
2000 x 240	0.0323	605 x 320	0.0266
2420 x 240	0.0339	1125 x 280	0.0273
4500 x 240	0.0380	2000 x 280	0.0306

The same structured grid described in Section 3.3.1 is adopted. Two different grid sensitivity study are necessary to define the correct grid to be used with the wall function and with the enhanced wall treatment. In fact, it is well known that although FLUENT uses the linear (laminar) law when y^+<11.225, the first grid point should be located far enough to avoid a fine mesh in the near wall region, as the wall function ceases to be valid in the viscous sub-layer. On the contrary, the enhanced wall treatment needs a first grid point y^+ value well inside the viscous sub-layer (y^+< 4 - 5) at least, with a most ideally value of the order of y^+=1. In the following, grid related to the wall function approach will be referred as Mesh A, while grid related to the enhanced wall treatment as Mesh B.

Table 3.7 Grid independence study for the enhanced wall treatment grid (Mesh B) and both the SIET pipe and Coil6

SIET pipe		**Coil6**	
Grid	f_D	Grid	f_D
1125 x 240	0.0372	605 x 280	0.0288
2420 x 240	0.0367	1125 x 280	0.0291
3125 x 240	0.0358	2000 x 280	0.0297
4500 x 240	0.0341	3125 x 280	0.0300
5120 x 240	0.0340	4500 x 280	0.0300

For Mesh A, 6 different grids were considered respectively for the SIET pipe and the Coil6. The results, obtained with the *k-ε* model with the standard wall function, are resumed in Table 3.6. In both coils, at the beginning the grid refinement seems to have no effect, as the friction coefficient remains almost constant, then it starts to increase when the number of nodes is increased further. The latter effect clearly indicates how an excessively fine mesh in the near wall region is unsuited for the wall function approach. The grids with 1125 x 240 (Figure 3.22) and 605 x 280 elements are selected for the two cases respectively, as they allow to obtain more detailed definition of all the other physical quantities in addition to the friction factor.

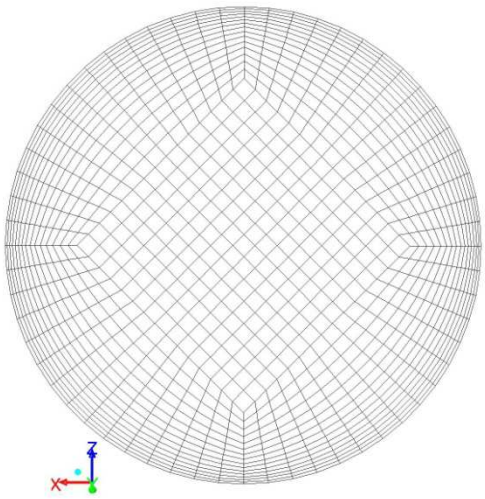

Figure 3.22 Mesh A for the SIET pipe.

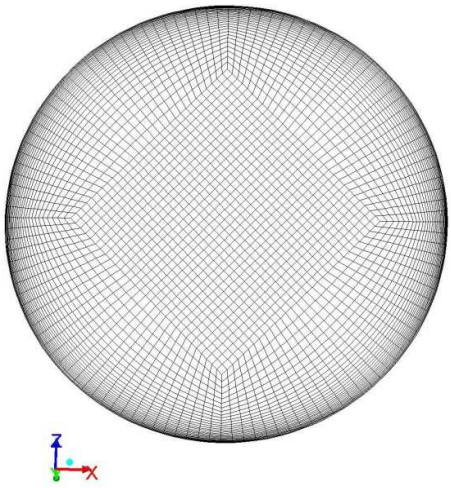

Figure 3.23 Mesh B for the SIET pipe.

Mesh B is examined for both the SIET pipe and Coil6 with the realizable *k-ε* model and the results are resumed in Table 3.7. Refining the grid, friction factor coefficient lowers until the difference with the values calculated with the next finer grid becomes negligible. Grid selected to be used with the enhanced wall treatment are 4500 x 240 (Figure 3.23) and 3125 x 280 respectively, so with an extremely higher number of cells with respect to the wall function case.

3.4.3 *Comparison with the experimental data*

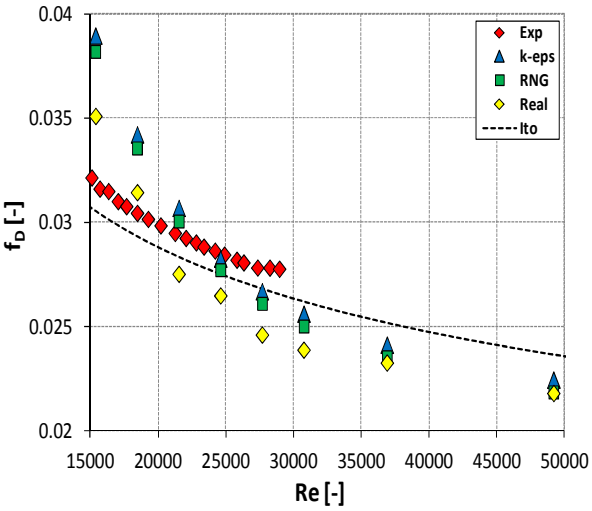

Figure 3.24 Comparison for the SIET pipe between the experimental data, the Ito correlation and the results of the three *k-ε* models with the standard wall function at medium-high *Re*.

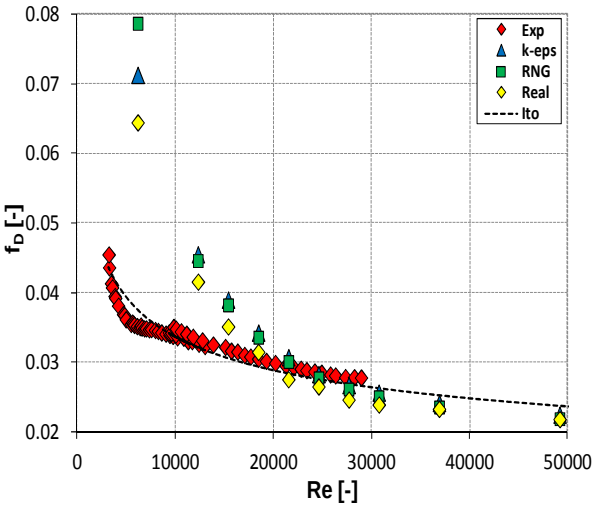

Figure 3.25 Comparison for the SIET pipe between the experimental data, the Ito correlation and the results of the three *k-ε* models with the standard wall function.

Figure 3.24 and Figure 3.25 compare the friction factor experimental data with the simulation results obtained with the three *k-ε* models and the standard wall function in the SIET pipe. The results are satisfactory for medium-high Reynolds numbers, where results of all the three models are almost overlapped and deviations from the experimental values and the Ito correlation are under the 10% on average (Figure 3.24).

In the medium-low Reynolds region, on the contrary, the friction coefficient is highly overestimated, not only in the transition region, where the CFD friction coefficients have values approximately double with respect to the experimental measurements, but also in the first section of the fully turbulent region (Figure 3.25). The standard *k-ε* model becomes reliable starting from a Reynolds number of about 20000, as both the model and the standard wall function are known to provide the better results at high Reynolds. Comparable results are obtained with the RNG *k-ε* model. The Realizable *k-ε* model provides the best results, although they are only slightly better with respect to the other models. The friction coefficient is lower at low Reynolds numbers and the results are satisfactory also in the region 15000 < *Re* < 20000.

Since the three *k-ε* models provide results almost equal or only slightly different, the overestimation of the frictional pressure drop at low Reynolds seems due to the treatment of the near wall region. In particular, the wall function becomes less reliable as the dimensionless distance between the first grid point and the wall reduces with the Reynolds number down to values belonging to the viscous sub-layer. The above reasoning is confirmed by the results of Coil6 (Figure 3.26). The friction factor is overestimated up to Reynolds of 15000 for the Realizable model and about 20000 for the standard *k-ε* and the RNG models. In the medium-high Reynolds number region the deviation from the experimental data remains under 10%. No improvements are obtained with the non-equilibrium wall function. Actually, the overestimation become higher in the low Reynolds number region. Figure 3.27 shows the results for all the three *k-ε* models.

The second order RSM introduces a higher degree of detail and complexity with respect to the *k-ε* model. The results obtained with the RSM and the wall function are resumed in Figure 3.28. No significant differences are found with respect to the realizable *k-ε* model, in both the low and the high Reynolds number regions. As a consequence, the higher complexity and the computational expense introduced with the RSM are not justified, at least as long as the wall function is adopted for solution of the near wall region. To sum up, the realizable *k-ε* model provides the best results, although the particular turbulence model does not have a particular relevance on the accuracy of the results. On the contrary, the wall treatment is proved to be most significant parameter. In particular, the wall function seems to be unable to correctly predict the friction coefficient for low-medium Reynolds numbers. In addition, also at high Reynolds the frictional pressure drop results slightly underestimated and the errors, even though satisfactory, are a little higher with respect to the Ito correlation.

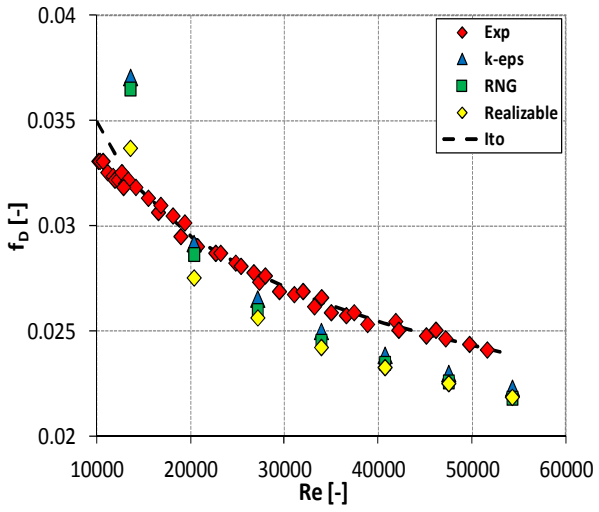

Figure 3.26 Comparison between the experimental data, the Ito correlation and the results of the three *k-ε* models with the standard wall function for Coil6.

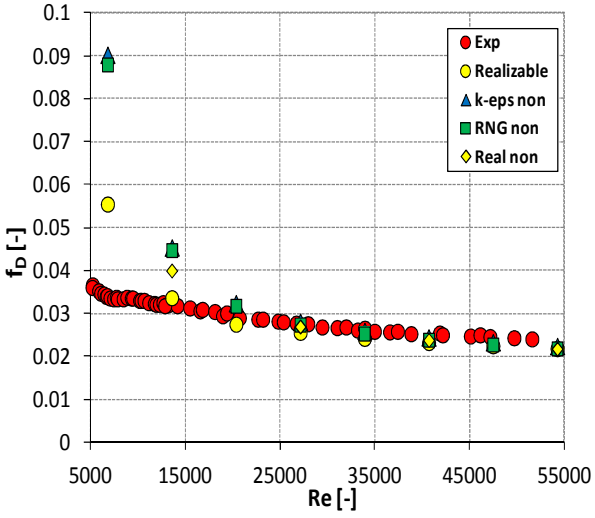

Figure 3.27 Comparison between the experimental data, the Ito correlation and the results of the three *k-ε* models with the non-equilibrium wall function for Coil6.

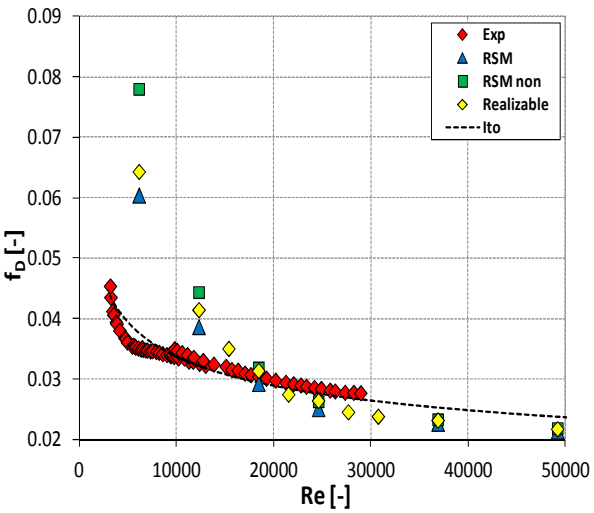

Figure 3.28 Comparison between the experimental data and the RSM model for the SIET pipe.

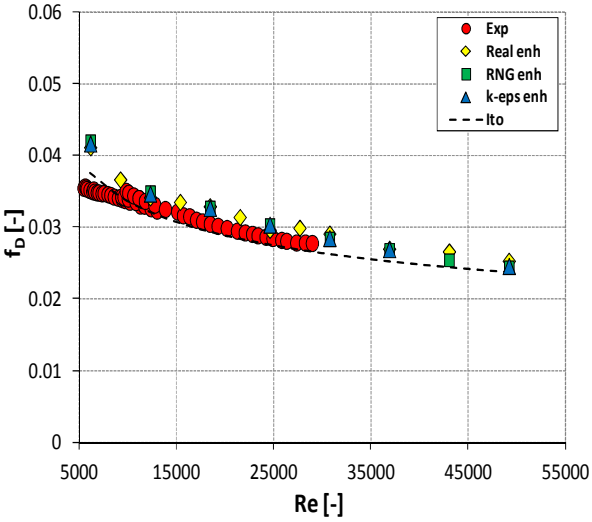

Figure 3.29 Comparison between the experimental data and the *k-ε* models with the enhanced wall treatment for the SIET pipe.

The friction factor simulated with the 3 *k-ε* models and the enhanced wall treatment is shown in Figure 3.29. The agreement with the experimental data is very good also at low Reynolds and the friction factor is slightly overestimated only in the first section of the transition region. In the fully turbulent region, the accuracy of the simulations are improved and the deviations from the experimental data are negligible and comparable or slightly better with respect to the Ito correlation. Similar behavior is shown for Coil6 (Figure 3.30), although the differences between the simulation results and the experimental data are higher. The higher errors, although decreasing with the Reynolds number, could indicate a dependence of the error on the pipe curvature. Between the different models, the Realizable *k*-ε provides slightly better results also with the enhanced wall treatment. Also the SST *k-ω* model solves the near wall region all way down to the wall, so it is compared with the realizable *k-ε* model in Figure 3.31 for the SIET pipe. At low Reynolds, the *k-ω* agrees better with the experimental data, whereas at medium-high Reynolds the model overestimates the frictional pressure drop. Comparable results are found also for Coil6.

To sum up, the treatment of the wall is the determining parameter, with the enhanced wall treatment that results particularly appropriate for the simulation of the counter rotating vortices and the secondary motion characterizing the helical pipe.

To support the previous statement, useful information can be gained from the analysis of the behavior of the wall shear stress provided by the code. Due to the presence of the centrifugal force field and the secondary motion, it is different with respect to straight pipes. In particular, it is interesting to compare the shear stress profiles obtained with the wall function and with the enhanced wall treatment. The analysis was made with the realizable *k-ε* model, but it can be extended to all the other turbulence models. The wall shear stress, as expected, is higher in the outer region of the pipe, where the velocity is higher for the centrifugal force effect induced by the tube geometry. As a consequence, higher is the velocity gradient at the wall. On the contrary, a lower shear stress peak corresponds to the inner region of the pipe, where the velocity is lower.

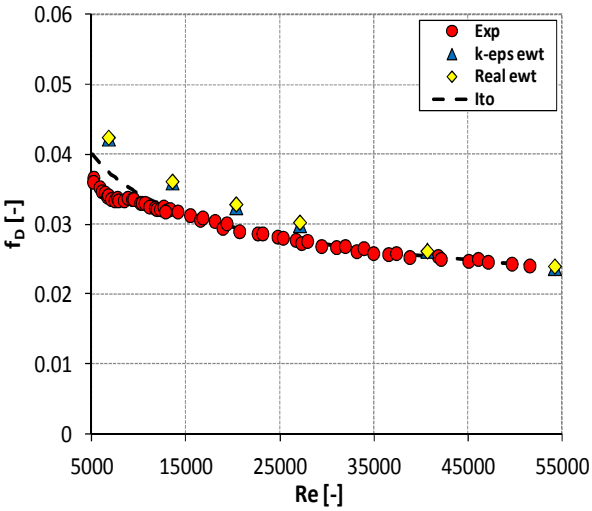

Figure 3.30 Comparison between the experimental data and the *k-ε* models with the enhanced wall treatment for Coil6.

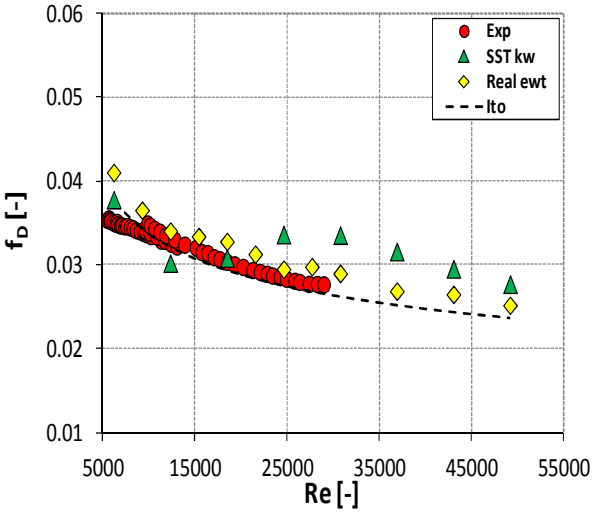

Figure 3.31 Comparison between the experimental data and the SST *k-ω* model for Coil6.

The wall shear stress profile obtained with the enhanced wall treatment appears very smooth, with two discontinuities corresponding to the higher and the lower pipe regions, more evident at higher Reynolds. In the high Reynolds number region (Figure 3.32), the wall shear stress profiles are qualitatively similar, with the higher values obtained with the enhanced wall treatment. Starting from medium Reynolds, the wall shear stress calculated with the standard wall function increases to finally exceed the enhanced wall treatment values at low Reynolds numbers (Figure 3.33).

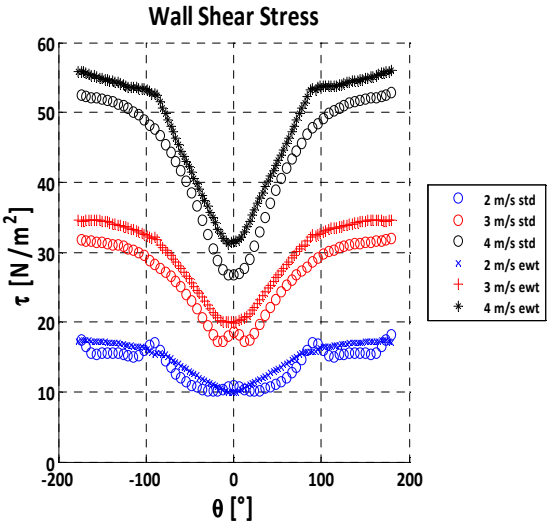

Figure 3.32 Wall shear stress in the medium-high Reynolds number region (std = standard wall function; ewt = enhanced wall treatment).

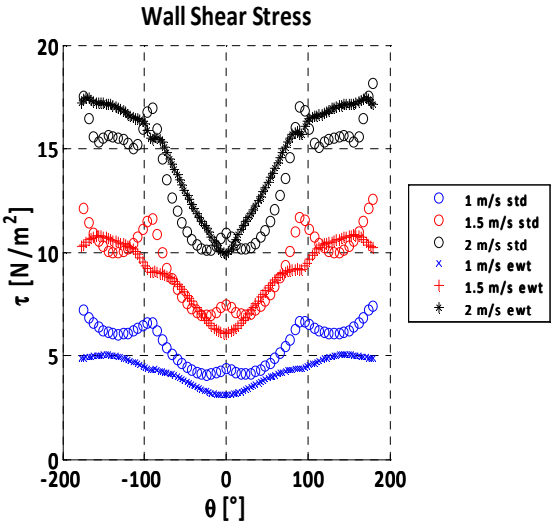

Figure 3.33 Wall shear stress in the medium-low Reynolds number region (std = standard wall function; ewt = enhanced wall treatment).

Moreover, the standard wall function profiles show different peaks in correspondence of outer, inner, higher and lower regions of the pipe. This effect is directly related to the use of

the wall function, as the dimensionless distance from the wall (y^+) is no more constant along the pipe circumference as in straight pipes, but it varies as a consequence of the secondary flow (Figure 3.34). Actually, y^+ shows lower peaks ending in the viscous sub-layer also when its average value is sufficiently higher. These y^+ lower peaks corresponds to wall shear stress higher peaks that cause the overestimation of the wall shear stress with the wall function in the medium-low Reynolds number region.

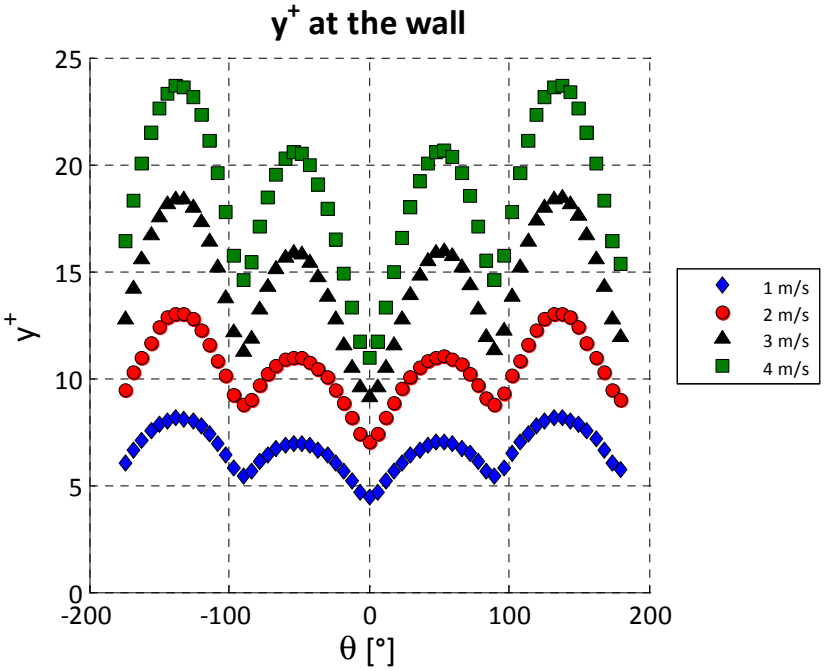

Figure 3.34 Circumferential y^+ profile for the realizable k-ε model with the standard wall function.

3.5 Conclusions

This chapter has been focused on the single-phase flow, considered as a starting point for the study of the thermal hydraulic of the two-phase flow inside the helically coiled pipe. The experimental data were compared to some correlations available in literature, regarding the laminar to turbulent flow transition and the friction coefficient. Since the available models and correlations allow a good and satisfactory estimation of both the transition point and the friction factor, no need for improvement seemed necessary. For the laminar to turbulent flow transition, which shows peculiar differences with respect to straight pipes, the formula developed by Cioncolini and Santini (2006) resulted pretty accurate. For the friction factor, the two correlations proposed by Ito (1959) returned the best results, with average relative errors with respect to the experimental data under the 5 %.

The laminar single-phase flow was extensively characterized with CFD simulations, performed with the commercial code ANSYS FLUENT. The physical phenomena characterizing the flow in the helical pipe have been understood and underlined. The centrifugal force field, introduced by the geometry, shifts the velocity maximum toward the external wall, generating a secondary motion on the channel cross section characterized by two counter rotating vortices. The secondary motion enhances the fluid mixing, so the heat

transfer and the frictional pressure drop with respect to straight ducts. A parametric study has been proposed on the effect of the torsion of the pipe. An increasing torsion tends to break the symmetry of the two vortices, that results almost perfect in a toroidal pipe (a curved pipe with zero torsion). Finally, the numerical results were compared to the experimental friction factor data, showing errors lower than 5 %, in agreement with the best literature correlations.

In the turbulent region, the CFD results were compared to the frictional pressure drop experimental data, to validate the predictions of different turbulence models. In relation to the estimation of the frictional pressure drop in the two analyzed coils, the results showed no relevant differences between the turbulence models, whereas the critical role is played by the treatment of the near wall region. Actually, satisfactory results were obtained in the whole range of Reynolds numbers only with the enhanced wall treatment, implemented in the ANSYS FLUENT code. The enhanced wall treatment solves the flow field all the way to the wall if the mesh is sufficiently fine. Therefore, the described wall treatment seems necessary to study the helical tube with a sufficient accuracy, as a consequence of the secondary motion that characterizes the flow. In particular, only the enhanced wall treatment allowed to correctly reproduce the behavior of the shear stress at the wall, that shows some differences with respect to straight ducts ascribable to the presence of the secondary motion.

References

S. Ali, 2001. Pressure drops correlations for flow through regular helical coil tubes. Fluid Dynamics Research 28, 295-310.

ANSYS Fluent 14.0 User Guide, 2011.

S.N. Barua, 1963. On secondary flow in stationary curved pipes. Quarterly Journal of Mechanics and Applied Mathematics 16, 61-77.

S.A. Berger, L. Talbot, L.S. Yao, 1983. Flow in curved pipes. Annual Review of Fluid Mechanics 15, 461-512.

W.H. Chen, R. Jan, 1992. The characteristics of laminar flow in helical circular pipe. Journal of Fluid Mechanics 244, 241-256.

D. Choudhury, 1993. Introduction to the Renormalization Group Method and turbulence modeling. Technical Memorandum TM-107, Fluent Inc.

S.E. Kim, D. Choudhury, 1995. A near-wall treatment using wall functions sensitized to pressure gradient. Separated and Complex Flows, ASME.

A. Cioncolini, L. Santini, 2006. An experimental investigation regarding the laminar to turbulent flow transition in helically coiled pipes. Experimental Thermal and Fluid Science 30, 367-380.

W.R. Dean, 1927. Note on the motion of fluid in a curved pipe. Philosophical Magazine Series 4, 208-223.

W.R. Dean, 1928. The stream-line motion of fluid in a curved pipe. Philosophical Magazine Series 5, 673-695.

I. Di Piazza, M. Ciofalo, 2010. Numerical prediction of turbulent flow and heat transfer in helically coiled pipes. International Journal of Thermal Sciences 49, 653-663.

J. Eustice, 1910. Flow of water in curved pipes. Proceedings of the Royal Society of London, Series A, Vol. 84, 107-118.

M. Germano, 1982. On the effect of torsion on a helical pipe flow. Journal of Fluid Mechanics 125, 1-8.

M. Germano, 1989. The Dean equations extended to a helical pipe flow. Journal of Fluid Mechanics 203, 289-305.

D. Greenspan, 1973. Secondary flow in a curved pipe. Journal of Fluid Mechanics 57, 167-176.

D. Hasson, 1955. Streamline flow resistance in coils. Res. Corresp. 1, S1.

T.J. Hüttl, R. Friedrich, 2000. Influence of curvature and torsion on turbulent flow in helically coiled pipes. International Journal of Heat and Fluid Flow 21, 345-353.

T.J. Hüttl, R. Friedrich, 2001. Direct numerical simulation of turbulent flows in curved and helically coiled pipes. Computers & Fluids 30, 591-605.

H. Ito, 1959. Friction factors for turbulent flow in curved pipes. Transactions of the ASME D, Journal of Basic Engineering 81, 123-124.

H. Ito, 1969. Laminar flow in curved pipes. Zeitschrift für Angewandte Mathematik und Mechanik 49, 653-663.

J.S. Jayakumar, S.M. Mahajani, J.C. Mandal, P.K. Vijayan, R. Bhoi, 2008. Experimental and CFD estimation of heat transfer in helically coiled heat exchangers, Chemical Engineering Research and Design 86, 221-232.

J.S. Jayakumar, S.M. Mahajani, J.C. Mandal, K.N. Iyer, P.K. Vijayan, 2010. CFD analysis of single-phase flows inside helically coiled tubes. Computers and Chemical Engineering 34, 430-446.

H.C. Kao, 1987. Torsion effect on fully developed flow in an helical pipe. Journal of Fluid Mechanics 184, 335-356.

V. Kumar, S. Saini, M. Sharma, K.D.P. Nigam, 2006. Pressure drop and heat transfer study in tube-in-tube helical heat exchanger. Chemical Engineering Science 61, 4403-4416.

B.E. Launder, 1989. Second-moment closure: present… and future?. International Journal of Heat and Fluid Flow 10(4), 282-300.

B.E. Launder, G.J. Reece, W. Rodi, 1975. Progress in the development of a Reynolds-Stress turbulence closure. Journal of Fluid Mechanics 68(3), 537-566.

B.E. Launder, D.B. Spalding, 1972. The numerical computation of turbulent flows. Computer Methods in Applied Mechanics and Engineering 3, 269-289.

L.J. Li, X.C. Lin, M.A. Ebadian, 1998. Turbulent mixed convective heat transfer in the entrance region of a curved pipe with uniform wall-temperature. International Journal of Heat and Mass Transfer 41, 3793-3805.

X.C. Lin, M.A. Ebadian, 1997. Developing turbulent convective heat transfer in helical pipes. International Journal of Heat and Mass Transfer 40(16), 3861-3873.

X.C. Lin, M.A. Ebadian, 1999. The effects of inlet turbulence on the development of fluid flow and heat transfer in a helically coiled pipe. International Journal of Heat and Mass Transfer 42, 739-751.

D.J. McConalogue, R.S. Srivastava, 1968. Motion of a fluid in a curved tube. Proceedings of the Royal Society A: Mathematical, Phisical and Engineering Sciences 307, 37-53.

F.R. Menter, 1994. Two-equation eddy-viscosity turbulence models for engineering applications. J 32, American Institute of Aeronautics and Astronautics.

P. Mishra, S.N. Gupta, 1979. Momentum Transfer in Curved Pipes 1. Newtonian Fluids; 2. Non-Newtonian Fluids. Industrial and Engineering Chemistry Process Design and Development 18, 130-142.

Y. Mori, W. Nakayama, 1965. Study on forced convective heat transfer in curved pipes. International Journal of Heat and Mass Transfer 8, 67-82.

S. Murata, Y. Miyake, T. Inaba, H. Ogawa, 1981. Laminar flow in a helically coiled pipe. Bulletin of the JSME 24, 335-356.

P. Naphon, S. Wongwises, 2006. A review of flow and heat transfer characteristics in curved tubes. Renewable and Sustainable Energy Reviews 10, 463-490.

L. Prandtl, 1949. Fuhrer dmchdie stromungslehre. 3rd Edition, Braunsschweigh. Essentials of Fluid Dynamics (English translation). Blackie and Son, London, 1954.

R.K. Shah, S.D. Joshi, 1987. Convective heat transfer in curved ducts. In: S. Kakac, R. K. Shah, W. Hung, Handbook of Single-Phase Convective Heat Transfer, Wiley Interscience, New York.

T.H. Shih, W.W. Liou, A. Shabbir, J. Zhu, 1995. A new k-ε eddy-viscosity model for high Reynolds number turbulent flows – model development and validation. Computer Fluids, 24(3), 227-238.

P.S. Srinivasan, S.S. Nandapurkar, F.A. Holland, 1968. Pressure drop and heat transfer in coils. The Chemical Engineering Journal 218, 113-119.

C.Y. Wang, 1981. On the low-Reynolds number flow in a helical pipe. Journal of Fluid Mechanics 108, 185-194.

C.M. White, 1929. Streamline flow through curved pipes. Proceedings of the Royal Society of London, Series A, Vol. 123, 645-663.

C.M. White, 1932. Fluid friction and its relation to heat transfer. Transaction of the Institute of Chemical Engineering 10, 66-86.

G.D. Xie, 1990. Torsion effect on secondary flow in helical pipes. International Journal of Heat and Fluid Flow 11, 114-119.

A. Yakhot, S.A. Orszag, 1986. Renormalization group analysis of turbulence. I. Basic theory. Journal of Scientific Computing 1(1), 1-51.

K. Yamamoto, T. Akita, H. Ikeuchi, Y. Kita, 1995. Experimental study of the flow in a helical circular tube. Fluid Dynamics Research 16, 237-249.

G. Yang, M.A. Ebadian, 1996. Turbulent forced convection in a helicoidal pipe with substantial pitch. International Journal of Heat and Mass Transfer 39(10), 2015-2022

CHAPTER 4

The two-phase flow: CFD study and drift-flux analysis of the results

While the previous chapter was focused on the single-phase flow inside the helical pipe, from this point forward the two-phase flow becomes the main actor. The analysis is started in this chapter with the CFD study of the two-phase flow. In Chapter 5 the focus is only on the two-phase frictional pressure drop, for which a correlation is developed. The study of the two-phase flow ends in Chapter 6, where the DWO instability in parallel channel is addressed. The results of the next two chapters merge in the analytical model developed for the study of the DWO in Chapter 6. Two correlations for the estimation of the frictional pressure drop and the void fraction are included in the model to improve the simulation of the helical pipe. The correlation for the void fraction is developed in the last part of this chapter following an analysis of the CFD results based on the drift-flux model.

As stated before, the subject of this chapter is the CFD study of the two-phase flow inside the helical tube. With respect to an empirical correlation as the one that will be presented in Chapter 5, the CFD simulation can provide many detailed results, needed for a complete characterization of the two-phase flow. In particular, the local, three dimensional values of void fraction and velocity allow to study the effect of the centrifugal force. In addition, the CFD can also provide an accurate quantitative estimation of parameters such as the frictional pressure drop and the void fraction. Following the analysis of the single-phase flow in Chapter 3, the ANSYS FLUENT code is applied also here for the study of the two-phase flow.

Recently, the two-phase CFD is increasingly applied in the nuclear field, as a promising way to extend the simulation capabilities for many nuclear reactor thermal hydraulic issues (Bestion, 2012). However, publications available for the helical tubes are rather limited, due to the significant modeling complexities. Jo et al. (2009) investigated the two-phase flow heat transfer in the helical tubes of a pressurised water reactor SG using the CFX code. They reported the formation of a liquid film on the outer portion of the tube and showed good agreement with experimental data. Jajakumar et al. (2010) presented a CFD analysis for the heat transfer of an air-water two-phase mixture flowing through a helically coiled heat exchanger. Chandratilleke et al. (2012) studied the flow boiling in curved pipes with a non-equilibrium model based on the Eulerian multiphase approach.

The fundamental step for a confident utilization of the numerical results is the assessment of their accuracy with experimental data. It is important to notice that for the void fraction no data are available from the SIET facility, neither from literature for a steam-water mixture at high pressure, except for the work of Unal (1978). Nevertheless, the void fraction is one of the

parameter of major interest. Therefore, the analysis starts from an air-water flow, for which numerous work are available in literature, including data on both the void fraction and the frictional pressure drop. In particular, the work of Akagawa et al. (1971) is considered for comparison.

The two-phase mixture is described with the Eulerian – Eulerian approach. Some parameters particularly critical for the results are identified, as the diameter of the dispersed phase and the treatment of the near wall region. The phase distribution on the channel cross section, the velocity field and the structure of the secondary motion are analyzed to study the effect of the centrifugal force field. Finally, the numerical results are validated through comparison with the experimental data for the void fraction and the frictional pressure drop.

Following the study of the air-water flow, the same model is applied to the adiabatic steam-water flow at high pressure. Also in this case, the characteristics of the two-phase flow and the effect of the centrifugal force are studied. In particular, an explanation is proposed for the peculiar peak in the frictional pressure drop profile based on the phase distribution, the flow regime and the wall shear stress. The numerical results are then compared to the adiabatic frictional pressure drop experimental data measured in the SIET facility. In addition, the behaviour of the void fraction is derived from the CFD results.

Following the CFD study, a large number of results are available to support the analysis of the two-phase flow, including data on the void fraction. An analysis based on the drift-flux formulation is proposed for the void fraction. In particular, the drift flux formulation is used to cluster all the information gained through the CFD and derive a simple but accurate empirical correlation. In addition, the formulation itself allows to further validate the CFD results, as regards the velocity and the void fraction distributions in the pipe cross section. The latter in particular is of fundamental importance, since local velocity or phase distribution cannot be considered completely validated only with an integral comparison, as the one made with the frictional pressure drop and the void fraction experimental data.

In the drift-flux model, the two-phase fluid is treated as a mixture and the relative motion between the phases is accounted for by a kinematic constitutive equation. The void fraction is expressed as function of two fundamental quantities, the concentration parameter C_0 and the average drift velocity weighted on the void fraction V_{gj}.

Starting from the air-water case, the two parameters C_0 and V_{gj} are first determined through correlation of the experimental data. Considering their basic definition, C_0 and V_{gj} are also calculated from the CFD numerical results, obtaining a similar and equally accurate correlation. The latter represents a further validation of the consistency and the reliability of the CFD results, that are therefore useful to support the development of an empirical correlation for the void fraction. The same methodology is applied to the steam-water results. A void fraction correlation is developed and some inconsistencies in the results at low flow quality are underlined.

4.1 Air-water two-phase flow

4.1.1 *The experimental data*

Among others, a comprehensive research on an air-water two-phase flow inside the helical coil was published by Akagawa et al. (1971). The work has been considered as the

reference for the validation of the CFD results. In the paper, the authors study through experiments the flow pattern, the void fraction and the frictional pressure drop for a two-phase air-water flow. Two different helices are addressed, having the same tube diameter *d* equal to 9.93 mm and coil diameter of 0.109 m and 0.225 m, for a *d/D* ratio respectively of 1/11 and 1/22.7. In addition to void fraction and frictional pressure drop measurements, also some observations on the flow pattern are provided by direct visualization of the flow. In particular, the water superficial velocity is included between 0.35 m/s and 1.16 m/s, while the gas superficial velocity between 0 m/s and 5 m/s. In particular, for each one of the four fixed values of the liquid flow rate, the air flow rate is gradually increased starting from a very low value. The frictional pressure drop data are shown in Figure 4.1 and Figure 4.2, where the four groups of data at constant liquid superficial velocity are clearly visible.

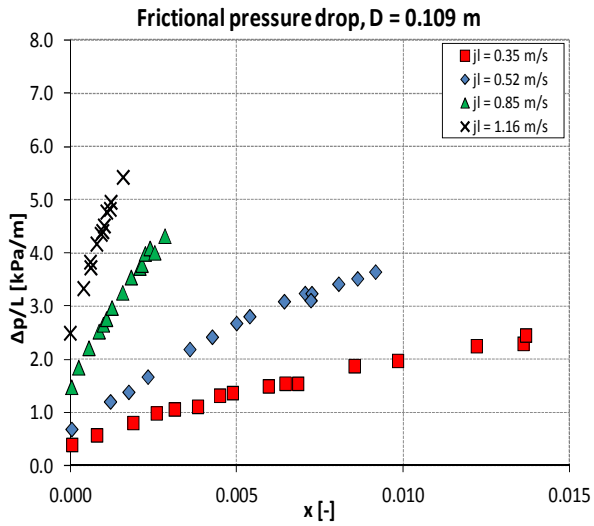

Figure 4.1 Frictional pressure drop experimental data for the *D* = 0.109 m helix (Akagawa et al., 1971).

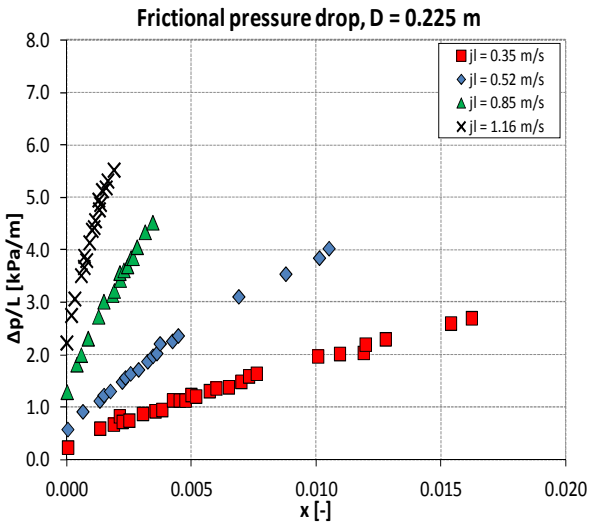

Figure 4.2 Frictional pressure drop experimental data for the *D* = 0.225 m helix (Akagawa et al., 1971).

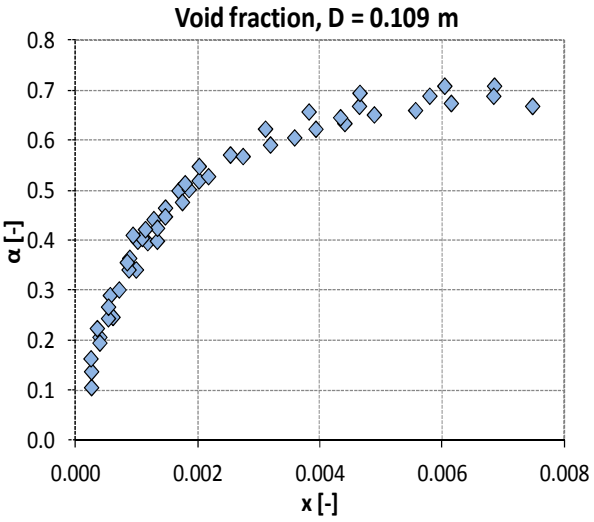

Figure 4.3 Void fraction experimental data for the *D* = 0.109 m helix (Akagawa et al., 1971).

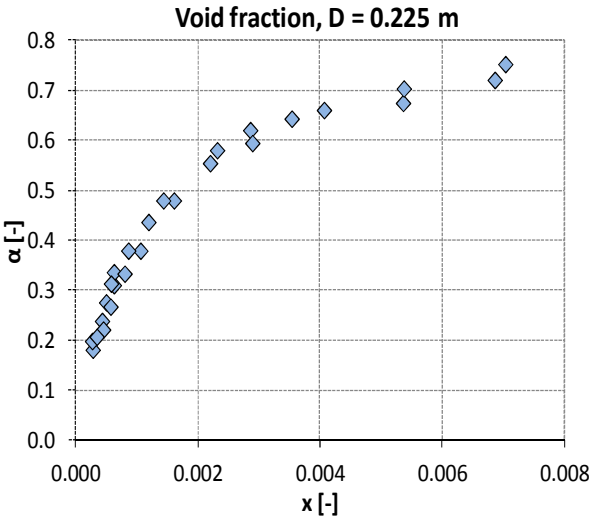

Figure 4.4 Void fraction experimental data for the *D* = 0.225 m helix (Akagawa et al., 1971).

The void fraction measurements are shown in Figure 4.3 and Figure 4.4. Three sets of data were considered for the assessment of the numerical results, at j_l = 0.85 m/s and 1.16 m/s for the 0.109 m diameter coil and at j_l = 0.35 m/s for the 0.225 m diameter coil.

4.1.2 *CFD model*

As in Chapter 3 for the single-phase flow, the CFD simulation of the air-water flow was again accomplished through the ANSYS FLUENT 14.0 (2011) code. The description of a multiphase flow is a very complex subject, as the distribution of the two phases changes continuously and in a random fashion. The presence of the interphase and the exchange of mass, momentum and energy at the interphase complicates enormously the analysis, since the shape of the interface is predictable only in a very restricted number of cases. In addition, since the interfacial exchanges take place in a dynamic way, multiphase flows are often not in thermal and velocity equilibrium, so that the two phases flow with different temperatures and velocities. Between the approaches available to describe the multiphase flow (a two-phase flow in this case), the Eulerian-Eulerian model has been preferred. The Eulerian model describes the two-phase flow as interpenetrating continua, where the conservation equations for each phase are based on an averaging procedure that allows both phases to co-exist at any point. In any point, the relative weight between the phases is quantified by the void fraction. In the interpenetrating media formulation, the presence and the characteristics of the interface are lost during the averaging process. Consequently, the detailed topology of the phases cannot be obtained and the flow regime cannot be determined, except by correlation with the average flow conditions. In the Eulerian model, the interfacial transfers are explicitly modeled as interfacial terms acting on each phase, resulting in closure laws governing the interfacial mass, momentum and energy exchanges.

The adiabatic air-water mixture is simulated neglecting the phase change and the heat transfer between the phases. Therefore, the two fluids are considered in thermal equilibrium. The fluid properties are also considered constant during the simulation, and their values are resumed in Table 4.1. The momentum transfer between the phases is taken into account only by a proper drag force in the momentum equation, neglecting all the other interfacial force terms. Therefore, the following set of conservation equations are solved for each phase:

$$\frac{\partial}{\partial t}(\alpha_n \rho_n) + \nabla \cdot (\alpha_n \rho_n \overline{v_n}) = 0 \tag{4.1}$$

$$\frac{\partial}{\partial t}(\alpha_n \rho_n \overline{v_n}) + \nabla \cdot (\alpha_n \rho_n \overline{v_n v_n}) = -\alpha_n \nabla p + \nabla \cdot \bar{\bar{\tau}}_n + \alpha_n \rho_n \bar{g} + \sum_{p=1}^{2} \bar{M}_{pn} \tag{4.2}$$

Considering the equation for phase 1, the interaction term between the phases M_{pn} assumes the following form:

$$\bar{M}_{21} = C_{21} \cdot (\bar{v}_2 - \bar{v}_1) \tag{4.3}$$

For the calculation of the interaction term, the model assumes the secondary phase to always form droplets or bubbles. If phase 1 represents the continuous phase, while phase 2 the dispersed phase, the exchange coefficient C is written in the following form:

$$C_{21} = \frac{\alpha(1-\alpha)\rho_2 f}{\tau_{rt,2}} \tag{4.4}$$

The term $\tau_{rt,2}$ represents the "particulate relaxation time", which reads:

$$\tau_{rt,2} = \frac{\rho_2 d_p^2}{18\mu_1} \tag{4.5}$$

Particularly important is the parameter d_p, which is the diameter of the bubbles or droplets of the dispersed phase, as it will be clear from the following section. In Eq.(4.4), f is the drag function, calculated using the universal drag law. In the universal drag law, the viscosity in Eq.(4.5) becomes an effective viscosity μ_e, accounting for the effects of family of particles in the continuum. The drag function is instead defined as:

$$f = \frac{C_D Re}{24} \tag{4.6}$$

where Re is the local relative velocity Reynolds number:

$$Re = \frac{\rho_1(\bar{v}_1 - \bar{v}_2)d_p}{\mu_e} \tag{4.7}$$

The drag coefficient C_D assumes different forms as a function of the type of two-phase flow and the flow regime (Kolev, 2005).

At the beginning, the k-ε turbulence model has been used to simulate the turbulent flow, with the standard wall function for the treatment of the near wall region. The pressure-velocity coupling is resolved using the Phase Coupled SIMPLE scheme. Momentum and turbulent quantities are discretised with the second order upwind scheme, while the QUICK scheme is used for the void fraction. A convergence criterion of 10^{-5} is applied for velocities, volume fraction and turbulent quantities. The no slip condition is applied at the tube wall, together with a constant outlet pressure boundary condition.

Table 4.1 Fluid properties used in the simulation of the air-water mixture

ρ_w [kg/m^3]	998.2
μ_w [Pa·s]	1.225
ρ_a [kg/m^3]	0.001
μ_a [Pa·s]	$1.79 \cdot 10^{-5}$
σ [N/m]	0.0727

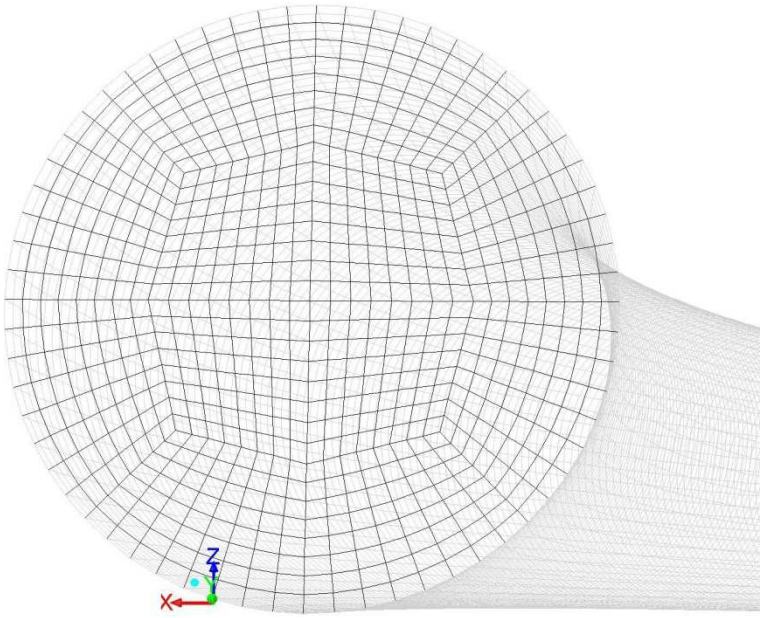

Figure 4.5 Grid developed for the CFD simulation of the air-water flow.

Time dependent simulations assure a better convergence of the results with respct to steady-state calculations. The following procedure has been adopted. For every simulated condition, initially a first calculation is made with a coarser grid, to reach a developed flow condition. A homogeneous mixture is considered as the inlet boundary condition. Outlet velocity and void fraction profiles from the first simulation are then applied as inlet conditions in successive simulations of short pipe sections, to obtain the final simulation results. Being the simulations made in the time domain, physical quantities are evaluated as a time average over an appropriate time interval after the reaching of steady-state conditions.

For the second set of simulations, a finer grid was implemented following a proper grid sensitivity study. A structured mesh was used with 768 elements in the pipe cross section (Figure 4.5), for a cell density of 23167 cells/cm^3.

4.1.3 Grid sensitivity study

Considering the 0.109 m diameter coil, the grid sensitivity study consisted of the simulation of three different flow conditions in four meshes, characterized by an increasing number of grid points. For every grid, the number of element in the axial direction has been determined to maintain as close as possible to 1 the aspect ratio of every hexahedral cell. The conditions simulated and the characteristics of the four grid are summarized in Table 4.2 and Table 4.3.

The values of the void fraction and the frictional pressure drop per unit length are shown in Figure 4.6 and Figure 4.7, as a function of the number of grid elements. While the void fraction remains almost constant, the frictional pressure drop seems to approach a stable value initially, to finally increase with the finest grid. The final increase can be a symptom of a too low y^+ near the wall. In fact, the y^+ goes down to a value of almost 10, which is too low for

the wall function to properly work. As a consequence, the mesh with 768 cells on the tube cross section seems the appropriate one.

Table 4.2 Conditions simulated in the grid sensitivity study.

Case	j_w [m/s]	j_a [m/s]	α_{in} [-]
1	0.9	0.2	0.1
2	0.8	0.6	0.2
3	0.855	0.165	0.1

Table 4.3 Grid implemented for the grid sensitivity study.

Mesh	n	n/V [cm^{-3}]
1	192 x 100	2896
2	432 x 148	9643
3	768 x 200	23167
4	1200 x 248	44887

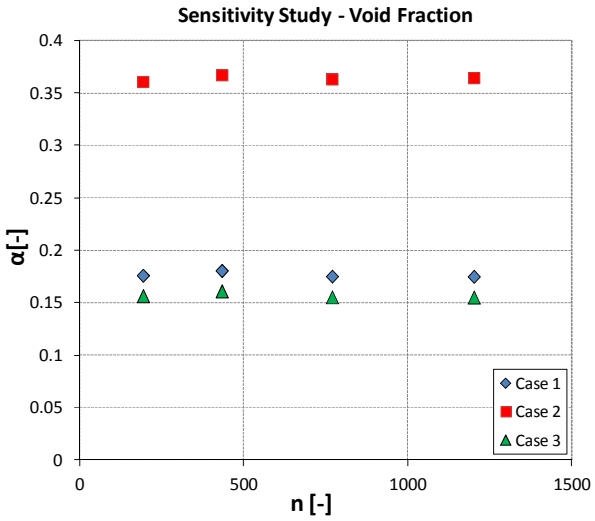

Figure 4.6 Void fraction behavior as a function of the number of elements in the grid.

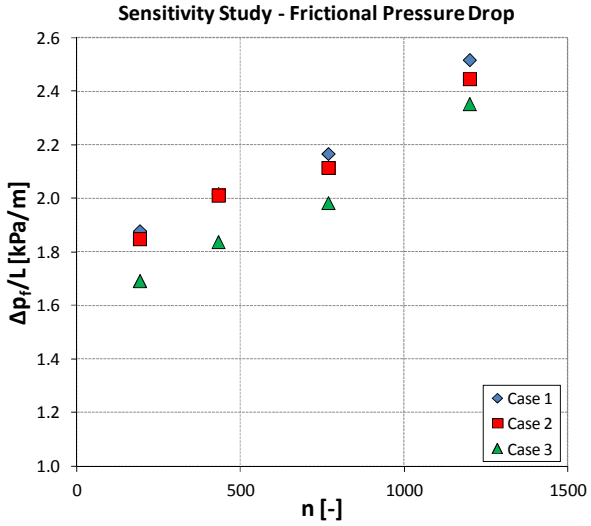

Figure 4.7 Frictional pressure drop behavior as a function of the number of elements in the grid.

4.1.4 *Influence of the diameter of the dispersed phase*

A large number of different parameters characterize the CFD simulation of a two-phase flow, making it a very challenging subject. One of the most important and sensitive parameter has been identified in the diameter of the dispersed phase. As stated before, the code assumes the secondary phase to form droplets or bubbles and uses the diameter of the dispersed phase, required as an input, to calculate the drag force between the phases. While a value of d_p = 0.1 mm has been assumed in the previous simulations, in this section a sensitivity study on its value is proposed.

The first case of the sensitivity study (Section 5.1.3) was repeated with different values of the dispersed phase diameter, ranging from 0.075 mm to 0.5 mm. Increasing the value of the bubble diameter, the average value of the void fraction in the channel cross section is reduced, and the slip ratio between the phases is consequently increased, since the mass flow rate of the two phases remains constant. In Figure 4.8 and Figure 4.9, the water volume fraction on the pipe cross section is shown for a dispersed phase diameter equal to 0.1 mm and 0.2 mm, respectively. Although the average value is only slightly different, as the void fraction is

reduced from α = 0.173 to α = 0.169, locally the differences are higher. In particular, a higher separation between the two phases appears as they flow along the channel. If the diameter is increased further, the separation between the two phases is almost complete and the void fraction results very low, so the frictional pressure drop (Figure 4.10). As an example, for d_p equal to 0.5 mm, the void fraction and the frictional pressure drop are respectively 0.080 and 1.25 kPa/m, with respect to 0.173 and 2.17 kPa/m found with d_p = 0.1 mm. At the same time, the simulations are characterized by convergence problems, oscillations and errors in the mass balance. Reducing the value of d_p to 0.075 mm, instead, does not alter significantly the results (Figure 4.11). A further decrease, however, leads to an increase of the void fraction and the frictional pressure drop. With a value of d_p sufficiently low, homogeneous flow conditions are reached. In other words, a higher diameter of the dispersed phase originates a weaker interaction between the two-phases, resulting in a clear separation between air and water, a higher value of the slip ratio and an extremely low value of the void fraction.

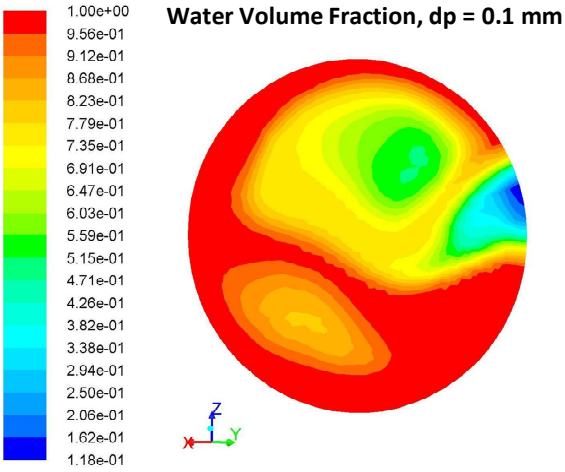

Figure 4.8 Water volume fraction for j_w = 0.9 m/s, j_a = 0.2 m/s and d_p = 0.1 mm.

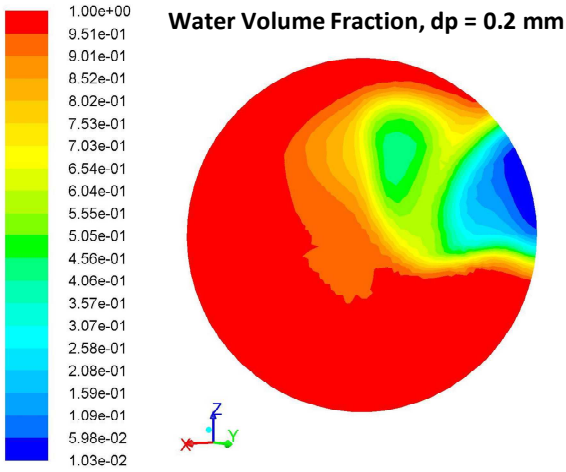

Figure 4.9 Water volume fraction for j_w = 0.9 m/s, j_a = 0.2 m/s and d_p = 0.2 mm.

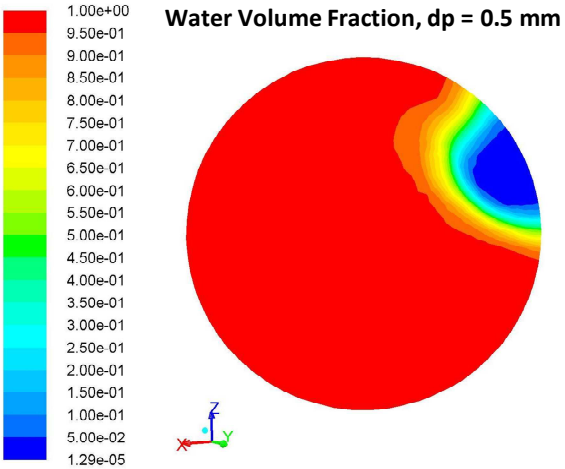

Figure 4.10 Water volume fraction for j_w = 0.9 m/s, j_a = 0.2 m/s and d_p = 0.5 mm.

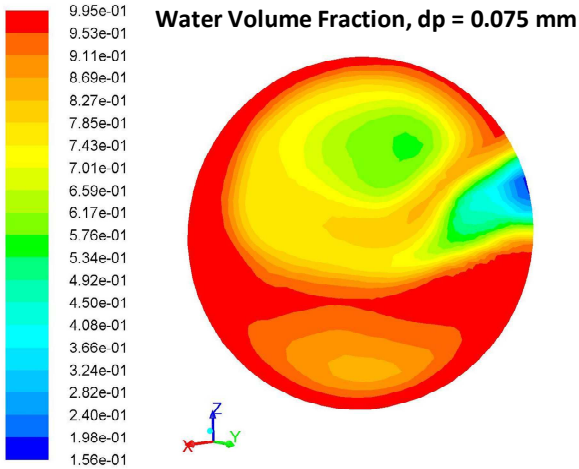

Figure 4.11 Water volume fraction for j_w = 0.9 m/s, j_a = 0.2 m/s and d_p = 0.075 mm.

A lower diameter value, on the contrary, originates a stronger interaction between air and water, a higher value of the air volume fraction and consequently a lower value of the slip ratio, up to the reaching of homogeneous flow conditions.

In the following sections, the value of d_p = 0.1 mm is maintained, since it permits to obtain reasonable results. Nevertheless, the problem of the diameter of the dispersed phase will be further addressed, due to the great influence it has on the simulation results.

4.1.5 Simulation results

After the sensitivity study, a first set of simulation was made with j_w = 0.85 m/s and seven different values of the air superficial velocity j_a, to study the whole range of void fraction. The simulated conditions are summarized in Table 4.4.

Figures from Figure 4.12 to Figure 4.15 show the water volume fraction profile and the phase distribution on the pipe cross section. For a very low value of the void fraction (Figure 4.12), the centrifugal force is dominant, since the lighter air is mainly concentrated on the upper portion of the duct. Nevertheless, a slight effect of the centrifugal force field is already observable, as the heavier water tends to occupy the external section of the pipe, whereas the air accumulates near the internal wall. In addition, a water film at the wall and a recirculation pattern of the water phase in the upper portion of the duct emerges in Figure 4.12, evidence of the presence of a secondary motion. As the air flow rate is increased, so the void fraction, the effect of the centrifugal force becomes clear. The heavier water is pushed toward the outer wall of the tube, while the lighter air phase occupies the inner portion of the pipe, creating a highly unsymmetrical flow pattern. This phenomenon becomes more evident as the air flow rate is further increased, as shown from Figure 4.13 to Figure 4.15.

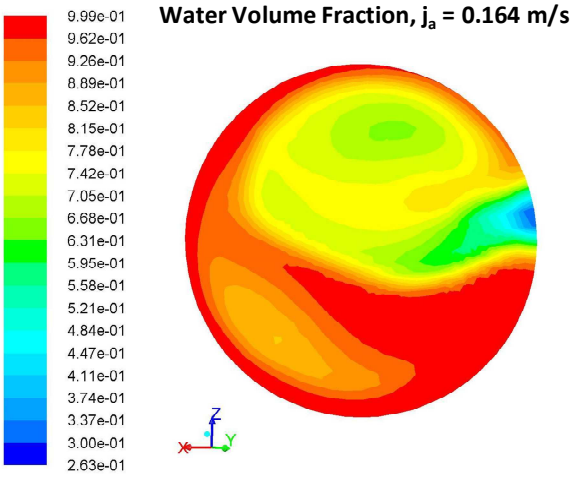

Figure 4.12 Profile of the water volume fraction on the tube cross section for j_w = 0.85 m/s, j_a = 0.164 m/s and α = 0.155.

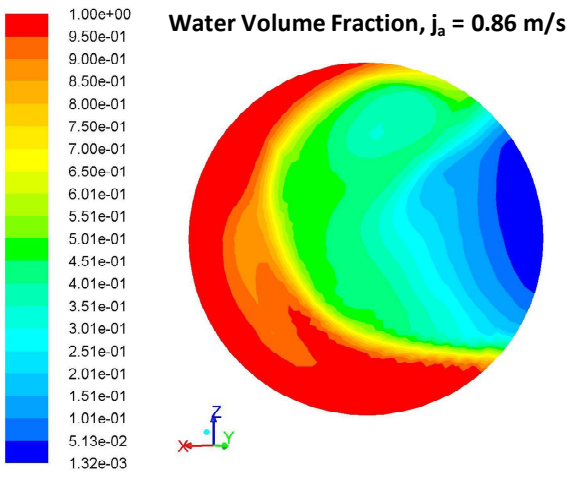

Figure 4.13 Profile of the water volume fraction on the tube cross section for j_w = 0.85 m/s, j_a = 0.86 m/s and α = 0.435.

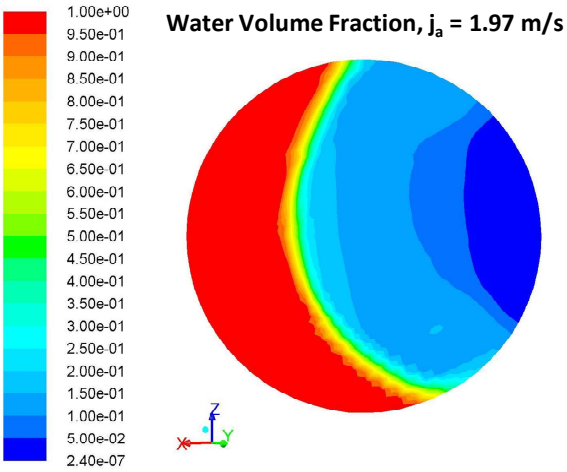

Figure 4.14 Profile of the water volume fraction on the tube cross section for j_w = 0.85 m/s, j_a = 1.97 m/s and α = 0.587.

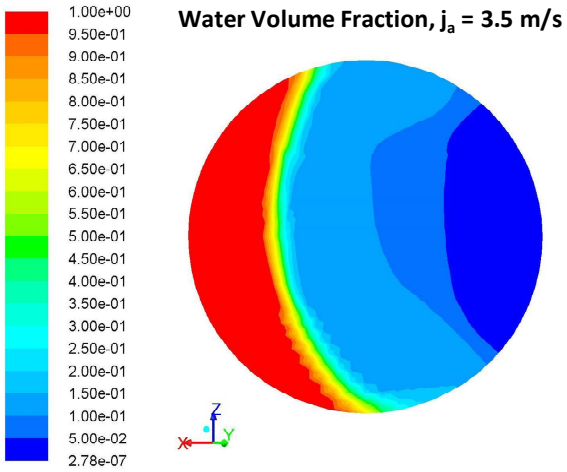

Figure 4.15 Profile of the water volume fraction on the tube cross section for j_w = 0.85 m/s, j_a = 3.5 m/s and α = 0.680.

Figure 4.16 and Figure 4.17 compare the CFD results code with some visual observations obtained through imaging tomography inside an helically coiled tube (Murai et al., 2005). A good qualitative agreement is found for the void fraction and the distribution of the phases. The latter, preliminary confirms that the rather simple CFD model adopted (only the drag force is considered for the interfacial momentum exchange between the phases) is able to catch the fundamental characteristics of the two-phase flow in the helical pipe. This suggests that it is the centrifugal force field that mainly influences the phase distribution and the interaction between the phases.

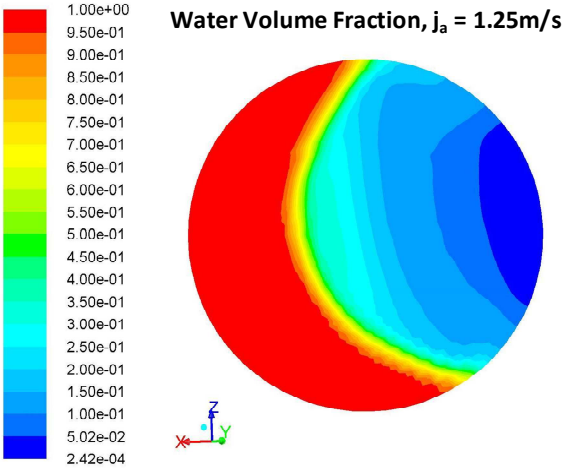

Figure 4.16 Profile of the water volume fraction on the tube cross section for j_w = 0.85 m/s, j_a = 1.25 m/s and α = 0.500.

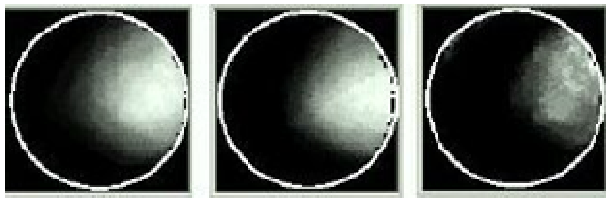

Figure 4.17 Visual observation through imaging tomography of an air-water flow inside an helically coiled tube (Murai et al., 2005).

Since the centrifugal force promotes a certain phase separation that increases with the void fraction, the velocity field reflects the particular phase distribution. The air, being the fluid with the lower density, flows with a higher velocity. In addition, the high separation between the fluids increases the relative velocity between air and water for the lower

interaction between them. As a consequence, the maximum of the velocity is shifted near the internal wall of the pipe, where the air accumulates under the effect of the centrifugal force field. On the opposite, the outer portion of the pipe becomes a low velocity region, being occupied by the water. This phenomenon becomes more and more evident as the air flow rate and consequently the void fraction are gradually increased, as in Figure 4.18 and Figure 4.19, where the velocity field is shown for j_a = 1.25 m/s and 2.5 m/s.

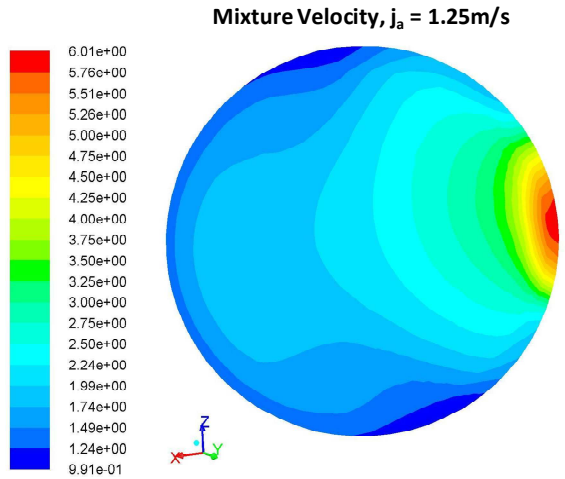

Figure 4.18 Mixture velocity on the duct cross section for j_w = 0.85 m/s, j_a = 1.25 m/s and α = 0.500.

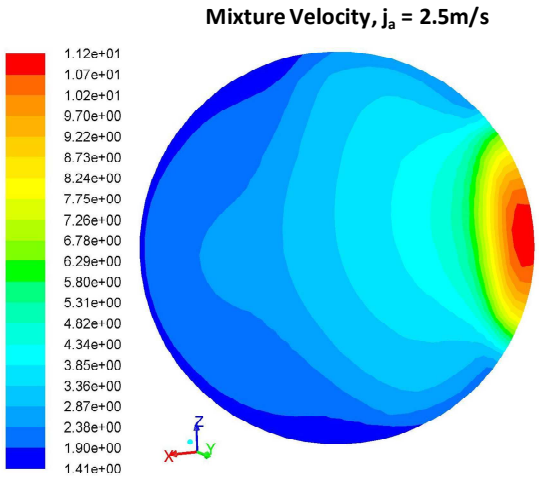

Figure 4.19 Mixture velocity on the duct cross section for j_w = 0.85 m/s, j_a = 2.5 m/s and α = 0.627.

Similarly to the single-phase flow, the centrifugal field generates a secondary motion on the channel cross-section in the form of counter rotating vortices. Figure 4.20 and Figure 4.21 illustrates the secondary motion in two different conditions, characterized by an increasing value of the air mass flow rate. In Figure 4.20, two counter rotating vortices are present in the region occupied by the water flow, so they are kept in the outer section of the pipe. Some recirculation phenomena are anyway present also inside the air flow, although they do not show a clearly defined structure. When the air flow rate is increased (Figure 4.21), two well defined, counter rotating vortices appears also in the air region, together with other recirculation structures located in the maximum velocity region. The recirculation is maintained also inside the water, but the two vortices are more confined toward the outside wall, being higher the void fraction, so the space occupied by the air flow.

Table 4.4 Simulation set for D = 0.109 m and j_w = 0.85 m/s.

Simulation	j_w [m/s]	j_a [m/s]	x [-]
1	0.85	0.164	0.000235
2	0.85	0.86	0.001227
3	0.85	1.25	0.001791
4	0.85	1.97	0.002806
5	0.85	2.5	0.003551
6	0.85	3.0	0.004269
7	0.85	3.5	0.004984

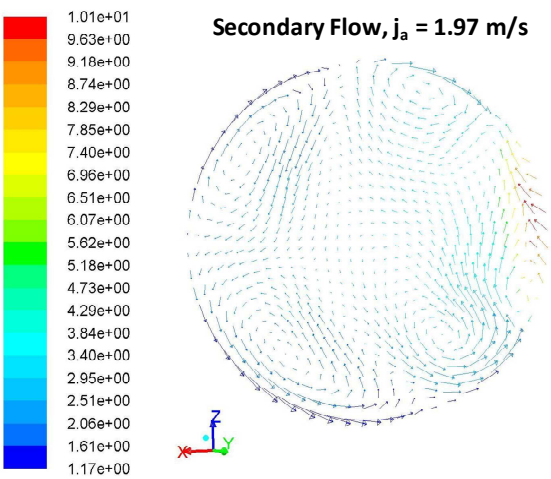

Figure 4.20 Secondary flow on the duct cross section for j_w = 0.85 m/s, j_a = 1.97 m/s and α = 0.587.

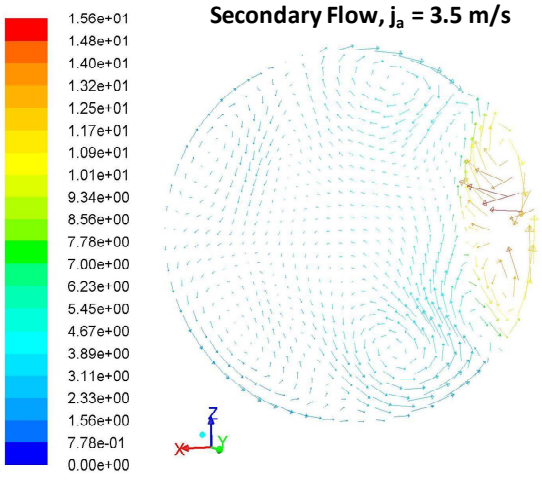

Figure 4.21 Secondary flow on the duct cross section for j_w = 0.85 m/s, j_a = 3.5 m/s and α = 0.680.

4.1.6 *Comparison with experiments*

The simulation results in the smallest coil (D = 0.109 m) at j_w = 0.85 m/s are presented in Table 4.5. A first comparison with the experimental data is shown in Figure 4.22 for the void fraction. The general agreement is very good and the average relative error is lower than 5 %. In more details, the largest error is found for the lowest value of the void fraction, that is underestimated of more than 15 %. Nevertheless, the absolute error remains very small and equal to about 0.03, being very small also the value of the void fraction. At the same time, the high error seems to suggest a more complex behavior of the phase distribution at low flow quality. Therefore, a dedicated model of the drag force can be required to improve the accuracy of the simulations. The results of the previous section, that indicate an interaction between the phases dominated by the centrifugal force, remain valid at higher void fraction, where the results are quiet good. In particular, neglecting the point at the lowest void fraction, the maximum deviations are always under 5 %, with an average error of about 2 %, that can be considered inside the experimental uncertainty.

Table 4.5 CFD results for D = 0.109 m and j_w = 0.85 m/s.

j_w [m/s]	j_a [m/s]	x	α	Δp/L [kPa/m]
0.85	0.164	0.000235	0.155	2.038
0.85	0.86	0.001227	0.438	2.579
0.85	1.25	0.001791	0.500	2.871
0.85	1.97	0.002806	0.587	3.507
0.85	2.5	0.003551	0.627	3.953
0.85	3.0	0.004269	0.657	4.308
0.85	3.5	0.004984	0.680	4.598

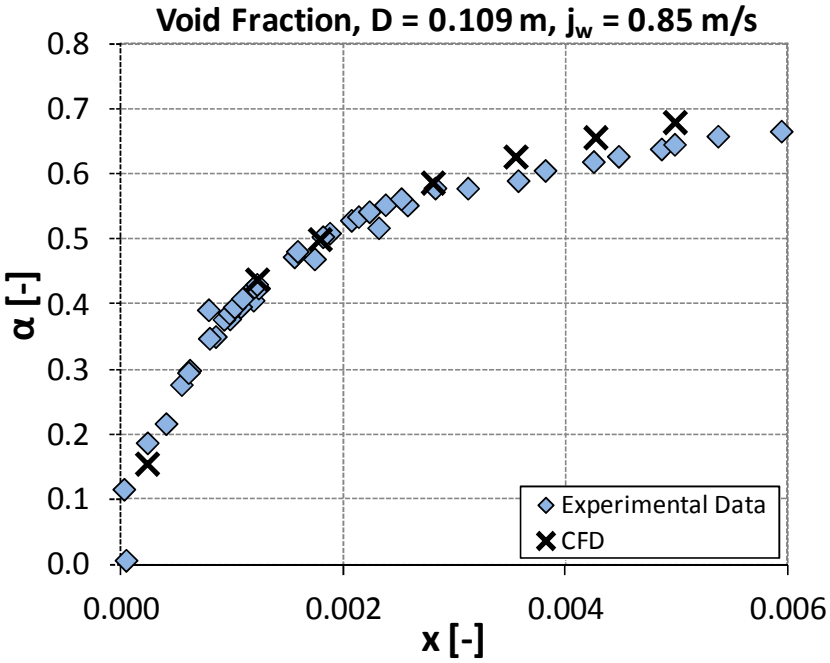

Figure 4.22 Void fraction comparison in the smallest coil between the CFD results and the experimental data at j_w = 0.85 m/s.

For the frictional pressure drop, the comparison is shown in Figure 4.23. The accuracy of the numerical results is very high at low flow quality, but a systematic underestimation of the experimental values emerges starting from the medium flow quality. The average relative error is about 15 %, with maximum deviations included in the range ± 20 %. Actually the results, although large is the possibility for improvement, can preliminary be considered satisfactory, as the errors are not significantly higher with respect to the best literature correlations, when applied on their original databases.

After the comparison with the first set of data, the results of the code were evaluated also in different experimental conditions. In particular, for the higher value of the liquid superficial velocity (j_w = 1.16 m/s) in the same helical pipe and at j_w = 0.35 m/s (the lower value of the liquid superficial velocity) also in the larger coil. Three experimental points were simulated for each case, at low, medium and high void fraction. For the 0.225 m diameter coil, the same grid described in Section 5.1.2 is appropriate, being equal the diameter of the pipe. Obviously, the simulation of a longer pipe section (for an equal number of helix turns) resulted in a higher number of hexahedral cells. The new simulations results are illustrated in Table 4.6.

Table 4.6 CFD results for D = 0.109 m, 0.225 m and j_w = 0.85 m/s, 1.16 m/s.

j_w [m/s]	j_a [m/s]	x	α	Δp/L [kPa/m]
1.16	0.380	0.0004	0.238	3.584
1.16	0.966	0.0010	0.433	4.999
1.16	1.500	0.0016	0.516	5.751
0.35	0.012	0.00004	-	-
0.35	1.013	0.0035	0.612	0.820
0.35	4.451	0.0153	0.810	2.238

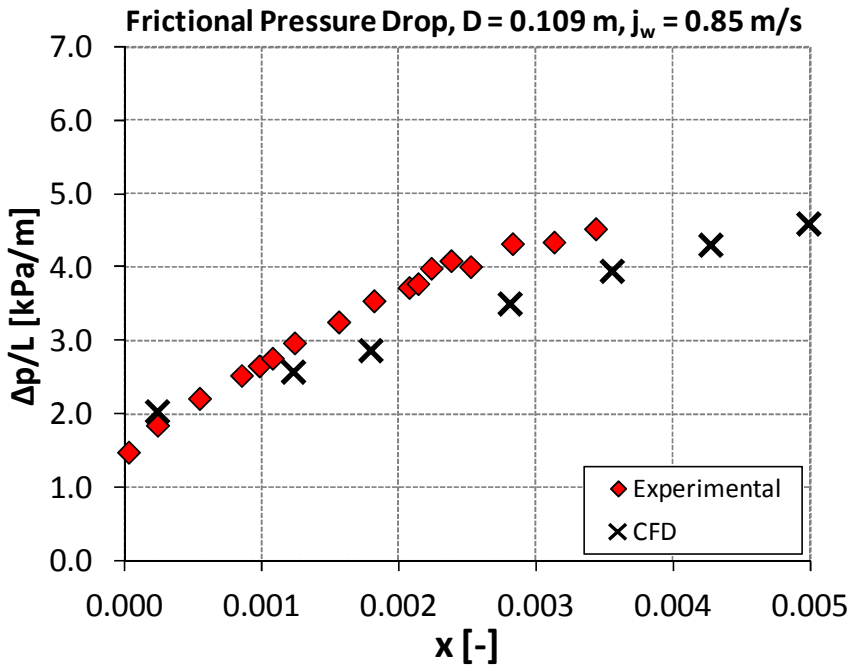

Figure 4.23 Comparison of the frictional pressure drop in the smallest coil between the CFD results and the experimental data at j_w = 0.85 m/s.

For j_w = 0.35 m/s, the point at the lowest void fraction is characterized by an extremely low value of the air velocity, so that the CFD result seem unreliable and has not been considered in the comparison. The results on the void fraction remain very good, with an average relative error under the 5 % with respect to the experimental data. It is reduced to only 3.2 % neglecting the point at the lowest void fraction, that shows again the highest deviation (Figure 4.24 and Figure 4.25). With respect to the frictional pressure drop, the average error is equal to 6.3 % for the data at j_w = 1.16 m/s (Figure 4.26) and about 12 % for the data at j_w = 0.35 m/s (Figure 4.27). Summarizing, a very good 4.5 % average error (reduced to 2.5 % without the points at $\alpha < 0.25$) is found for the void fraction and a satisfactory 12.3 % for the frictional pressure drop. A global recap of the results is proposed in Table 4.7. Most important, the differences from the experimental data are almost comparable changing the flow conditions and the geometry of the coil and maintaining the same simulation parameters. Since the diameter of the dispersed phase has been identified as a critical parameter in Section 5.1.4, some simulations from the first set (D = 0.109 m, j_w = 0.85 m/s) were repeated with a different value of d_p

Table 4.7 Recap of the accuracy of the CFD simulations.

Conditions	**α absolute error**	**$\Delta p_{fr}/L$ absolute error**
D = 0.109 m, j_w = 0.85 m/s	4.5 %	15.2 %
D = 0.109 m, j_w = 1.16 m/s	4.8 %	6.3 %
D = 0.109 m, j_w = 0.35 m/s	2.0 %	13.0 %
Global	4.55 %	12.3 %

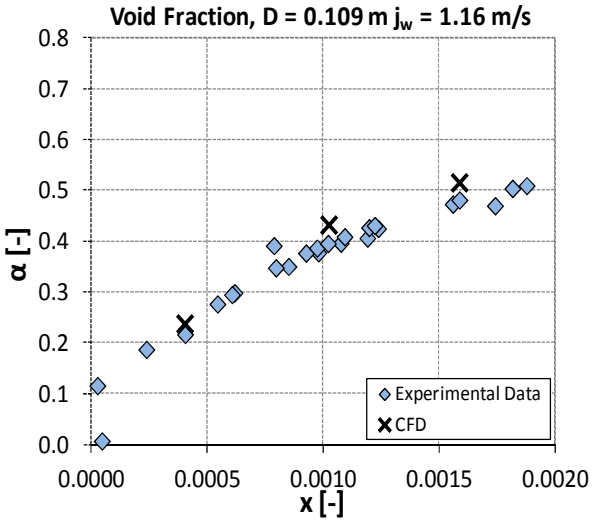

Figure 4.24 Comparison of the void fraction in the smallest coil between the CFD results and the experimental data at j_w = 1.16 m/s.

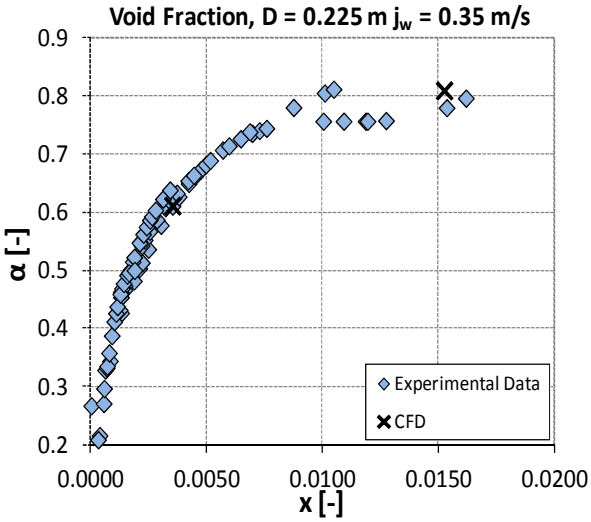

Figure 4.25 Comparison of the void fraction in the largest coil between the CFD results and the experimental data at j_w = 0.35 m/s.

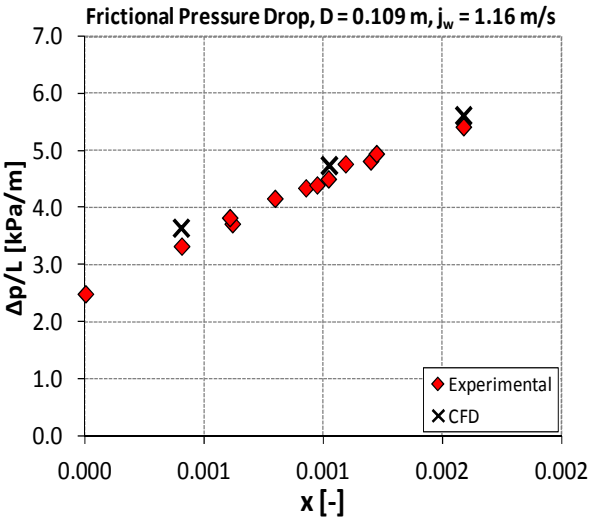

Figure 4.26 Comparison of the frictional pressure drop in the smallest coil between experiments and CFD at j_w = 1.16 m/s.

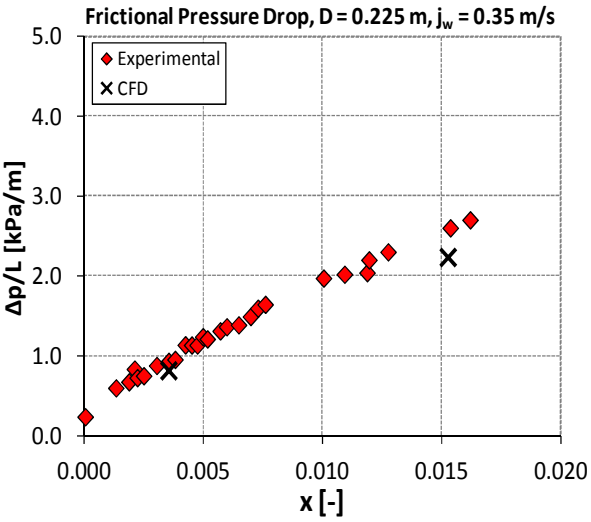

Figure 4.27 Comparison of the frictional pressure drop in the smallest coil between experiments and CFD j_w = 0.35 m/s.

Since no differences were found for the void fraction, the results are shown in Figure 4.28 only for the frictional pressure drop. They are compared with the experimental data and the previous simulations. At low flow quality, no significant differences are found. At medium-high flow qualities, an higher value of the frictional pressure drop is generally estimated by the code, closer to the experimental data. The average relative error becomes 8.2 %, from the 15.2 % obtained with the first value of the dispersed phase diameter. Although it is possible to further improve the simulation results with a fine tuning of the diameter of the dispersed phase, the above is out of the scope of this work. Actually, the main objective is to demonstrate the possibility to estimate with a satisfactory degree of accuracy the void fraction and the frictional pressure drop in many different conditions. As a consequence, no more work has been done to improve the results with a fine tuning of the dispersed phase diameter.

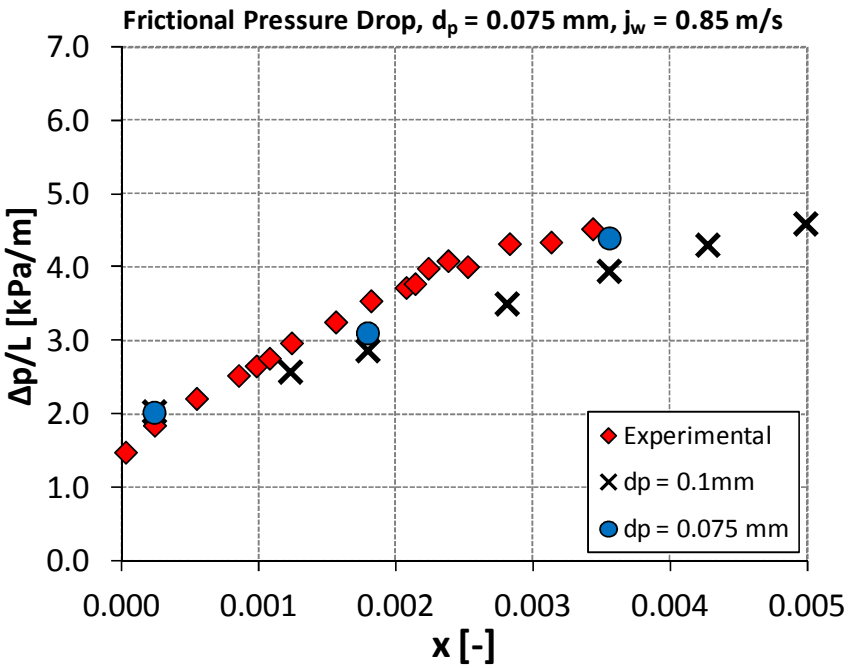

Figure 4.28 Frictional pressure drop comparison in the smallest coil between the CFD results and the experimental data at j_w = 0.85 m/s and for different values of the dispersed phase diameter d_p.

4.1.7 *Effect of the wall treatment on the results*

A further study has examined the influence of the treatment of the near wall region on the results. Chapter 3 demonstrated the importance of the treatment at the wall for a correct estimation of the frictional pressure drop in presence of fluid recirculation and secondary motion. In this section, the enhanced wall treatment of the FLUENT code, which solves the flow field all way down to the wall, is adopted also for the two-phase flow, to assess its influence on the results.

First, since the enhanced wall treatment requires a sufficiently fine mesh, a new grid has been developed, introducing a finer boundary layer in the mesh of Figure 4.5. The new grid, composed by 1024 cells in the cross section, is shown in Figure 4.29. The three experimental points used in the previous section for the effect of the dispersed phase diameter were simulated. Numerical results are resumed in Table 4.8.

Table 4.8 Results of the simulation with the enhanced wall treatment.

j_w [m/s]	j_a [m/s]	x	α	Δp/L [kPa/m]
0.856	0.161	0.0002	0.151	2.055
0.857	1.254	0.0018	0.501	3.671
0.860	2.486	0.0035	0.634	5.913

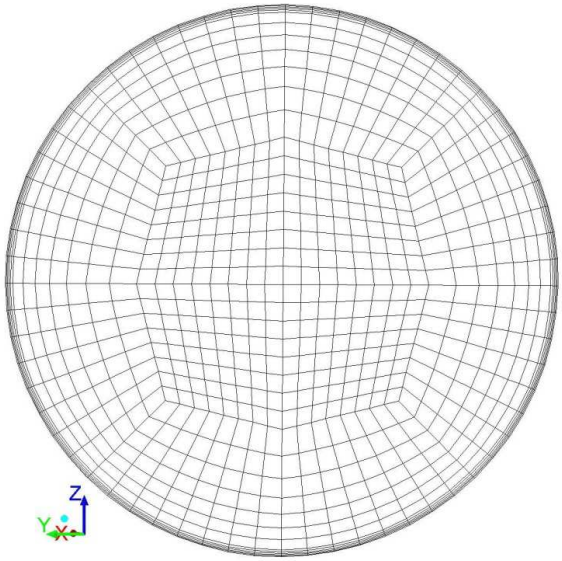

Figure 4.29 Mesh developed for the simulations with the enhanced wall treatment.

The presence of the boundary layer allows a better definition of the phase distribution in the cross section of the pipe, in particular for the liquid film at the wall. Figure 4.30 and Figure 4.31 show a comparison between the same experimental conditions simulated with the enhanced wall treatment and the wall function. For the major part, the results are completely unchanged. Instead, in the region occupied by the air phase, a liquid film at the wall is present only when the enhanced wall treatment is enabled. On the contrary, no liquid film is visible when the wall function is used. Actually, the enhanced wall treatment allows for a far better definition of the wall region. In particular, the liquid film covers the majority of the wall and only the internal portion is excluded.

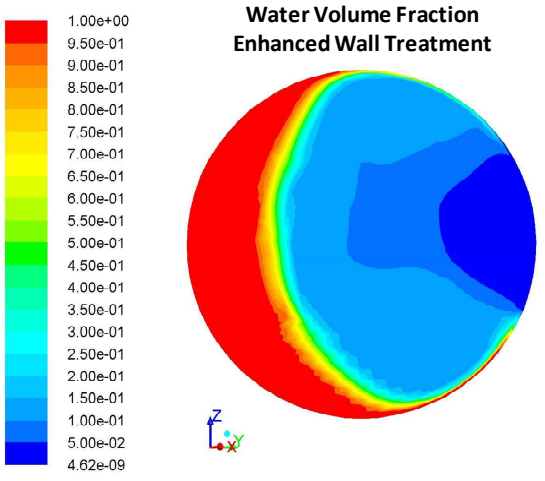

Figure 4.30 Profile of the water volume fraction calculated with the enhanced wall treatment (D = 0.109 m, j_w = 0.85 m/s, j_a = 2.5 m/s).

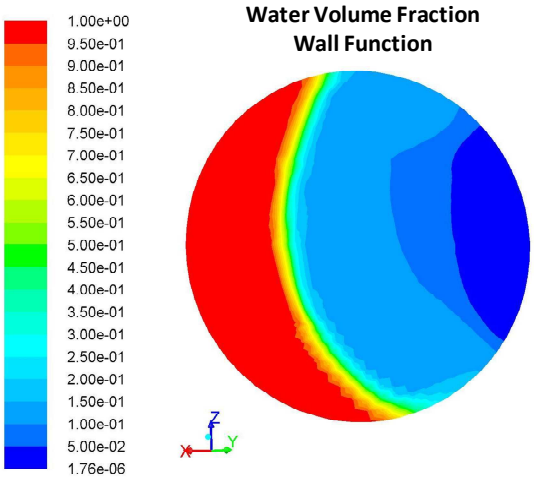

Figure 4.31 Profile of the water volume fraction calculated with the wall function (D = 0.109 m, j_w = 0.85 m/s, j_a = 2.5 m/s).

From a quantitative point of view, the average cross section values of the void fraction are unchanged with respect to the wall function results. The frictional pressure drop is well predicted until the medium values of the void fraction. However, it is significantly overestimated at high void fraction (Figure 4.32). Finally, to improve the results, new simulations were made with a reduced dimension of the last cell near the wall, to reduce also the value of the y^+. The result is a slight improvement at high void fraction. However, the frictional pressure drop remains overestimated (Figure 4.32). Although it seems that a further reduction of the $y+$ at the wall leads to a further improvement of the results, no additional simulations were made. Actually, a reduction in the dimension of the last cell means an increase of the total number of grid cells, to maintain a reasonable ratio between the dimensions of two consecutive elements. That is, a significant increase of the needed computational resources. In addition, the value of the y^+ in the previous simulations is already significantly low and equal to about 1.0 – 1.5.

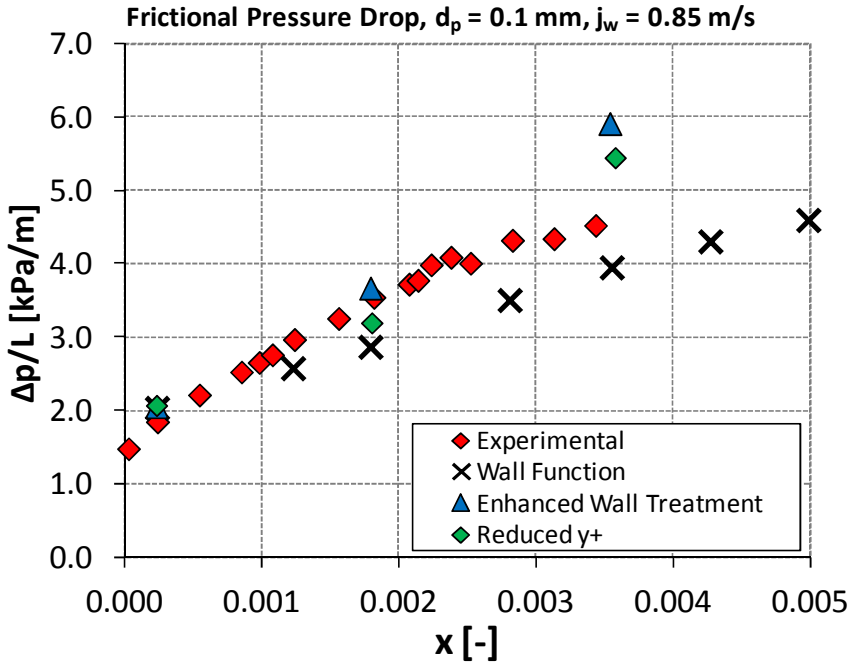

Figure 4.32 Comparison between CFD frictional pressure drop results obtained with the enhanced wall treatment and the wall function.

4.2 Simulation of the SIET steam-water data

In Section 4.1, the CFD simulation of an air-water flow has been validated with experimental data for the void fraction and the frictional pressure drop. Some images obtained with imaging tomography allowed also for a qualitative validation of the phase distribution on the channel cross section. The simulation of the air-water flow resulted necessary, since the large amount of experimental studies available in literature permitted an extensive validation of the CFD results. The attention is now focused on the steam-water two-phase mixture. Therefore, the adiabatic frictional pressure drops measured at SIET laboratories (Section 2.3) are now used to assess the accuracy of the simulation. The numerical results are used to gain

information on the void fraction and the phase distribution and to characterize the two-phase flow inside the helical pipe.

4.2.1 *CFD model and mesh*

The same Eulerian – Eulerian model is used also for the simulation of the steam-water flow. Also the code settings and the numerical schemes are equal to Section 4.1.2. As for the air-water case, an adiabatic flow is considered (consistently with the SIET data), neglecting phase change and heat and mass transfer between the phases. Again, the momentum exchange between the phases is due only to the drag force, with the drag coefficient calculated through the universal drag law. The *k-ε* turbulence model is adopted with the enhanced wall treatment. The enhanced wall treatment is used because the simulations cover the entire range of the flow quality (up to the single-phase vapor flow), so of the void fraction. At high void fraction, since the amount of liquid is limited, a better evaluation of the liquid film at the wall is of fundamental interest. In addition, the behavior of the liquid film at the wall can be crucial for the explanation of the peak in the frictional pressure drop as a function of the flow quality.

The mesh developed for the air-water case must be modified and adjusted to fit with the geometry of the SIET tube and the requirements of the simulation. The number of cells in the pipe cross section is proportional to the number of cells of the air-water case, weighted on the pipe dimensions. A fine boundary layer has been included, necessary for the use of the enhanced wall treatment. The mesh, presented in Figure 4.33, includes 1280 elements on the channel cross section, with a density of 35764 cells/cm^3. The number of grid points guarantees that the dimensions of consecutive elements in the pipe cross section do not vary more than 20 % and maintains the aspect ratio of the hexahedral cell in the range 1 - 4, at least outside of the boundary layer.

The simulation scheme was maintained from the previous section. For every condition, a first simulation is made with a coarser mesh and a sufficient tube length to assure fully developed flow conditions. Outlet conditions are then imposed at the inlet of a successive sequence of simulations, made with the finer mesh. Results are then calculated as a time average over a proper time period. The frictional pressure drop is evaluated as the pressure difference between average values in successive pipe cross sections, neglecting the inlet and the outlet zones.

4.2.2 Simulation results

The first set of simulations was made for the databank at 40 bar and 400 kg/m^{2}s, with a sufficient number of simulations to explore the whole range of flow quality. The conditions and the fluid properties are summarized in Table 4.9 and Table 4.10. The fluid properties are considered constant through the simulation. The hypothesis of constant properties is not expected to significantly affect the results, since the change in pressure (so in the saturation properties) is limited with respect to its absolute value.

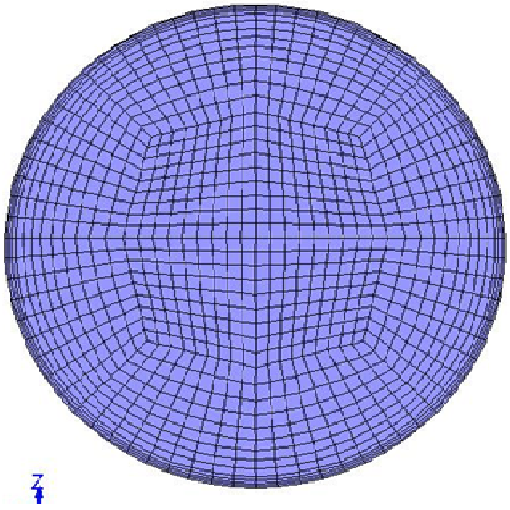

Figure 4.33 Mesh developed for the simulation of the SIET pipe.

Figure 4.34 Single section of the pipe used for the sequence of simulations.

The behavior of the void fraction is shown from Figure 4.35 to Figure 4.46, for the entire range of flow quality. At low quality, the gravitational force seems predominant and a separated flow typical of horizontal pipes is established (Figure 4.35, Figure 4.36 and Figure 4.37). Starting from x = 0.15 (Figure 4.38), the centrifugal force starts to influence the flow and the liquid phase is pushed towards the outer wall. As the quality is further increased ($x \geq$ 0.25, Figure 4.39), the liquid phase accumulates near the wall in the lower-outer portion of the pipe and a liquid film starts to appear at the wall. The amount of liquid is gradually reduced increasing the void fraction (Figure 4.40 to Figure 4.43), until the accumulation near the outer wall disappears at x = 0.78 (Figure 4.44). Although the liquid film is not completely well defined along the wall even with the fine mesh, it allows for some interesting remarks.

Table 4.9 Summary of the explored conditions.

Simulation	j_l [m/s]	j_v [m/s]	x [-]
1	0.48	0.20	0.01
2	0.48	0.53	0.025
3	0.46	1.57	0.075
4	0.41	3.064	0.15
5	0.36	5.11	0.25
6	0.31	7.74	0.38
7	0.25	10.21	0.5
8	0.20	12.05	0.59
9	0.18	13.06	0.67
10	0.10	15.96	0.78
11	0.07	17.36	0.85
12	0.03	19.02	0.93

Table 4.10 Fluid properties

p_{out} [bar]	38
G [kg/m^{2}s]	390
T_{sat} [°C]	247.3
ρ_l [kg/m^3]	802.82
ρ_v [kg/m^3]	19.059
μ_l [Pa·s]	1.078e-04
μ_v [Pa·s]	1.744e-05
σ [N/m]	0.027

In particular, the liquid film characterizes the wall up to a flow quality of x = 0.7. Starting from x = 0.78, the flow regime is more similar to a dispersed flow. Actually, the near wall region is always characterized by a lower void fraction, but its value remains high also near the wall at high quality. That is, the flow structure seems close to a dispersed phase flow with a higher concentration of liquid droplets near the wall, caused probably by the recirculation pattern established in the helical pipe. This recirculation pattern, with liquid droplets recirculated along the wall to the inner region and then pushed towards the outer wall, is partially observed at high flow quality in Figure 4.45 and Figure 4.46.

At low quality, the velocity profile is characterized by the higher velocity vapor flowing in the upper region of the pipe (Figure 4.47). When the centrifugal force starts to act on the phase distribution, the higher velocity vapor phase is concentrated in the inner portion of the pipe, so the velocity maximum (Figure 4.48). As the flow quality is increased, the vapor phase starts to occupy the majority of the pipe cross section. As a consequence, the centrifugal field pushes the higher velocity vapor towards the outer wall and the velocity maximum is shifted to the external region of the pipe (Figure 4.49). The shift of the velocity maximum is more evident as the flow quality is further increased (Figure 4.50 and Figure 4.51). At the highest value of the flow quality, as the condition of single-phase vapor flow is approached, the velocity field reproduces the one obtained for the single-phase liquid flow in Chapter 3.

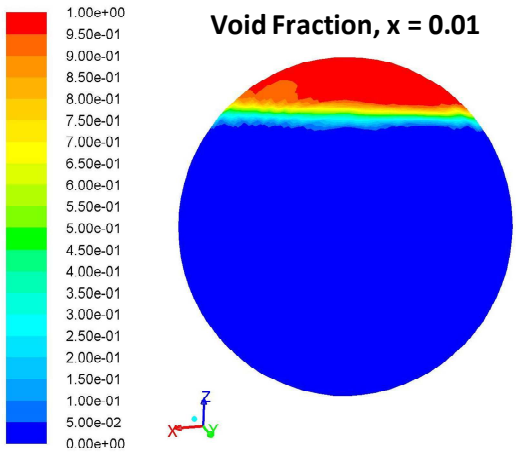

Figure 4.35 Void fraction profile at x = 0.01 (p = 40 bar; G = 400 kg/m^{2}s).

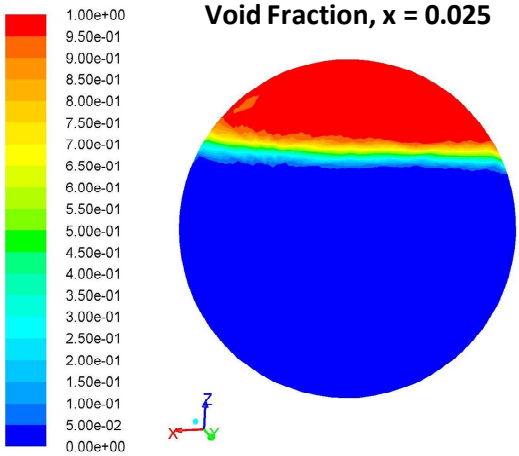

Figure 4.36 Void fraction profile at x = 0.025 (p = 40 bar; G = 400 kg/m^{2}s).

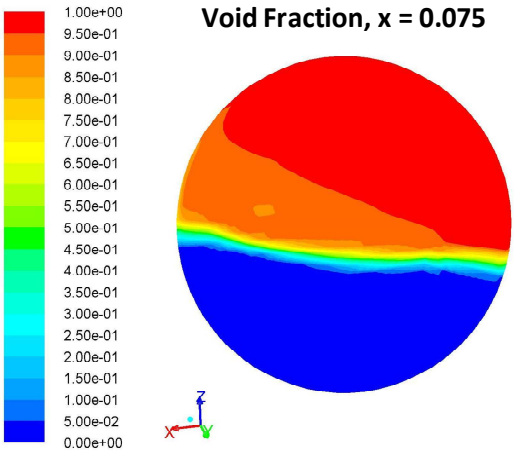

Figure 4.37 Void fraction profile at x = 0.075 (p = 40 bar; G = 400 kg/m^{2}s).

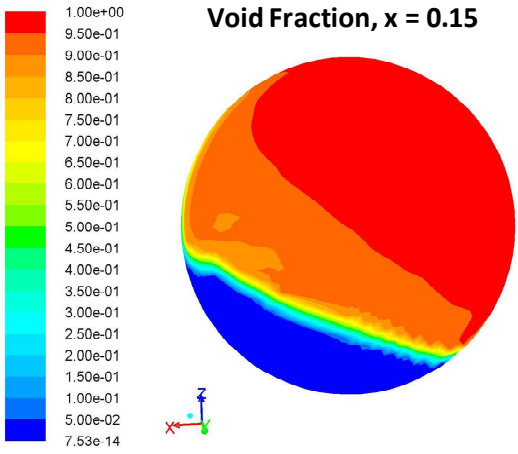

Figure 4.38 Void fraction profile at x = 0.15 (p = 40 bar; G = 400 kg/m^{2}s).

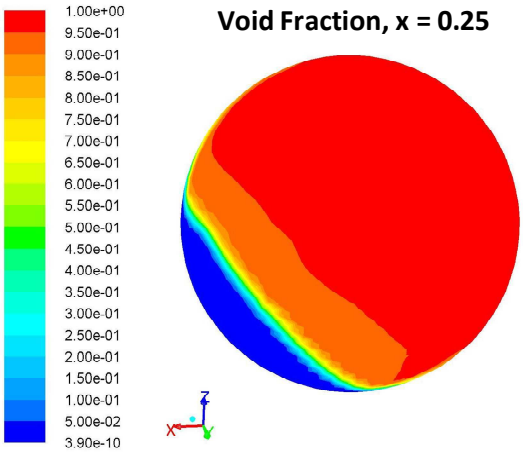

Figure 4.39 Void fraction profile at x = 0.25 (p = 40 bar; G = 400 kg/m^{2}s).

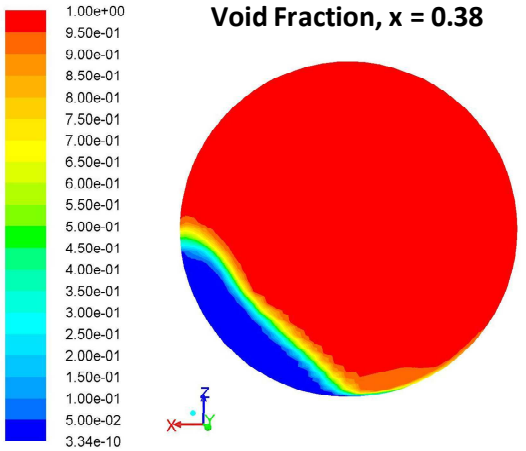

Figure 4.40 Void fraction profile at x = 0.38 (p = 40 bar; G = 400 kg/m^{2}s).

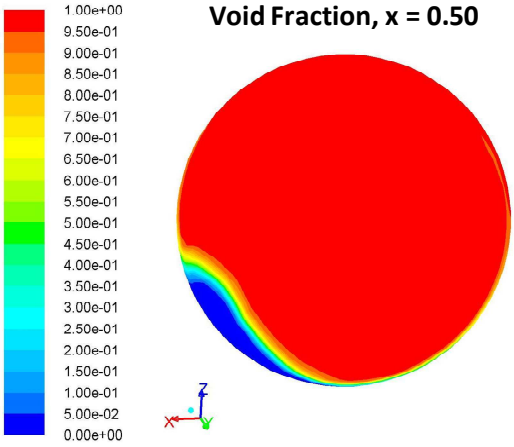

Figure 4.41 Void fraction profile at x = 0.50 (p = 40 bar; G = 400 kg/m^{2}s).

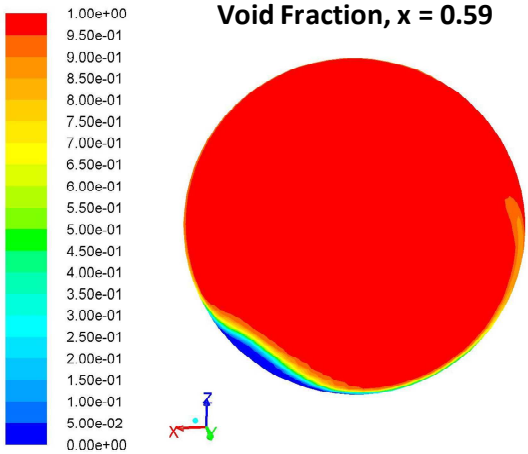

Figure 4.42 Void fraction profile at x = 0.59 (p = 40 bar; G = 400 kg/m^{2}s).

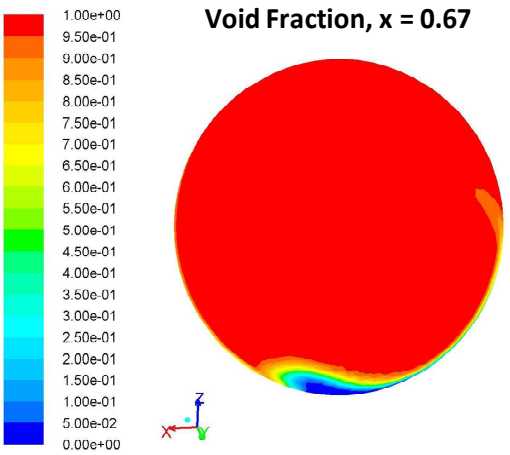

Figure 4.43 Void fraction profile at x = 0.67 (p = 40 bar; G = 400 kg/m^{2}s).

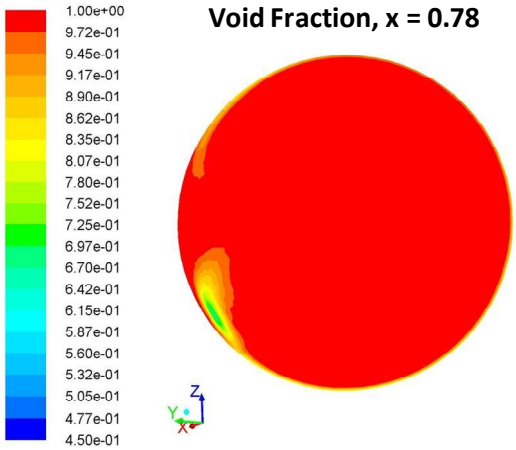

Figure 4.44 Void fraction profile at x = 0.78 (p = 40 bar; G = 400 kg/m^{2}s).

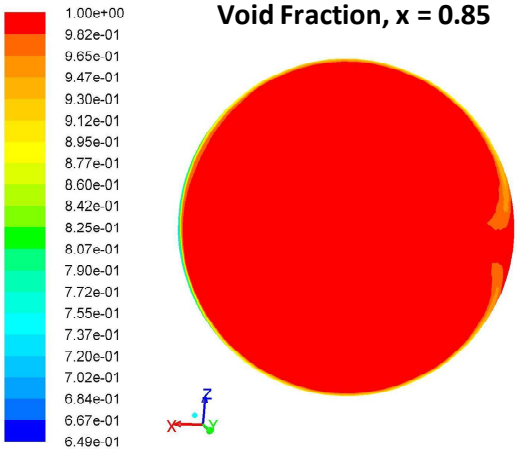

Figure 4.45 Void fraction profile at x = 0.85 (p = 40 bar; G = 400 kg/m^{2}s).

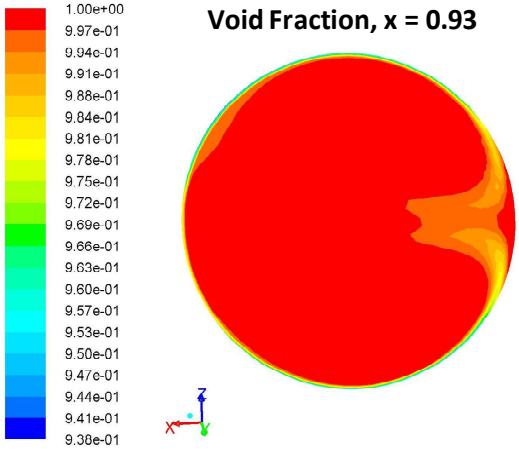

Figure 4.46 Void fraction profile at x = 0.93 (p = 40 bar; G = 400 kg/m^{2}s).

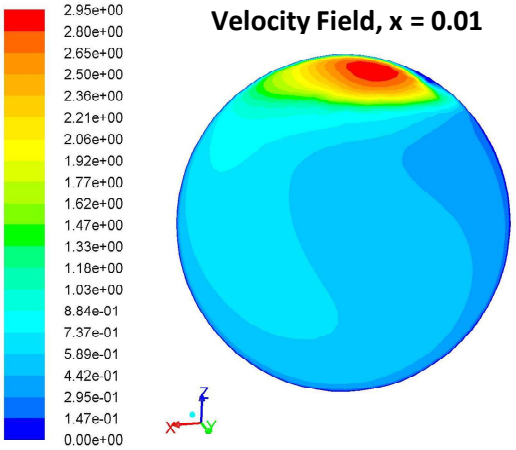

Figure 4.47 Velocity profile at x = 0.01. (p = 40 bar; G = 400 kg/m^{2}s).

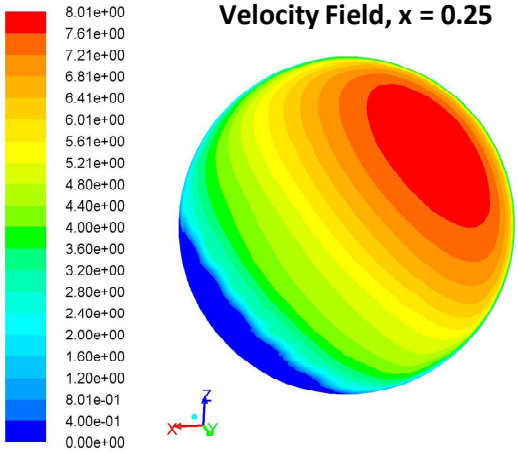

Figure 4.48 Velocity profile at x = 0.25. (p = 40 bar; G = 400 kg/m^{2}s).

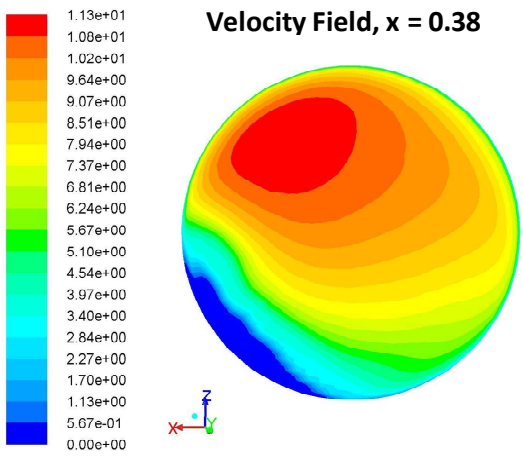

Figure 4.49 Velocity profile at x = 0.38. (p = 40 bar; G = 400 kg/m^{2}s).

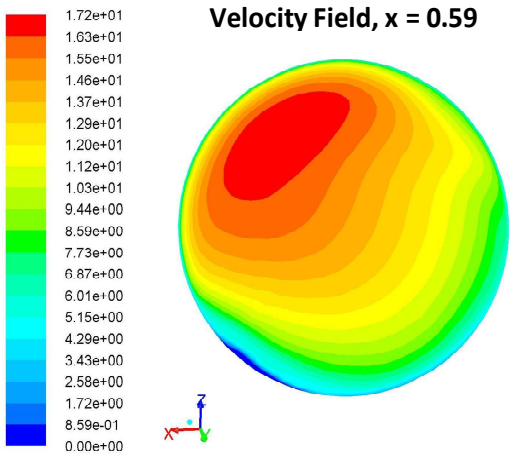

Figure 4.50 Velocity profile at x = 0.59. (p = 40 bar; G = 400 kg/m^{2}s).

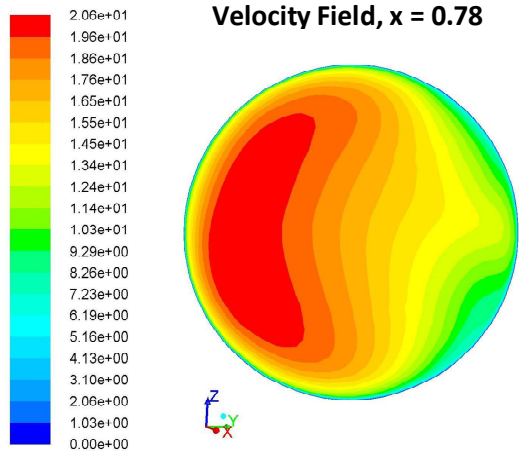

Figure 4.51 Velocity profile at x = 0.78. (p = 40 bar; G = 400 kg/m^{2}s).

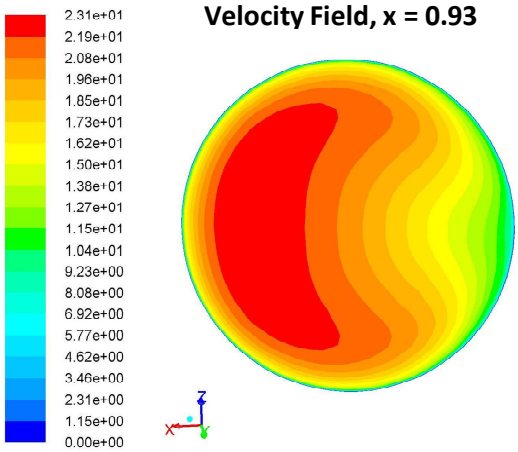

Figure 4.52 Velocity profile at x = 0.93. (p = 40 bar; G = 400 kg/m^{2}s).

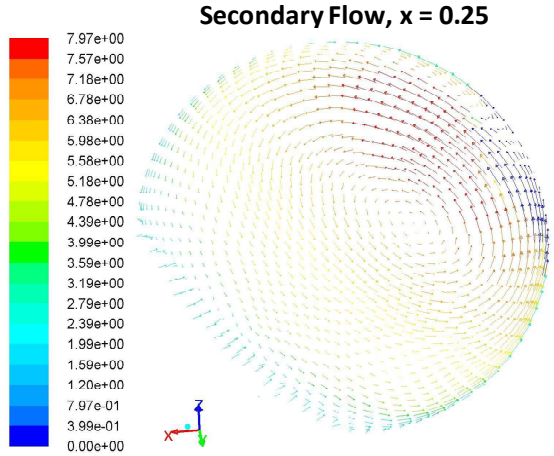

Figure 4.53 Secondary flow at x = 0.25. (p = 40 bar; G = 400 kg/m^{2}s).

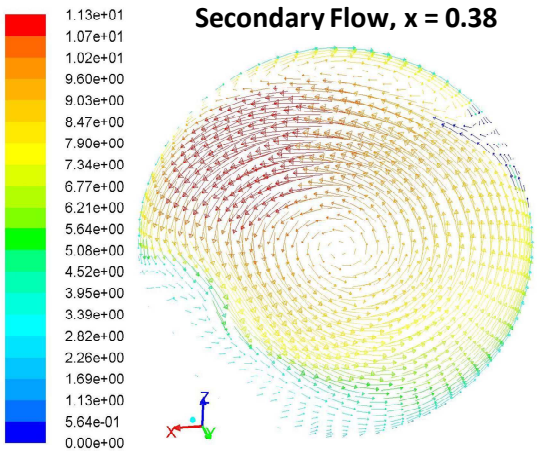

Figure 4.54 Secondary flow at x = 0.38. (p = 40 bar; G = 400 kg/m^{2}s).

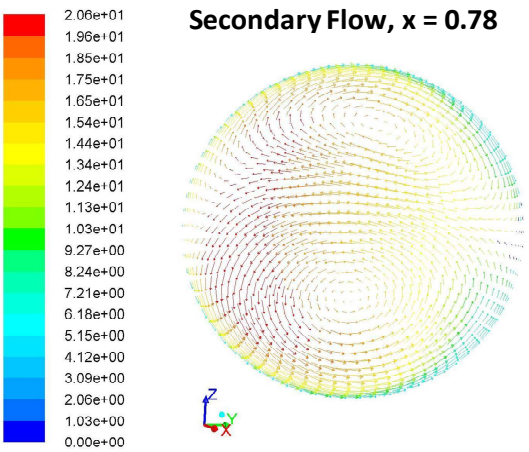

Figure 4.55 Secondary flow at x = 0.78. (p = 40 bar; G = 400 kg/m^{2}s).

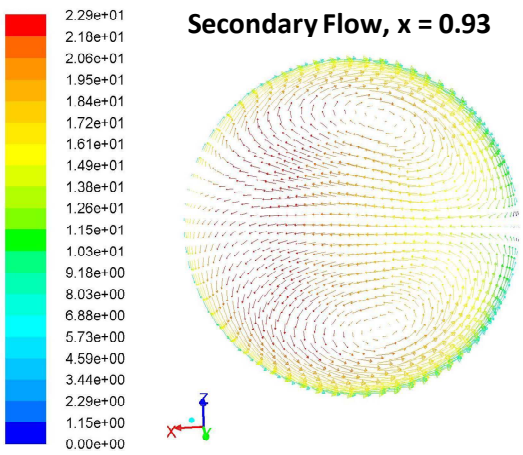

Figure 4.56 Secondary flow at x = 0.93. (p = 40 bar; G = 400 kg/m^{2}s).

The structure of the secondary flow on the tube cross section supports the previous analysis. At low quality, a single vortex characterizes the vapor, that starts to occupy a significant portion of the pipe (Figure 4.53). At higher quality, a second vortex appears in the upper portion of the pipe (Figure 4.54). Its size grows with the quality, becoming similar to the lower one (Figure 4.55). At x = 0.93, two almost symmetric counter rotating vortices mark the reaching of a flow regime very close to single-phase vapor (Figure 4.56). These vortices can cause the recirculation of the remaining liquid droplets and their accumulation along the pipe wall.

4.2.3 Comparison with experiments

For the validation of the quantitative accuracy of the numerical results, the adiabatic two-phase pressure drops measured at SIET laboratories (Section 2.3) have been considered for comparison. Two other set of simulations were made, at different pressure and mass flow rate, to enlarge the validity of the assessment. The complete list of the simulations can be found in Table 4.11, with results for the void fraction and the frictional pressure drop.

The numerical results for the frictional pressure drop are compared to the experimental data in Figure 4.57 at 40 bar and 400 kg/m^{2}s, and in Figure 4.58 and Figure 4.59 at 40 bar and 600 kg/m^{2}s and 60 bar and 600 kg/m^{2}s, respectively. Starting from Figure 4.57, the numerical results not only show a good qualitative agreement with the experimental frictional pressure drop profile, but also a satisfactory quantitative agreement. In particular, the peak in the frictional pressure drop profile is correctly reproduced by the code. Quantitatively, numerical estimations are particularly good at low and high flow quality, whereas the highest errors are found at medium quality. Globally, the average relative error is a good 14.3 %, with a maximum deviation of about 25 % for the point at x = 0.60. That point in particular, however, can be considered a unique case, since it shows a significantly higher error with respect to the others and looks more like an outlier. A change in pressure or mass flow rate does not influence the accuracy of the simulations. At 60 bar and 600 kg/m^{2}s, the average error is

comparable and equal to 13.5 %. A slightly higher difference (more than 15 %) is found at 40 bar and 600 kg/m^{2}s, at which the frictional pressure drop are generally underestimated.

Table 4.11 Conditions simulated with the CFD and results.

p = 40 bar, G = 400 kg/m^{2}s				
j_l [m/s]	**j_v [m/s]**	**x [-]**	**α [-]**	**Δp/L [kPa/m]**
0.48	0.20	0.01	0.108	2.042
0.48	0.53	0.025	0.216	1.893
0.46	1.57	0.075	0.585	1.235
0.41	3.064	0.15	0.793	1.457
0.36	5.11	0.25	0.875	2.645
0.31	7.74	0.38	0.904	2.860
0.25	10.21	0.5	0.954	6.630
0.20	12.05	0.59	0.968	8.963
0.18	13.06	0.67	0.965	8.965
0.10	15.96	0.78	0.990	8.900
0.07	17.36	0.85	0.994	8.404
0.03	19.02	0.93	0.998	6.742
p = 40 bar, G = 600 kg/m^{2}s				
j_l [m/s]	**j_v [m/s]**	**x [-]**	**α [-]**	**Δp/L [kPa/m]**
0.71	0.31	0.01	0.138	2.147
0.62	4.52	0.15	0.792	2.263
0.55	7.54	0.25	0.839	3.394
0.45	11.45	0.38	0.909	7.651
0.35	15.08	0.50	0.947	12.495
0.24	20.21	0.66	0.974	18.916
0.14	23.57	0.80	0.987	25.052
0.10	25.70	0.86	0.994	22.563
0.05	28.08	0.93	0.998	14.574
p = 60 bar, G = 600 kg/m^{2}s				
j_l [m/s]	**j_v [m/s]**	**x [-]**	**α [-]**	**Δp/L [kPa/m]**
0.72	0.80	0.026	0.210	1.988
0.69	2.37	0.075	0.488	1.658
0.65	4.70	0.15	0.706	1.918
0.57	7.86	0.25	0.817	3.175
0.37	15.72	0.50	0.918	7.404
0.25	22.0	0.68	0.966	13.692
0.07	28.34	0.91	0.995	8.842

To sum up, the results can be considered satisfactory. The same numerical model, applied with success to an air-water flow at atmospheric pressure (Section 4.1), allows to obtain an accuracy of about 15 % also with respect to the SIET data (steam-water mixture at high pressure and in a much larger coil). The mentioned accuracy is comparable to the best correlation available in literature, although it is normally guarantee by correlations only in a limited range of conditions.

In addition to the quantitative accuracy, the correct estimation of the peak in the frictional pressure drop with the CFD model suggests the possibility to explain the physical phenomena at the origin of the peculiar peak. In the previous chapter, it was mentioned that an analysis of the phase distribution can indicate a transition to a dispersed flow from a flow regime

characterize by the presence of a liquid film at the wall. It cannot strictly be considered an annular flow regime, as the code is unable to completely resolve the liquid film at the wall. Since the flow regime transition is identified at a flow quality of about 0.7 – 0.8, it seems directly related to the peak and subsequently decrease of the frictional pressure drop. Therefore, the peak can be explained as due to a progressive thinning and subsequently rupture of the liquid film at the wall. As more and more vapor occupy the near wall region, the frictional pressure drop decreases to the value of the single-phase vapor flow.

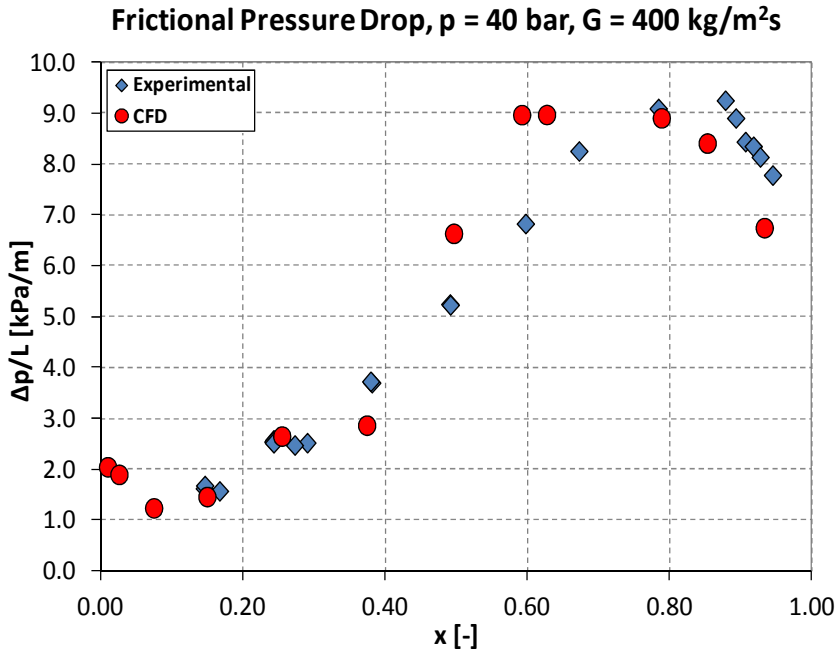

Figure 4.57 Comparison between CFD simulations and experimental data of frictional pressure drop at p = 40 bar and G = 400 kg/m^{2}s.

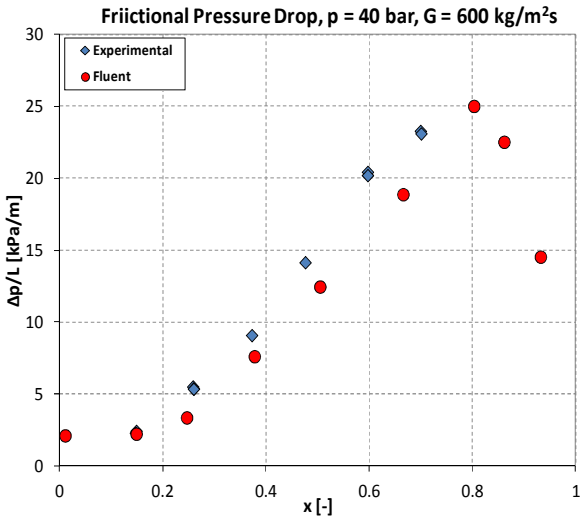

Figure 4.58 Comparison between CFD simulations and experimental data of frictional pressure drop at p = 40 bar and G = 600 kg/m^{2}s.

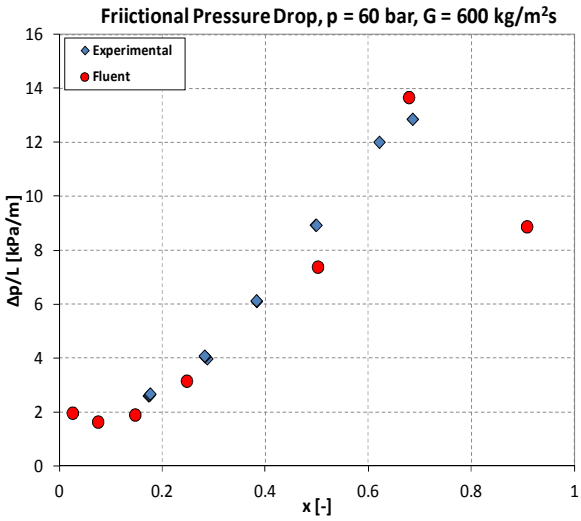

Figure 4.59 Comparison between CFD simulations and experimental data of frictional pressure drop at p = 60 bar and G = 600 kg/m^{2}s.

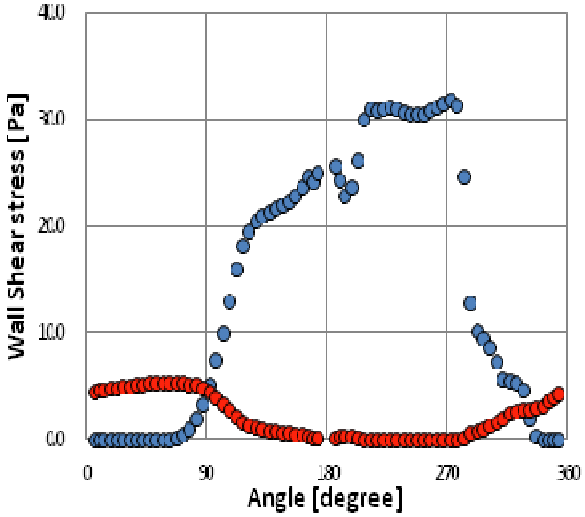

Figure 4.60 Wall shear stress profile for the liquid-phase (blue line) and the vapor phase (red line) at x =0.38 (M. Santinello, 2012).

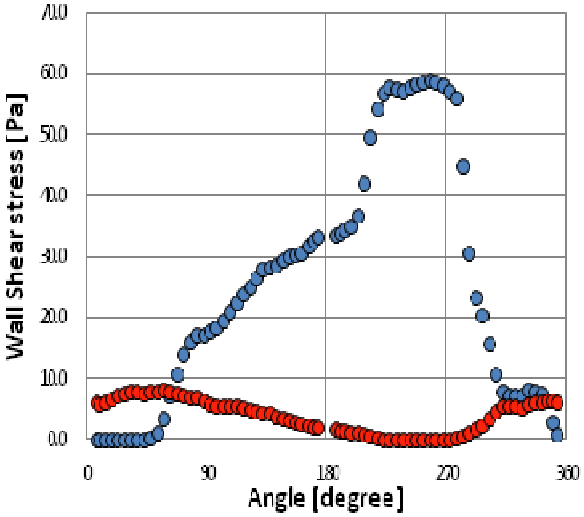

Figure 4.61 Wall shear stress profile for the liquid-phase (blue line) and the vapor phase (red line) at x =0.67 (M. Santinello, 2012).

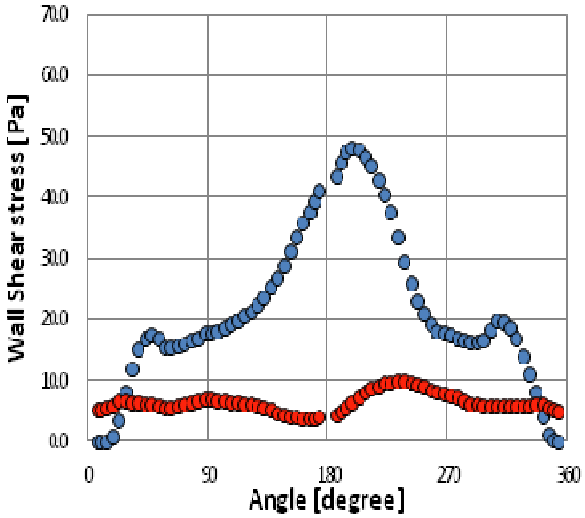

Figure 4.62 Wall shear stress profile for the liquid-phase (blue line) and the vapor phase (red line) at x =0.85 (M. Santinello, 2012).

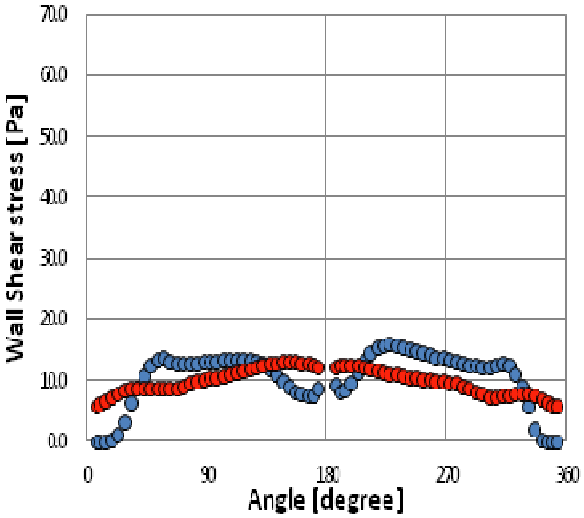

Figure 4.63 Wall shear stress profile for the liquid-phase (blue line) and the vapor phase (red line) at x =0.93 (M. Santinello, 2012).

To support the previous assumption, a further analysis was conducted, focused on the wall shear stress at the wall. The code returns the value of the liquid and the vapor components of the wall shear stress. The entire analysis, reported only partially here, can be found in the thesis work of Santinello (2012). The wall shear stress profile along the pipe circumference is shown from Figure 4.60 to Figure 4.63 for the case at 40 bar and 400 kg/m^{2}s. On the horizontal axis, the 0° value corresponds to the inner wall and a counter clockwise convention is adopted. Figure 4.60 and Figure 4.61 show how is the wall shear stress due to the liquid-phase that plays the major role. In particular, the peak in the liquid wall shear stress corresponds to the liquid accumulation region in the lower – outer portion of the pipe. As the flow quality becomes really high, the liquid wall shear stress starts to decrease following the rupture of the liquid film (Figure 4.62). At the highest quality (x = 0.93), no more liquid film

is present at the wall and the wall shear stress becomes very low, causing the decrease in the frictional pressure drop.

Finally, data on the void fraction, not available otherwise, have been derived from the CFD results. They are resumed in Figure 4.64 for the three sets of data as a function of the flow quality.

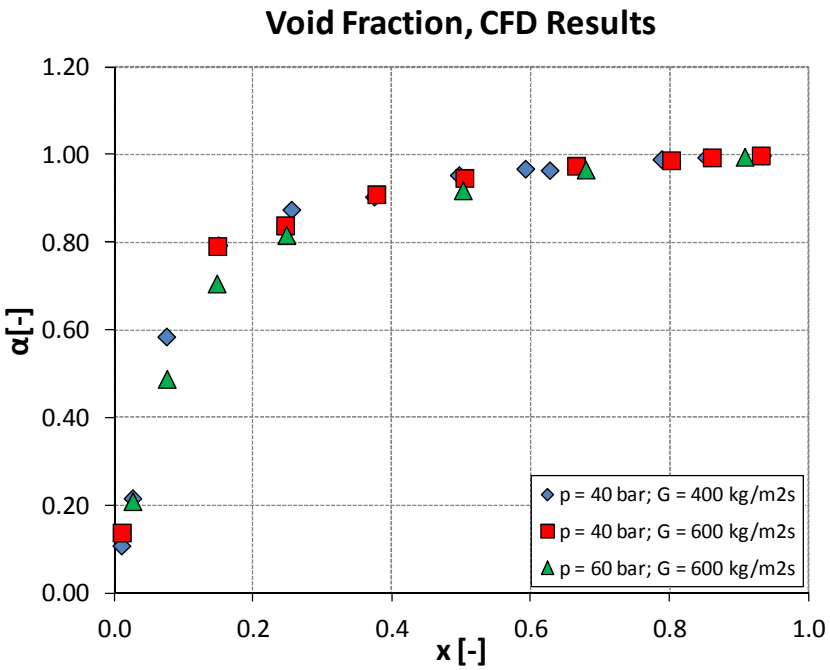

Figure 4.64 CFD results for the void fraction.

4.3 The drift-flux model

The drift-flux formulation, introduced by Zuber and Findlay (1965), is probably the best mixture model presently available for the description of a two-phase flow. In the drift-flux model, the motion of the whole mixture is expressed by the mixture momentum equation and the relative motion between the phases is taken into account by a kinematic constitutive equation. The drift-flux formulation uses the local volumetric fluxes of the phases j_l and j_g and their cross sectional averages:

$$\langle j_l \rangle = \langle \mathrm{v}_l(1-\alpha) \rangle = \langle \mathrm{v}_l \rangle_l \langle 1-\alpha \rangle = \frac{\Gamma(1-x)}{\rho_l} \tag{4.8}$$

$$\langle j_g \rangle = \langle \mathrm{v}_g \alpha \rangle = \langle \mathrm{v}_g \rangle_g \langle \alpha \rangle = \frac{\Gamma x}{\rho_g} \tag{4.9}$$

$$\langle j \rangle = \langle j_g \rangle + \langle j_l \rangle \tag{4.10}$$

The average volumetric fluxes, or superficial velocities, represent the rates of volumetric flow per unit area. For the mixture, the average volumetric flux (Eq.(4.10)) is the average velocity of the center of volume. In this section, the symbol < > is used to indicate the average value of a scalar or a vector variable *Y* over the cross sectional area of the duct[1]:

$$\langle Y \rangle = \frac{1}{A} \int Y dA \tag{4.11}$$

Instead, the symbol $< >_k$ indicates the average value of a phase variable Y_k over the area of the channel occupied by the phase *k* only:

$$\langle Y_k \rangle_k = \frac{1}{A_k} \int Y_k dA_k \tag{4.12}$$

To derive the drift flux model, let's consider the local drift velocity of the gas phase, that is the velocity of the gas with respect to the mixture center of volume, which travels with velocity *j*:

$$\mathrm{v}_{gj} = \mathrm{v}_g - j \tag{4.13}$$

Integrating the local velocities over the cross sectional area, the average velocity of the gas phase is obtained:

$$\langle \mathrm{v}_g \rangle = \langle \frac{j_g}{\alpha} \rangle = \langle j \rangle + \langle \mathrm{v}_{gj} \rangle \tag{4.14}$$

A more advantageous form can be obtained multiplying Eq.(4.13) for the void fraction and considering the weighted mean value of a quantity *Y*:

$$\bar{Y} = \frac{\langle \alpha Y \rangle}{\langle \alpha \rangle} = \frac{\frac{1}{A} \int \alpha Y dA}{\frac{1}{A} \int \alpha dA} \tag{4.15}$$

Integrating over the duct allows to find the weighted average velocity of the gas phase:

$$\bar{\mathrm{v}}_g = \frac{\langle j_g \rangle}{\langle \alpha \rangle} = \frac{\langle \alpha j \rangle}{\langle \alpha \rangle} + \frac{\langle \alpha \mathrm{v}_{gj} \rangle}{\langle \alpha \rangle} \tag{4.16}$$

In must be noticed that the average gas velocity defined in Eq.(4.14) is in general different from the weighted average velocity above. Eq.(4.16) constitutes the fundamental relation of the drift-flux model, when it is written in the form:

[1]In this section, the symbol < > is used as it is necessary to distinguish between local and cross sectional averaged values.

$$\bar{v}_g = \frac{\langle j_g \rangle}{\langle \alpha \rangle} = C_0 \langle j \rangle + V_{gj} \tag{4.17}$$

C_0 is the concentration parameter, which accounts for the non uniform distribution of the flow inside the channel and the concentration profile. V_{gj} is the average drift velocity weighted on the void fraction, that accounts for the local relative velocity between the phases:

$$C_0 = \frac{\langle \alpha j \rangle}{\langle \alpha \rangle \langle j \rangle} = \frac{\frac{1}{A}\int j \alpha dA}{\frac{1}{A}\int j dA \frac{1}{A}\int \alpha dA} \tag{4.18}$$

$$V_{gj} = \frac{\langle \alpha v_{gj} \rangle}{\langle \alpha \rangle} \tag{4.19}$$

Through Eq.(4.16), the weighted mean velocity of the gas phase, so the relative velocity between the phases, is related to the average volumetric flux of the mixture, once appropriate expressions for the concentration parameter and the average drift velocity are provided. The value of the average void fraction is known from Eq.(4.17):

$$\langle \alpha \rangle = \frac{\langle j_g \rangle}{C_0 \langle j \rangle + V_{gj}} \tag{4.20}$$

4.4 Correlation of the air-water experimental data

4.4.1 Zuber-Findlay model

Eq.(4.17) provides a useful tool for analyzing the experimental data and developing a correlation for the average void fraction. In fact, the average volumetric fluxes are between the system input parameters usually available from the experiments. From the experimental measurements, the concentration parameter and the average drift velocity can be determined. They can be represented as single numerical values or more or less complicated expressions, usually function of the flow regime. Actually, a large number of correlations were developed based on the drift-flux formulation, frequently obtaining simplicity and a very good accuracy (Chexal et al., 1991; Coddington and Macian, 2002; Woldesemayat and Ghajar, 2007).

First the experimental data of Akagawa et al. (1971) are considered. Eq.(5.17) suggests a plot of the weighted mean velocity of the gas phase versus the average volumetric flux of the mixture, as it is shown in Figure 4.65 for the data in the smallest coil (D = 0.109 m). A good correlation is obtained, as the data lie on a straight line also shown in the figure. The angular coefficient represent the concentration parameter C_0, whereas the point of intersection with the vertical axis is the average drift velocity weighted on the void fraction. Therefore, the correlation for the void fraction assumes the following form:

$$\langle \alpha \rangle = \frac{\langle j_g \rangle}{1.24 \langle j \rangle - 0.07} \tag{4.21}$$

It is interesting to note that the average drift velocity surprisingly has a negative value. Although, its value is really low, almost negligible, and even a small error can change it from positive to negative and vice versa.

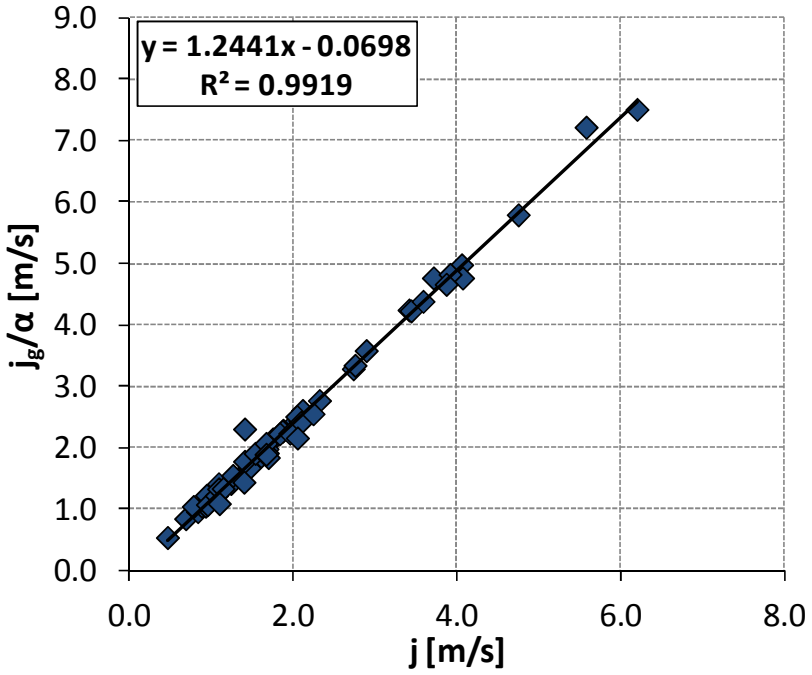

Figure 4.65 Correlation of the data of Akagawa et al. (1971) for the D =0.109 m coil with the drift-flux model proposed by Zuber and Findlay (1965).

4.4.2 Correlation based on the CFD results

The availability of the CFD numerical results allows also the possibility to directly calculate C_0 and V_{gj} from Eq.(4.18) and Eq.(4.19), that is from the local values of velocity and void fraction. Within these respects, the drift-flux model represent a useful tool for a further validation of the numerical results. Actually, local CFD results must produce coherently values of C_0 and V_{gj} when inserted into Eq.(4.18) and Eq.(4.19) to be considered reliable.

Using the CFD results for the 0.109 m diameter coil, presented in Section 5.1.6, the following correlation is obtained:

$$\langle \alpha \rangle = \frac{\langle j_g \rangle}{1.175\langle j \rangle + 0.0003} \tag{4.22}$$

The above formula is very close to Eq.(5.21). In this case the value of the average drift velocity is positive, even if it is probably more correct to say that its value is almost zero.

4.4.3 *Comparison between correlations and experimental data*

A first comparison between Eq.(4.21) and Eq.(4.22) with the Akagawa et al. database (for the D = 0.109 m coil only) is shown in Figure 4.66. A very good agreement is found for both the correlations, with an average relative error of about 5 %. Obviously, it is necessary to

extend the comparison, since the data in Figure 4.66 are the same used for the development of the correlations. However, the possibility to evaluate the void fraction with a correlation developed from the CFD results it's a further confirmation of the consistency of the numerical results.

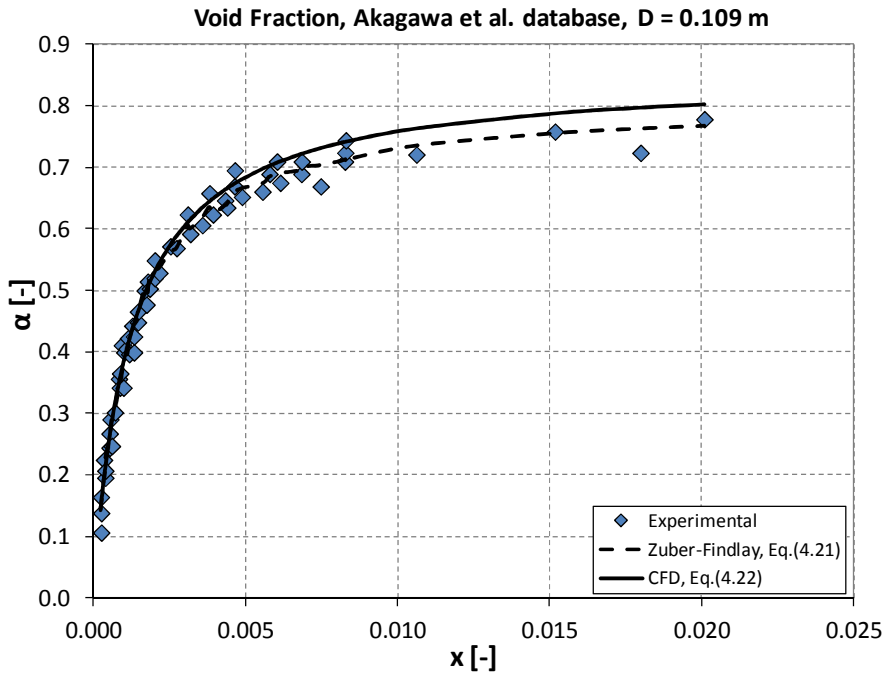

Figure 4.66 Comparison between the void fraction from the D = 0.109 m diameter coil of the Akagawa et al. data (1971) and the two drift-flux correlations developed with the model of Zuber and Findlay and from the CFD results.

An additional comparison is made with the data of Akagawa et al., but related to the largest diameter helix (D = 0.225 m). Also for this case, the agreement of both the correlation is very good and the error is around the 5 %. For all the data of Akagawa et al., the results are summarized in Table 4.12. As mentioned before, the two correlations show a very good agreement with the experimental measures in Figure 4.67. In particular, the correlation derived from CFD better predicts the data at D=0.225 m and shows in both cases average relative errors around the 5%, that should be considered comparable with the experimental uncertainty.

Table 4.12 Results of the comparison between the void fraction correlations and the experimental data of Akagawa et al. (1971).

Correlation	D = 0.109 m	D = 0.225 m
Zuber-Findlay (Eq.(4.21))	4.60 %	6.35 %
CFD (Eq.(4.22))	5.08 %	4.97 %

To further enlarge the assessment, two other literature works are now considered, due to Watanabe et al. (1986) and Mandal and Das (2003). Both studied an adiabatic air-water flow in helically coiled pipes of different geometries. The agreement between the correlations and the experimental data is very good also for the two new set of experimental data (Figure 4.68

and Figure 4.69). In the two figures, the void fraction is presented as a function of the volumetric flow quality, as it was the quantity available from the experiments. Slightly higher errors are found for the CFD correlation and the data of Mandal and Das (the global agreement is anyway remarkable, being 7.1% the average error), that are oversestimated. Average errors between the two correlations and the different set of data are resumed in Table 4.13.

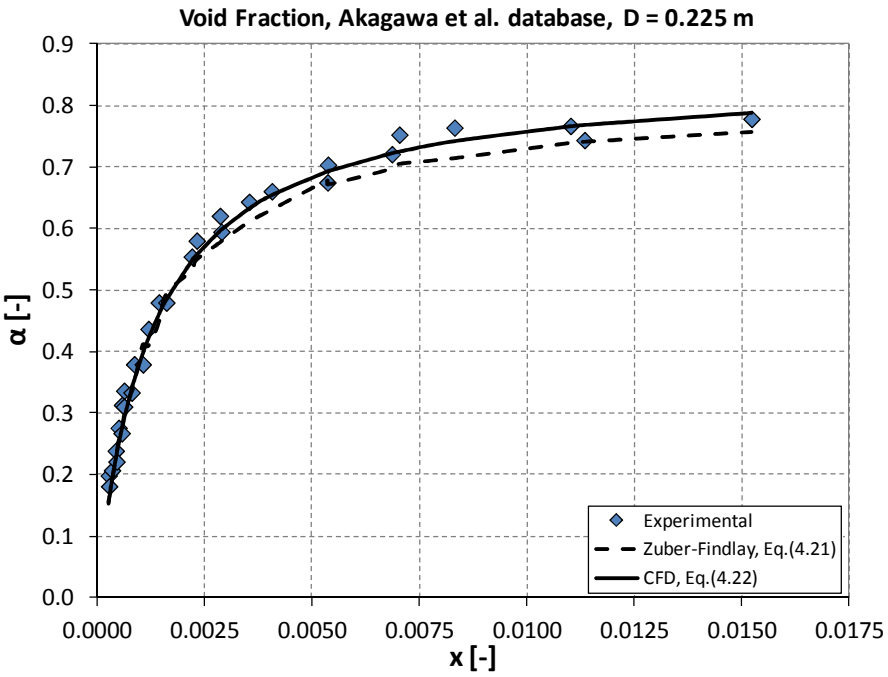

Figure 4.67 Comparison between the void fraction from the D = 0.225 m diameter coil of the Akagawa et al. data (1971) and the two drift-flux correlations developed with the model of Zuber and Findlay and from the CFD results.

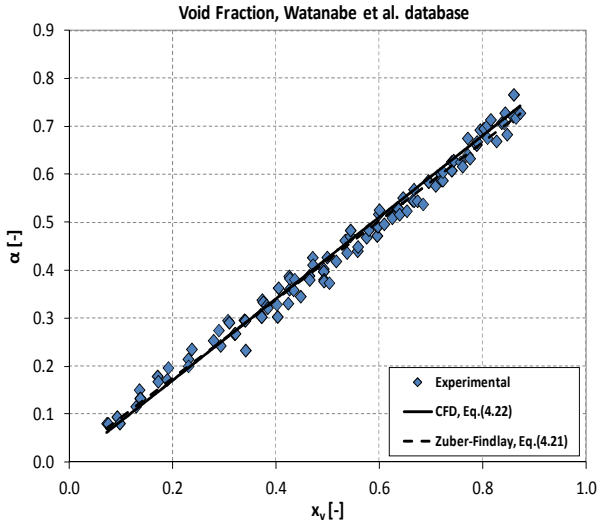

Figure 4.68 Comparison between the experimental data of Watanabe et al. (1986) and the two drift-flux correlations.

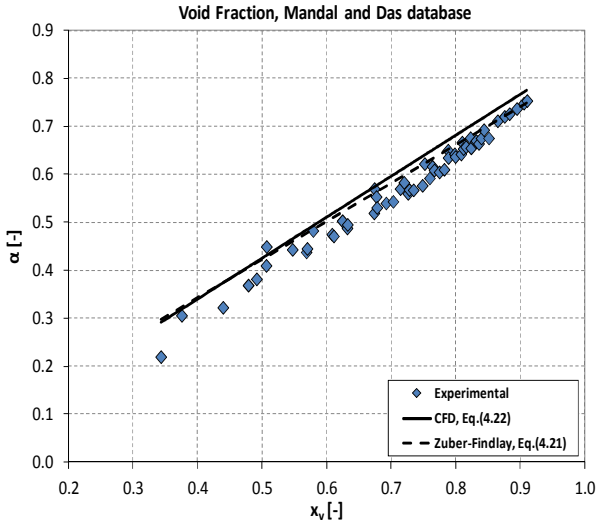

Figure 4.69 Comparison between the experimental data of Mandal and Das (2003) and the two drift-flux correlations.

Table 4.13 Average relative errors between the two correlations for the void fraction and the experimental values.

Databank	**Zuber – Findlay (Eq.(4.21))**	**CFD (Eq.(4.22))**
Akagawa et al. (1971), D = 0.109 m	4.60 %	5.08 %
Akagawa et al. (1971), D = 0.225 m	6.35 %	4.97 %
Watanabe et al. (1986)	4.55 %	7.11 %
Mandal and Das (2003)	5.0 %	5.41 %

4.4.4 Additional consideration for the void fraction correlations

It is interesting to consider the low value of the average drift velocity weighted on the void fraction in both Eq.(4.21) and Eq.(4.22). Neglecting the average drift velocity in Eq.(4.20), the following relation is obtained:

$$\langle \alpha \rangle = \frac{1}{C_0}\frac{\langle j_g \rangle}{\langle j \rangle} = \frac{1}{C_0} x_v = K_B x_v \tag{4.23}$$

The parameter K_B is exactly the flow parameter obtained in the theoretical analysis of Bankoff (1960), equal to the inverse of the flow parameter C_0, as indicated by Zuber and Findlay (1965). The flow parameter K_B is therefore equivalent to the ratio of the void fraction to the volumetric flow quality:

$$K_B = \frac{\langle \alpha \rangle}{x_v} \tag{4.24}$$

An expression of the form of Eq.(4.23) was obtained by Armand (1946). It was extensively used in the Russian literature to correlate experimental data obtained at high mass flow rate over a large pressure range. In particular the correlation proposed by Armand reads:

$$\langle \alpha \rangle = 0.833 x_v \tag{4.25}$$

Eq.(4.25) is indicated to provide good results also in helical pipes, when an air-water flow at atmospheric pressure is addressed (Akagawa et al., 1971; Czop et al., 1994). Considering the two correlations developed, they can be rewritten in the following form, neglecting the average drift velocity:

$$\langle \alpha \rangle = 0.806 x_v \qquad \text{(Zuber – Findlay)} \tag{4.26}$$

$$\langle \alpha \rangle = 0.851 x_v \qquad \text{(CFD)} \tag{4.27}$$

Eq.(4.26) and Eq.(4.27) are quite close to the original empirical formulation by Armand. The latter confirms again the validity of the correlation developed from the CFD results, so the reliability of the numerical estimation of phase distribution and velocity fields.

4.5 Correlation of the CFD void fraction results for the steam-water flow

In the previous section, a further validation of the CFD results presented in Section 4.1 has been proposed through the drift-flux model. In addition, a simple but accurate correlation for the void fraction has been successfully developed starting from the numerical results. In this section, the same approach is applied to the adiabatic steam-water flow simulated in Section 4.2.

For the air-water flow, the developed correlation is characterized by a constant value of the concentration parameter C_0. In this case, a constant value is not acceptable, since the results include the whole range of flow quality up to x = 1.0. In fact, a constant value of C_0 higher than one will inevitably lead to an underestimated void fraction as the volumetric flow quality approaches unity. The void fraction will tend to a value equal to its inverse, the parameter K in Eq.(4.23). Actually, both the correlation of Armand (1946) and the model of Bankoff (1960) are indicated by their respective authors to be valid in the bubbly flow regime. Also Zuber and Findley (1965) in their original paper suggests different values of C_0, to be used with different flow regimes. Within these respects, a correlation form similar to that proposed by Rouhani (Rouhani and Axelsson, 1970) can be of interest:

$$C_0 = 1 + 0.2(1 - x) \tag{4.28}$$

A concentration parameter similar to Eq.(4.28) assures a proper value in the bubbly regime and also respects the condition of a void fraction equal to 1 for a volumetric quality equal to unity. The same procedure described in the previous section has been applied, calculating the concentration parameter and the average drift velocity from the CFD results with Eq.(4.18) and Eq.(4.19). Knowing the flow quality, a new parameter can be determined from the value of C_0 with the following expression:

$$C_0 = 1 + a(1 - x) \tag{4.29}$$

A most proper value of a = 0.117 is found. Therefore the final form of the correlation results:

$$\langle \alpha \rangle = \frac{\langle j_g \rangle}{[1 + 0.117(1 - x)]\langle j \rangle + 0.0016} \tag{4.30}$$

In Figure 4.70, the prediction of Eq.(4.30) are compared with the void fraction estimations obtained with CFD in Section 4.2. Data are related to the adiabatic two-phase flow in the three conditions examined (p = 40 bar, G = 400 kg/m^{2}s; p = 40 bar, G = 600 kg/m^{2}s; p = 60 bar; G = 600 kg/m^{2}s). Instead, the prediction of the correlation are shown only for the two different values of the pressure, since it is independent from the mass flow rate.

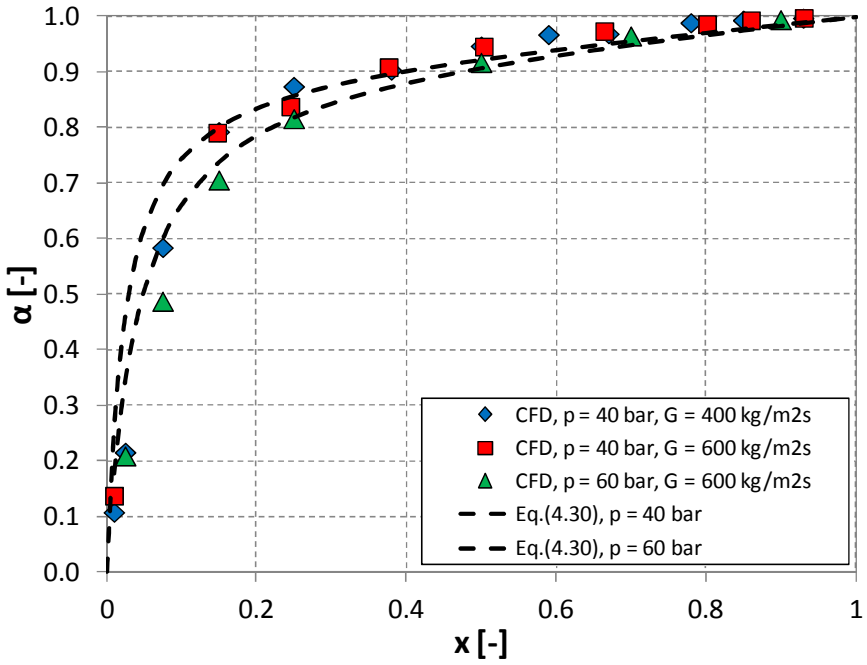

Figure 4.70 Void fraction CFD results from the simulation of a two-phase flow inside the SIET pipe and estimation obtained with Eq.(4.30).

A final remark can be made, considering the CFD data at 40 bar and 400 kg/m^{2}s. The value of C_0 and V_{gj} calculated for every single numerical run are summarized in Table 4.14. The concentration parameter results really high at low quality. In particular, for $x < 0.05$, the value of C_0 seems too high and extremely unreliable. Some difficulties in a correct prediction of the void fraction at low flow quality were also mentioned in Section 4.1.6 for the air-water flow. In particular, the probable necessity for a more accurate model of the drag force was underlined, as the phase distribution results from a complicate interaction between the gravitational and the centrifugal force fields. Within these respects, Table 4.14 is a further confirmation of the usefulness of using the drift-flux formulation for the validation of the CFD simulations. In support to the experimental data, it allows to assess also locally the numerical simulations and identify inconsistent or unreliable results.

Table 4.14 Value of C_0 and V_{gj} from every CFD run at 40 bar and 400 kg/m^{2}s (Section 4.2.2).

x [-]	C_0 [-]	V_{gj} [m/s]
0.01	2.68	0.0013
0.025	2.43	0.0010
0.075	1.32	0.0006
0.15	1.11	0.0006
0.25	1.07	0.0010
0.38	1.06	0.0008
0.5	1.03	0.0018
0.59	1.016	0.0024
0.67	1.017	0.0021
0.78	1.004	0.0017
0.85	1.002	0.0013
0.93	1.001	0.0006

4.6 Conclusions

The two-phase flow in an helical pipe, main subject of the whole thesis work, has been study in this chapter through numerical CFD. Coherently with the numerical analysis developed in Chapter 3 for the single-phase flow, the ANSYS FLUENT code has been selected for the simulations. The two-phase flow was modeled with the Eulerian-Eulerian approach, neglecting phase change and mass and energy exchanges between the phases. Actually, an adiabatic flow has been addressed in all the simulations, considering only the drag force for the momentum exchange between the phases.

The CFD study reached different goals. Qualitatively, it allowed the detailed description of the phase interaction and the distribution of the phases inside the duct under the influence of the centrifugal force field. Starting from detailed local results, a physical explanation was provided for the particular profile of the frictional pressure drop as a function of the flow quality, characterized by a marked peak. Quantitatively, the frictional pressure drop were predicted with a satisfactory accuracy in completely different geometries and conditions, using the same numerical model. In particular, the numerical results showed an average error between 10 % and 15 % in almost all the conditions examined, comparable with the best literature correlations when they are applied on their original databases. The numerical model, instead, is not dependant on a particular set of data or range of parameters, although it requires high simulation time and computational resources. Finally, the numerical results resulted successful in support of the experimental measurements, in some particular case where the latter are scarce or unavailable. In particular, data on the void fraction for the SIET facility were derived from numerical results, since it was not possible to experimentally measure the void fraction.

Since a detailed assessment of the CFD results was necessary, an air-water flow has been first simulated. Actually, the significantly higher number of available literature studies made easy the validation procedure. In particular, the experimental data of Akagawa et al. (1971), measured in small helices (D = 0.109 m and D = 0.225 m), have been considered for comparison. Qualitatively results on the phase distribution, characterized by water flowing on the external region of the pipe and air in the internal portion of the cross sectional area, were compared with observations made with imaging tomography. For the void fraction, a great accuracy is shown by the CFD, with average relative errors lower than 5 %. For the frictional pressure drop, the average error is included between 10 % and 15 %. Some drawbacks were also underlined, in particular the dependency of the results from the diameter of the dispersed phase, which is an input for the numerical model.

The simulation of the two-phase flow in the SIET pipe (D = 1.0 m) was then addressed, comparing the results with the adiabatic frictional pressure drop data described in Chapter 2. The two-phase flow was characterized in details, in terms of phase distribution, flow regime, velocity field and secondary motion. An explanation was given to the peak in the frictional pressure drop profile, based on the change of flow regime and supported by an analysis of the wall shear stress behavior. The frictional pressure drop resulted again estimated with an average absolute error between 10 % and 15 %. Numerical estimations of the void fraction were made available for all the simulated conditions.

The drift-flux model, introduced by Zuber and Findlay (1965), has been used for the analysis of the void fraction data obtained from the CFD calculations. For the air-water case, two correlations have been developed, starting respectively from the experimental data of Akagawa et al. (1971) and the CFD results. Both the correlations show a satisfactory accuracy, with an average relative error around 5 %, also when compared against other databases available in literature. The correlation built from CFD results, in particular, represents a further validation of their consistency, being developed starting from local void fraction and velocity numerical values.

After the successful application to the air-water flow, the same methodology was applied to the CFD results obtained for the SIET pipe. A void fraction correlation for the two-phase flow inside an helically coiled pipe has been developed. In addition, some inconsistencies were identified in the results at low flow quality, suggesting the necessity for an improvement of the numerical model in that quality region, already noticed in Section 5.1.6 for the air-water flow.

References

B.K. Akagawa, T. Sakaguchi, M. Ueda, 1971. Study on a gas-liquid two-phase flow in helically coiled tubes. Bulletin of the Japan Society of Mechanical Engineers 14(72), 564-571.

A.A. Armand, 1946. The resistance during the movement of a two-phase system in horizontal pipes. Atomic Energy Research Establishment Transaction 828.

ANSYS Fluent 14.0 User Guide, 2011.

S.G. Bankoff, 1960. A variable density single-fluid model for two-phase flow with particular reference to steam-water flow. Journal of Heat Transfer 82, 265-272.

D. Bestion, 2012. Applicability of two-phase CFD to nuclear reactor thermalhydraulics and elaboration of Best Practice Guidelines. Nuclear Engineering and Design 253, 311-321.

T.T. Chandratilleke, N. Nadim, R. Narayanaswamy, 2012. An investigation of flow boiling with secondary flow interaction in curved pipes. ECI 8th International Conference on Boiling and Condensation Heat Transfer, Lausanne, Switzerland, 3-7 June.

B. Chexal, J. Horowitz, G.S. Lellouche, 1991. An assessment of eight void fraction models. Nuclear Engineering and Design 126, 71-88.

P. Coddington, R. Macian, 2002. A study of the performance of void fraction correlations used in the context of drift-flux two-phase flow models. Nuclear Engineering and Design 215, 199-216.

V. Czop, D. Barbier, S. Dong, 1994. Pressure drop, void fraction and shear stress measurements in an adiabatic two-phase flow in a coiled tube. Nuclear Engineering and Design 149, 323-333.

N.I. Kolev, 2005. Multiphase flow dynamics 2: thermal and mechanical interactions. Springer, Berlin, Germany, 2nd Edition.

J.S. Jayakumar, S.M. Mahajani, J.C. Mandal, K.N. Iyer, P.K. Vijayan, 2010. Thermal hydraulic characteristics of air-water two-phase flows in helical pipes. Chemical Engineering Research and Design 88, 501-512.

J.C. Jo, W.S. Kim, C.Y. Choi, Y.K. Lee, 2009. Numerical simulation of subcooled flow boiling heat transfer in helical tubes. ASME Journal of Pressure Vessel Technology 131.

S.N. Mandal, S.K. Das, 2003. Gas-liquid flow through helical coils in vertical orientation. Industrial & Engineering Chemistry Research 42(14), 3487-3494.

Y. Murai, H. Oiwa, T. Sasaki, K. Kondou, S. Yoshikawa, F. Yamamoto, 2005. Backlight imaging tomography for gas-liquid two-phase flow in a helically coiled tube. Measurement Science and Technology 16, 1459-1468.

S.Z. Rouhani, E. Axelsson, 1970. Calculation of void volume fraction in the sub cooled and quality boiling regions. International Journal of Heat and Mass Transfer 13, 383-393.

M. Santinello, 2012. Experimental and CFD investigations of single-phase and two-phase steam-water flow in helically coiled tubes. M.Sc. Thesis, Nuclear Engineering Division, Department of Energy, Politecnico di Milano, Milano, Italy.

H.C. Unal, 1978. Determination of void fraction, incipient point of boiling, and initial point of net vapor generation in sodium-heated helically coiled steam generator tubes. Transaction of the ASME, Journal of Heat Transfer 100, 268-274.

O. Watanabe, O. Tajima, T. Nakano, M. Shimoya, 1986. Flow and heat transfer of a gas and liquid two-phase flow in helical coils. Transaction of the Japan Society of Mechanical Engineers B 54(507), 3192-3199.

M.A. Woldesemayat, A.J. Ghajar, 2007. Comparison of void fraction correlations for different flow patterns in horizontal and upward inclined pipes. International Journal of Multiphase Flow 33, 347-370.

N. Zuber, J.A. Findlay, 1965. Average volumetric concentration in two-phase flow systems. Journal of Heat Transfer 87, 453-468.

CHAPTER 5

The two-phase flow: correlation for two-phase frictional pressure drop

In this chapter, the development of a correlation for the estimation of the two-phase frictional pressure drop is presented. Although numerous correlations are already available in literature, none of them is reliable in a wide range of geometrical parameters and operating conditions. On the contrary, several of them are only valid within a limited range of parameters. In addition, they generally show a complicated form, being the result of multivariable regressions.

Starting from an existing database (Santini et al., 2008), a new correlation is developed. The starting point are some models valid in straight geometry, as they could be considered of general validity and have been applied with satisfactory results in a wide range of conditions. In particular the noteworthy Lockhart-Martinelli correlation (Lockhart and Martinelli, 1949) is chosen, as reported by many authors to work fairly well also in the helical geometry. In this framework, proper modifications are introduced starting from the analysis of the experimental results and their physical interpretation, while keeping the number of the needed empirical constants as lowest as possible to avoid complicated formulations. Furthermore, a form of the correlation aiming to be valid over a wide range of geometrical and operating parameters is sought. For verification purposes, the same corrective parameters are applied also to the Friedel correlation (1979).

To extend as much as possible the validity of the correlation, also data from the work of Zhao et al. (2003) are later included, as they are related to quite different geometry and operating conditions. Working with the complete dataset, a new improved form of the correlation is derived, that outperform all the other correlations considered for comparison in the whole range of geometries and operating conditions.

5.1 Literature review

In the past, different authors addressed the problem of the two-phase frictional pressure drop in the helical coil, starting from their own experimental results to derive proper correlations. Generally speaking, two different approaches have been applied. In the former, starting from widely known models and correlations developed for straight pipes, suitable modifications have been introduced to match experimental measures. Differently, some researchers developed their own predictive tools without referencing to straight channels.

Most of them developed multivariable fits to correlate the experimental data with the most significant parameters characterizing the two-phase flow. However, in certain cases, it is difficult to delineate a clear boundary between the two approaches. As an example, the use of a two-phase multiplier, introduced for the first time by Lockhart and Martinelli (1949), has been later adopted in many works. However, frequently the proposed multiplier expression is completely different from the original form.

Early works on the two-phase frictional pressure drop in the helical coils found a satisfactory agreement between their experimental data and the original or slightly modified correlation of Lockhart and Martinelli (Rippel et al., 1966; Owhadi et al., 1968; Banerjee et al., 1969; Akagawa et al., 1971; Katsuri and Stepanek, 1972). All the authors reported a maximum error always lower than 50% and average deviations between 20% and 40%, in a large number of different coils and operating conditions. Awwad et al. (1995) and Xin et al. (1996; 1997) modified the original form of the Lockhart-Martinelli multiplier as a function of the Froude number *Fr* and the pipe diameter to coil diameter ratio (*d/D)*. They reported a maximum error always lower than 35% for circular and annular channels, with both vertical and horizontal orientations. Nariai et al. (1982) adopted the correlation for straight tube due to Martinelli and Nelson (1948), evaluating the single-phase pressure drop with the correlation proposed by Ito (1959). Comparison with data from a test rig of an integrated type marine water reactor showed agreement within the 30%. Slightly better results were obtained using a modified version of the correlation proposed by Kozeki et al. (1970), based on a different form of the two-phase pressure drop multiplier. Czop et al. (1994) considered the experimental data obtained with an adiabatic water-SF6 mixture in a helically coiled tube and found better agreement with the Chisholm correlation (Chisholm and Sutherland, 1969) than using the Lockhart and Martinelli method. Other models proposed for straight tubes have been tested by different authors, in particular the Dukler approach (Dukler et al., 1964) in Katsuri and Stepanek (1972) and correlations by Thom (1964) and Baroczy (1965) in Nariai et al. (1982), finding always higher errors than the Lockhart and Martinelli correlation.

Among the correlations developed without referring to straight channel models, Ruffel (1974) proposed a different form of the liquid only friction multiplier, based on the experimental results in three different coils tested to study the AGR secondary system. Unal et al. (1981) developed a model to calculate the frictional pressure losses after testing three different coils heated by a sodium flow, in order to investigate the behaviour of a Liquid Metal Fast Breeder Reactor (LMFBR). Chen and Zhou (1981), based on a steam-water mixture flowing in three different helical coils, obtained a relation for the liquid only friction multiplier including the effect of the void fraction α and the *d/D* ratio. Guo et al. (2001) proposed a correlation for the liquid only friction multiplier based on the data from two helical tubes with four different axial inclinations of the helix. They reported a maximum error always lower than 40%. A liquid only friction multiplier correlation was developed for horizontal helically coiled pipes by Zhao et al. (2003), reaching an average deviation within 15%. Mandal and Das (2003), starting from data relative to different helical pipes, proposed an empirical correlation based on various dimensionless quantities to reach an average deviation of about 15%. Santini and co-authors (2008) completed an experimental investigation on the helically coiled tube of the IRIS reactor (Carelli et al., 2004). The empirical correlation proposed correlates the frictional pressure drop with flow rate, mixture density and tube diameter. In addition, it accounts for the mixture quality by a cubic function.

The authors indicate an average deviation of about 9%, with about 95% of the data within a deviation ±15%. However, the correlation does not account for the effect of the coil curvature and it seems difficult to extend its validity to a wider range of geometrical parameters and operating conditions. Actually it is a best-fit of experimental data, coming from an engineering approach very useful in the study of the reactor design. Since the considered correlations are representative of many different experimental conditions (from air-water two component flow in atmospheric conditions to steam-water two-phase flow at high pressure), their ranges of applicability are summarized in Table 5.1.

Table 5.1 Summary of the correlations available for frictional two-phase pressure drops in helical pipes and their ranges of applicability.

Authors	Geometrical parameters	Operating conditions
Rippel et al. (1966)	Vertical tube, descending flow d=12.7 mm, D=0.2032 m	Air-water, He-water and Freon 12-water in atmospheric conditions
Owhadi et al. (1968)	Vertical tube, ascending flow d=12.5 mm, D=0.25 m, β=7.2°,	Steam-water at atmospheric pressure Γ=35-139 kg/h, q"=60-256 kW/m^2
Banerjee et al. (1969)	Vertical tube, ascending flow d=15.9–54.8 mm, D=0.152–0.610 m β=2-8°	Air-water in atmospheric conditions Re_l=100-8000, Re_g=550-40000
Akagawa et al. (1971)	Vertical tube, ascending flow d=9.92 mm, D=0.109 m, 0.225 m β=1.2°, 2.5°	Air-water in atmospheric conditions j_l=0.35-1.16 m/s, j_g=0-5 m/s
Katsuri and Stepanek (1972)	Vertical tube, ascending flow d=12.5 mm, D=0.665m	Air-water in atmospheric conditions, Γ_l=0.01-0.22 l/s, Γ_g=0.1-8.5 l/s
Ruffel (1974)	Vertical tube, ascending flow d=10.7-18.6 mm, d/D=0.0054-0.16	Steam-water p=6-18 MPa, G=300-1800 kg/m^{2}s
Unal et al. (1981)	Vertical tube, ascending flow d=18 mm, d/D=0.012-0.0256	Steam-water p=14.9-20.1 MPa, G=296-1829 kg/m^{2}s, x=0.15-1.0
Chen and Zhou (1981)	Vertical tube, ascending flow d=18 mm, d/D=0.0198, 0.04 , 0.0763	Steam-water p=4.2-22 MPa, G=400-2000 kg/m^{2}s
Nariai et al. (1982)	Vertical tube, ascending flow d=14.3 mm, D=0.595 m	Steam-water p=2-5 MPa, G=150-850 kg/m^{2}s
Czop et al. (1994)	Vertical tube, ascending flow d=19.8 mm, D=1.17 m, β=7.27°	Water-SF6 p=1-13.5 bar, G=500-3000 kg/m^{2}s, x=0.04-0.6
Awwad et al. (1995)	Horizontal tube, d=12.7-38.1 mm, D=0.330-0.670 m β=0.5-20°	Air-water in atmospheric conditions, j_l=0.008-2.2 m/s, j_g=0.2-50 m/s
Xin et al. (1996)	Vertical tube, ascending flow d=12.7-38.1 mm, D=0.305-0.609 m β=0.5-10°	Air-water in atmospheric conditions, j_l=0.008-2.2 m/s, j_g=0.2-50 m/s
Guo et al. (2001)	Vertical, horizontal and inclined tube d=10 mm, 11 mm, D=0.132 m, 0.256 m β=4.27°, 5.36°	Steam-water p=0.5-3.5 MPa, G=150-1760 kg/m2s q"=0-540 kW/m2, x=0.01-1-2
Zhao et al. (2003)	Horizontal tube d=9 mm, D=0.292 m, β=1.9°	Steam-water p=0.5-3.5 MPa, G=236-943 kg/m^{2}s q"=0-900 kW/m^2, x=0-0.95
Mandal and Das (2003)	Vertical tube, ascending flow d=10 mm, 13 mm, D=0.131-0.222 m β=0-12°	Air-water in atmospheric conditions, Q_l=0.13-5.25·10^{-4} m^3/s, Q_g=3.65-14.2·10^{-5} m^3/s

5.2 The database

The database used for the development of the new correlation was built during a previous doctoral project (Santini, 2008), using the same facility presented in Section 2.1. It includes measures of diabatic (different from the adiabatic experimental data of Section 2.3) two-phase pressure drops in the range 10 to 65 bar for the pressure, 200 to 800 kg/m^{2}s for the mass flux and from 0 to 1 for the quality. Starting from the total pressure drop measures, the local mixture properties are calculated considering both the reference pressure and the thermodynamic quality as the arithmetic mean between the values corresponding to two consecutive pressure taps (Table 2.2). Liquid and vapor saturation properties are then calculated at the reference pressure. The frictional pressure drop can be derived from a mixture momentum balance[2]. For steady-state, one dimensional two-phase flow, this reads[3]:

$$\frac{dp}{dz} = -\tau\frac{P}{A} - g[\alpha\rho_v + (1-\alpha)\rho_l]\sin\beta - G^2\frac{d}{dz}\left[\frac{x^2 v_v}{\alpha} + \frac{(1-x)^2 v_l}{(1-\alpha)}\right] \tag{5.1}$$

In the hypothesis of homogeneous flow, that implies thermal equilibrium between the phases and equal liquid and vapor velocities, Eq.(5.1) greatly simplifies as void fraction, flow quality and mixture density become:

$$\alpha = \frac{1}{1 + \frac{(1-x)}{x}\frac{\rho_v}{\rho_l}} \tag{5.2}$$

$$x = \frac{h_m - h_l}{h_v - h_l} \tag{5.3}$$

$$\rho_m = \left[\frac{x}{\rho_v} + \frac{1-x}{\rho_l}\right] \tag{5.4}$$

Furthermore, if the assumptions of linear quality increase with the axial coordinate and constant saturation properties are made, Eq.(5.1) becomes:

$$\frac{dp}{dz} = -\tau\frac{P}{A} - g\,\rho_m\sin\beta - G^2\frac{d}{dz}v_m \tag{5.5}$$

Integrating over the path between two consecutive pressure taps, the experimental frictional pressure drop per unite length is obtained as:

[2] In the work of Santini (2008), the frictional pressure drop is derived starting from an energy balance equation.

[3] Differently from Section 4.3, in this section all the quantities are cross sectional averaged values.

$$\frac{\Delta p_F}{L} = \frac{(p_1 - p_2)}{L} - g\rho_m sin\beta - G^2(v_2 - v_1) \tag{5.6}$$

where the subscript 2 refers to the outlet section and the subscript 1 to the inlet section. The frictional pressure drop are reported for the four values of mass flux investigated in Figure 5.1, Figure 5.2, Figure 5.3 and Figure 5.4.

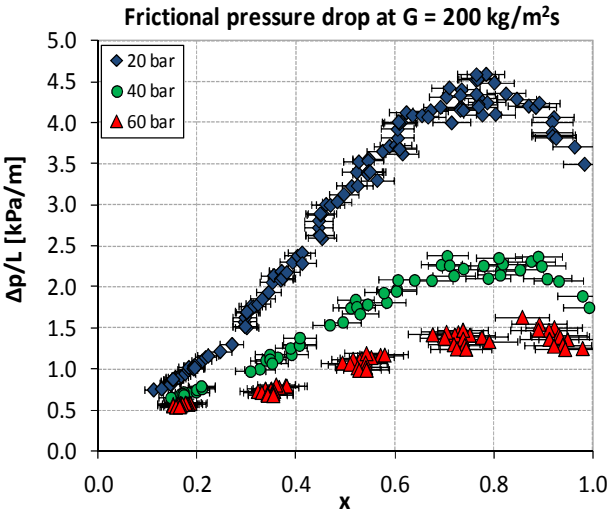

Figure 5.1 Frictional pressure drops per unit length at 200 kg/m^{2}s as a function of thermodynamic quality.

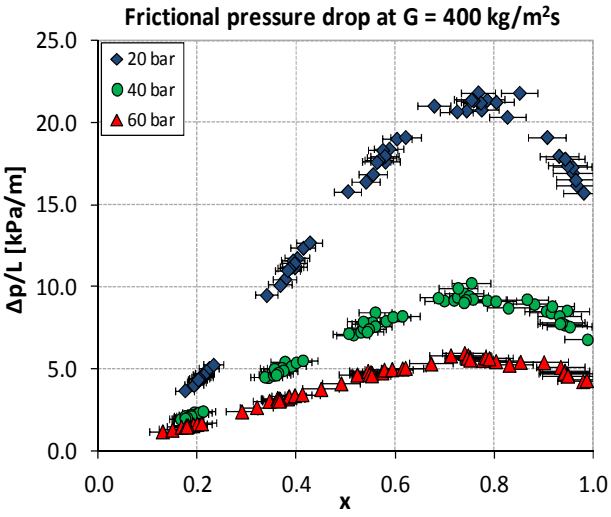

Figure 5.2 Frictional pressure drops per unit length at 400 kg/m^{2}s as a function of thermodynamic quality.

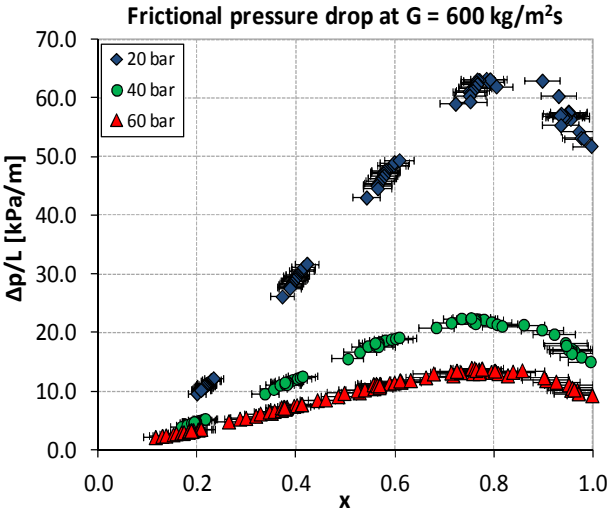

Figure 5.3 Frictional pressure drops per unit length at 600 kg/m^{2}s as a function of thermodynamic quality.

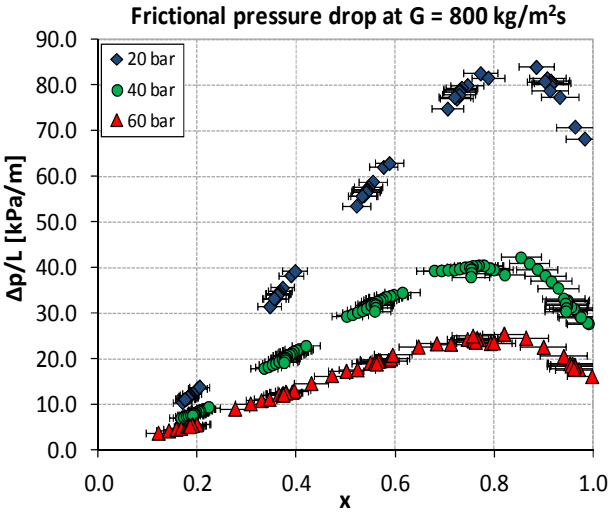

Figure 5.4 Frictional pressure drops per unit length at 800 kg/m^{2}s as a function of thermodynamic quality.

A linear error analysis (Moffatt, 1988) resulted in an average uncertainty on the experimental values of frictional pressure drop of about 1%, with maximum uncertainties of about 10% for a small number of points at high pressure and low mass flux. The comments previously made in Section 2.3 discussing the adiabatic two-phase frictional pressure drop

experimental data can be confirmed. An increase in the pressure always decreases the pressure drop, as the density ratio is reduced. Moreover, the distinct peak of the pressure drop as a function of the flow quality is again observable, as the pressure drop exhibits a maximum for $0.7< x <0.8$ and then decreases to approach the single-phase (vapor) value.

5.3 Correlation of the experimental data with the Lockhart-Martinelli method

A first attempt was made to predict the frictional pressure drop with the well known correlation of Lockhart and Martinelli (1949). The two-phase frictional pressure drop can be related to the pressure drop of the liquid phase as flowing alone in the channel:

$$\left(\frac{\Delta p}{L}\right)_{tp} = \Phi_l^2 \left(\frac{\Delta p}{L}\right)_l \tag{5.7}$$

where Φ_l^2 is the only-liquid friction multiplier:

$$\Phi_l^2 = \frac{f_{tp}}{f_l}\frac{\rho_l}{\rho_m}\frac{1}{(1-x)^2} \tag{5.8}$$

The friction multiplier for the liquid phase can be correlated to the Martinelli parameter χ, i.e. the ratio of the single-phase liquid pressure drop to the single-phase vapor pressure drop:

$$\chi^2 = \frac{\left(\frac{\Delta p}{L}\right)_l}{\left(\frac{\Delta p}{L}\right)_v} = \left[\frac{(1-x)}{x}\right]^{1.8}\frac{\rho_v}{\rho_l}\left(\frac{\mu_l}{\mu_v}\right)^{0.2} \tag{5.9}$$

in the form:

$$\Phi_l^2 = 1 + \frac{C}{\chi} + \frac{1}{\chi^2} \tag{5.10}$$

A value of C equal to 20 is chosen, as proposed in the work of Lockhart and Martinelli for a turbulent flow of both the liquid and the vapor phases. To determine the two-phase frictional pressure drop with Eq.(5.7), is then necessary to calculate the pressure drop due to the liquid phase as flowing alone in the channel:

$$\left(\frac{\Delta p_{fr}}{L}\right)_l = \frac{f_D}{2}\frac{G^2}{\rho_l d} \tag{5.11}$$

In Section 3.2, the Ito correlation (Ito, 1959) has been found to be the most accurate for the determination of the Darcy friction coefficient. As almost all the data points belong to the turbulent regime, the correlation for the turbulent flow is used:

$$f_D = 0.304Re^{-0.25} + 0.029(d/D)^{0.5} \tag{5.12}$$

The Lockhart and Martinelli correlation returned an average error of about 35%, with nearly 70% of the data within ±40%, in agreement with the previously mentioned literature results. The comparison with the experimental data is shown in Figure 5.5, Figure 5.6, and Figure 5.7 for the three different values of the system pressure.

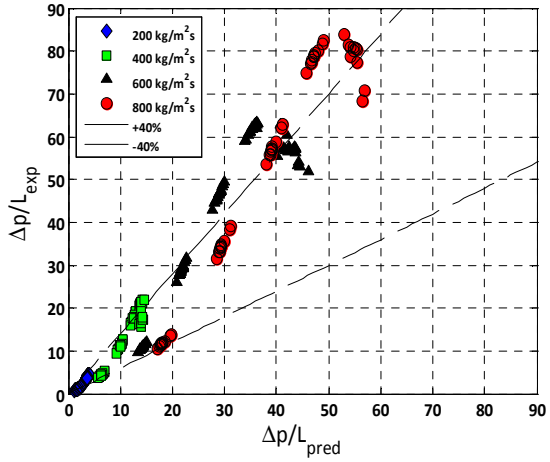

Figure 5.5 Comparison between experimental data and the Lockhart – Martinelli correlation (Eq.(5.10)) at 20 bar.

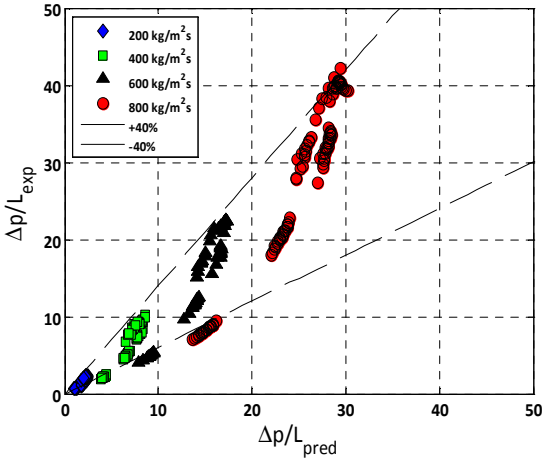

Figure 5.6 Comparison between experimental data and the Lockhart – Martinelli correlation (Eq.(5.10)) at 40 bar.

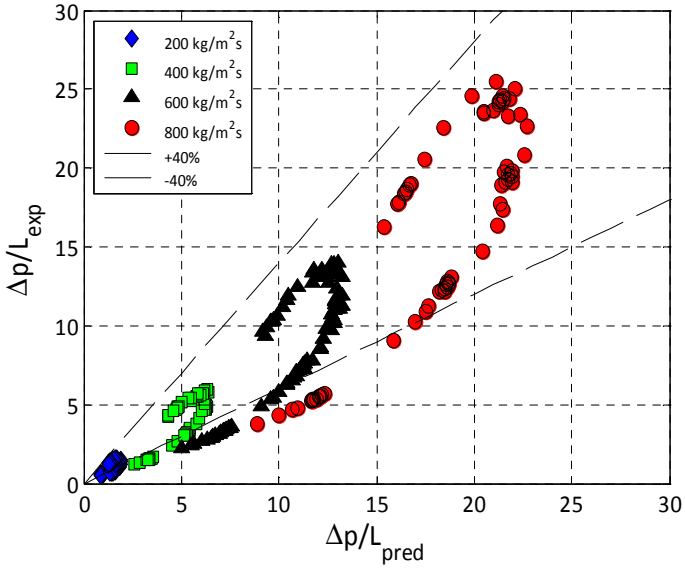

Figure 5.7 Comparison between experimental data and the Lockhart – Martinelli correlation (Eq.(5.10)) at 60 bar.

Although the data point are quite scattered, it can be stated that the Lockhart-Martinelli correlation tends to underestimate the pressure drop for the lower values of the system pressure, whereas it overestimates it at the higher pressure value. In addition to the effect of the system pressure, a dependence of the results on the mass flow rate, already observed by Lockhart and Martinelli, is clearly visible.

It is interesting to compare the values of the experimental friction multiplier as a function of the Martinelli parameter χ with the values returned by Eq.(5.10), as shown in Figure 5.8, Figure 5.9 and Figure 5.10. The experimental friction multiplier can be obtained from Eq.(5.8), introducing a two-phase friction factor calculated from the experimental data:

$$f_{tp} = \frac{2\left(\frac{\Delta p}{L}\right)_{exp} \rho_m d}{G^2} \tag{5.13}$$

The Lockhart-Martinelli correlation returns a lower value of the multiplier for low values of χ, that correspond to high flow qualities. The situation is reversed for χ close to unity, so for a low value of the quality, where the two-phase friction multiplier is always higher than the experimental data. Furthermore, the largest differences are found in the region where the Martinelli parameter is close to unity. These larger error is considered as the starting point to develop the modified correlation, presented in the following section.

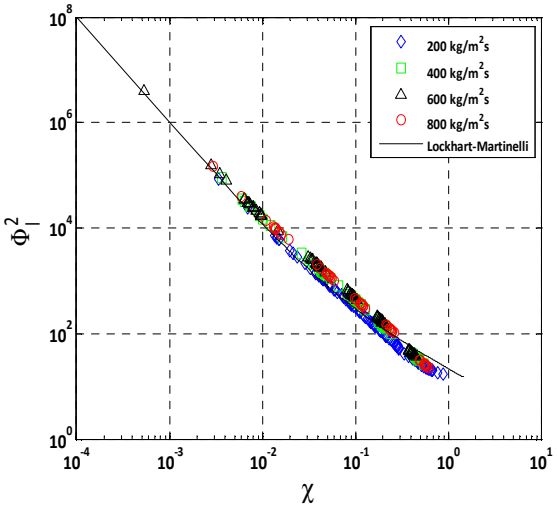

Figure 5.8 Comparison between experimental only-liquid friction multiplier and the Lockhart-Martinelli correlation (Eq.(5.10)) at 20 bar.

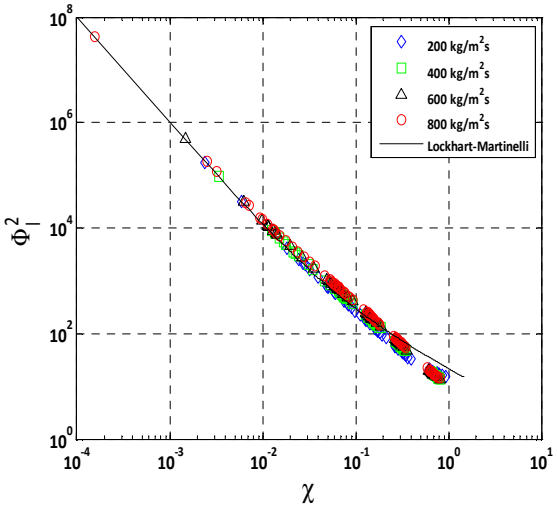

Figure 5.9 Comparison between experimental only-liquid friction multiplier and the Lockhart-Martinelli correlation (Eq.(5.10)) at 40 bar.

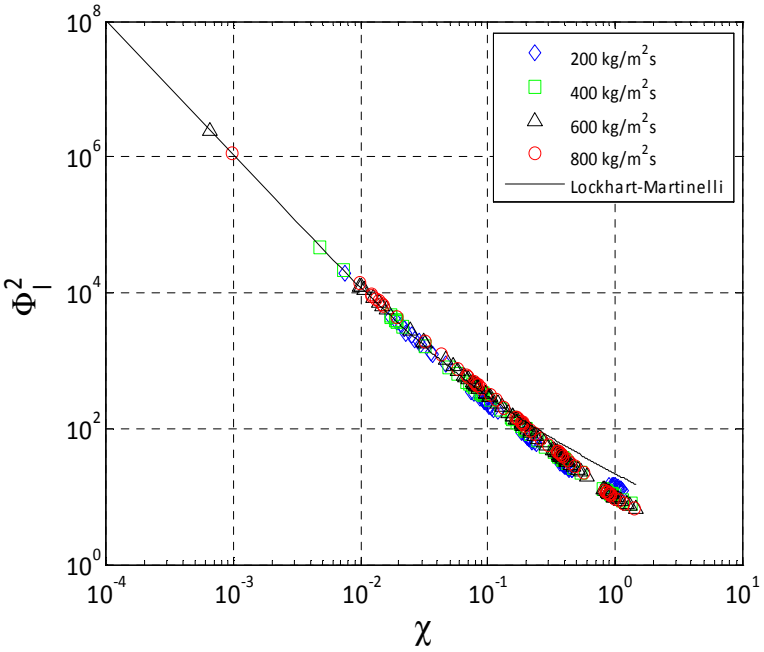

Figure 5.10 Comparison between experimental only-liquid friction multiplier and the Lockhart-Martinelli correlation (Eq.(5.10)) at 60 bar.

5.4 The new correlation

Since the Lockhart-Martinelli correlation was developed for the two-phase pressure drop in horizontal straight tubes, some modifications seemed necessary to attain a satisfactory accuracy also in the helical geometry. In particular, as in the majority of the correlations valid for the single-phase flow, the action of the centrifugal force can be taken into account by the Dean number, defined as:

$$De = Re\sqrt{\frac{d}{D}} \tag{5.14}$$

It can be expected that the centrifugal force, being proportional to the fluid density, affects mainly the liquid-phase, as long as the density ratio is higher than the slip ratio. Consequently, the liquid is drawn from the center to the wall of the tube, as confirmed by visual inspections (Lacey, 1967) and more recently by backlight imaging tomography (Murai et al., 2005). This seems also suggested by the higher deviation between the Lockhart-Martinelli multiplier and the experimental data at low values of the flow quality, found in the previous section. For this reason, the Dean number of the liquid-phase as flowing alone in the channel has been selected as the first corrective parameter:

$$De_l = Re_l\sqrt{\frac{d}{D}} = \frac{G(1-x)d}{\mu_l}\sqrt{\frac{d}{D}} \tag{5.15}$$

In addition, a value of C equal to 10 has been adopted in Eq.(5.10), as suggested by Chenoweth and Martin (1955) to correlate data at higher pressure with respect to the conditions considered by Lockhart and Martinelli. The modified expression of the two-phase friction multiplier was then determined with a regression through the least square method:

$$\Phi_l^2 = \left(1 + \frac{10}{\chi} + \frac{1}{\chi^2}\right)\left(1.46 - 2.07De_l^{-0.58}\right) = \Phi_{LM}^2\left(1.46 - 2.07De_l^{-0.58}\right) \tag{5.16}$$

With Eq.(5.16), the value of the two-phase multiplier is estimated with an average relative error reduced to about the 23%, with nearly 70% of the data within ±30%. Figure 5.11 shows the comparison between the experimental data and the predicted values of the frictional pressure drop. The error dependence on the mass flow rate is greatly reduced, although a significant effect due to pressure is found to remarkably affect the results. It is just mentioned that a comparable error is obtained starting from a single-phase friction factor correlation valid in straight tubes instead of the Ito correlation (Eq.(5.12)). Actually, referring to Eq.(5.7), it seems more important to account for the effect of the centrifugal force in the two-phase multiplier than in the single-phase frictional pressure drop.

To account for the effect of the system pressure, a density ratio has been included in the correlation as a second corrective parameter, as made by other authors in the study of different two-phase flow phenomena (Ishii and Zuber, 1970). In particular, the mixture to liquid density ratio was considered. The mixture density, calculated with Eq.(5.4), seems to be more appropriate than the vapor density, because differences between results at different pressures show also a dependence on the mixture quality. Indeed, Figure 5.12 reports the ratio between the experimental values of the liquid-phase friction multiplier and the estimations obtained with Eq.(5.16) as a function of the only-liquid Dean number. (Eq.5.15)). The effect of the pressure is higher for the intermediate values of the Dean number ($1500 < De_l < 6000$), i.e. for intermediate values of the mixture quality.

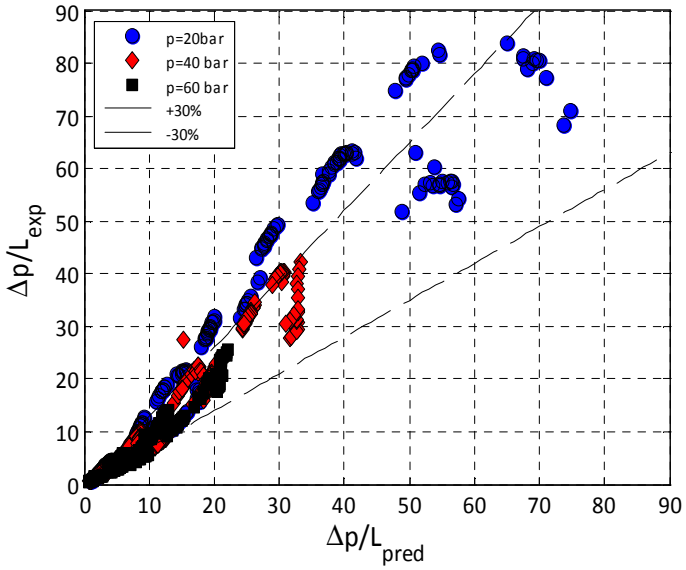

Figure 5.11 Comparison between experimental data and Eq.(5.16).

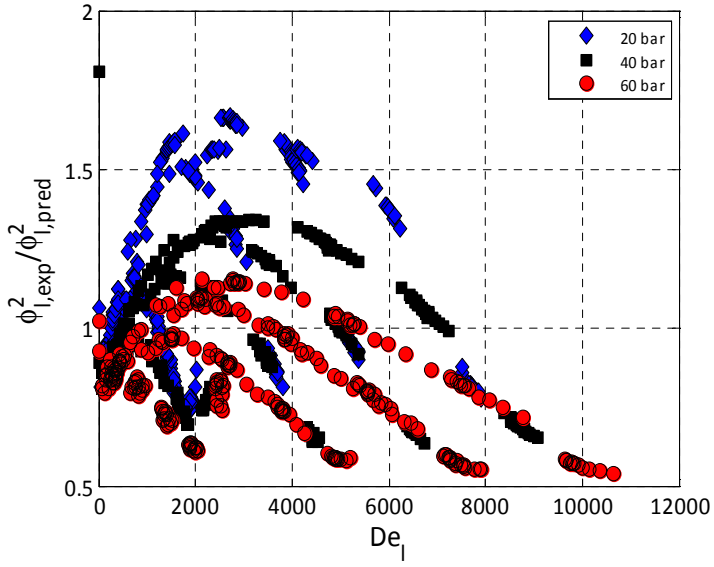

Figure 5.12 Comparison between experimental only-liquid friction multiplier and Eq.(5.16) as a function of the Dean number.

The final form of the correlation reads:

$$\Phi_l^2 = \Phi_{LM}^2 a_1 De_l^{a_2} \left(\frac{\rho_m}{\rho_l}\right)^{a_3} \tag{5.17}$$

The values of the three empirical coefficients a_1,a_2 and a_3 were determined thanks to a multivariable regression through the least square method:

$$\frac{\partial}{\partial a_k} \sum_i \left[\Phi_{exp,i}^2 - \Phi_{LM,i}^2 a_1 De_{l,i}^{a_2} \left(\frac{\rho_{m,i}}{\rho_{l,i}}\right)^{a_3} \right]^2 = 0 \tag{5.18}$$

Resolution of Eq.(5.18) for the three empirical coefficients allowed to define the final form of the new correlation for the two-phase friction multiplier:

$$\Phi_l^2 = 0.13 \Phi_{LM}^2 De_l^{0.15} \left(\frac{\rho_m}{\rho_l}\right)^{-0.37} \tag{5.19}$$

Eq.(5.19) predicts the two-phase frictional pressure data with an average relative error of 11.5%, with more than 75% of the data within ±15% and 88% of the data within ±20%. Comparison between the experimental data and Eq.(5.19) is shown in Figure 5.13, Figure 5.14 and Figure 5.15 for the three system pressures. It is worth noting that the introduction of the density ratio into the correlation effectively allows to better account for the effect of the pressure.

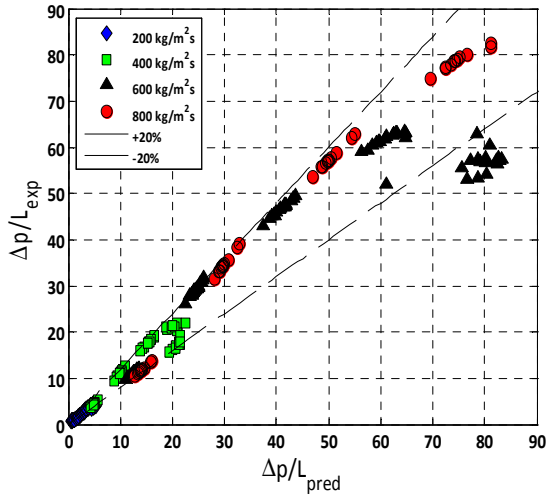

Figure 5.13 Comparison between experimental data and Eq.(5.19) at 20 bar.

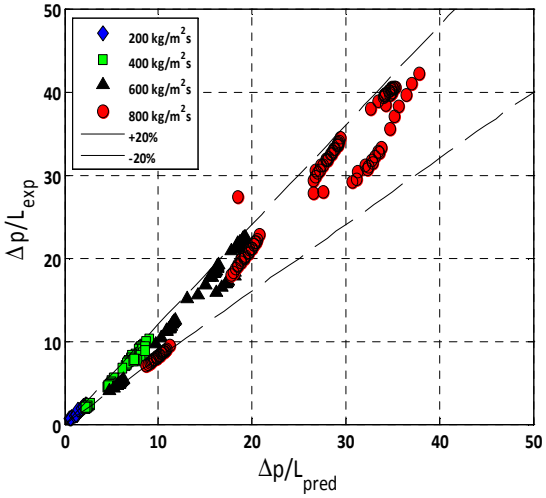

Figure 5.14 Comparison between experimental data and Eq.(5.19) at 40 bar.

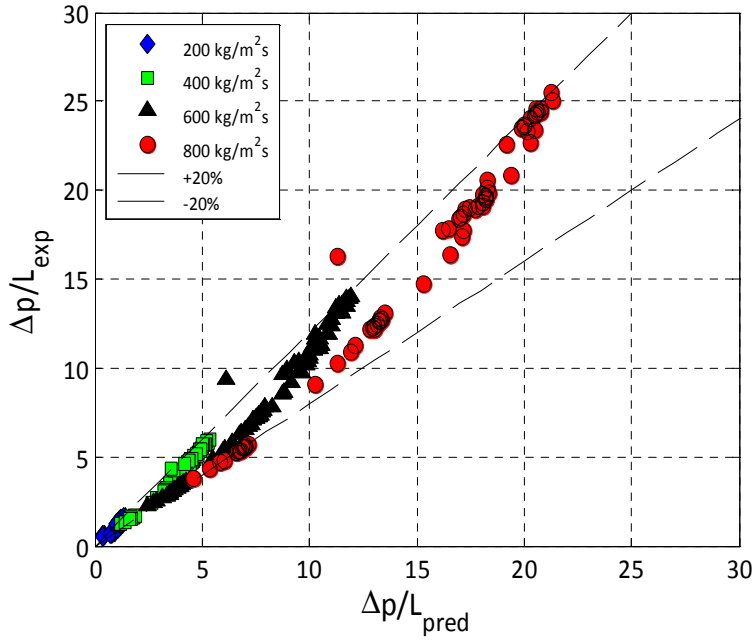

Figure 5.15 Comparison between experimental data and Eq.(5.19) at 60 bar.

To obtain a further validation of the procedure adopted to develop Eq.(5.19), it has been applied also to the Friedel correlation. This correlation was developed for the two-phase flow in straight pipes and it includes the Weber number, to account for interfacial effects, the Froude number, to account for gravity and other empirical coefficients to best fit the data. In addition, differently from the Lockhart-Martinelli model, in the Friedel correlation the liquid phase is considered as flowing at the same mass flux of the two-phase mixture:

$$\Phi_{lo}^2 = A_1 \frac{3.24 A_2 A_3}{Fr^{0.045} We^{0.035}} \tag{5.20}$$

$$A_1 = (1-x)^2 + x^2\left(\frac{\rho_l f_{vo}}{\rho_v f_{lo}}\right) \tag{5.21}$$

$$A_2 = x^{0.78}(1-x)^{0.224} \tag{5.22}$$

$$A_3 = \left(\frac{\rho_l}{\rho_v}\right)^{0.91}\left(\frac{\mu_v}{\mu_l}\right)^{0.19}\left(1-\frac{\mu_v}{\mu_l}\right)^{0.7} \tag{5.23}$$

Application of Eq.(5.20) without any modification resulted in an average relative error of about 29%, with a general underestimation of the frictional pressure drop (Figure 5.16). As in the case of the Lockhart-Martinelli correlation, the inclusion of both the Dean number and the mixture to liquid density ratio determines a remarkable improvement of the correlation accuracy. The modified form of Friedel correlation reads:

$$\Phi_{lo}^2 = 0.12\Phi_{FR}^2 De_l^{0.21}\left(\frac{\rho_m}{\rho_l}\right)^{-0.26} \tag{5.24}$$

Eq.(5.24) predicts the experimental data with an average relative error of about 12.5%, slightly higher than the modified Lockhart-Martinelli correlation (Eq.(5.19)). In this case, 83% of the experimental data are predicted within ±20%, as shown in Figure 5.17.

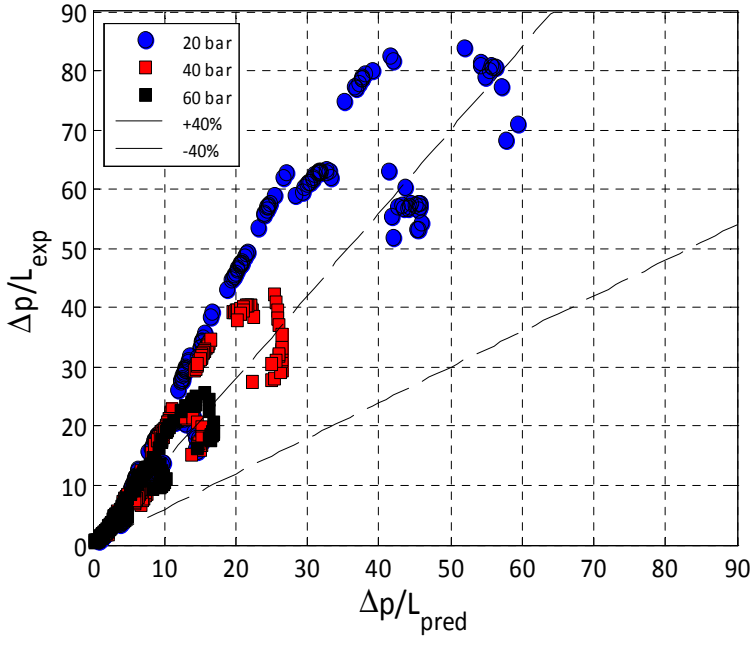

Figure 5.16 Comparison between the experimental data and the Friedel correlation, Eq.(5.20).

The accuracy of the correlation results again almost independent from the single-phase friction factor, as an average relative error is 12.8% using the Ito correlation instead of a formula valid in straight pipes. In summary, starting from two different correlations developed for straight tubes, the introduction of the same corrective parameters allows in both cases to reach a satisfactory and comparable evaluation of the frictional pressure drop in the

helical pipe. Moreover, the use of the modified Lockhart-Martinelli correlation leads to a better accuracy and takes the advantage of a simpler formulation.

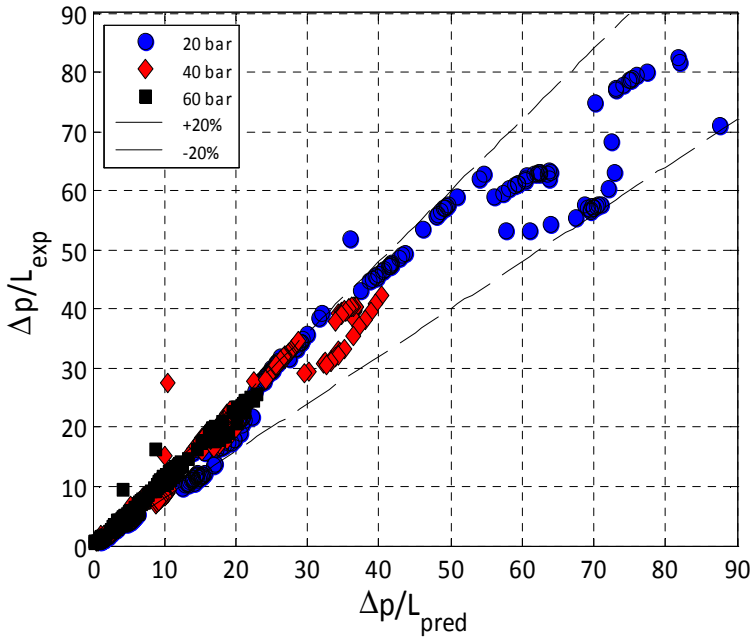

Figure 5.17 Comparison between the experimental data and the Friedel correlation, Eq.(5.24).

5.5 Comparison with literature

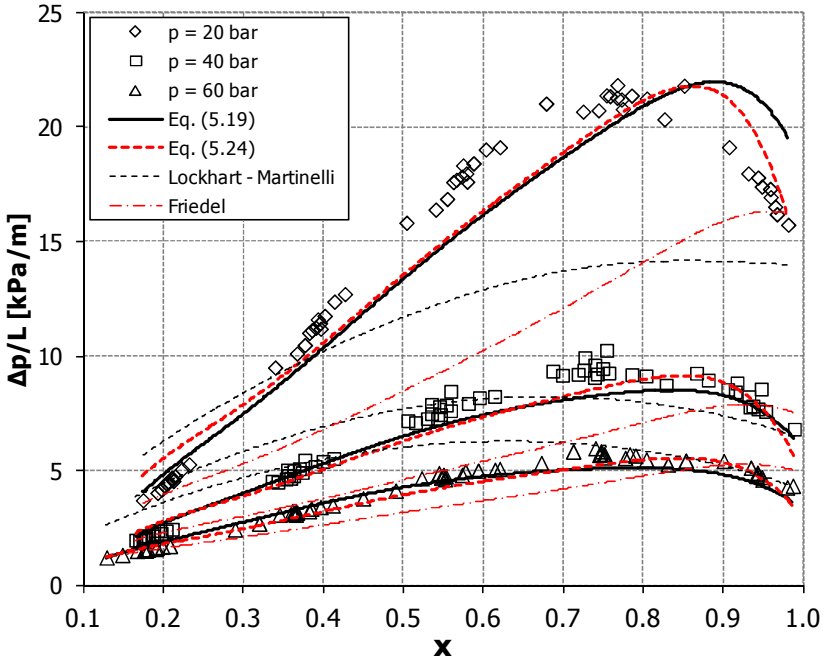

Figure 5.18 Frictional pressure drops per unit length at 400 kg/m^{2}s calculated with Eq.(5.19), Eq. (5.24), the Lockhart-Martinelli correlation (Eq.(5.10)) and the Friedel correlation (Eq.(5.20)). The correlations are compared with the experimental data at 20, 40 and 60 bar.

In this section, the new correlations developed are compared with other correlations available in literature. First of all, in Figure 5.18 the frictional pressure drop per unit length calculated with Eq.(5.19) and Eq.(5.24) is plotted together with the correlations of Lockhart-Martinelli and Friedel. The experimental data at G = 400 kg/m^{2}s and p = 20, 40, 60 bar are included for comparison. Eq.(5.19), developed from the original Lockhart and Martinelli correlation, properly reproduces the experimental data for all the three pressure levels considered, while Eq.(5.24) provides worse results in these conditions, although they can be considered anyway satisfactory.

A remarkable improvement is obtained with respect to the original correlations, which are unable to predict the behavior of the frictional pressure drop in the helical tube, being developed for the straight geometry. In particular, the Friedel correlation always underestimates the pressure drop, while the Lockhart-Martinelli correlation overestimates the pressure drop at low quality and underestimates it at high quality. Most important, both the new correlations are able to reproduce the right position of the peak in the pressure drop versus quality curve, differently from the original Lockhart-Martinelli and Friedel correlations.

Finally, the results from Eq.(5.19) and Eq.(5.24) are compared to some of the most representative correlations available in literature. The correlations of Santini et al. (2008), Ruffel (1974), Awwad et al. (1995), Xin et al. (1996), Guo et al. (2001) and Zhao et al. (2003) are considered. Table 5.2 reports the average deviations from the experimental data for all the correlations, while Figure 5.19, Figure 5.20 and Figure 5.21 show the comparison at 400 kg/m^{2}s and all the system pressures considered in the experiments. Apart from the Santini et al. correlation, which as pointed out in the introduction arises from a best-fit of the experimental data, the other correlations return significant errors, some of them even higher than those obtained with Lockhart-Martinelli and Friedel correlations.

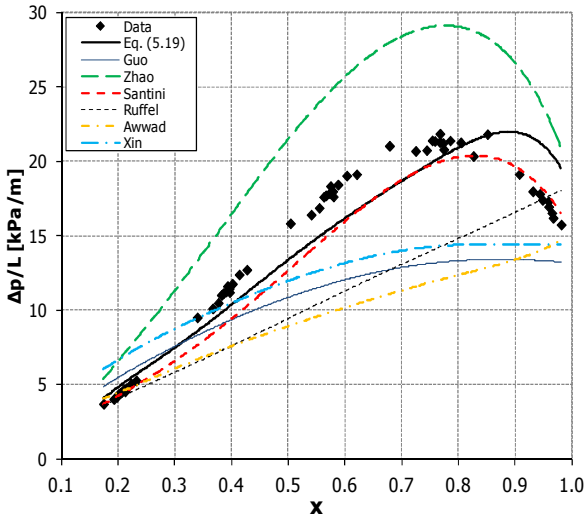

Figure 5.19 Comparison between the different correlations and the experimental data at 20 bar and 400 kg/m^{2}s.

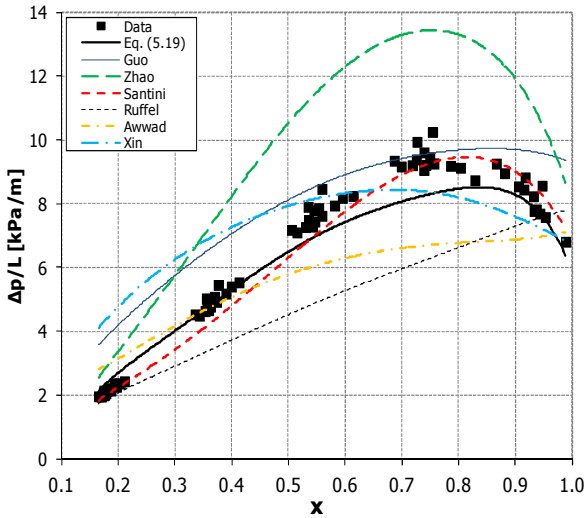

Figure 5.20 Comparison between the different correlations and the experimental data at 40 bar and 400 kg/m^{2}s.

Table 5.2 Average relative errors between the compared correlations and the experimental data.

Correlation	Average Error [%]	Correlation	Average Error [%]
Eq.(5.19)	11.6	Ruffel	23.5
Eq.(5.24)	12.6	Awwad	27.5
Friedel	29.1	Xin	39.6
Lockhart – Martinelli	35.7	Guo	54.4
Santini	8.4	Zhao	47.8

Best predictions are given by the Ruffel and the Awwad et al. correlations, the latter developed for horizontal helically coiled pipes. However, both the correlations are unable to reproduce the peak in the pressure drop versus quality curve. The existence of the maximum value of the pressure drop is predicted by the Zhao et al. correlation. In addition, also the correlation by Xin et al. reproduces the peak, although it generally overestimates the pressure drop.

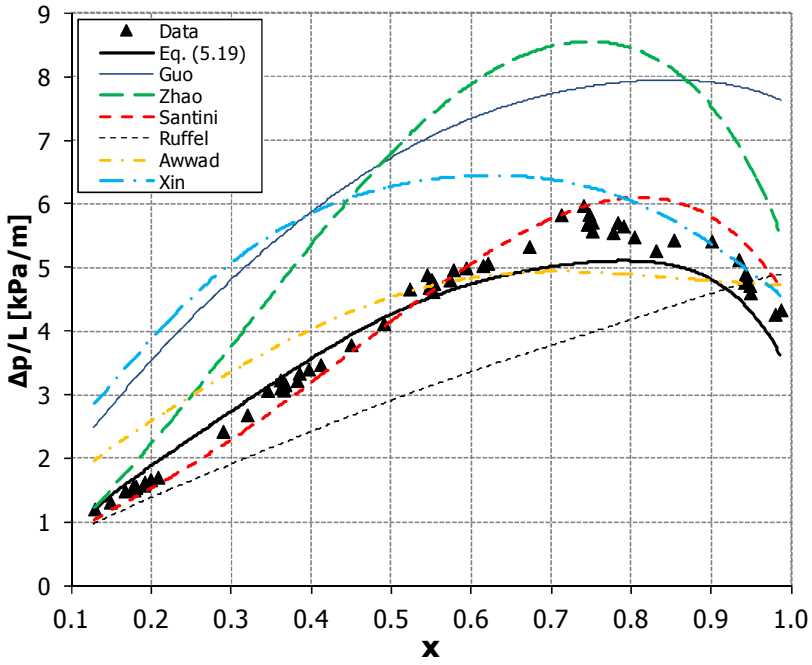

Figure 5.21 Comparison between the different correlations and the experimental data at 40 bar and 600 kg/m^{2}s.

5.6 Enlargement of the database

The results justify the use of the corrective parameters included in the new correlation. They seem appropriate to reproduce the influence of system parameters such as the pressure and the mass flow rate as well as the effect of the coil curvature, peculiar of the helical geometry. In further support, almost the same errors are obtained applying the corrective parameters to two different correlations, the Lockhart-Martinelli and the Friedel correlations. Despite the positive results, an additional verification is however necessary for the effect of

the coil curvature, as the starting data bank contains measurements relative to only one coil diameter. Therefore new data available in literature and measured in a different coil were included into the database, aiming at a further improvement of the correlation.

Additional data were taken from the work of Zhao et al. (2003), measured in an horizontal helically coiled tube with a coil diameter D = 0.292 m and a tube diameter d = 0.9 cm. 190 experimental points were considered, in the ranges 7.5 bar < p < 30 bar for the pressure and 400 kg/m^{2}s < G < 900 kg/m^{2}s for the mass flux. Looking at Table 5.1, it is interesting to note that the experimental conditions are closer to the ranges of validity of the other correlations, generally limited to smaller diameter coils with respect to the SIET facility. In addition, not so many works include measurements at high pressure, numerous being related to an air-water two-phase flow at atmospheric pressure.

The results from all the correlations considered in the previous section are summarized in Table 5.3. Except for the correlation developed by the author, that obviously shows the better accuracy, the new correlation (Eq.(5.19)) returns the lowest average relative error, equal to 25.3%, with all the other correlations over the 30%. In particular, the correlation of Santini et al., developed without trying to account for the effect of the coil curvature, shows the highest errors (46% on average). It is just mentioned that, being the experimental values of the two-phase multiplier available from the work of Zhao et al., the values of the multiplier are considered for the comparison. For the correlation of Santini et al., however, the frictional pressure drop is compared, since the correlation does not include the multiplier. Nevertheless, only a negligible difference of few percents could be expected. Although the differences from the other correlations are not really high, the result confirms again the effectiveness of the corrective parameters, in particular for the effect of the coil curvature, which is considerably lower in the new data, as mentioned before.

Table 5.3 Average errors between the compared correlations and the experimental data of Zhao et al. (2003).

Correlation	**Average Error [%]**	**Correlation**	**Average Error [%]**
Eq.(5.19)	25.3	Ruffel	34.7
Lockhart – Martinelli	32.3	Awwad	39.7
Santini	46.0	Xin	32.3
Zhao	12.8	Guo	31.8

5.7 Improvement of the correlation

Following the positive results obtained testing the new correlation in quite different conditions with respect to the database used for its development, the new data were included in the least square regression procedure. A new improved form of the correlation was derived:

$$\Phi_l^2 = 0.0986\Phi_{LM}^2 0.13 De_l^{0.19} \left(\frac{\rho_m}{\rho_l}\right)^{-0.40} \tag{5.25}$$

Considering the whole dataset, the correlation predict the frictional pressure drop with a satisfactory 14.42 % average relative error. For the Santini database, the accuracy is slightly worsened, as the error increases to 12.14 %, starting from the 11.6 % of Eq.(5.19). Focusing only on the new data (Zhao et al.), Figure 5.22 and Figure 5.23 show a comparison with the other correlations considered. The two-phase multiplier is estimated with a relative error that is the 17.4 % on average, far better than all the other correlations tested in the previous section, except for the one derived by the authors. It must be pointed out, however, that the correlation developed by Zhao et al. returns an unsatisfactory 47.8 % when applied to the Santini database. Finally, when adopted in a wide range of geometries and operating conditions, Eq.(5.25) shows a big improvement with respect to the Santini et al. correlation, originally developed from the database built at SIET laboratories.

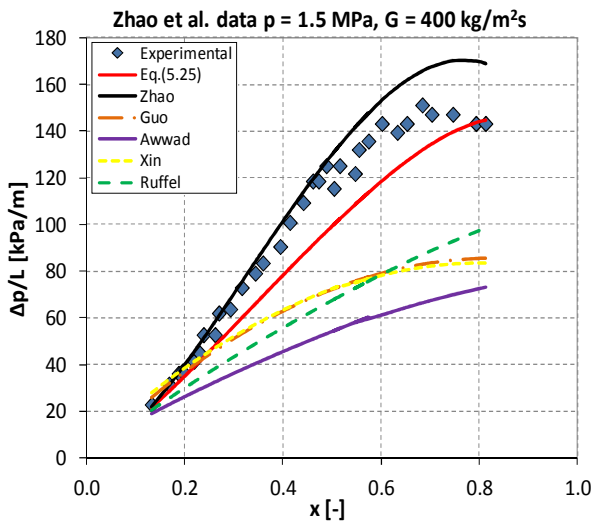

Figure 5.22 Comparison between Zhao et al (2003) experimental data (p = 15 bar, G = 400 kg/m^{2}s), Eq.(5.25) and the other correlations available in literature.

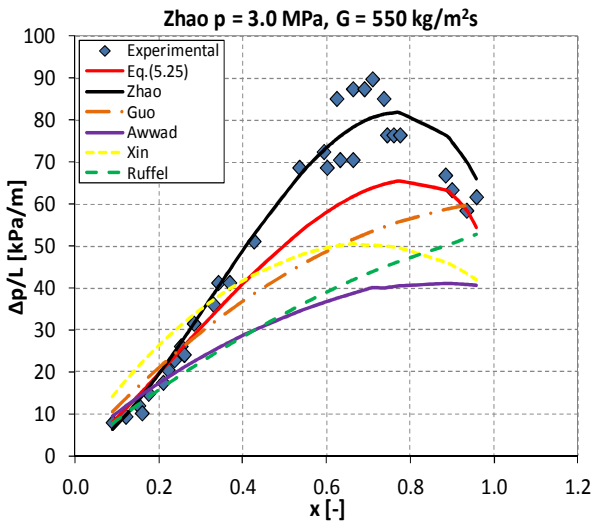

Figure 5.23 Comparison between Zhao et al (2003) experimental data (p = 30 bar, G = 550 kg/m^{2}s), Eq.5.25) and the other correlations available in literature.

5.8 Conclusions

In this chapter a new correlation for the prediction of the two-phase frictional pressure drop in helically coiled tubes has been developed. Numerous correlations are available in literature, although for the additional complexity introduced by the presence of the two-phase mixture, none of them can be considered of general validity, neither applied to a wide range of geometrical parameters and operating conditions.

The new correlation is based on the model of Lockhart and Martinelli, which was reported by different authors to reach a satisfactory agreement also for helical tubes. Starting from an existing database (Santini et al., 2008), proper modifications have been introduced to account for the physics of the phenomenon, in the effort to obtain a general form suitable for a greater range of geometrical parameters and operating conditions, while keeping as low as possible the number of empirical constants. The effect of the coil curvature has been

introduced with the Dean number of the liquid phase as flowing alone in the channel, as the centrifugal force is expected to affect mainly the liquid phase. In addition, the mixture to liquid density ratio accounts for the effect of the system pressure. The correlation returns an average deviation of about 11.5%, with more than 75% of the data between ±15% and 88% of the data within ±20%. For verification purposes, the same parameters have been applied to the Friedel correlation. The results confirm the validity of the corrective parameters, as the modified Friedel correlation shows an average deviation of about 12.5%, with 83% of the data within ±20%. A comparison made with numerous other correlations available in literature revealed slightly better results only from the correlation of Santini (Santini et al., 2008), being developed from the same dataset. All the others showed average errors greater than 23.5%.

The analysis was then extended to the experimental work of Zhao et al. (2003), made in a quite different geometry and operating conditions. The new correlation resulted again the most accurate, except for the correlation developed by the authors. On the contrary, the Santini correlation showed very large errors (~ 46 % on average). In the same way, the correlation of Zhao et al. resulted really inaccurate when applied to the SIET database (~ 48 % error on average).

The new correlation, after a final improvement, predicted the frictional pressure drop of the whole database with an average error of 14.4 %, outperforming all the other tested correlations. Considering only the data of Zhao et al., it showed an average deviation of 17.4 %, with all the other correlations over the 30 %. Therefore, it demonstrated to be reliable in a wider range of geometries and operating conditions, satisfying the initial objective of the study.

References

B.K. Akagawa, T. Sakaguchi, M. Ueda, 1971. Study on a gas-liquid two-phase flow in helically coiled tubes. Bulletin of the Japan Society of Mechanical Engineers 14(72), 564-571.

A. Awwad, R.C. Xin, Z.F. Dong, M.A. Ebadian, H.M. Soliman, 1995. Measurement and correlation of the pressure drop in air-water two-phase flow in horizontal helicoidal pipes. International Journal of Multiphase Flow 21(4), 607-619.

S. Banerjee, E. Rhodes, D.S. Scott, 1969. Studies on concurrent gas-liquid flow in helically coiled tubes. I. Flow patterns, pressure drop and holdup. The Canadian Journal of Chemical Engineering 47, 445-453.

C.J. Baroczy, 1965. A systematic correlation for two-phase pressure drop. 8th National Heat Transfer Conference, Los Angeles.

M.D. Carelli, L.E. Conway, L. Oriani, B. Petrovic, C.V. Lombardi, M.E. Ricotti, A.C.O. Barroso, J.M. Collado, L. Cinotti, N.E. Todreas, D. Grgic, M.M. Moraes, R.D. Boroughs, H. Ninokata, D.T. Ingersoll, F. Oriolo, 2004. The design and safety features of the IRIS reactor, Nuclear Engineering and Design 230(1), 151-167.

X.J. Chen, F.D. Zhou, 1981. An investigation of flow pattern and frictional pressure drop characteristics of air-water two-phase flow in helical coils. Proceedings of the fourth Miami International Conference on Alternate Energy Sources, Miami, FL, 120-129.

J.M. Chenoweth, M.W. Martin, 1955. Turbulent two-phase flow. Petroleum Refiner 34(10), 151-155.

D. Chisholm, L.A. Sutherland, 1969. Prediction of pressure gradients in pipeline systems during two-phase flow. Symposium of Fluid Mechanics and Measurements in Two-Phase Flow Systems, University of Leeds.

V. Czop, D. Barbier, S. Dong, 1994. Pressure drop, void fraction and shear stress measurements in an adiabatic two-phase flow in a coiled tube. Nuclear Engineering and Design 149, 323-333.

A.E. Dukler, M. Wicks III, R.G. Cleveland, 1964. Frictional pressure drop in two-phase flow: B. An approach through similarity analysis. American Institute of Chemical Engineers Journal 10(1), 44-51.

L. Friedel, 1979. Improved friction pressure drop correlations for horizontal and vertical two-phase pipe flow. European Two-Phase Flow Group Meeting, Ispra, Italy, June 1979, Paper E2.

L. Guo, Z. Feng, X. Chen, 2001. An experimental investigation of the frictional pressure drop of steam-water two-phase flow in helical coils. International Journal of Heat and Mass Transfer 44, 2601-2610.

M. Ishii, N. Zuber, 1970. Thermally induced flow instabilities in two-phase mixture. Proceedings of the 4th International Heat Transfer Conference, Paris, France.

H. Ito, 1959. Friction factors for turbulent flow in curved pipes. Transactions of the ASME D, Journal of Basic Engineering 81, 123-124.

J. Katsuri, J.B. Stepanek, 1972. Two-phase flow – I. Pressure drop and void fraction measurements in concurrent gas-liquid flow in a coil. Chemical Engineering Science 27, 1871-1880.

M. Kozeki, H. Nariai, T. Furukawa, K. Kurosu, 1970. A study of helically coiled tube once-through steam generator. Bulletin of the Japan Society of Mechanical Engineers 13(66), 1485-1494.

P.M.C. Lacey, 1967. Regimes of deteriorated heat transfer at forced flow of fluids in curvilinear channels. Proceedings of the Third International Heat Transfer Conference, American Institute of Chemical Engineers, New York, NY, Vol.6, 137-139.

R.W Lockhart, R.C. Martinelli, 1949. Proposed correlation of data for isothermal two-phase two-component flow in pipes. Chemical Progress 45(39).

S.N. Mandal, S.K. Das, 2003. Gas-liquid flow through helical coils in vertical orientation. Industrial & Engineering Chemistry Research 42(14), 3487-3494.

R.C. Martinelli, D.B. Nelson, 1948. Prediction of pressure drop during forced circulation boiling of water. Transaction of the American Society of Mechanical Engineering 70(695).

R.J. Moffat, 1988. Describing the uncertainties in experimental results. Experimental Thermal and Fluid Science 1(1), 3-17.

Y. Murai, H. Oiwa, T. Sasaki, K. Kondou, S. Yoshikawa, F. Yamamoto, 2005. Backlight imaging tomography for gas-liquid two-phase flow in a helically coiled tube. Measurement Science and Technology 16, 1459-1468.

H. Nariai, M. Kobayashi, T. Matsuoka, 1982. Friction pressure drop and heat transfer coefficient of two-phase flow in helically coiled tube once-through steam generator for

integrated type marine water reactor. Journal of Nuclear Science and Technology 19(11), 936-947.

A. Owhadi, K.J. Bell, B. Crain Jr, 1968. Forced Convection Boiling Inside Helically-Coiled Tubes. International Journal of Heat and Mass Transfer 11, 1779-1793.

G.R. Rippel, C.M. Eidt Jr, H.B. Jordan Jr, 1966. Two-phase flow in a coiled tube. Pressure drop, holdup and liquid phase axial mixing. Industrial & Engineering Chemistry Process Design and Development 5(1), 32-39.

A.E. Ruffel, 1974. The application of heat transfer and pressure drop data to the design of helical coil once-through boilers. Institution of Chemical Engineers Symposium Series 38, Paper 15.

L. Santini, 2008. Thermalhydraulic issues of IRIS nuclear reactor helically coiled steam generator and emergency heat removal system. Ph.D. Thesis, XX Cycle, Politecnico di Milano, Milano, Italy.

L. Santini, A. Cioncolini, C. Lombardi, M. Ricotti, 2008. Two-phase pressure drops in a helically coiled steam generator, International Journal of Heat and Mass Transfer 51, 4926-4939.

J.R.S. Thom, 1964. Prediction of pressure drop during forced circulation boiling of water. International Journal of Heat and Mass Transfer 7.

H.C. Unal, M.L. van Gasselt, P.M. van't Veerlat, 1981. Dryout and two-phase pressure drop in sodium heated helically coiled steam generator tubes at elevated pressures. International Journal of Heat and Mass Transfer 24, 285-298.

R.C. Xin, A. Awwad, Z.F. Dong, M.A. Ebadian, H.M. Soliman, 1996. An investigation and comparative study of the pressure drop in air-water two-phase flow in vertical helicoidal pipes. International Journal of Heat and Mass Transfer 39(4), 735-743.

R.C. Xin, A. Awwad, Z.F. Dong, M.A. Ebadian, 1997. An experimental study of single-phase and two-phase flow pressure drop in annular helicoidal pipes. International Journal of Heat and Fluid Flow 18(5), 482-488.

L. Zhao, L. Guo, B. Bai, Y. Hou, X. Zhang, 2003. Convective boiling heat transfer and two-phase flow characteristics inside a small horizontal helically coiled tubing once through steam generator. International Journal of Heat and Mass Transfer 46, 4779-4788.

CHAPTER 6

DENSITY WAVE OSCILLATIONS IN PARALLEL CHANNELS

The last chapter of the thesis work is dedicated to the analysis of the DWO instability in parallel helically coiled channels. Introduced in Chapter 2 during the presentation of the experimental campaigns, the physical phenomena at the origin of the DWOs have been explained in details. DWOs were described as a dynamic two-phase flow instability, characterized by self-sustained oscillations of the mass flow rate, under the condition of constant pressure drop boundary condition (commonly provided by two or more parallel channels). When two parallel channels are included in the system, as in the SIET experimental facility, the mass flow rate in the two channels oscillates in counter phase, being constant its total value.

DWOs are commonly encountered in all the parallel channel systems characterized by the presence of a two-phase flow, as the SG or the BWR core in nuclear power plants. Since they are very difficult to be detected immediately as the total mass flow rate in the system remains stable, DWOs represent a serious issue for all the steam power systems, as they can significantly alter the normal operating conditions. As a consequence, the availability of proper simulation tools for a correct estimation of the system instability thresholds become of fundamental importance.

In the chapter, the overall analysis method applied during the whole thesis work is even reinforced. The DWOs are first addressed with an analytical dynamic model, the predictions of which are evaluated with a comparison against the experimental data. Furthermore, also a numerical study is proposed, as the same experimental data are used for the assessment of the RELAP5 system code.

The analytical formulation considers as a starting point a model previously developed by Papini (2011). It is a lumped parameter, moving boundary, dynamic model, including 9 non linear Ordinary Differential Equations (ODEs), solved through the SIMULINK platform of the MATLAB software (The Math Works, Inc., 2005). The model, based on the homogeneous flow assumption, allowed a characterization of the DWO instability, with identification of the crucial parameters and a reasonably preliminary prediction of the SIET experimental data. In this chapter, the model is upgraded utilizing the drift-flux formulation. The empirical correlations developed throughout the thesis work are included, for a more accurate simulation of the helical tube experimental facility. The improvement in the model results is evaluated through comparison with the experimental data.

The second part of the chapter is focused on a numerical analysis of the DWOs through the RELAP5 system code. The RELAP5 best-estimate system code is a six equations code,

based on the non equilibrium model for the two-phase flow. It was designed for the analysis of operational transients and postulated accidents in LWRs, including LOCAs. Since the RELAP5 code is extensively used in the nuclear field for the safety analysis of nuclear reactors, an assessment of the code capability to simulate DWOs is of fundamental interest. Using the RELAP5/MOD3.3 version (US NRC, 2001), the assessment starts from the simple case of a single vertical channel. The layout is gradually complicated to finally address the case of two parallel helically coiled pipes. For the latter, the accuracy of the code is verified through a comparison with the SIET experimental data and a significant code drawback is identified.

6.1 Previous work

DWOs have been extensively studied in the past, being recognized as the most common type of instability encountered in boiling systems. Between the numerous literature reviews, remarkable are the works of Bouré et al. (1973), Yadigaroglu (1981) and Kakaç and Bon (2008). Despite the large number of studies made on the subject, almost no work is available on the DWO in helical pipe, except for some researches made by Unal (1982; 1985). Consequently, an extensive study was started in recent years by the Nuclear Engineering Division, inside the Department of Energy of the Politecnico di Milano (Papini et al., 2011). It constitutes the main subject of a recent doctoral thesis (Papini, 2011), which provides all the details on the development of the research work and the results achieved.

Among the many interesting subjects, of particular interest is an analytical model developed for the simulation of the system dynamic behaviour and the prediction of the instability threshold. The dynamic model is used in this chapter as a starting point and some modifications are introduced to improve its agreement with the experimental data. The analytical model is a non linear, lumped parameter, 0-D dynamic model, based on the space integration of the conservation equations. This type of modeling has been commonly used to study the stability and the dynamic behavior of various systems (Munoz-Cobo et al., 2002; Schlichting et al., 2010). The boiling channel is divided into two regions, the single-phase region and the two-phase region, divided by the boiling boundary, following the so-called moving boundary modeling approach (Han and Stanley, 1999; Li et al., 2008). Differential conservation equations of mass and energy are considered separately for each region, whereas the momentum equation is integrated along the whole channel. The wall dynamics is accounted for in the two distinctive regions, following the lumped wall temperature dynamics, by means of the respective heat transfer balances. The two-phase flow is described with the homogeneous equilibrium model, that is same velocity and same temperature (always equal to the saturation) shared by the two-phases. In addition, the system pressure is constant with time, so the liquid and vapour saturation properties in the two-phase region. The condition of parallel channel is obtained imposing the same, constant with time Δp boundary condition across the two channels.

After integration, the system of 9 non linear ODEs has been solved through the MATLAB software SIMULINK (The Math Works, Inc., 2005). The simulation of many transients, obtained through a step by step increase of the supplied thermal power, allowed the

estimation of the system stability boundary in different operating conditions. The model allowed also a complete characterization of the DWOs and was applied to numerous system configurations, starting from a straight single tube, to identify the critical parameters for a correct estimation of the instability thresholds. A detailed description of the model development can be found in Papini et al. (2012). In the following, the new analytical formulation, based on the drift-flux model, will be presented.

6.2 Model development

The modified model maintains almost all the features and hypothesis of the original version, described in the previous section. The significant difference is the upgrade to a description of the two-phase flow based on the drift-flux formulation, with respect to the simpler homogeneous equilibrium model. Since in the drift-flux model the relative motion between the phases is accounted for by a kinematic constitutive equation, also the conservation equation of the secondary phase is available in the two-phase region, making it a 4 equations model (Ishii and Hibiki, 2006). The model is derived directly on the helical geometry. The starting point are again the 1-D conservation equations, with a single momentum balance for the whole channel. Starting from a one dimensional representation, the channel is considered as an inclined straight channel with the same inclination angle of the helix. The coordinate *z* is directed along the axis of the pipe, which has a total length *L* equal to the total length of the helical coil. In the single-phase region, the mass and energy balance equations read (Todreas and Kazimi, 1993)[4]:

$$\frac{\partial \rho}{\partial t} + \frac{\partial G}{\partial z} = 0 \tag{6.1}$$

$$\frac{\partial \rho h}{\partial t} + \frac{\partial G h}{\partial z} = q'' \cdot \frac{P}{A} \tag{6.2}$$

For the two-phase region, the conservation equations are set in the following form, neglecting the pressure variation with time (Ishii and Hibiki, 2006). The mixture continuity equation:

$$\frac{\partial \rho_m}{\partial t} + \frac{\partial \rho_m v_m}{\partial z} = 0 \tag{6.3}$$

The secondary phase continuity equation:

$$\frac{\partial \alpha \rho_g}{\partial t} + \frac{\partial \alpha \rho_g v_m}{\partial z} = \Gamma_g - \frac{\partial}{\partial z}\left(\alpha \cdot \frac{\rho_l \rho_g}{\rho_m} \cdot V_{gj}^*\right) \tag{6.4}$$

[4] Differently from Section 4.3, all the parameters are an average value over the channel cross section, being included in 1-D conservation equations. As a consequence, to simplify the writing, the symbol < > has been omitted, as it is not necessary to distinguish between local and averaged values.

The mixture energy equation:

$$\frac{\partial \rho_m h_m}{\partial t} + \frac{\partial \rho_m v_m h_m}{\partial z} = q'' \cdot \frac{P}{A} - \frac{\partial}{\partial z}\left(\frac{\rho_l - \rho_g}{\rho_m} \cdot \frac{\rho_l \rho_g}{(\rho_l - \rho_g)} \cdot V_{gj}^* \cdot h_{lg}\right) \tag{6.5}$$

With respect to the homogeneous flow model, the continuity equation for the secondary phase is added (Eq.(6.4)). In addition, new terms accounting for the relative motion between the phases appear in the energy balance (Eq.(6.5)) and in the momentum balance, as it will be shown in the following. The density of the mixture is weighted on the void fraction:

$$\rho_m = \alpha \rho_g + (1 - \alpha)\rho_l \tag{6.6}$$

whereas the mixture velocity is weighted on the density, so it represents the average velocity of the center of mass:

$$v_m = \frac{\alpha \rho_g v_g + (1 - \alpha)\rho_l v_l}{\alpha \rho_g + (1 - \alpha)\rho_l} \tag{6.7}$$

The appropriate mean drift velocity is defined as:

$$V_{gj}^* = V_{gj} + (C_0 - 1) \cdot j \tag{6.8}$$

As mentioned before, the momentum equation is integrated along the whole channel (Papini, 2011):

$$\int_0^L \frac{\partial G(z,t)}{\partial t} dz = \Delta p(t) - \Delta p_{acc} - \Delta p_{grav} - \Delta p_{fr} - \Delta p_{drift} \tag{6.9}$$

As stated before, a term of pressure drop is present in Eq.(6.9) that is due to the relative motion between the phases, accounted for with the average drift velocity V_{gj}.

6.2.1 Mixture volumetric flux

Introducing the mixture density as defined in Eq.(6.6) and in Eq.(6.3), after some manipulations the mixture continuity equation can be rewritten in the following form:

$$\frac{D\alpha}{Dt} = \left(\frac{\rho_l}{\rho_{lg}} - \alpha\right)\frac{\partial v_m}{\partial z} \tag{6.10}$$

If the previous expression is inserted into the continuity equation of the secondary phase, the following equation is obtained:

$$\frac{\rho_l}{\rho_{lg}}\frac{dv_m}{dz} = \frac{\Gamma_g}{\rho_g} - \frac{d}{dz}\left(\alpha \cdot \frac{\rho_l}{\rho_m} \cdot V_{gj}^*\right) \tag{6.11}$$

In the drift flux formulation, the average volumetric flux of the mixture can be expressed as the sum of the average mixture velocity and an additional term function of the average drift velocity (Hibiki and Ishii, 2003):

$$j = v_m + \frac{\alpha \cdot \rho_{lg}}{\rho_m} \cdot V_{gj}^* \tag{6.12}$$

Deriving with respect to space:

$$\frac{dj}{dz} = \frac{dv_m}{dz} + \frac{d}{dz}\left[\frac{\alpha \cdot \rho_{lg}}{\rho_m} \cdot V_{gj}^*\right] \tag{6.13}$$

Substituting Eq.(6.13) into Eq.(6.12) allows to derive the propagation equation for the mixture volumetric flux:

$$\frac{dj}{dz} = \frac{\Gamma_g \cdot \rho_{lg}}{\rho_l \cdot \rho_g} = \frac{q \cdot \rho_{lg}}{A \cdot H \cdot h_{lg} \cdot \rho_l \cdot \rho_g} = \Omega(t) \tag{6.14}$$

Integrating Eq.(7.14) from the boiling boundary (z_b) to an arbitrary value of z belonging to the two-phase region:

$$j(z,t) = j_{in} + \Omega \cdot (z - z_b) = \frac{G_{in}}{\rho_l} + \Omega \cdot (z - z_b) \tag{6.15}$$

Eq.(6.15) represents the value of the mixture volumetric flux at the coordinate z in the two-phase region. Then, the mixture volumetric flux at the outlet of the channel can be calculated:

$$j_{out}(t) = \frac{G_{in}}{\rho_l} + \Omega \cdot (L - z_b) \tag{6.16}$$

Consequently, the average value of the mixture volumetric flux in the two-phase region:

$$\bar{J} = \frac{G_{in}}{\rho_l} + \frac{\Omega \cdot (L - z_b)}{2} \tag{6.17}$$

6.2.2 Momentum equation

The integration of the momentum equation (Eq.(6.9)) requires to solve the integral of the time derivative of the mass flux on the whole channel. First, the integral can be split into two parts, dividing the single and the two-phase regions:

$$\int_0^L \frac{\partial G(z,t)}{\partial t} dz = \int_0^{z_b} \frac{\partial G}{\partial t} dz + \int_{z_b}^L \frac{\partial \rho_m v_m}{\partial t} dz \tag{6.18}$$

The first term on the right-hand side is the integral in the single-phase region, which is easily solved applying the Liebnitz rule (Todreas and Kazimi, 1993):

$$\int_0^{z_b} \frac{\partial G}{\partial t} dz = \frac{d}{dt} \int_0^{z_b} G_{in} dz - G_{in} dz_b = z_b \frac{d}{dt} G_{in} \tag{6.19}$$

The integration of the second term in Eq.(6.18) is certainly more complicated. Starting from Eq.(6.6) and Eq.(6.7) for the definition of the mixture density and velocity, and introducing the superficial velocities, the following relation can be derived:

$$\rho_m v_m = j \cdot \left(\rho_l - x_v \cdot \rho_{lg}\right) \tag{6.20}$$

The volumetric flow quality in the above equation is equal to the void fraction when an homogeneous flow is assumed, that is:

$$x_v = \frac{j_g}{j} = \frac{1}{1 + \frac{(1-x)}{x} \cdot \frac{\rho_g}{\rho_l}} \tag{6.21}$$

therefore:

$$\rho_m v_m = j \cdot \frac{\rho_l \cdot \rho_g}{\rho_g + x \cdot \rho_{lg}} \tag{6.22}$$

Using Eq.(6.22), Eq.(6.15) for the mixture volumetric flux and applying the Liebniz rule, the second term on the right hand side of Eq.(6.18) can be rewritten as:

$$\int_{z_b}^L \frac{\partial \rho_m v_m}{\partial t} dz = \frac{d}{dt} \int_{z_b}^L \left[\frac{G_{in}}{1 + x \cdot \frac{\rho_{lg}}{\rho_g}} + \frac{\rho_l \cdot \Omega \cdot (z - z_b)}{1 + x \cdot \frac{\rho_{lg}}{\rho_g}} \right] dz + G_{in} \cdot \frac{dz_b}{dt} \tag{6.23}$$

The above equation can be integrated, if the hypothesis of a linear increase of the quality is made:

$$x = x_{out} \cdot \frac{z - z_b}{L - z_b} \tag{6.24}$$

Finally, Eq.(6.9) reads:

$$(c_3 + z_b)\cdot\frac{dG_{in}}{dt} = -(c_1 + z_b)\cdot\frac{dz_b}{dt} - c_2\cdot\frac{dx_{out}}{dt} - c_4\cdot\frac{d\Omega}{dt} + \Delta p(t) - \Delta p_{acc} - \Delta p_{grav} - \Delta p_{fr} - \Delta p_{drift} \quad (6.25)$$

The 4 coefficients that appear in Eq.(6.25) assume the following form:

$$c_1 = \frac{\rho_g}{x_{out}\rho_{lg}}\ln\left(1 + x_{out}\frac{\rho_{lg}}{\rho_g}\right)\left[\frac{2\,\Omega\rho_l\rho_g(L - z_b)}{x_{out}\rho_{lg}} - G_{in}\right] - \frac{2\,\Omega\rho_l\rho_g(L - z_b)}{x_{out}\rho_{lg}} \quad (6.26)$$

$$c_2 = -\frac{\Omega\rho_l\rho_g(L - z_b)^2}{x_{out}^2\rho_{lg}} + \frac{(L - z_b)}{x_{out}\left(1 + x_{out}\frac{\rho_{lg}}{\rho_g}\right)}\left[G_{in} - \frac{\Omega\rho_l\rho_g(L - z_b)}{x_{out}\rho_{lg}}\right] + \frac{\rho_g(L - z_b)}{x_{out}^2\rho_{lg}}\ln\left(1 + x_{out}\frac{\rho_{lg}}{\rho_g}\right)\left(\frac{2\,\Omega\rho_l\rho_g(L - z_b)}{x_{out}\rho_{lg}} - G_{in}\right) \quad (6.27)$$

$$c_3 = \frac{\rho_g(L - z_b)}{x_{out}\rho_{lg}}\ln\left(1 + x_{out}\frac{\rho_{lg}}{\rho_g}\right) \quad (6.28)$$

$$c_4 = \frac{\rho_l\rho_g(L - z_b)^2}{x_{out}\rho_{lg}}\left[1 - \frac{\rho_g}{x_{out}\rho_{lg}}\ln\left(1 + x_{out}\frac{\rho_{lg}}{\rho_g}\right)\right] \quad (6.29)$$

From the integral in Eq.(6.23), it is also possible to calculate the average value of the mass flux in the two-phase region:

$$\bar{G}_{2\theta} = \frac{\Omega\rho_l\rho_g(L - z_b)}{x_{out}\rho_{lg}} + \frac{\rho_g}{x_{out}\rho_{lg}}\ln\left(1 + x_{out}\frac{\rho_{lg}}{\rho_g}\right)\left(G_{in} - \frac{\Omega\rho_l\rho_g(L - z_b)}{x_{out}\rho_{lg}}\right) \quad (6.30)$$

Finally, it is necessary to correctly define the pressure drop term in Eq.(6.25). The total pressure drop across the channel is simply the difference between the inlet and the outlet sections:

$$\Delta p(t) = p_{in} - p_{out} \quad (6.31)$$

The accelerative pressure drop is defined as:

$$\Delta p_{acc} = G_{out}^2\left[\frac{x_{out}^2}{\alpha_{out}\rho_g} + \frac{(1 - x_{out})^2}{(1 - \alpha_{out})\rho_l}\right] - \frac{G_{in}^2}{\rho_l} \quad (6.32)$$

The gravitational pressure drop results:

$$\Delta p_{grav} = g\rho_l\sin\beta\, z_b + g\sin\beta\,(L - z_b)\left[\bar{\alpha}\rho_g + (1 - \bar{\alpha})\rho_l\right] \quad (6.33)$$

In the frictional pressure drop term, both the pressure drop due to friction and the concentrated pressure drops are included:

$$\Delta p_{fr} = \left(K_{in} + f\frac{z_b}{D}\right)\frac{G_{in}^2}{\rho_l} + f\Phi_{lo}^2\frac{\bar{G}_{2\theta}^2}{2\rho_l}\frac{(L-z_b)}{D} + K_{out}\Phi_{lo,out}^2\frac{G_{out}^2}{2\rho_l} \tag{6.34}$$

Finally, the drift term account for the effect of the relative velocity between the phases:

$$\Delta p_{drift} = \frac{\rho_l - \rho_{m,out}}{\rho_{m,out} - \rho_g}\frac{\rho_l\rho_g}{\rho_{m,out}}V_{gj,out}^{*2} \tag{6.35}$$

Eq.(6.25) allows to describe the dynamics of the flow rate entering one of the two channels. To the aim, three more equations are needed, describing the dynamics of the boiling boundary, the exit quality and the reaction frequency Ω.

6.2.3 Boiling boundary dynamics

The dynamics of the boiling boundary can be derived from the integration of the energy conservation equation in the single-phase region (Eq.(6.2)). No differences are introduced with respect to the original model developed by Papini (2011). The Liebnitz rule is again applied for the integration of the time derivative term. As a further hypothesis, the single-phase enthalpy is considered constant in all the single-phase region and it is assumed equal to the average between the inlet and the liquid saturation values:

$$\bar{h} = \frac{h_l + h_{in}}{2} \tag{6.36}$$

The ODE describing the time behavior of the boiling boundary reads:

$$\frac{dz_b}{dt} = \frac{2G_{in}}{\rho_l} - \frac{2qz_b}{AL\rho_l(h_l - h_{in})} = c_5 \tag{6.37}$$

6.2.4 *Exit quality dynamics*

The equation accounting for the dynamics of the exit quality is derived starting from the void fraction formula, available from the drift flux-formulation (Eq.(4.20)):

$$\alpha = \frac{j_g}{C_0 j + V_{gj}} \tag{6.38}$$

A correlation for the void fraction in an helical pipe characterized by a two-phase flow at high pressure has been derived in Section 4.5, starting from the CFD simulation of the helical

coil installed at SIET laboratories. Being the model developed for the simulation of the DWOs in the same helical coil, the correlation structure identified in Section 4.5 is used. In particular, the value of C_0 is function of the flow quality, to have coherent values of the void fraction in the whole range of quality. In addition, looking at the results of Section 4.5, the value of V_{gj} is found negligible with respect to C_0. Therefore, it can be neglected here with negligible effects on the results but a remarkable simplification in the calculations, as it will be clear in the following. Therefore:

$$\alpha = \frac{1}{\big(1 - a(1-x)\big)} \frac{j_g}{j} = \frac{1}{\big(1 - a(1-x)\big)} x_v \tag{6.39}$$

Remembering that the volumetric quality is equal to the void fraction for an homogeneous flow, a relationship between the void fraction and the quality is found:

$$\alpha = \frac{1}{\big(1 - a(1-x)\big)} \frac{1}{1 + \frac{(1-x)}{x} \cdot \frac{\rho_g}{\rho_l}} \tag{6.40}$$

Integrating and introducing $\gamma = \rho_g / \rho_l$, one obtains an equation for the average value of the void fraction:

$$\begin{aligned} \bar{\alpha} = \frac{1}{x_{out}} \int_0^{x_{out}} \alpha dx \\ = \frac{\gamma}{x_{out}(\gamma - 1)(a - \gamma + 1)} \ln\left[\frac{\gamma + x_{out}(1-\gamma)}{\gamma}\right] \\ - \frac{a+1}{a x_{out}(a - \gamma + 1)} \ln\left[\frac{1 + a(1 - x_{out})}{1 + a}\right] \end{aligned} \tag{6.41}$$

Derivation of Eq.(6.41) allows to find an equation for the dynamics of the exit quality:

$$\frac{d\bar{\alpha}}{dt} = c_6 \frac{dx_{out}}{dt} \tag{6.42}$$

$$\begin{aligned} c_6 = \frac{a+1}{x_{out}(a - \gamma + 1)} \left[\frac{1}{a x_{out}} \ln\left[\frac{1 + a(1 - x_{out})}{1 + a}\right] + \frac{1}{1 + a(1 - x_{out})}\right] \\ - \frac{\gamma}{x_{out}(a - \gamma + 1)} \left[\frac{1}{x_{out}(\gamma - 1)} \ln\left[\frac{1 + x_{out}(1-\gamma)}{\gamma}\right] \ldots \right. \\ \left. + \frac{1}{\gamma + x_{out}(1-\gamma)}\right] \end{aligned} \tag{6.43}$$

A further step is necessary to remove the time derivative of the average void fraction from the final equation. Remembering the continuity equation in the two-phase region and integrating it in space:

$$\frac{d\overline{\alpha}}{dt} = \frac{G_{out} - G_{in}}{\rho_{lg}(L - z_b)} + \frac{\overline{\alpha}}{(L - z_b)}\frac{dz_b}{dt} \tag{6.44}$$

Combining the above expression with the derivative of Eq.(6.41), the ODE for the dynamics of the exit quality is finally obtained as:

$$\frac{dx_{out}}{dt} = c_7 + c_8 c_5 \tag{6.45}$$

$$c_7 = \frac{1}{c_6}\frac{G_{out} - G_{in}}{\rho_{lg}(L - z_b)} \tag{6.46}$$

$$c_8 = \frac{1}{c_6}\frac{\gamma}{x_{out}(\gamma - 1)(a - \gamma + 1)(H - z_b)}\ln\left[\frac{\gamma + x_{out}(1 - \gamma)}{\gamma}\right] - \frac{a + 1}{a x_{out}(a - \gamma + 1)(H - z_b)}\ln\left[\frac{1 + a(1 - x_{out})}{1 + a}\right] \tag{6.47}$$

6.2.5 Reaction frequency dynamics

The dynamics of the reaction frequency is given by the following equation:

$$\frac{d\Omega}{dt} = c_9 = \frac{\rho_{lg}}{ALh_{lg}\rho_l\rho_g}\frac{dq}{dt} \tag{6.48}$$

The dynamics of the thermal power is governed by the dynamics of the heated wall, that is unchanged with respect to the model of Papini (2011), where it can be found in more details. In particular, the dynamics of the wall temperature is evaluated by a heat transfer balance with a lumped two-region approach (single-phase region and two-phase region):

$$\frac{dq_{1\theta}}{dt} = M_{w,1\theta}C_{w,1\theta}\frac{dT_{w,1\theta}}{dt} = q_{1\theta} - (hS)_{1\theta}\left(T_{w,1\theta} - T_{f,1\theta}\right) \tag{6.49}$$

$$\frac{dq_{2\theta}}{dt} = M_{w,2\theta}C_{w,2\theta}\frac{dT_{w,2\theta}}{dt} = q_{2\theta} - (hS)_{2\theta}\left(T_{w,2\theta} - T_{f,2\theta}\right) \tag{6.50}$$

The Dittus-Boelter correlation and the Kandlikar correlation are used for the calculation of the heat transfer coefficients, respectively in the single-phase region and in the two-phase region.

6.3 Model implementation

The model is based on the ODEs derived in the previous section. The final form of the equations is not considerably different with respect to the model derived by Papini (2011).

The major differences are found in the equation for the exit quality dynamics, derived from the definition of the void fraction (Eq.(6.45)). To model the parallel channel case, specific boundary conditions are required. In particular, the same pressure drop dependence with time is imposed across each channel. In addition, a constant total mass flow rate condition is imposed:

$$\Delta p_1(t) = \Delta p_2(t) = \Delta p(t) \tag{6.51}$$

$$G_{in,1}(t) + G_{in,2}(t) = const \tag{6.52}$$

Deriving with time the second boundary condition one obtains:

$$\frac{dG_{in,1}}{dt} = -\frac{dG_{in,2}(t)}{dt} \tag{6.53}$$

For parallel channels, the complete set of ODEs in Section 6.2 must be written for each one of the two channels. If the equation for the inlet mass flow rate dynamics (Eq.(6.25)) is written for both channels:

$$\begin{aligned}\left(c_{3,1} + z_{b,1}\right) \cdot \frac{dG_{in,1}}{dt} &= -\left(c_{1,1} + z_{b,1}\right) \cdot \frac{dz_{b,1}}{dt} - c_{2,1} \cdot \frac{dx_{out,1}}{dt} - c_{4,1} \cdot \frac{d\Omega_1}{dt} + \Delta p_1(t) \\ &- \Delta p_{acc,1} - \Delta p_{grav,1} - \Delta p_{fr,1} - \Delta p_{drift,1}\end{aligned} \tag{6.54}$$

$$\begin{aligned}\left(c_{3,2} + z_{b,2}\right) \cdot \frac{dG_{in,2}}{dt} &= -\left(c_{1,2} + z_{b,2}\right) \cdot \frac{dz_{b,2}}{dt} - c_{2,2} \cdot \frac{dx_{out,2}}{dt} - c_{4,2} \cdot \frac{d\Omega_2}{dt} + \Delta p_2(t) \\ &- \Delta p_{acc,2} - \Delta p_{grav,2} - \Delta p_{fr,2} - \Delta p_{drift,2}\end{aligned} \tag{6.55}$$

The differential equation for the inlet mass flow rate in one of the two channels is finally obtained subtracting Eq.(6.53) from Eq.(6.52) and considering the boundary condition expressed by Eq.(6.51):

$$\begin{aligned}\left(c_{3,1} + z_{b,1} + c_{3,2} + z_{b,2}\right) \frac{dG_{in,1}}{dt} &= \left(c_{1,2} + z_{b,2}\right) \frac{dz_{b,2}}{dt} - \left(c_{1,1} + z_{b,1}\right) \frac{dz_{b,1}}{dt} + c_{2,2} \frac{dx_{out,2}}{dt} - c_{2,1} \frac{dx_{out,1}}{dt} \\ &+ c_{4,2} \cdot \frac{d\Omega_2}{dt} - c_{4,1} \cdot \frac{d\Omega_1}{dt} + \Delta p_{acc,2} - \Delta p_{acc,1} + \Delta p_{grav,2} - \Delta p_{grav,1} \\ &+ \Delta p_{fr,2} - \Delta p_{fr,1} + \Delta p_{drift,2} - \Delta p_{drift,1}\end{aligned} \tag{6.56}$$

The dynamics of the two channels is therefore governed by a set of 9 non linear ODEs, in the form:

$$\frac{dy_i}{dt} = f_i(y) \tag{6.57}$$

where the state variables are:

$$\begin{array}{lllll} y_1 = z_{b,1} & y_2 = z_{b,2} & y_3 = x_{out,1} & y_4 = x_{out,2} & y_5 = G_{in,1} \\ y_6 = T_{w,1}^{1\theta} & y_7 = T_{w,1}^{2\theta} & y_8 = T_{w,2}^{1\theta} & y_9 = T_{w,2}^{2\theta} & \end{array} \tag{6.58}$$

The system of ODEs has been implemented and solved with the MATLAB software SIMULINK (The Math Works, Inc., 2005). First the steady-state conditions are calculated solving the system of equations with the time derivatives set to zero. The steady-state values are then used as initial conditions, to integrate the system of differential equations and obtain the time evolution of the system. To excite the density wave instability mode, a perturbation is introduced in the power input, as it is increased gradually starting from stable conditions up to the instability appearance.

6.4 Simulation of the SIET experimental database

6.4.1 Application to the SIET helical coil

In this section, the dynamic model presented in Section 6.3 and based on the drift-flux formulation is applied to the DWO experimental data measured at SIET laboratories. Actually, some modifications are necessary for a proper simulation of the helical geometry. The geometrical data of the facility were shown in Table 2.1, whereas the operating conditions considered during the experiments can be found in Section 2.4.1.

The presence of the unheated riser, given by the final 8 m of the test section, is accounted for introducing the proper pressure loss terms in the momentum equation. Since no thermal power is supplied to the two-phase mixture along the riser, the void fraction and the quality can be considered constant and equal to x_{out} and α_{out}. As a consequence, no accelerative pressure drops are generated in the riser section, which is characterized only by frictional and gravitational pressure drops:

$$\Delta p_{grav}^{R} = g L_R \sin\beta \left[\alpha_{out}\rho_g + (1-\alpha_{out})\rho_l\right] \tag{6.59}$$

$$\Delta p_{fric}^{R} = f \Phi_{lo,out}^2 \frac{G_{out}^2}{2\rho_l}\frac{L_R}{D} \tag{6.60}$$

In conclusion of his work, Papini (2011) remarked the difficulty of predicting with a high accuracy the specific stability features of the analyzed system. In particular, he suggested a better reproduction of the two-phase frictional pressure drop of the helix through an improved correlation. Actually, Papini identified the pressure drop distribution as one of the most critical parameter for a correct estimation of the instability threshold. Moreover, he recommended the development of a specific void fraction model appropriate for the helical

geometry, to improve the results of the homogeneous model. Within these respects, the whole activity presented in the previous chapters gains an additional importance for its application in the dynamic model, which becomes therefore the proper conclusive subject of the thesis work.

As concerns the void fraction, the correlation developed in Chapter 4 and based on the drift flux formulation is used (Eq.(4.30)). The correlation was built starting from CFD results, due to the lacking of experimental data on the subject. The whole dynamic model has been derived from the drift-flux formulation, and the specific void fraction expression was included in the governing equations and integrated in space (Section 6.2.4). To ease the integration, a simplified version of Eq.(4.30) was considered, neglecting the average drift velocity, being its value very low:

$$\alpha = \frac{1}{[1 + 0.117(1 - x)]}\frac{j_g}{j} = \frac{1}{[1 + 0.117(1 - x)]}x_v \tag{6.61}$$

For the frictional pressure drop, the correlation developed in Chapter 4 is used, in particular in the form developed from the SIET experimental data only (Eq.(5.19)). The correlation is based on the only-liquid approach, in which only the liquid is considered as flowing alone in the channel. An additional term is therefore required, to fit the correlation with the liquid-only approach adopted for the model, which considers the whole flow as liquid (Todreas and Kazimi, 1993):

$$\Phi_l^2 = 0.13\Phi_{LM}^2 De_l^{0.15}\left(\frac{\rho_m}{\rho_l}\right)^{-0.37}(1 - x)^{1.75} \tag{6.62}$$

The single-phase friction coefficient, required for the evaluation of the two-phase frictional pressure drop in addition to the one related to the single-phase region, is evaluated accordingly to the correlations proposed by Ito (1959). Ito correlations have been identified in Chapter 3 between the numerous correlations available as the best for the SIET coil, for both the laminar and the turbulent regions:

$$\frac{f_c}{f_s} = \frac{21.5De}{(1.56 + \log_{10} De)^{5.73}} \tag{6.63}$$

$$f = 0.304Re^{-0.25} + 0.029\left(\frac{d}{D}\right)^{0.5} \tag{6.64}$$

Also the laminar to turbulent flow transition is evaluated with the correlation proposed by Ito (1959):

$$Re_{cr} = 20000\left(\frac{d}{D}\right)^{0.32} \tag{6.65}$$

Finally, the concentrated pressure drop at the inlet is imposed equal to the pressure loss measured experimentally across the valve. At the outlet, instead, no concentrated pressure drop is required.

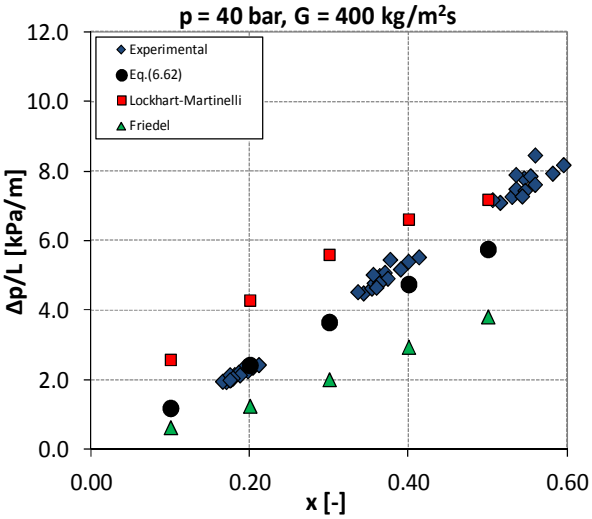

Figure 6.1 Comparison between the frictional pressure drop experimental data and the results of the analytical model with different correlations at 40 bar and 400 kg/m^{2}s.

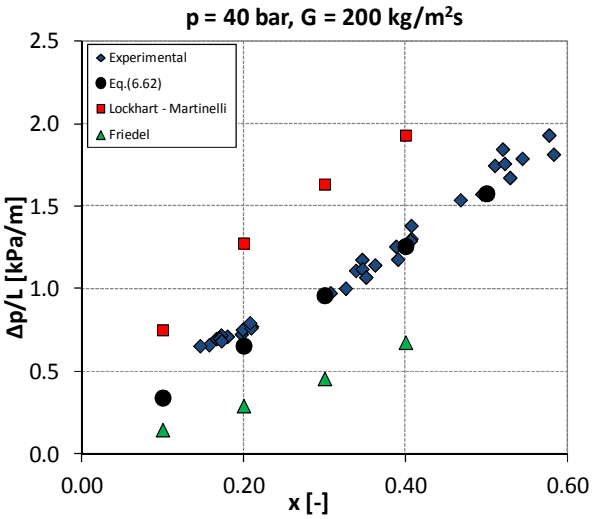

Figure 6.2 Comparison between the frictional pressure drop experimental data and the results of the analytical model with different correlations at 40 bar and 200 kg/m^{2}s.

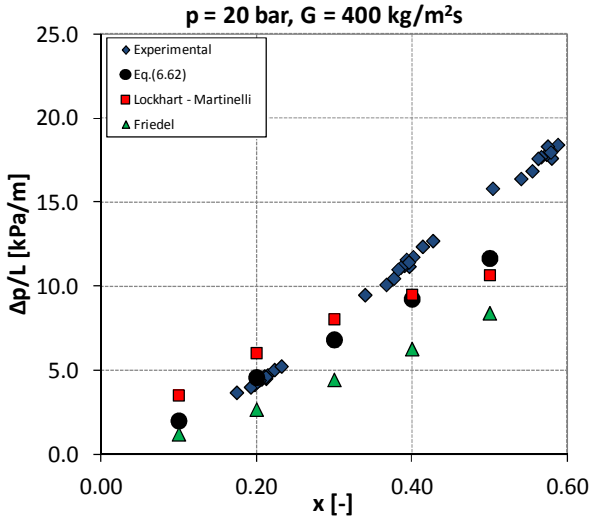

Figure 6.3 Comparison between the frictional pressure drop experimental data and the results of the analytical model with different correlations at 20 bar and 400 kg/m^{2}s.

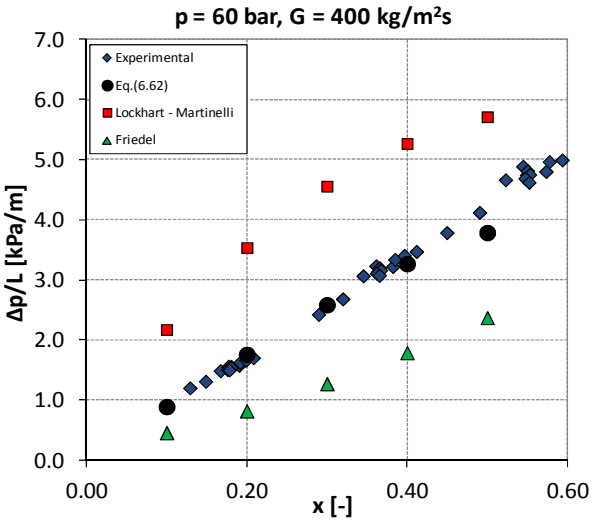

Figure 6.4 Comparison between the frictional pressure drop experimental data and the results of the analytical model with different correlations at 60 bar and 400 kg/m^{2}s.

To verify the accuracy of the model for the evaluation of the frictional pressure drop, they are estimated at steady-state and then compared with the experimental data. In addition to Eq.(6.62), also the Lockhart-Martinelli and Friedel correlations are compared, as they were previously considered also by Papini (2011) in his sensitivity analysis on the effect of the two-phase friction multiplier. The comparison is shown from Figure 6.1 to Figure 6.4. As it is possible to notice, the agreement with the experimental data is very good for the newly developed correlation, that results therefore appropriate for the model. The comparison is limited to a flow quality equal to 0.6 for two reasons: the average value of the quality is

considered, as returned by the model, and the fact that DWOs characterize mainly the low-medium quality region.

6.4.2 Comparison with the experimental data

The developed analytical model, optimized for the simulation of the SIET facility, has been used for the simulation of numerous experimental conditions included in the database described in Section 2.4. Therefore, a comparison between model and experiments is proposed for different stability thresholds, covering the whole set of pressure and mass flow rate. In particular, stability maps and limit powers at 40 bar and at the three different mass flow rates (200 kg/m^{2}s, 400 kg/m^{2}s and 600 kg/m^{2}s) are presented from Figure 6.5 to Figure 6.10. Stability maps and limit power at 20 bar and 200 kg/m^{2}s are shown in Figure 6.11 and Figure 6.12, and the ones at 80 bar and 400 kg/m^{2}s in Figure 6.13 and Figure 6.14.

The stability of the system is generally underestimated, as the model predicts a lower heated power to reach the unstable operating region. A general underestimation of the instability thresholds was already observed in the work of Papini (2011), using the homogeneous equilibrium model. The upgrade to a drift-flux formulation guarantees a certain improvement of the accuracy. In more details, the greater improvement is obtained at low mass flow rates (Figure 6.7 and Figure 6.11), whereas it is not so significant at high mass flow rate (Figure 6.9). This could suggest a slight better accuracy at low mass flow rates of the models developed for the helical geometry. In addition to a general improvement, the estimation of the stability boundary results particularly good at low flow rate (Figure 6.7 and Figure 6.11) and high pressure (Figure 6.13). It must be noticed that at high pressure all the data are very close in the $N_{sub} - N_{pch}$ plane.

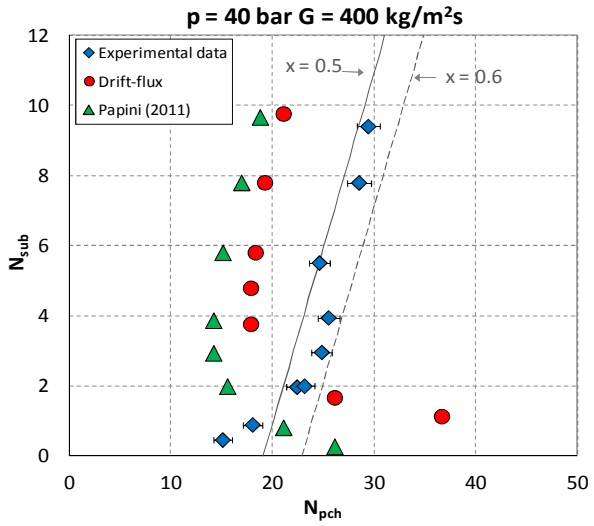

Figure 6.5 Stability map at 40 bar and 400 kg/m^{2}s. Comparison between the analytical model results and the experimental data.

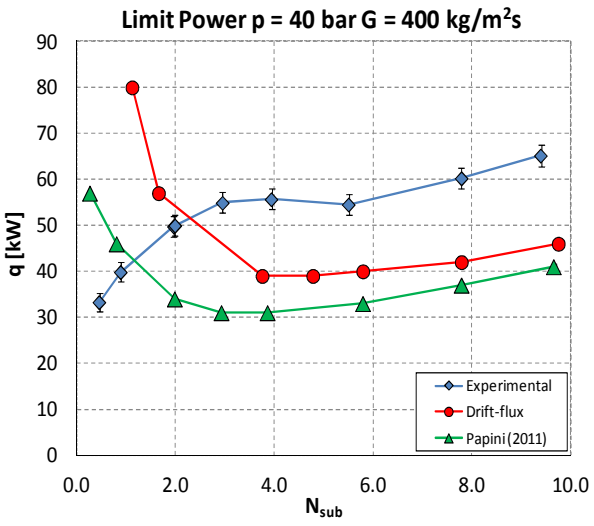

Figure 6.6 Limit power for instability inception at 40 bar and 400 kg/m^{2}s. Comparison between the analytical model results and the experimental data.

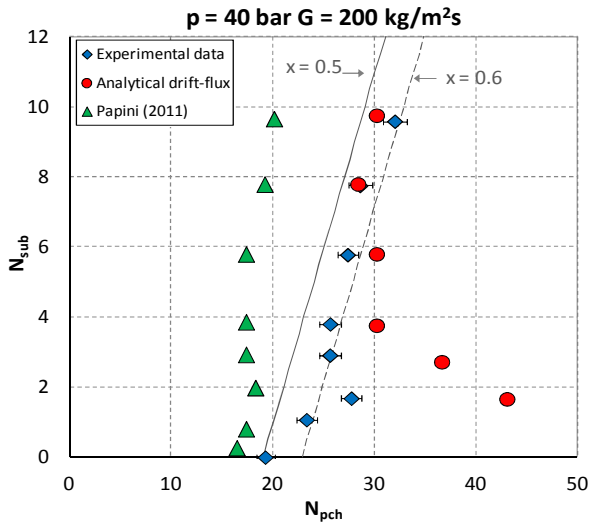

Figure 6.7 Stability map at 40 bar and 200 kg/m^{2}s. Comparison between the analytical model results and the experimental data.

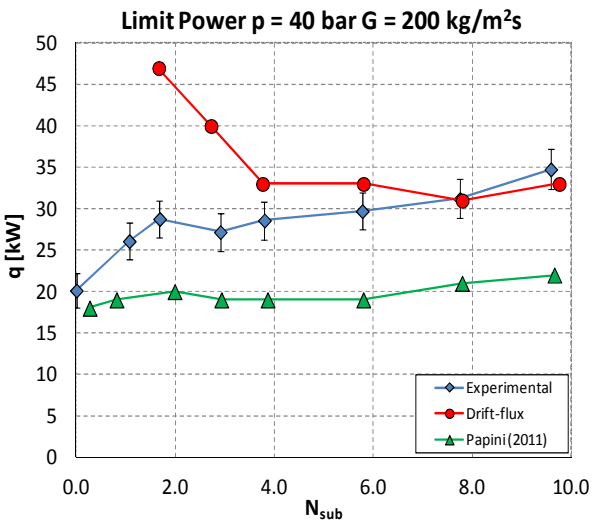

Figure 6.8 Limit power for instability inception at 40 bar and 200 kg/m^{2}s. Comparison between the analytical model results and the experimental data.

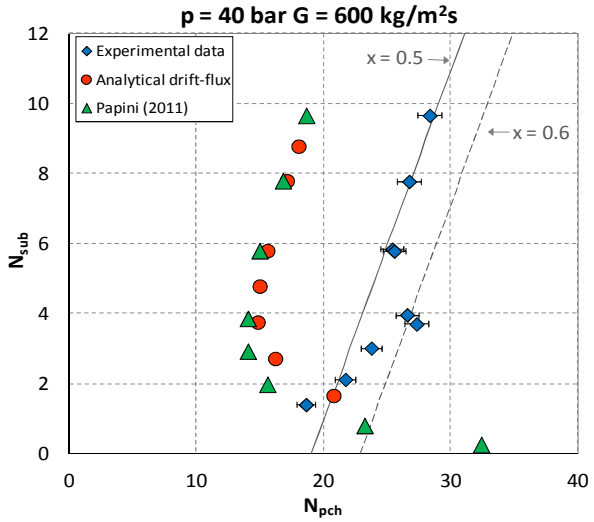

Figure 6.9 Stability map at 40 bar and 600 kg/m^{2}s. Comparison between the analytical model results and the experimental data.

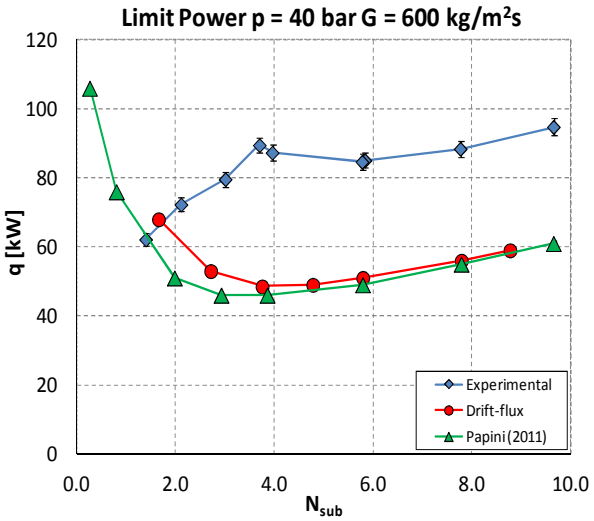

Figure 6.10 Limit power for instability inception at 40 bar and 600 kg/m^{2}s. Comparison between the analytical model results and the experimental data.

Actually, the same difference in the limit power for inception of the instability results in a small difference in the dimensionless plane. For major clarity, also the comparison for the limit power at instability inception is shown in Figure 6.14.

Nevertheless, the high accuracy is limited to the medium and high subcooling regions. At low subcoolings, the model continues to show a different trend with respect to the experimental data. While the experiments show a system stabilization for a subcooling increase, the model return the "L shape" of the stability boundary typical of straight tubes, not observed during the test at the SIET facility. Within these respects, no improvement is obtained with respect to the homogeneous equilibrium model, as the model remains unable to

reproduce the particular behavior at low subcoolings. On the contrary, for the lower value of the mass flow rate, the behavior more similar to the experimental data obtained with the homogeneous flow model is not appearent after the upgrade to drift-flux (Figure 6.7 and Figure 6.11).

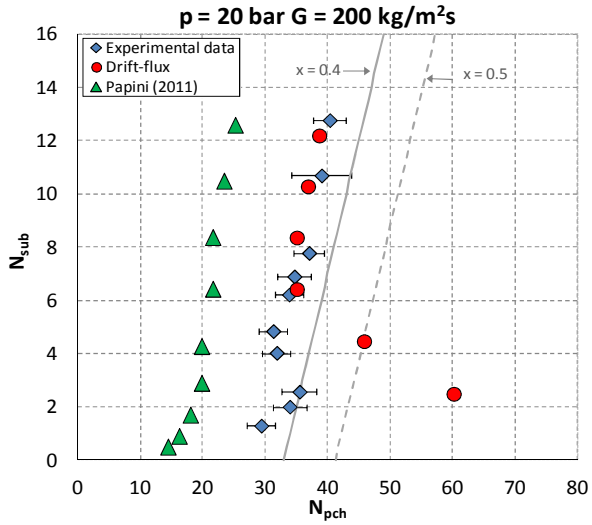

Figure 6.11 Stability map at 20 bar and 200 kg/m^{2}s. Comparison between the analytical model results and the experimental data.

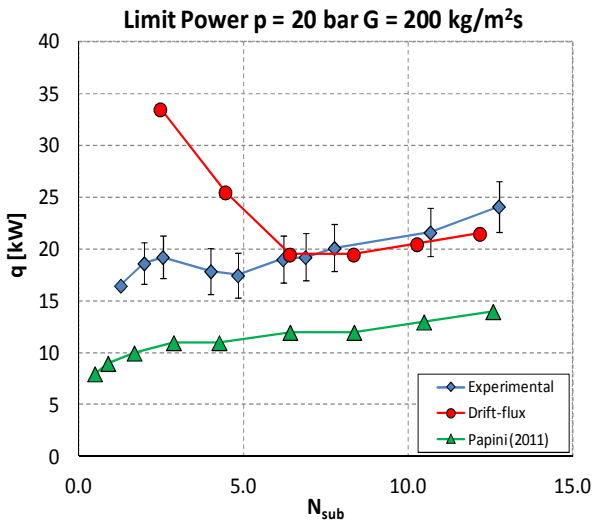

Figure 6.12 Limit power for instability inception at 20 bar and 200 kg/m^{2}s. Comparison between the analytical model results and the experimental data.

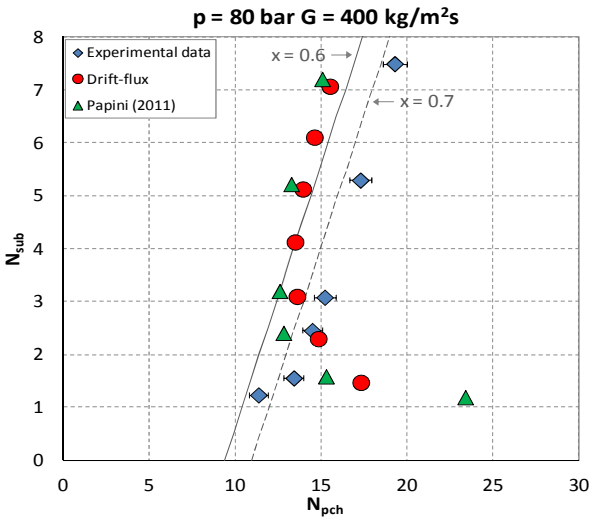

Figure 6.13 Stability map at 80 bar and 400 kg/m^{2}s. Comparison between the analytical model results and the experimental data.

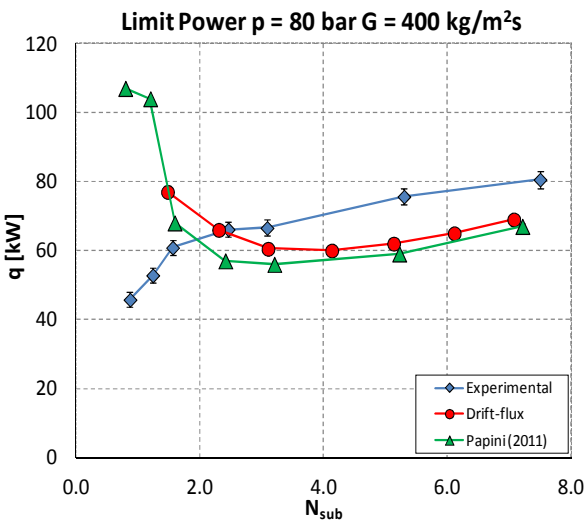

Figure 6.14 Limit power for instability inception at 80 bar and 400 kg/m^{2}s. Comparison between the analytical model results and the experimental data.

Globally, a satisfactory agreement with the experimental stability maps is reached, together with a significant improvement of the results with the upgrade to a drift-flux formulation and the inclusion of the new correlations. The results are particularly good at low mass flow rate and high pressure, whereas further improvements are possible at high mass

flow rate. Despite the positive results, the system remains particularly difficult to predict at low subcoolings, where the model continues to show the classical "L shape" of the stability boundary. In this view, more work is needed to improve the results also at low subcoolings. In particular, it could be of interest to include in the model the effect of the subcooled boiling, with a model specifically developed for the helical geometry.

6.5 RELAP5 study of the DWO phenomena

The subject of DWO is addressed also with the RELAP5 system code, with the aim to study the code capability to detect the DWO inception. The code assessment procedure allows to highlights its strengths and weaknesses with respect to the prediction of the instability. Initially, a simple test case is studied, i.e. a single boiling channel with imposed inlet and outlet pressures. This configuration was investigated by many authors and different works are available in literature (Yadigaroglu, 1981; Rizwan-Uddin, 1994; Ambrosini et al., 2000; Ambrosini and Ferreri, 2006). Ambrosini and Ferreri (2006) performed a detailed analysis on the subject using both a simplified single channel model and the RELAP5 code. The authors analyzed the influence on the code results of the different models available, as well as of the nodalization and the numerical scheme.

It must be noticed that the imposition of a constant Δp across the heated section is not a realistic assumption with respect to a typical experimental setup, where the mass flow rate is forced by an external feedwater pump. In such a case, the constant pressure drop boundary condition can be assured by connecting a large bypass tube to the boiling channel (Solberg, 1966; Saha et al., 1976). Even if the flow rate is forced in the system, it freely evolves in the heated section until the bypass is large enough to accommodate the flow rate perturbation. The presence of a large bypass is also studied with the RELAP5 code, since its accuracy in this typical experimental configuration has not been evaluated yet. The presence of the bypass was studied experimentally by Collins and Gacesa (1969) and theoretically by Carver (1970). In accordance with their results, a sufficiently large bypass ratio (i.e. the ratio of bypass cross sectional area to heated channel cross sectional area) is required to maintain the constant pressure drop boundary condition. Moreover, the stability is independent on the bypass ratio when its value is sufficiently large, even though a stiff boundary condition (high bypass ratio) is found to be destabilizing.

After the analysis of the single channel case, the parallel channel configuration is addressed, starting from straight typical BWR subchannels and ending with parallel helically coiled tubes. In comparison with the single channel setup, few studies investigated the instabilities in a parallel channel system with the RELAP5 code (Hamidouche and Bousbia-salah, 2006; Yun et al., 2010). Initially, the geometry simulates a typical BWR subchannel and the results are compared with the single heated channel case. Afterwards, the geometry is modified in order to simulate the helical coil experimental facility. Because only straight pipe elements are implemented in the code and all the models and correlations refer to straight geometry, a fictitious configuration is introduced. The two parallel tubes are inclined in order to reproduce both tube length and height of the facility. A sensitivity study is provided to underline the influence of tube length and inclination on the predicted instability thresholds.

6.5.1 Single channel

This section is focused on the single heated channel. In Section 6.5.1.1 RELAP5 models of the two configurations studied (with imposed Δp and with the bypass) are presented, together with the code models and numerical schemes selected. Section 6.5.1.2 presents the simulation results. First, simulations performed with fixed inlet and exit pressures are discussed and the criterion adopted to detect the instability threshold is explained. Then, the introduction of the bypass is analyzed via comparison with the experimental data. Finally, a sensitivity study on the bypass area is presented, to define its influence on the stability of the single heated channel.

6.5.1.1 RELAP5 model and numerical settings

The simplest system to study boiling channel instabilities is a single heated channel with an imposed Δp across. Such layout is modeled with the RELAP5/MOD3.3 code (US NRC, 2001), with a single pipe of circular cross section connected to inlet and outlet plena kept at imposed pressures. Form loss coefficients are introduced to account for local inlet and outlet pressure losses (Figure 6.15). Uniform heating along the channel axis is considered. Moreover, the heat structures are assumed very thin and present high thermal conductivity and low heat capacity, to avoid distortions in the imposed thermal flux condition, and to neglect tube wall dynamic behavior as well.

The work of Ambrosini and Ferreri (2006) is considered as a starting point. The UVUT (Unequal Velocity Unequal Temperature) model is used, because it is found to be more robust and reliable when compared with the EVET (Equal Velocity Equal Temperature) model, which is indeed more conservative. The semi-implicit numerical scheme is selected. Calculations rarely crash due to numerical problems, and the introduction of numerical diffusion is limited with respect to the nearly-implicit numerical scheme. To reduce as much as possible the amount of numerical diffusion introduced also with the semi-implicit scheme, a control variable that forces the time step to be equal to 95% of the Courant limit has been developed. Physical size of the channel and operating parameters, which are inspired to the classical values of a BWR subchannel (Table 6.1), are derived from the work of Ambrosini and Ferreri too, to make easier a comparison of the simulation results. A number of nodes equal to 48 is selected, to assure a smoother prediction of the stability boundary, even though the UVUT model have proved to be less sensitive to variations in the number of nodes.

Table 6.1 RELAP5 parameters for the single channel simulation.

Heated Channel		**Operating Parameters**	
Diameter [m]	0.0124	Exit pressure [Pa]	$7.0 \cdot 10^{6}$
Length [m]	3.658	Inlet temperatures [°C]	151.3-282.3
Roughness [m]	$2.5 \cdot 10^{-5}$	K_{in}	23
		K_{out}	5

As stated before, a large bypass tube is usually connected to the boiling channel to maintain the constant pressure drop boundary condition during experiments. The experimental setup is modeled with the RELAP5 code connecting a pipe component of different diameter

to the heated section through the common lower and upper headers (Figure 6.16). The inlet mass flow rate is imposed, therefore the pressure drop across the channel is determined by the exit pressure, the mass flow rate and the characteristics of the channel.

The following procedure is adopted to reach the instability boundary: at the beginning of each run specific values of exit pressure, mass flow rate and inlet water temperature are selected as initial conditions. Flow circulation in the system starts at zero power, then power generation in the heat structures is increased gradually till the unstable condition is reached. The increase rate is higher at the beginning of the transient, to quickly approach the unstable region, then it is lowered to guarantee an easier detection of the onset of instability.

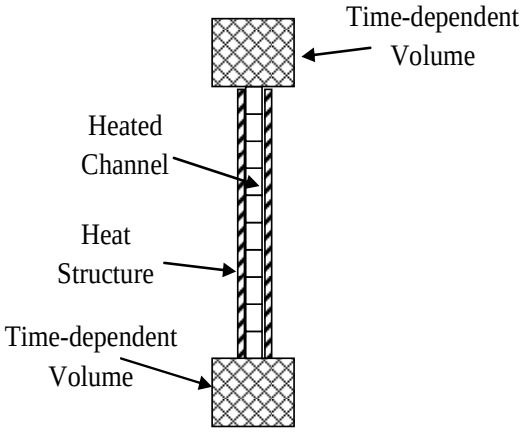

Figure 6.15 RELAP5 nodalization for the single channel.

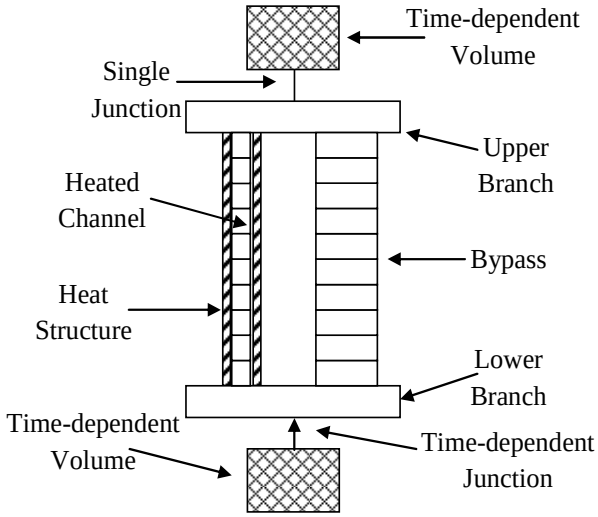

Figure 6.16 RELAP5 nodalization for the single channel with the bypass

6.5.1.2 Simulation results

As stated in the previous section, unstable operating conditions were reached by gradually increasing the thermal power supplied to the test section. Results are reported in Figure 6.17 in the dimensionless space N_{pch}-N_{sub}. The stability threshold exhibits the classical "L shape". Constant exit quality lines are also reported to identify system operating regions. In agreement with the results of Ambrosini and Ferreri (2006), the onset of DWO instability in a single channel can be correctly predicted with the RELAP5 code. Some remarks are needed on the determination of the exact point where the system crosses the stability boundary. A typical transient is shown in Figure 6.18. Mass flow rate decreases with time as the supplied power is increased, until it starts to oscillate when the instability threshold is approached. Clearly, no universal detection criteria exist. In this work the system was considered unstable when mass flow rate oscillation amplitude reached the 100% of its steady-state value. For verification purposes, the same results were analyzed according to a visual detection criterion, in which the system was considered unstable when mass flow rate oscillations appeared fully-developed. The visual detection was viable thanks to the almost flat power ramps imposed near the instability inception (causing the mass flow rate to vary

slightly). As it is shown in Figure 6.17, no significant differences were found. Hereby, all the results are presented in the followings by using the 100% detection criterion.

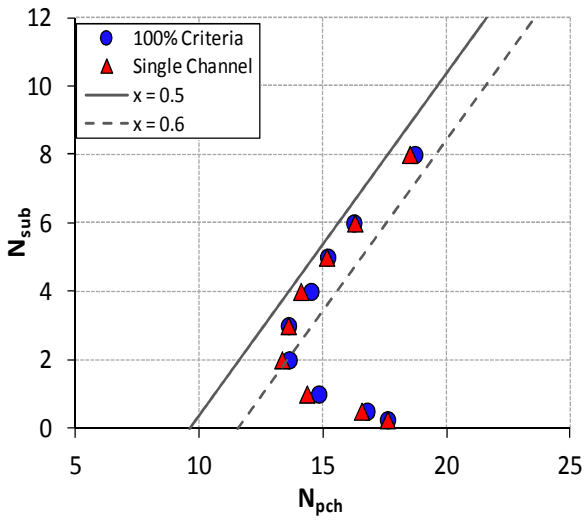

Figure 6.17 Stability map for a single channel with an imposed Δp across. Comparison between different instability detection criteria.

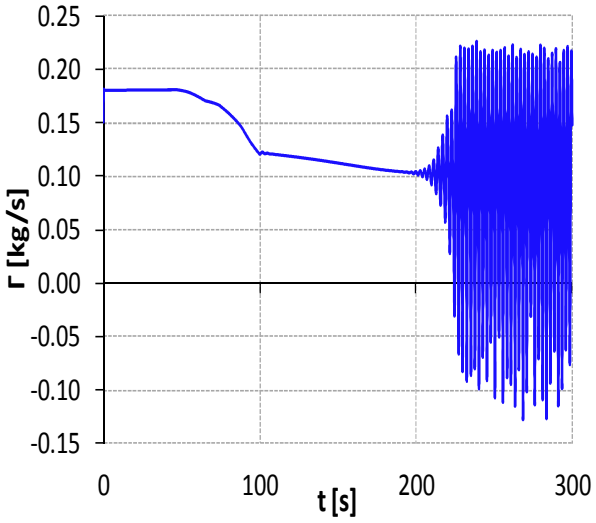

Figure 6.18 Mass flow rate behavior in the heated channel during a DWO transient.

Results obtained for the bypass case are now discussed. The first set of data were collected adopting a bypass ratio equal to 100 and exploring different inlet temperatures. Figure 6.19 shows a comparison with the simplified nodalization limited to a single channel only. The same total pressure drop (about 80 kPa) is considered in both cases. Connection of the single heated channel with a large bypass is demonstrated to reproduce the conditions that lead to instability occurrence, which are properly detected by the code. In Figure 6.19, RELAP5 results are compared also with the experimental data of Solberg (1966), which studied density wave instabilities with a simple bypass layout. The ranges of investigated conditions are summarized in Table 6.2. A good agreement is found for the higher values of the subcooling number, that is for the lower inlet temperatures. Decreasing the inlet subcooling, code predictions deviate slightly from the experimental data. Unfortunately, no data are available for inlet temperatures close to saturation value. The experimental validation of the developed RELAP5 model can be considered however successfully attempted.

Table 6.2 Parameters of the Solberg's experiment (1966).

Heated Channel		**Operating Parameters**	
Diameter [m]	0.00525	Exit pressure [Pa]	$8.11 \cdot 10^{6}$
Length [m]	2.9	Inlet temperatures [°C]	139.6-291.8
Roughness [m]	$2.5 \cdot 10^{-5}$	K_{in}	17.8
		K_{out}	0.03

According to classical description, the period of oscillations should be of the order of twice the mixture transit time (Yadigaroglu, 1981). Moreover, being related to the mixture transit time, the period is expected to grow with the subcooling number, as an increase in inlet

subcooling results in a longer single-phase region, hence a higher mixture transit time. Period of the oscillations is correctly reproduced by the RELAP5 code, as it is shown in Figure 6.20, where the period over transit time ratio is presented. The mixture transit time in the heated channel was calculated directly by the code with a control variable. The period over transit time ratio does not exhibit significant differences in the two configurations (single channel alone and with the bypass), except for a lower increase at high inlet subcoolings in the first case. For the sake of comparison, the code results are compared with an analytical calculation of the mixture transit time based on classical homogeneous flow theory (Eq.(2.9)). The analytical period over transit time ratio, despite being always slightly higher than the value calculated by the code, shows exactly the same qualitative behavior found with the bypass configuration.

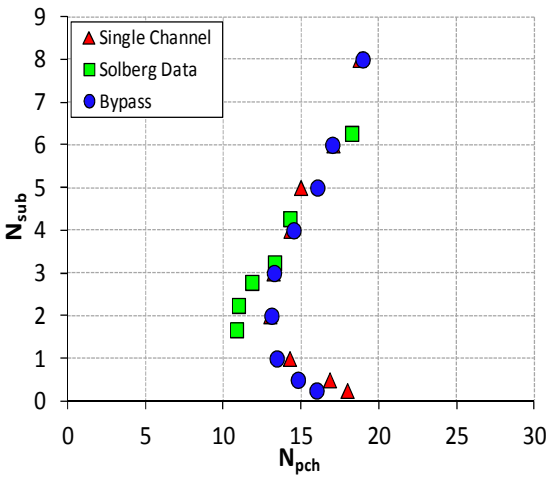

Figure 6.19 Stability map for the bypass case and the single channel case and comparison with the experimental data of Solberg (1966).

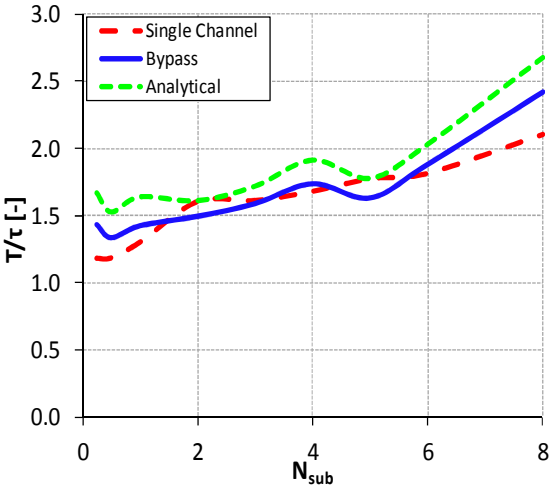

Figure 6.20 Ratio between the period of oscillations and the transit time and comparison with the analytical calculation.

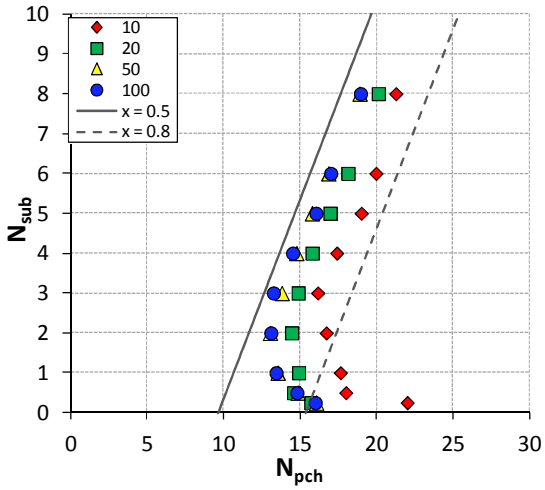

Figure 6.21 Stability map for different values of the bypass ratio.

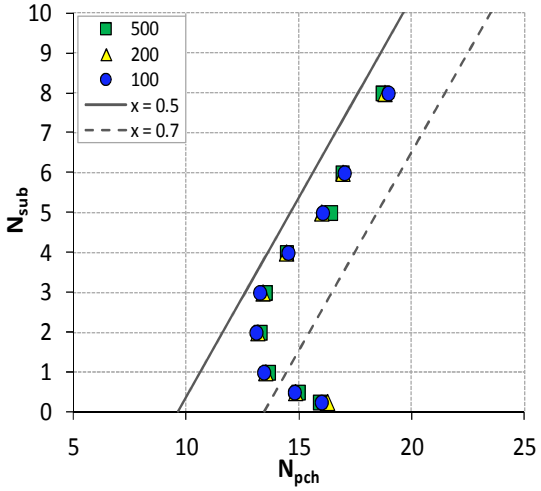

Figure 6.22 Stability map for different values of the bypass ratio.

Finally, a sensitivity analysis on the bypass ratio is presented. The ratio is at first reduced to find out the value required to guarantee a constant pressure drop across the heated channel. The results are presented in Figure 6.21. Halving the bypass ratio (R_{by}= 50) does not modify the stability of the heated channel. On the contrary, the system becomes more stable with a further reduction. In particular, the present results point out that the stability boundary is not modified by a reduction of the bypass area up to the value of R_{by}= 20. A further reduction (R_{by}=10) turns out indeed in a marked stabilization of the system. On the other hand, a bypass area higher than the considered nominal one (up to 200 and 500 respectively) does not affect significantly the stability of the system (Figure 6.22). Thus, the system stability is shown to be independent on the bypass ratio for a sufficiently large value of R_{by}.

6.5.2 Parallel channels

6.5.2.1 BWR subchannel geometry

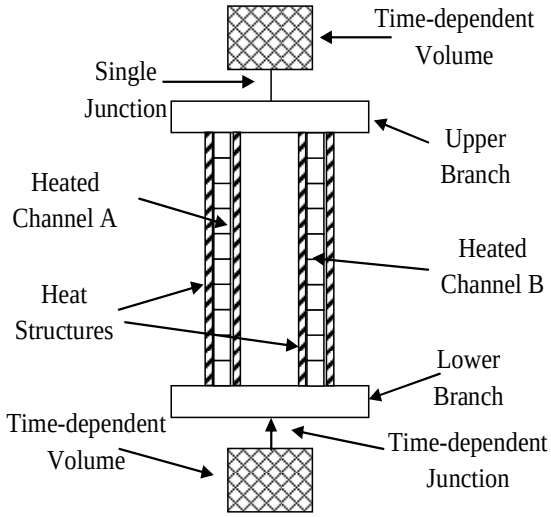

Figure 6.23 RELAP5 nodalization for parallel straight tubes with common lower and upper headers.

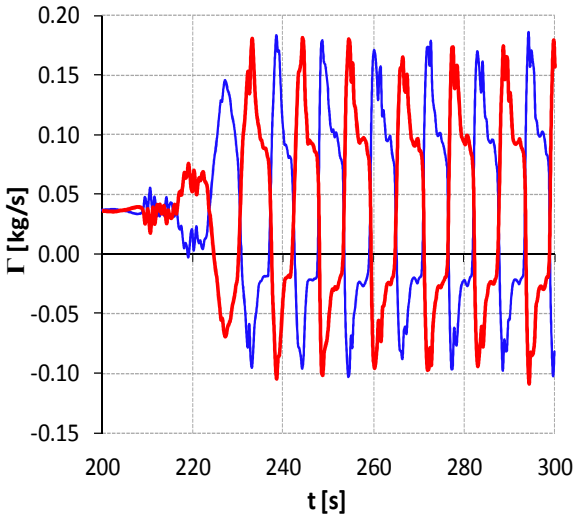

Figure 6.24 Mass flow rate oscillations during DWO in parallel channels.

A description of the two parallel channel nodalization developed in RELAP5 is provided in Figure 6.23. A twin channel is added to the system, with connection through common lower and upper headers. The physical parameters and the tube size are kept equal to the values reported in Table 6.1, as the BWR core subchannel geometry is simulated. Code models and numerical settings are exactly the same as in Section 7.5.1, thus the UVUT model, the semi-implicit numerical scheme and a time step always equal to the 95% of the Courant limit. In a system of two parallel channels, density wave instability occurs with counter-phase oscillations of the flow rate in the two channels (Figure 6.24). Stability map for two parallel tubes is shown in Figure 6.25, where it is compared to the stability thresholds of the single channel. Except for small deviations at low inlet subcooling, density wave instability exhibits the same behavior in the three different systems. Hereby, with the correct

settings, RELAP5 shows satisfactory prediction capability with respect to DWOs also in a parallel channel system featuring the simple geometry of a BWR subchannel.

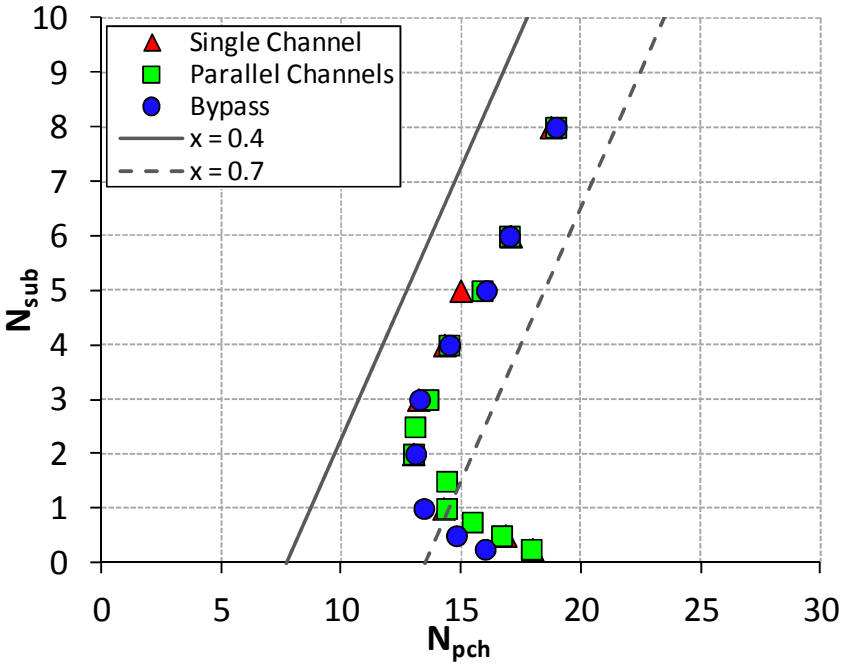

Figure 6.25 Stability maps for a parallel channel system compared with single channel and bypass configurations.

6.5.2.2 SIET experimental facility

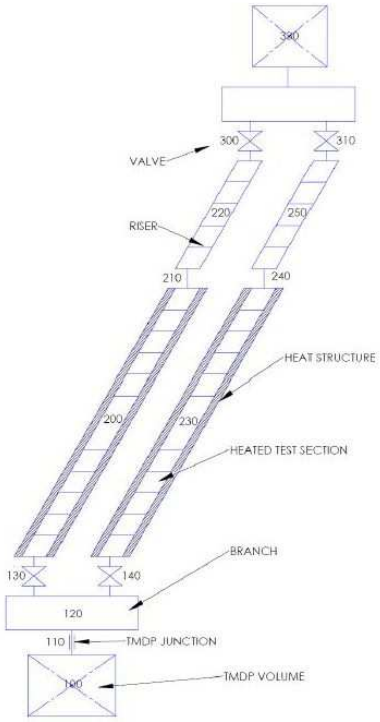

Figure 6.26 RELAP5 nodalization for the helically coiled parallel channel facility.

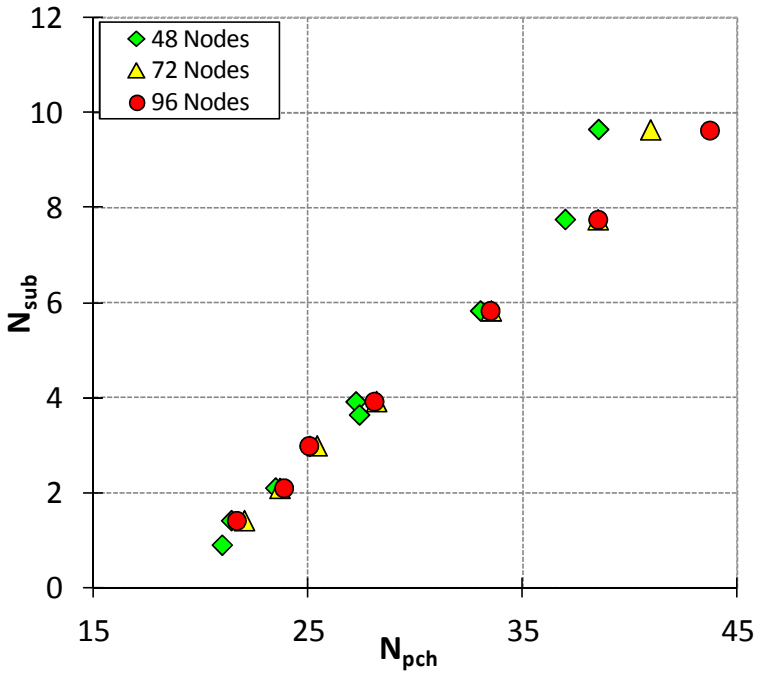

Figure 6.27 Sensitivity study on the number of nodes in the pipe elements for the SIET facility RELAP5 nodalization.

The SIET experimental facility is modeled with its real dimensions shown in Table 2.1. The RELAP5 nodalization is shown in Figure 6.26. The RELAP5 code allows only to represent rectilinear duct, being a 1-D code. Therefore, to reproduce the length and the height of the facility, a straight inclined tube has been assumed, with the same inclination of the helical coil. In this way, as for the analytical model in Section 7.1, both the gravitational and the frictional pressure drops are properly taken into account. Every channel includes two pipe elements, to reproduce the first 24 heated meters of the test section and the final 8 meters of the riser. As a consequence, heat structures are connected to the fluid volumes only for the first 24 meters. For the heated pipes, the number of elements is set to 96 after a sensitivity study, shown in Figure 6.27 for the case at 40 bar and 600 kg/m^{2}s. Finally, no concentrated pressure drops are present at the outlet of the test section. The first set of simulations made with the RELAP5 code exhibited marked differences with respect to the experimental data. In particular, the code overestimates considerably the instability threshold in all conditions, as it is shown from Figure 6.28 to Figure 6.31. The overestimation is particularly high at high subcoolings, whereas an acceptable agreement is only found at low-medium pressure and low subcooling. At high pressure (Figure 6.31), the overestimation is so high that the instability is predicted at an exit quality significantly higher than one. As a consequence, the RELAP5 code seems not a reliable simulation tool for the prediction of the DWO instability, at least with helically coiled parallel tubes. Differently, the results were quite good with the BWR geometry. For this reason, it can be interesting to modify tube length and inclination one by one (starting from BWR geometry), to study their influence on the system stability. The system exhibits a marked stabilization when increasing the length of the channel maintaining the inclination fixed (straight vertical duct).

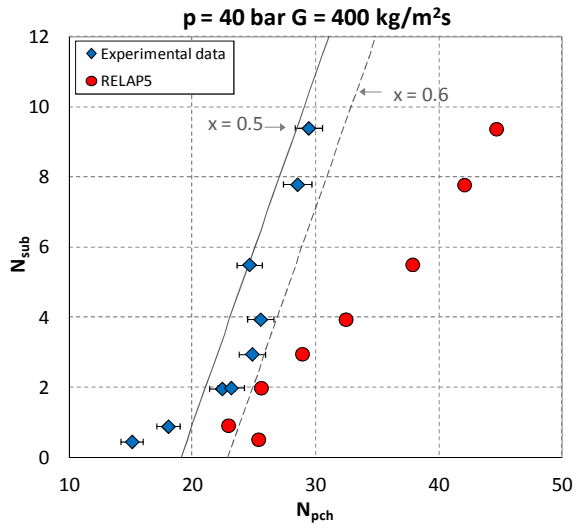

Figure 6.28 Comparison between the experimental data and the RELAP5 results at p = 40 bar and G = 400 kg/m^{2}s.

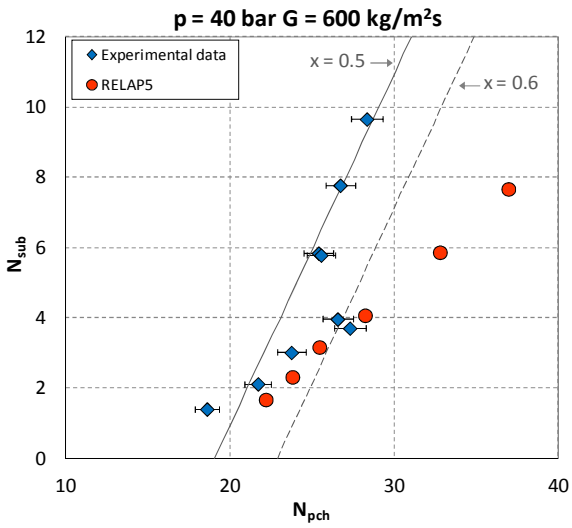

Figure 6.29 Comparison between the experimental data and the RELAP5 results at p = 40 bar and G = 600 kg/m^{2}s.

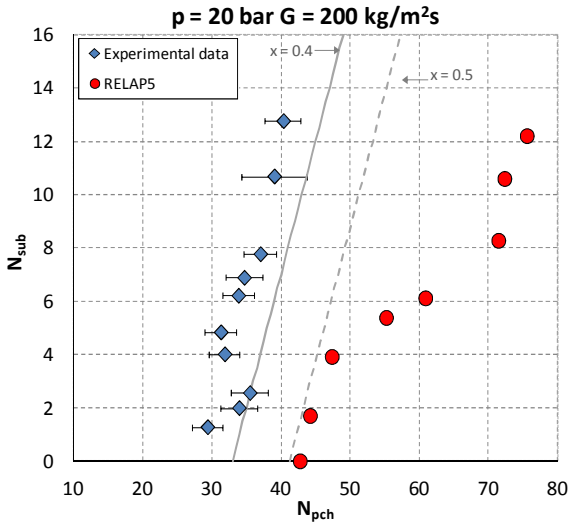

Figure 6.30 Comparison between the experimental data and the RELAP5 results at p = 20 bar and G = 200 kg/m^{2}s.

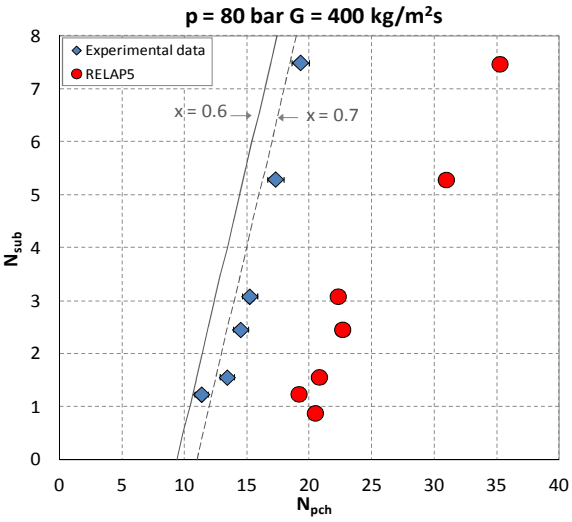

Figure 6.31 Comparison between the experimental data and the RELAP5 results at p = 80 bar and G = 400 kg/m^{2}s.

In Figure 6.32, three different tube lengths are presented: BWR subchannel (3.66 m), experimental facility tube (32 m), and a vertical channel with length equal to the height of the experimental facility (8 m). Obviously, the stabilization is larger passing from 8 m to 32 m. The effect of tube length appears somewhat strange, because it is expected to increase of the same relative amount both frictional and gravitational pressure terms, which are proportionally to tube length. Although the gravitational pressure drop is not negligible in a straight vertical tube, one expects the two-phase frictional pressure drop to be the most important term in total pressure drop balance. An increase of two-phase frictional pressure losses, concentrating the pressure drop near the channel exit, is expected to increase system propensity to instability (Rizwan-uddin, 1994).

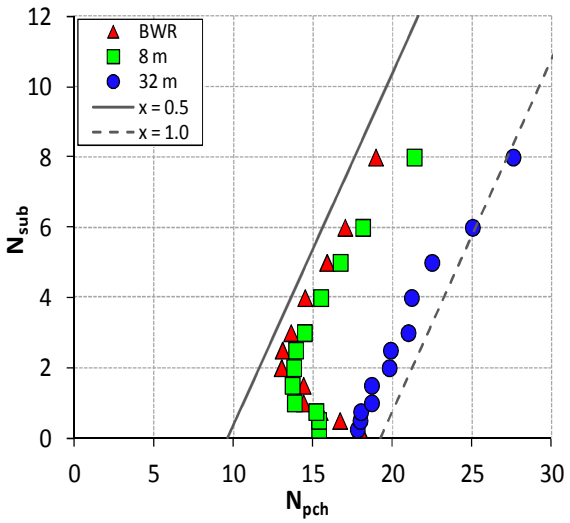

Figure 6.32 Stability maps in parallel channels for different channel lengths.

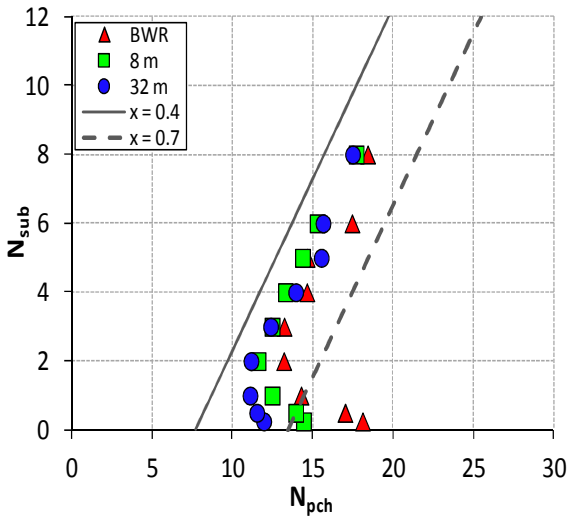

Figure 6.33 Stability maps in a single channel for different channel lengths.

When only a single channel is considered, tube length influence seems to disappear (Figure 6.33) and the stability threshold remains almost unchanged. The latter result could suggest some difficulties of the RELAP5 code in addressing a more complex geometry (as the stabilization highlighted in Figure 6.32 when increasing tube length could be induced just by numerical diffusion, introduced to assure the convergence of the calculations).

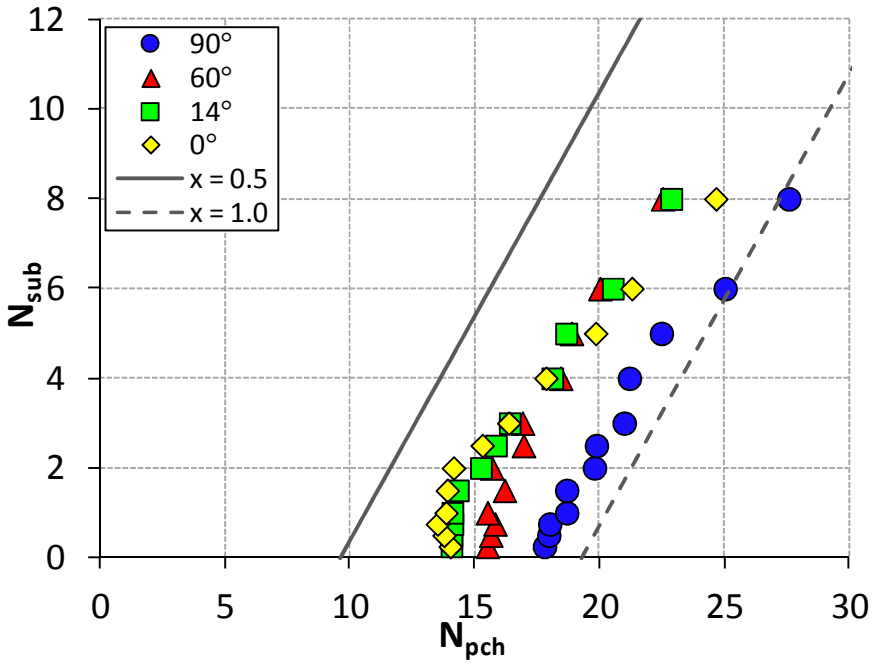

Figure 6.34 Stability maps in parallel channels for different channel inclinations, from an horizontal (0°) to a vertical channel (90°).

Figure 6.34 reports the stability maps obtained with the RELAP5 varying tube inclination while maintaining fixed the channel length. The stable region widens as the tube approaches the vertical orientation (starting from an horizontal duct). An increase in inclination (hence

from horizontal to vertical duct) turns out in a higher gravitational pressure drop term, concentrated in the single-phase region, where higher is the density of the fluid. Increase in single-phase region pressure drop, close to channel inlet section, reinforces system stability. As concerns tube inclination, the RELAP5 code shows the capability to qualitatively reproduce its physical influence on the instability inception.

The marked stable system obtained with parallel helical tubes does not appear if a slight difference in length between the two tubes is included in the simulation. The stability maps shown from Figure 6.28 to Figure 6.31 were repeated considering a different in length of 1 cm between the two channels. Even with a very small difference in length, the results are totally different, as it shown from Figure 6.35 to Figure 6.38. The system is always unstable with respect to the experimental data, but the results are closer to the real behavior of the system and the code results seem generally more consistent. The numerical results, in particular in the medium-high subcooling region, are now aligned on a constant quality line, in agreement with the experimental findings and the literature theory. In addition, accurate predictions of the stability boundary are obtained, in particular at high pressure and low mass flow rate (Figure 6.37 and Figure 6.38). Further improvements are certainly possible, as an example with the implementation in the code of some proper models for the helical geometry. Despite the more consistent results using slightly different channel lengths, the difference in the stability maps continue to confirm some difficulties of the RELAP5 code when dealing with a more complex geometry. Since there are no physical explanations for the noteworthy modification of the system stability, it can be ascribed to some numerical errors. The latter is anyway a relevant code drawback that needs further future investigations.

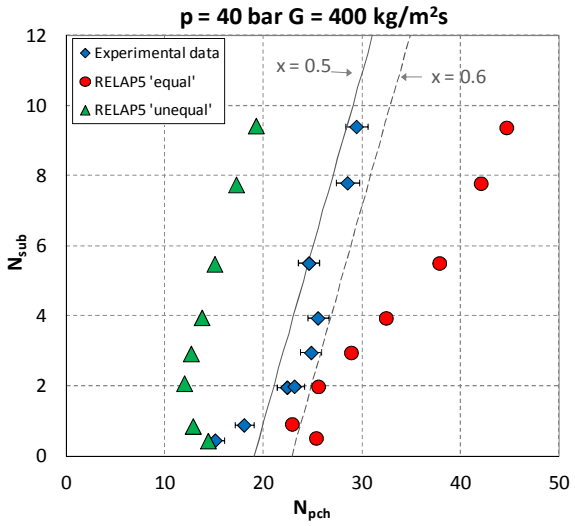

Figure 6.35 Comparison between the experimental data and the RELAP5 results with "unequal" and "equal" channel lengths at p = 40 bar and G = 400 kg/m^{2}s.

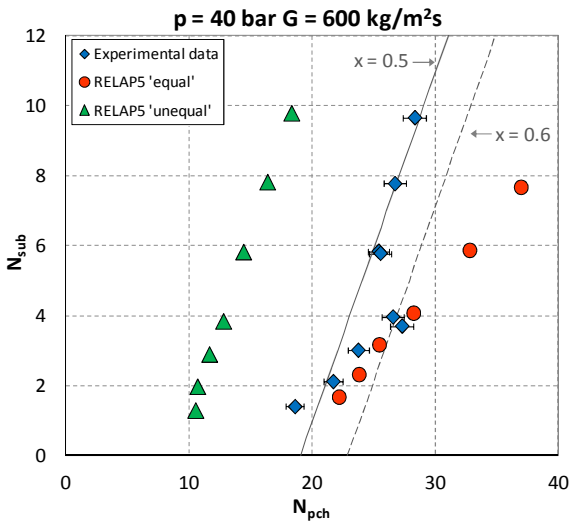

Figure 6.36 Comparison between the experimental data and the RELAP5 results with "unequal" and "equal" channel lengths at p = 40 bar and G = 600 kg/m^{2}s.

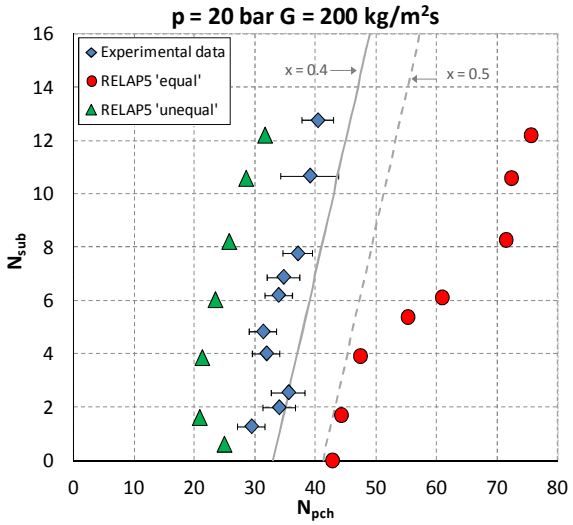

Figure 6.37 Comparison between the experimental data and the RELAP5 results with "unequal" and "equal" channel lengths at p = 20 bar and G = 200 kg/m^{2}s.

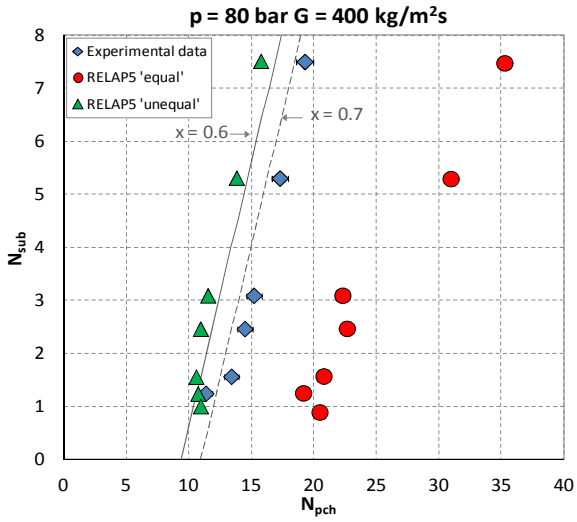

Figure 6.38 Comparison between the experimental data and the RELAP5 results with "unequal" and "equal" channel lengths at p = 80 bar and G = 400 kg/m^{2}s.

6.6 Conclusions

In this final chapter of the thesis work, the subject of DWOs in parallel helically coiled channel has been addressed. As in the whole thesis, a modeling tool appropriate for a proper simulation of the phenomenon under study has been developed. At the same time, also a numerical study of the subject has been completed, this time with the RELAP5 best estimate system code, extensively used in the nuclear field for the analysis of transients and postulated accidents in LWRs.

First, an analytical dynamic model has been developed, starting from an available model built in a recent thesis work (Papini, 2011). The model is based on a lumped parameter, moving boundary approach, and describes the two-phase flow with the assumption of an homogeneous flow. The dynamic behavior of the system is described through the set of 9 non linear ODEs, that are solved in the SIMULINK platform of the MATLAB software. The model developed by Papini (2011) represented a precious starting point. The non linear character of the model equations allowed to consider the complex interactions between different system parameters, which are at the origin of the instability phenomena.

In this thesis, the model has been upgraded from the homogeneous flow model to a drift-flux model, that allows to account for the relative velocity between the phases and should generally produce a more accurate description of the two-phase flow. The empirical correlations for the frictional pressure drop and the void fraction, developed during the thesis work, has been inserted into the model, obtaining a more accurate characterization of the helically coiled pipe under study. In addition, the inclusion of the two correlations guarantees an additional value to the work presented in the previous chapters of the thesis. Within these respects, this final chapter becomes the appropriate ending of all the research work developed throughout the whole thesis work.

The results of the analytical model has been compared with the experimental data collected at the SIET facility. The accuracy of the model is generally improved, with particularly good results obtained at low mass flow rate and at high pressure. Nevertheless, the region of the low subcoolings remains very difficult to predict, as the model continues to show the classical "L-shape" of the stability boundary, typical of straight vertical tubes. On the contrary, the experimental data show an unusual behavior, where an increase in the inlet subcooling stabilizes the system also at low subcoolings. The latter result represents an incentive for more work on the subject, with the aim to obtain a proper description of the stability boundary also at low subcoolings. In particular, can be of interest a further upgrade to a 1-D description and the inclusion in the model of the effect of the subcooled boiling, with a model specifically developed for the helical geometry.

The numerical study with the RELAP5 allowed to assess the capability of the code to reproduce the DWO instability. Numerous layouts have been simulated, starting from the simple case of a single vertical channel. The RELAP5 code shows good results until the geometry of the system under study is relatively simple. Accurate stability boundaries have been obtained also with parallel channels, reproducing the typical geometry of a BWR subchannel. Instead, a code drawback was identified in the simulation of helically coiled parallel channels. They have been modeled in the code as inclined straight tubes, therefore maintaining both the length and the height of the SIET facility, since no models for the helical geometry are included in the code. The results with an identical channel length shows a particularly stable system, far more stable with respect to the experimental data. Stability maps more closer to experiments, but also more consistent although more unstable than experiments are obtained using slightly different channel lengths. Since there are no physical explanations for the marked stabilization observed with an exactly equal channel length, it has been ascribed to some numerical errors. In any case, it represents a relevant code drawback that surely needs further future investigations.

References

W. Ambrosini, P. Di Marco, J.C. Ferreri, 2000. Linear and nonlinear analysis of density wave instability phenomena. International Journal of Heat and Technology 18, 27-36.

W. Ambrosini, J.C. Ferreri, 2006. Analysis of basic phenomena in boiling canne instabilities with different flow models and numerical schemes. Proceedings of the 14th International Conference on Nuclear Engineering (ICONE 14), Miami, Florida, USA, July 17-20.

J.A. Bouré, A.E. Bergles, L.S. Tong, 1973. Review of two-phase flow instability. Nuclear Engineering and Design 25, 165-192.

M.B. Carver, 1970. Effect of by-pass characteristics on parallel-channel flow instabilities. In: Fluid Mechanics and Measurements in Two-Phase Flow Systems, Proceedings of the Institution of Mechanical Engineers 1969-1970 184 , 3C, 84-92.

D.B. Collins and M. Gacesa, 1969. Hydrodynamic instability in a full scale simulated reactor channel. Proceedings of the Symposium on Two Phase Flow Systems, Leeds, Institute of Mechanical Engineers, London, England.

T. Hamidouche, A. Bousbia-salah, 2006. RELAP5/3.2 assessment against low pressure onset of flow instability in parallel heated channels. Annals of Nuclear Energy 33, 510-520.

G.Y. Han, T.P. Stanley, 1999. Thermal-hydraulic transient analysis of light water reactor using moving boundaries. Annals of Nuclear Energy 26, 301-326.

T. Hibiki, M. Ishii, 2003. One-dimensional drift flux model and constitutive equations for relative motion between phases in various two-phase flow regimes.

M. Ishii, T. Hibiki, 2006. Thermo-fluid dynamics of two-phase flow. Springer, New York, NY, USA.

S. Kakaç, B. Bon, 2008. A review of two-phase flow dynamic instabilities in tube boiling systems. International Journal of Heat and Mass Transfer 51, 399-433.

H. Li, X. Huang, L. Zhang, 2008. A lumped parameter dynamic model of the helical coiled once-through steam generator with movable boundaries. Nuclear Engineering and Design 238, 1657-1663.

G. Masini, G. Possa, F.A. Tacconi, 1968. Flow instability thresholds in parallel heated channels. Energia Nucleare 15(12), 777-786.

J.L. Munoz-Cobo, M.Z. Podowski, S. Chiva, 2002. Parallel channel instabilities in boiling water reactor systems: boundary conditions for out of phase oscillations. Annals of Nuclear Energy 29, 1891-1917.

D. Papini, 2011. Modelling and experimental investigation of helical coil steam generator for IRIS Small-medium Modular Reactor. Ph.D. Thesis, Doctoral Program in Radiation Science and Technology, XXIII Cycle, Politecnico di Milano, Milano, Italy.

D. Papini, A. Cammi, M. Colombo, M.E. Ricotti, 2011. On density wave instability phenomena: modelling and experimental investigation. In: A. Ashan (Ed.), Two-phase flow, phase change and numerical modelling, InTech Publisher, Rijeka, 257-284, ISBN 978-953-307-584-6.

D. Papini, A. Cammi, M. Colombo, M.E. Ricotti, 2012. Time-domain linear and non-linear studies on density wave oscillations. Chemical Engineering Science 81, 118-139.

Rizwan-Uddin, 1994. Physics of density wave oscillations. International Journal of Multiphase Flow 20, 721-737.

P. Saha, M. Ishii, N. Zuber, 1976. An experimental investigation of the thermally induced flow oscillations in two-phase systems. Journal of Heat Transfer 98, 616-622.

W.R. Schlichting, R.T. Lahey Jr., M.Z. Podowski, 2010. An analysis of interacting instability modes, in a phase change system. Nuclear Engineering and Design 240, 3178-3201.

K.O. Solberg, 1966. Resultats des essais d'instabilites sur la boucle "Caline" et comparaisons avec un code de calcul. Centre d'Etudes Nucléaires de Grenoble (CENG), Note 225.

The Math Works, Inc., 2005. SIMULINK software.

N. Todreas, M. Kazimi, 1993. Nuclear Systems I. Thermal Hydraulic Fundamentals. Taylor & Francis.

US NRC Nuclear Safety Analysis Division, December 2001. RELAP5/MOD3.3 Code Manual. NUREG/CR-5535/Rev 1.

G. Yadigaroglu, 1981. Two-phase flow instabilities and propagation phenomena. In: J.M. Delhaye, M. Giot, M.L. Riethmuller, (Ed.), Thermohydraulics of two-phase systems for

industrial design and nuclear engineering, Hemisphere Publishing Corporation, Washington, 353-396.

G. Yun, H. Jun, X. Genglei, Z. Heyi, 2010. Experimental investigation on two-phase flow instability in a parallel twin-channel system. Annals of Nuclear Energy 37, 1281-1289.

CONCLUSIONS

In the framework of the intense research activity dedicated to the development of new reactor projects of Generation III+ and Generation IV, the helically coiled SG has been the main subject of this doctoral thesis work. An helical coil provides numerous advantages with respect to the same straight duct, not limited to higher heat and mass transfer rates. In addition, the helical geometry guarantees an excellent behaviour in presence of severe thermal expansions and a more compact design of the SG, limiting the required floor space. In view of the listed characteristics and following the ordinary utilization in many industrial fields and some specific applications in the past of the nuclear power industry, helical pipes are today sustained for the application in some Generation IV reactor projects. Even more attention characterizes the pressurized water SMR projects of Generation III+ which adopt an integral layout. Actually, helical coil SGs are very attractive because of the resulting design compactness, which is fundamental for an integral layout, where all the primary system component are located inside the reactor vessel.

The doctoral work found its starting point in the study of the helically coiled SG of the IRIS reactor, carried out in recent years at the Politecnico di Milano by the Nuclear Engineering Division of the Department of Energy. However, the work has not been focused exclusively on the IRIS reactor, but it has been devoted to the study of various aspects of the thermal hydraulic of the helical pipe, without referencing to a specific reactor project. Actually, many SMRs under study foresee helical pipes for their SGs (among others, SMART and NuScale reactors). A double result has been pursued along the thesis; on one hand, the development of proper instruments able to estimate with a good accuracy some of the thermal hydraulic parameters characterizing the helical pipe. Good quantitative estimations of parameters such as the frictional pressure drop, the void fraction and the system stability boundary are indeed fundamental for the engineers involved in the SG design process. On the other hand, the research for improvement in the understanding of some basic physical phenomena characterizing the helical pipe, where the centrifugal force field plays a significant role. It is easy to understand how a detailed analysis and a complete knowledge of all the phenomena that can occur is fundamental for the safe application of a component in a critical field as the nuclear industry. Even more sensitive is the application of the helical coil SG in SMRs, where it fulfils fundamental safety features to assure core cooling during accidents.

In view of the established goals, an overall analysis method has been applied. Experimental data measured on purpose have been the starting point. They have been used for the development of empirical correlations on the two-phase frictional pressure drop and the void fraction, other than the validation of an analytical dynamic model for the study of the two-phase flow instability. At the same time, the fluid flow inside the helical pipe has been studied through numerical simulations, starting from the single-phase flow and ending with the two-phase flow. To the aim, the CFD has been selected as the numerical simulation tool, to obtain the required level of detail in the results. In particular, the ANSYS FLUENT code

has been employed. Also numerical results have been continuously validated through comparison with the experimental data.

The experimental data which constitute the starting point of this doctoral thesis have been measured in an experimental facility installed at the SIET laboratories in Piacenza. The facility was built in the frame of the research on the IRIS reactor and reproduces in full scale its helically coiled SG. It includes two helically coiled tube connected in parallel and it is designed for the simulation of the real reactor operating conditions. Main subjects of the experiments were the frictional pressure drop and the instability of the two-phase flow in a parallel channel system. First, the frictional pressure drops for single-phase liquid flow were measured. Then, also the two-phase frictional pressure drops in adiabatic condition were studied. For the latter case, an analysis exposed a particularly peaked profile of the frictional pressure drop as a function of the flow quality. The peak is considerably more pronounced and shifted to lower values of the flow quality with respect to straight pipes.

As concerns the instability of the two-phase flow, experiments regarded mainly the Density Wave Oscillations (DWOs), with some measurements made also on Ledinegg type instability. It must be noticed that the helical geometry and the characteristics of the test section render the experimental database a unique test case in the field of DWO studies. Discrepancies with the DWO classical theory were observed in the effect of the inlet subcooling and in the period of the oscillations to transit time ratio. For the inlet subcooling, an increase maintains its stabilizing effect also at low subcoolings, in contrast with what happens in straight parallel vertical tubes. For the period of oscillations to transit time ratio, it is found very low at high subcooling and it is increased up to 1.5 – 2 if the subcooling is reduced.

After the presentation of all the experimental data, the thesis work has been focused on different subjects related to the thermal hydraulic of helical pipe.

Single-phase flow. A comparison with the experimental data on the friction coefficient and the laminar to turbulent flow transition revealed a good agreement with correlations available from literature. The best correlations have been identified and no need for further improvement seemed necessary.

The single-phase flow has been extensively characterized with CFD simulation in the laminar regime. Numerical results exhibited the effect of the centrifugal force field, which shifts the velocity maximum towards the outer wall and generates a secondary motion on the pipe cross section with the appearance of two counter rotating vortices. Also the effect of the torsion has been studied, which tends to break the symmetry of the two vortices. Numerical results show an average relative error lower than 5 % with respect to friction factor experimental data. The discrepancies are comparable to those returned by the most accurate literature correlations.

In the turbulent region, the results of the CFD simulations were compared to the frictional pressure drop experimental data, to validate the predictions of different turbulence models. Actually, for the conditions investigated in the study, it is the wall treatment that plays the dominant role to determine the accuracy of the simulation. Satisfactory results were obtained in the whole range of Reynolds numbers only with the enhanced wall treatment, which solves the flow field all the way to the wall Therefore, the wall treatment seems necessary to

reproduce the correct behavior of the wall shear stress, which is modified with respect to the case of a straight duct by the presence of the secondary motion.

Two-phase flow. The CFD study has been extended to the two-phase flow, main subject of the whole thesis work. An adiabatic flow has been modeled with the Eulerian-Eulerian approach, considering only the drag force for the momentum exchange between the phases. Before simulating the SIET experimental data, a detailed validation of the CFD model was necessary. An air-water flow at atmospheric pressure has been simulated at first. Actually, the significantly higher number of available literature studies made easy the validation. Phase distribution was qualitatively compared with literature images obtained with the imaging tomography technique. Void fraction and two-phase frictional pressure drop were successfully validated through comparison with the data of Akagawa et al. (1971). After the validation, the simulation of the two-phase flow in the SIET facility has also been also addressed.

The CFD study reached different goals. Qualitatively, it allowed the detailed description of the phase interaction and the distribution of the phases inside the duct under the influence of the centrifugal force field. For the SIET case, a physical explanation has been provided for the marked peak in the frictional pressure drop profile. It is ascribable to a rupture of the liquid film at the wall, that causes the shift to a dispersed liquid flow regime. Quantitatively, the frictional pressure drops were predicted with a satisfactory average relative error included between 10 % and 15 % for all the conditions examined, even though they were remarkably different (from air-water in atmospheric conditions to steam water at high pressure; from small helices with coil diameter under 0.225 m to the larger SIET coil with D = 1 m). The numerical results showed an average error comparable with the best literature correlations when they are applied on their original databases. The numerical model, instead, has been demonstrated to be not dependant on a particular set of data or range of parameters, although it requires high simulation time and computational resources. The void fraction has been predicted with a very good average relative error lower than 5 % in the air-water case. In addition, the numerical results can successfully support the experimental measurements, as for the void fraction. Void fraction data for the SIET conditions were derived from CFD results, since it was not possible to measure them in the facility.

Void fraction analysis and correlation. The void fraction inside the helically coiled pipe obtained from CFD has been analyzed using the drift-flux model, to further assess the numerical results. Calculation of the drift flux model parameters (the distribution parameter C_0 and the average drift velocity V_{gj}) from local CFD values of volumetric flux and void fraction constituted a further demonstration of their consistency.

Starting from the CFD results, an empirical correlation for the void fraction has been derived for the air-water case:

$$\langle \alpha \rangle = \frac{\langle j_g \rangle}{1.175\langle j \rangle + 0.0003}$$

The correlation shows an average relative error lower than 5 % with respect to different literature datasets. An empirical correlation has been developed from CFD results also for the SIET pipe:

$$\langle \alpha \rangle = \frac{\langle j_g \rangle}{[1 + 0.117(1 - x)]\langle j \rangle + 0.0016}$$

Finally, the analysis based on the drift-flux model allowed to identify some inconstancies at low flow quality, suggesting the necessity to improve the model in that quality region.

Correlation for the frictional pressure drop. A new correlation for the prediction of the two-phase frictional pressure drop has been developed, aiming at a formula appropriate for an large range of geometries and operating conditions. Actually, numerous correlations were available in literature, although none of them can be considered of general validity, neither applied to a wide range of geometrical parameters and operating conditions. The new correlation is based on the model of Lockhart and Martinelli with proper modification parameters:

$$\Phi_l^2 = 0.0986 \Phi_{LM}^2 De_l^{0.19} \left(\frac{\rho_m}{\rho_l}\right)^{-0.4}$$

The correlation shows an average relative error of 14.4 % when compared to two different datasets, due to Zhao et al. (2003) and Santini et al. (2008). The two datasets include data from different geometries and operating conditions. The new correlation outperforms all the other correlations considered for comparison, demonstrating the capability to be reliable in a wider range of geometries and operating conditions, reaching the initial objective of the study.

DWO instability. DWOs in parallel helically coiled channel constituted the final subject of the thesis work. First, an analytical dynamic non linear model has been developed, starting from an available model built in a recent thesis work (Papini, 2011). The model was based on a lumped parameter, moving boundary approach, and described the two-phase flow with the assumption of homogeneous flow. The model has been upgraded from the homogeneous flow model to a drift-flux model. The empirical correlations developed for the frictional pressure drop and the void fraction have been included into the model, obtaining a more accurate characterization of the helically coiled pipe under study. Within these respects, this final chapter becomes the appropriate ending of all the research work developed throughout the whole thesis work. The results of the analytical model have been compared with the experimental data collected at the SIET facility. The accuracy of the model is generally improved, with particularly good results obtained at low mass flow rate and at high pressure. Nevertheless, the region of the low subcoolings remains very difficult to predict, as the model continues to show the classical “L-shape” of the stability boundary.

Also a numerical study with the RELAP5 was made, to assess the capability of the code to reproduce the DWO instability. The RELAP5 code shows good results until the geometry of the system under study is relatively simple. Accurate stability boundaries have been obtained also with parallel channels, reproducing the typical geometry of a BWR subchannel. Instead, a code drawback was identified in the simulation of helically coiled parallel channels. Consistent estimations of the stability boundary, although with a system always depicted

more unstable with respect to experiments, were obtained using slightly different channel lengths. With identical channel lengths, instead, a particularly stable system is shown, far more stable with respect to the experimental data. This relevant code drawback, which needs further future investigations, has been ascribed to some numerical errors, since no physical explanation exists for such behavior.

Future developments. Notwithstanding the large amount of work made, future improvement are desirable on different subjects:

- Considering the good results obtained with the CFD simulation of the two-phase flow, more work can be made to upgrade the model. First, the model should be improved in the low flow quality region, to eliminate the discrepancies in the results underlined with the drift-flux analysis. In addition, the model can be upgraded from an adiabatic flow, considering the effect of thermal power, boiling and heat transfer up to the thermal crisis occurrence;
- Further validation is necessary for the void fraction empirical correlation, if experimental data become available.
- Although improvements were obtained, the analytical model for the simulation of the DWO instability should be improved further to obtain a proper description of the stability boundary also at low subcoolings. In particular, can be of interest a further upgrade to a 1-D description and the inclusion in the model of the effect of the subcooled boiling, with a model specifically developed for the helical geometry. More work is also necessary to better understand the drawback identified in the predictions of the DWOs in helically coiled parallel channels with the RELAP5 code.

Appendix A

Uncertainty analysis of the experimental data

A.1 Error analysis of the experimental results

The uncertainty analysis is a fundamental step for any experimental data reduction, which allows quantifying the validity of the results obtained from the experiments. The main steps leading to the definition of the error bars introduced within the experimental data graphs are presented in this Appendix. The error analysis is the study and the evaluation of the uncertainties, to which all the physical quantities are unavoidably subject. Throughout all the thesis work, the linear analysis introduced by Moffat (1998) has been applied to the experimental data (except for the single-phase flow, as mentioned in Chapter 2).

The correct way to express the correct result of any measurement is to give the best estimate of the quantity under examination as well as the interval within it is confident it can be included. Thus, the result of any measured quantity x is composed by the best estimate of the quantity x_{best} and an associated uncertainty or error δx. This means that the real value of the quantity x is reasonably confident to fall between $x_{best} - \delta x$ and $x_{best} + \delta x$. Other than the absolute error δx, also the relative measurement error can be obtained dividing the absolute error by the best estimate of the quantity x_{best}.

During experiments, some physical quantities are directly measurable, whereas many other can be derived by the measured ones. In the same way, the errors of the not measurable quantities must be derived propagating and combining the uncertainties of the measurable ones. Moffat (1998) introduced the root sum square concept for the error propagation, implemented, with the hypothesis of independent and random errors, according to three simple rules here resumed:

Uncertainty in addition and difference

Considering a quantity y calculated from different measurable quantities in the following way:

$$y = x + \cdots + z - (u + \cdots + w) \tag{A.1}$$

The absolute error associated to the variable y can be derived as the root sum square of the absolute error associated to the initial quantities:

$$\delta y = \sqrt{(\delta x)^2 + \cdots + (\delta z)^2 + (\delta u)^2 + \cdots + (\delta w)^2} \tag{A.2}$$

Uncertainty in multiplication and division

Considering some measured quantities *x*, …, *w* and their associated uncertainties δ*x*, …, δ*w*, which are used to derive the following quantity *y*:

$$y = \frac{x \ldots z}{u \ldots w} \tag{A.3}$$

The uncertainty associated to the quantity *y* is calculated as the root sum square of the initial relative errors:

$$\frac{\delta y}{y} = \sqrt{\left(\frac{\delta x}{x}\right)^2 + \cdots + \left(\frac{\delta z}{z}\right)^2 + \left(\frac{\delta u}{u}\right)^2 + \cdots + \left(\frac{\delta w}{w}\right)^2} \tag{A.4}$$

Uncertainty in any function

If a quantity *x*, measured with an uncertainty δ*x*, is used to calculate any function *q(x)*, then the final error δ*q* is given by:

$$\delta y = \left(\frac{dy}{dx}\right)\delta x \tag{A.5}$$

The above rules have been applied for the calculation of the uncertainties of the experimental data measured at the SIET laboratories and presented in Section 2. To the aim, the uncertainties associated to the different measured quantities are of fundamental importance and the starting point. They have been shown in Table 2.3 of Chapter 2, that it is here proposed again.

Table A.1 List of the relative uncertainties of the measured physical quantities.

Water flow rate	± 1%
Fluid bulk and wall temperature	± 0.7 °C
Absolute pressure	± 0.1%
Differential pressure	± 0.4%
Supplied electrical power	± 2.5%
Evaluated thermal losses	± 15%

A.2 Calculation of the frictional pressure drop data uncertainties

For the error analysis of the two-phase frictional pressure drop experimental data, the uncertainties of the frictional pressure drop data and of the quality must be determined. The quality is calculated with an energy balance (thermodynamic quality), so its uncertainty depends on the inlet enthalpy in the preheater, the mass flow rate and the thermal power supplied to the mixture. The uncertainties of the saturation properties due to pressure have

been neglected, so all the uncertainties in fluid properties due to pressure. The thermal power supplied to the fluid is obtained as the difference between the electrical power measurement minus the thermal losses. Therefore its uncertainty:

$$\delta q = \sqrt{(\delta q_{el})^2 + (\delta q_{loss})^2} \tag{A.6}$$

The uncertainties of the electrical power and the thermal losses follow from their measured and calculated quantities and their relative uncertainties, known from Table A.1:

$$\delta q_{el} = q_{el} \cdot 2.5\% \tag{A.7}$$

$$\delta q_{loss} = q_{loss} \cdot 15\% \tag{A.8}$$

The uncertainty of the mass flow rate is simply known from its measured value and its relative uncertainty. Therefore, the relative uncertainty related to the enthalpy increase in the preheater results:

$$\frac{\delta \Delta h}{\Delta h} = \sqrt{\left(\frac{\delta q}{q}\right)^2 + \left(\frac{\delta \Gamma}{\Gamma}\right)^2} \tag{A.9}$$

The quality uncertainty is due to the enthalpy increase uncertainty and the uncertainty of the enthalpy at the preheater inlet. For the inlet enthalpy, it is related to the uncertainty in the temperature measurements, used to calculate the pre heater inlet fluid properties. Therefore:

$$\delta h = \sqrt{(\delta h_{in})^2 + (\delta \Delta h)^2} \tag{A.10}$$

$$\frac{\delta x}{x} = \frac{\delta h}{h} \tag{A.11}$$

The frictional pressure drop is calculated subtracting the gravitational pressure drop from the total pressure drop measurement. The uncertainty in the measurement is obtained from the relative uncertainty in Table A.1. The uncertainty in the gravitational pressure drop is due to the mixture density, which is function of the uncertainty in the quality:

$$\delta \Delta p_{fr} = \sqrt{\left(\delta \Delta p_{exp}\right)^2 + \left(\delta \Delta p_{grav}\right)^2} \tag{A.12}$$

$$\frac{\delta \Delta p_{grav}}{\Delta p_{grav}} = \frac{\delta x}{x} \tag{A.13}$$

A.3 Calculation of the instability data uncertainty

For the instability data, the objective of the analysis is to provide an estimate of the error bars of the subcooling number and the phase change number, N_{sub} and N_{pch}:

$$N_{sub} = \frac{\Delta h_{in}}{h_{lg}} \frac{v_{lg}}{v_l} \tag{A.14}$$

$$N_{pch} = \frac{\Omega}{\frac{v_{in}}{L}} = \frac{\frac{q}{AL}\frac{v_{lg}}{h_{lg}}}{\frac{v_{in}}{L}} = \frac{q}{\Gamma h_{lg}} \frac{v_{lg}}{v_l} \tag{A.15}$$

Neglecting again the uncertainties related to the saturation properties, the uncertainties on the subcooling number is known from the enthalpy at the inlet of the test section, calculated in Eq.(A.10):

$$\frac{\delta N_{sub}}{N_{sub}} = \frac{\delta h}{h} \tag{A.16}$$

The uncertainty of the phase change is instead due to the thermal power supplied to the test section and the mass flow rate:

$$\frac{\delta N_{pch}}{N_{pch}} = \sqrt{\left(\frac{\delta q}{q}\right)^2 + \left(\frac{\delta \Gamma}{\Gamma}\right)^2} \tag{A.17}$$

The term in Eq.(A.17) has been derived in the previous section.

ACKNOWLEDGEMENTS

Ringrazio il prof. Marco Ricotti per le opportunità concessemi in questi tre anni di dottorato e la possibilità di fare ricerca su argomenti tanto stimolanti. Ringrazio il dott. Antonio Cammi e il dott. Luigi Colombo per il costante indirizzo, aiuto e supporto durante tutta l'attività di ricerca. Voglio ringraziare anche il prof. Fabio Inzoli, per i fondamentali suggerimenti durante l'esecuzione delle simulazioni CFD.

Un ringraziamento particolare va a Davide Papini, con cui ho condiviso almeno metà del percorso di dottorato e gli sforzi su alcuni degli argomenti di questa tesi, oltre alle indimenticabili trasferte in SIET. Ringrazio anche Marco Santinello, Jacopo De Amicis e Mirko Millefanti, per l'opportunità di collaborare con loro durante le loro tesi di laurea, risultate fondamentali per il raggiungimento di alcuni dei risultati contenuti in questa tesi. Voglio ringraziare Gael Guedon per l'aiuto con le simulazioni CFD e la pazienza dimostrata nel far girare le mie simulazioni. Ringrazio inoltre tutti gli altri dottorandi e tesisti del gruppo con cui ho avuto l'onore di condividere gli sforzi, i momenti brutti e quelli più belli di questi ultimi tre anni. Ponci, Stefano, Manu, Vito, Sara, Pietro, Giovanni, Carlo, Claudia, Alberto, Matteo e Giacomo, grazie ad ognuno di voi. Non dimentichiamo anche il mitico mazzo di carte, animatore insostituibile delle nostre pause pranzo.

Un sentito ringraziamento a tutte le persone incontrate durante le prove sperimentali in SIET. In particolare Gustavo Cattadori e Andrea Achilli, per la loro disponibilità e l'aiuto nella progettazione delle campagne di prova. Stefano Gandolfi, per l'assistenza e supervisione durante le prove. Matteo Greco e Gaetano Tortora, instancabili operatori di impianto ed esecutori di ogni nostro desiderio.

Desidero ringraziare Lara per essere sempre stata al mio fianco e per la pazienza dimostrata in questi tre anni. Con questa tesi si conclude un capitolo della nostra vita e speriamo di iniziarne uno nuovo al più presto. Ringrazio tutta la mia famiglia, per il costante supporto durante tutti questi anni di studio e l'opportunità di poter fare tutte le scelta nella più totale serenità. Un ringraziamento particolare a tutti gli amici, vecchi e nuovi, e a tutti i compagni del Lonate basket.

Finally, I wish to thank all the amazing people I met in Corvallis. In particular Dr. Jose Reyes, Dr. Sooyun Joh and Dr. Kent Welter, wonderful engineers and even better persons. I want to thank all the friends and in particular Kenny, Russell, Brian and Natasha, Mike and Julie, thank you, you made me feel like at home and I hope to see you soon.